NATIONAL UNIVERSITY OF IRELAND MAYNOOTH

Quasi-Optical Modelling of Telescope Systems for Planck and STEAMR

by

Daniel Wilson

A thesis submitted in partial fulfillment for the degree of Doctor of Philosophy

in the

Faculty of Science and Engineering
Department of Experimental Physics

May 2014

Declaration of Authorship

I, Daniel Wilson, declare that this thesis titled, 'Modelling of Telescope Systems for Planck and STEAMR' and the work presented in it are my own. I confirm that:

- This work was done wholly or mainly while in candidature for a research degree at this University.
- Where any part of this thesis has previously been submitted for a degree or any other qualification at this University or any other institution, this has been clearly stated.
- Where I have consulted the published work of others, this is always clearly attributed.
- Where I have quoted from the work of others, the source is always given. With the exception of such quotations, this thesis is entirely my own work.
- I have acknowledged all main sources of help.
- Where the thesis is based on work done by myself jointly with others, I have made clear exactly what was done by others and what I have contributed myself.

Signed: _____

Date: _____

“c’est en faisant n’importe quoi qu’on devient n’importe qui”

Rémi Gaillard

Abstract

This thesis is concerned with the high-frequency quasi-optical modelling of telescope systems, with special attention paid to the Planck satellite, but further work is also performed on the Stratosphere-Troposphere Exchange And climate Monitor Radiometer (STEAMR) and the Far Infrared Instrument (FIRI). The primary work surrounds the modelling of far sidelobe (FSL) patterns of the Planck telescope, with a view to replicating features seen in some of the difference maps made by the 857-GHz channel of Planck's High Frequency Instrument (HFI). This is done using a variety of techniques in a number of software packages. The General Reflector Antenna Software Package (GRASP9) is used for accurate characterisation of the FSLs using two analysis methods: Physical Optics (PO), and Geometrical Optics (GO) with the Geometrical Theory of Diffraction (GTD). This is then compared against two simplified paraxial lens models of the telescope, namely the Projected-Aperture (PA) technique and Gaussian Beam Mode Analysis (GBMA). PA is performed by Fresnel integration of fields from source to sky, while GBM requires decomposition of a field into a set of Gauss-Laguerre modes which are propagated from source to sky using a ray matrix formalism. The motivation for analysing the Planck FSL structure is to test the assumption that features in the difference map are a result of manufacturing imperfections in the detector horns. To test this hypothesis a number of altered horn geometries are modelled using the NUI Maynooth Experimental Physics departments in-house waveguide mode-matching software called SCATTER, and these are then used in the analysis of the telescope system. Further use of SCATTER is illustrated in work on ultra-Gaussian horns for STEAMR, and here it is tested against commercial waveguide modelling software Microwave Wizard (μWW).

Further modelling is performed for the Cardiff test-bed of the Planck telescope simulator, which was used for qualification of the Planck HFI flight horns pre-launch. Here we test the hypothesis that manufacturing imperfections could be missed if the effects on beam pattern were imperceptible to measurement. This is done using GRASP9, as is the modelling of FIRI, a multi-beam spectral/spatial interferometer which will hopefully break current constraints on angular resolution obtainable at infra-red wavelengths.

In general, this thesis aims to provide insight into the modelling of quasi-optical telescope systems, with particular emphasis on multi-moded systems, providing useful information for future data analysis by the Planck project team.

Acknowledgements

First and foremost I owe a debt of gratitude to my supervisor, Dr. Créidhe O'Sullivan, for imparting on me some of her vast expertise in quasi-optics, as well as for four years of unrelenting support, and for undertaking the arduous process of correcting this thesis. I also wish to thank the head of department, Professor Anthony Murphy, whose incisive mathematical knowledge of many areas of quasi-optics proved extremely helpful. Further thanks go to Dr. Marcin Gradziel for extending and maintaining the Maxwell cluster, allowing me to perform lengthy simulations for this thesis which would have otherwise proved impossible. I also wish to thank Ian McAuley whose work on Planck proved extremely useful to my own, and for never rubbing it in too hard in when Villa got thrashed by United. I further wish to acknowledge Ken Ganga and Sylvain Mottet of APC, Paris, whose the insight and assistance with regard to Planck was very helpful. I must also acknowledge the efforts of the staff of IAP, most especially Dr. Mark Whale, who made my time in Switzerland extremely enjoyable, and ultimately a fruitful endeavour for this work. I would also like to thank my office colleagues Donnacha Gayer and Stephen Scully for the constant distraction from work, and my good friend Enda McLoughlin, whose presence in the department in 2008 was one of the main factors that influenced me to do this PhD. Further I wish to thank the entire Department of Experimental Physics at NUI Maynooth for taking me on, as well as SFI for the financial support afforded me the last four years. Finally I must thank my gorgeous engineer Anthea Middleton, for so much help throughout the four years; helping me write code I was too useless to do myself, proof-reading, listening to my presentations, and mostly my endless woes.

Contents

Dedicated to my parents, Louis and Gladys; without your infinite love and support I would never have had the chance to write this document.

Chapter 1

Introduction

Recent, rapid developments in the field of (0.3-3) THz physics have paved the way for more accurate measurement of the Cosmic Microwave Background than ever before. One such development has been the design and optimisation of highly sensitive horn antennae with well understood beam patterns, which afford good stray light rejection across wide bandwidths. In particular, multi-moded horn antennae have proved very successful in measurement at THz frequencies, and they are the primary topic of this thesis. Herein we shall discuss their merits (and indeed their limitations), and also describe their implementation on the High Frequency Instrument of the Planck telescope. Here we shall investigate some anomalous features arising from the Planck results which directly arise from it's multi-moded horns, and we shall also gain insight into the various techniques useful for high-frequency modelling of telescope systems. Further work on multi-moded horns for the STEAMR mission will be highlighted, as well as modelling of the Planck HFI pre-flight measurement test-bed on which the multi-moded HFI horns were validated. Modelling of the FIRI interferometer test-bed is also performed, with a view to understanding system spillover.

1.1 Introduction to the Cosmic Microwave Background

The CMB, or Cosmic Microwave Background, is the electromagnetic remnant of the very early Universe, from a time when it was a lot smaller and therefore a lot more hot and dense than it is today. When the Universe was less than 380,000 years old, all the matter we see today formed a primordial soup of elementary particles; electrons,

protons & photons. The mean free path of particles and light was small and they collided constantly, preventing the formation of stable nuclei. However as the Universe expanded and cooled neutral hydrogen began forming, an era known as *recombination* (a misleading term in fact, as there had never been a previous time where protons and electrons formed stable atoms). Since neutral hydrogen has a scattering cross-section considerably smaller than that of a free electron, photons began travelling unimpeded throughout the Universe, and once photon energy dropped below the ionising energy of neutral hydrogen (13.6 eV) the Universe became transparent, a process known as *decoupling*. This occurred slowly however, as the photon-to-baryon ratio in the early Universe was roughly 10^9. This meant that if even one photon in a blackbody distribution of 10^9 photons had an energy greater than 13.6 eV it would be enough to keep the Universe fully ionised. It has thus been deduced that the Universal temperature at decoupling was in the region of 3000-4000 K equivalent to a redshift of $z \approx 1000$, i.e. the Universe was one thousand times smaller than its present size. As the Universe has since expanded and further cooled, we now see these photons arriving to us at much longer wavelengths and a temperature of merely 2.7 K. When we measure the CMB today those original photons are the relic radiation we detect. They have travelled to us unimpeded for roughly 13.7 billion years, so by measuring them we can map the sky at the epoch of decoupling. Understanding them is critical to cosmology, as any theory of the Universe must accurately take into account their existence, and the fluctuations in their current observable signal across the sky. Figure 1.1 shows the CMB wall and the subsequent evolution of matter distribution, while a chronological history of the Universe is shown in figure 1.2.

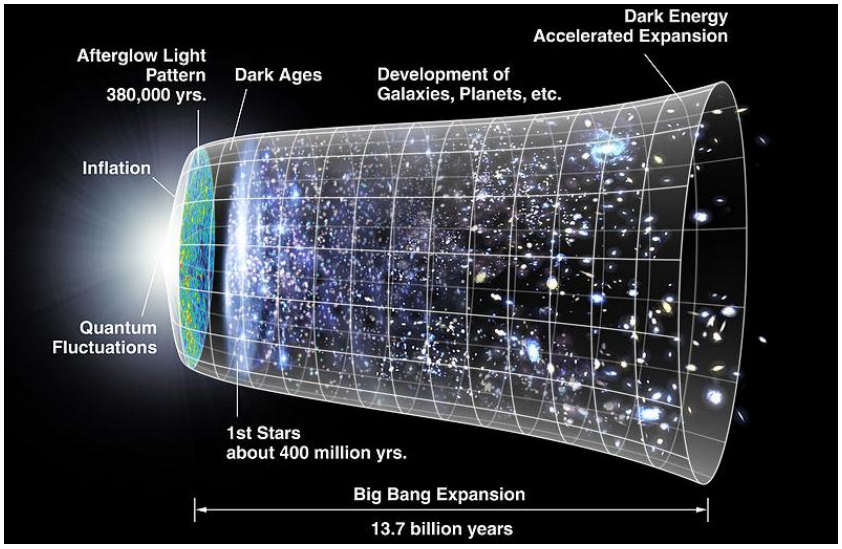

FIGURE 1.1: Visualisation of the expansion of the Universe from Big Bang to present day, highlighting the rapid acceleration in size during Inflation, and the gradual change in matter density distribution following decoupling.

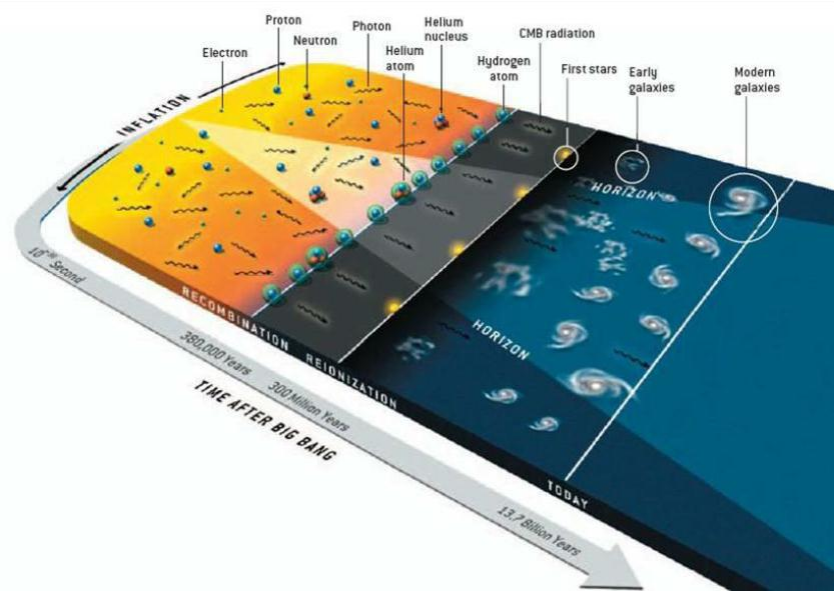

FIGURE 1.2: Chronological history of the Universe, depicting the various processes at work at each stage of it's evolution.

1.2 Discovery & Early Observations of the CMB

Though officially discovered by Penzias and Wilson in 1964 [1], the first observations of the CMB were made my McKellar in 1940 using interstellar molecules [2]. Further mention of the CMB was made by the early astrochemist Gerhard Herzberg in 1950, who hinted at its existence in [3]. While measuring the molecular spectra of diatomic molecules in interstellar space he noted a continuous 2.3 K emission during observations of Cyanide (CN) and hydrocarbons (CH, CH^+), which he believed should be due to the difference between the two lowest rotational states of the hydrocarbonous molecules. Though oblivious to the scale of his find he went on to win a Nobel prize in chemistry for his contributions to the knowledge of electronic structure and geometry of molecules in 1971. It was not until 1964 however that Arno Penzias and Robert Wilson officially (and again accidentally) discovered the Cosmic Microwave Background Radiation (CMB), while unable to filter noise from their microwave antenna signal [1]. No matter where in the sky they looked, this troublesome low-level background radiation was encountered, leading to it being coined CMB. It pervaded the sky at extremely low levels of roughly 2.7K, and was very quickly discovered to be of significant importance to cosmology and to theories surrounding the origins of the Universe which were prevalent at the time. Since then many missions have been undertaken to characterise the CMB with ever-increasing detail, including COBE, BOOMERANG, WMAP, and Planck, all of which will be discussed later.

Going back a few decades we can trace the origins of our understanding of the CMB

to Alexander Friedmann, who was the first to propose a Universe which could either expand or contract, governed by a set of equations he derived and published in 1922. Crucially they fit with Einstein's theory of General Relativity, thus providing a new perspective on the issue rather than flying in the face of conventional belief [4]. Independent consolidation of his idea was made by Lemaître in 1927 (significantly, not published in English until 1931), who first proposed that galaxies recede from each other at rates proportional to the distance between them [5], governed by an equation subsequently mis-attributed to Edwin Hubble, and now known as Hubble's Law:

$$v = H_0 d, \tag{1.1}$$

where v is the velocity at which the galaxy recedes from the observer, d is the distance from the galaxy to observer, and H_0, the key constant of proportionality, describes the rate of expansion of the Universe. Hubble subsequently proposed the equation in 1929 after measuring the distance to 22 nearby galaxies and the redshifts in their spectra, leading Lemaître to confidently propose the Big Bang theory (originally known as the 'theory of the primeval atom') on verification of his work.

In 1948 George Gamow and his doctoral students Ralph Alpher and Robert Herman consolidated the work of Lemaître by outlining how the present levels of fundamental elements in the Universe, namely hydrogen and helium, could be explained by reactions spawned during the Big Bang. Under very high temperature and density sub-atomic particles fuse to form basic elements [6]. Though the presence of heavier elements went unaccounted for, it was soon after discovered by Fred Hoyle that the heavier elements formed later inside early stars [7]. Gamow also predicted a unique blackbody distribution of the big bang radiation intensity as a function of wavelength, due to the mean free path of photons being so short pre-decoupling that the Universe was in thermal equilibrium. This was expanded on by Alpher and Herman in 1948 [8], [9], who noted that as the Universe expanded the temperature would drop and the wavelength of the photons would be proportionally redshifted such that they should now appear to arrive from every direction in space with a constant temperature of $\sim$5 K.

Robert Dicke, unaware of previous work, independently derived a prediction of the CMB radiation at roughly 20 K in the early 1960's. Later he would put forward a suggestion that the Universe may be very close to the critical density above which it would expand forever, beginning the debate on the ultimate fate of our Universe. Having invented the differential microwave radiometer (Dicke radiometer) to search for the CMB signal, in cooperation with David Todd Wilkinson and Peter G. Roll, he was beaten to the punch by Penzias and Wilson, who while working with a large Dicke radiometer only a few

miles away accidentally stumbled upon an isotropic background signal which pervaded all of space and could only be produced by a 3 K blackbody source [1]. Following discussion with Dicke and his subsequent verification of the signal [10] it was concluded that this must indeed be the CMB radiation predicted, validating the Big Bang theory and paving the way for deeper insight into the early Universe.

1.3 CMB Temperature Fluctuations

While the blackbody spectrum of the CMB and the formation of basic elements are well described in the Big Bang model, there are many peculiarities that cannot be explained by this theory alone. The mystery surrounding the origins of structure and why matter clumped together (galaxies, super-clusters, etc.) is known as the 'structure problem', and the fact all of this matter appears redshifted confirms that the Universe is expanding, but why? There is also a mystery surrounding the geometry of the Universe. General relativity allows for three possible Universal geometries; closed - in which the Universe will re-collapse on itself after expansion, open - in which it will tend to expand forever, or flat. For the Big Bang model to work the Universe at the time of Planck density must have been almost precisely flat, i.e. the curvature couldn't have exceeded one part in 10^{59}, which seems incredibly unlikely, but yet we find ourselves in just such a flat universe. Another important problem with the Big Bang model is the fact that the Universe appears almost perfectly isotropic. Any two regions of the Universe will appear to have the same temperature despite having never been in causal contact. This is known as the 'horizon problem', which along with the structure, expansion and flatness problems meant the Big Bang model can not alone explain the current state of the Universe.

The Lambda-CDM model arose in the early 90's from a necessity to harmonise the conflicting observations of cosmologists at the time. It is the simplest model of the Universe which provides a reasonable match to observations, and works by assuming the existence of cold dark matter (CDM) alongside a cosmological constant, Λ, equivalent to the energy-density of empty space. From this arose inflationary theory, which suggests that following the Big Bang a brief period (10^{-32} s) of exponential expansion occurred in which regions originally in causal contact were separated by such large distances that they now appear isolated with respect to each other. This solves the horizon problem as it assumes that there was a brief period during which all regions of the Universe were in causal contact and the ultimate properties of the Universe were determined [11]. In fact, the Universe is not exactly isotropic on all scales. A significant temperature dipole

anisotropy in the CMB, with an amplitude of $3.5 \pm 0.6 \times 10^{-3}$ K [12] was discovered in 1977. This ~ 3 mK fluctuation in temperature across the entire sky is the consequence of the Doppler Effect due to our motion with respect to the CMB. In 1992, however, even smaller temperature fluctuations were detected by the COBE-DMR mission [13], the first space-based experiment to measure the CMB anisotropy, and it was this discovery of the blackbody form and anisotropy of the CMB which led to the eventual award of a nobel prize in physics to George Smoot. The measured CMB power spectrum in figure 1.3 describes the size of the temperature fluctuations as a function of the angular scale on which they are measured. To elucidate somewhat, the largest possible angular scale on which we can measure signal is obviously going to be the entire sky, so this would correspond to an angular scale of 360 °, or conversely, a multipole moment of $l = 0$ (see figure 1.4 for illustration of the angular scales being measured for increasing multipole). On this scale the CMB is isotropic, and we see no fluctuations. At $l = 1$ (corresponding to an angular scale of 180 °) we observe the dipole fluctuation due to our motion through the Universe, which red- and blue-shifts the CMB with respect to us, but divulges no primordially relevant information. Our first useful observations can be made at $l = 2$ (angular scale of 90 °) which still clearly contains information about very large scale structure. As we can only observe one possible realisation of all possible Universes, and from one particular vantage point, an uncertainty known as 'cosmic variance' is imparted on any measurement, which declines with increasing l. We must incorporate a relatively large margin for error into our low-l measurements, since the CMB will appear slightly different if observed from another arbitrary point in the Universe at which the same physical laws, inflation, etc. obviously hold. This error must also remain within the bounds imposed by the ΛCDM Big bang model, which dictates variance on large scales via the range of possible Universes which *could* form, given our basic model and it's constituent parameters.

Continuing up through multipole moments the scale of the observed CMB fluctuations decreases, and we see the largest peak in the power spectrum at 1 °. Further peaks arise at smaller and smaller scales, the error in measurements toward this end clearly being limited by the telescope itself. Overall the temperature anisotropies vary as little as one part in every 100,000 from one point in the sky to another, however their very existence means the Universe was not completely isotropic during the radiation era, and their refinement further constrains the parameters of our ΛCDM model.

Multipole moment is mathematically useful for mapping the CMB as one can describe any scalar field on a sphere (in this case CMB temperature fluctuations) as a sum of

spherical harmonic multipoles :

$$\frac{\Delta T}{T}(\theta,\phi) = \Sigma_{lm} a_{lm} Y_{lm}(\theta,\phi) \tag{1.2}$$

where $Y_{lm}(\theta,\phi)$ are multipole moments, θ and ϕ representing right ascension and declination respectively on the observational sphere. A plot of the $0 < m < l$ real $\frac{\Delta T}{T}(\theta,\phi)$ patterns for each value of l is shown in figure 1.4. The Legendre multipole, l, is given by $l = \frac{\pi}{\theta}$ where θ is the angular separation between two points on the sky. As outlined, the determination of multipole amplitudes C_l is critical to CMB astronomy, and they are given by $C_l = \left\langle |a_{lm}|^2 \right\rangle$. A more convenient representation of angular power as a function of angular size on the sky is obtained by scaling the amplitude coefficients with their multipole moment, as shown in figure 1.3

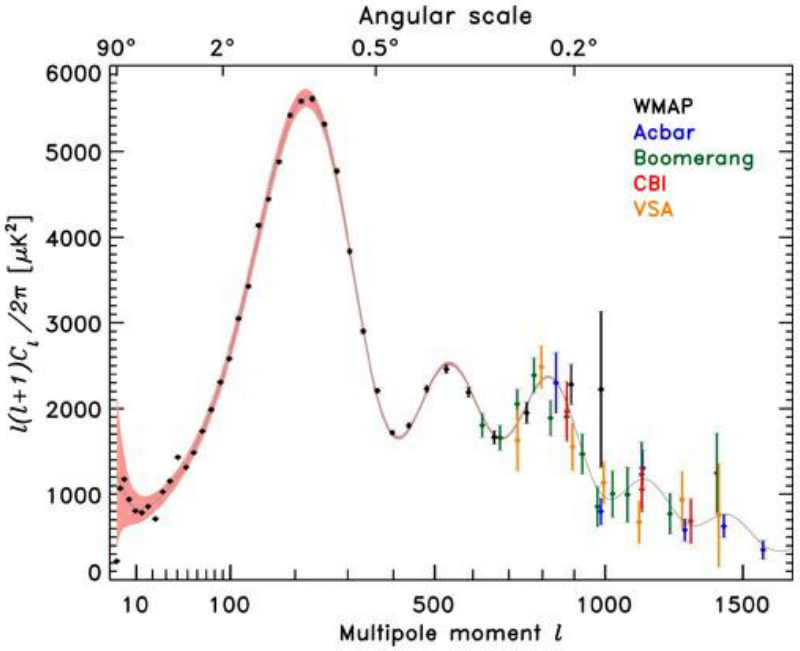

FIGURE 1.3: The CMB Angular power spectrum, and the constraints placed on it by successive experiments before Planck.

The $l = 0$ harmonic corresponds to the monopole measured by COBE and found to have a blackbody distribution. The $l = 1$ harmonic corresponds to the dipole CMB fluctuation caused by the Doppler effect due to our motion through the Universe, and so on. Polarisation of the CMB photons arise from *local* temperature quadrupole anisotropy ($l = 2$) which will now be discussed further.

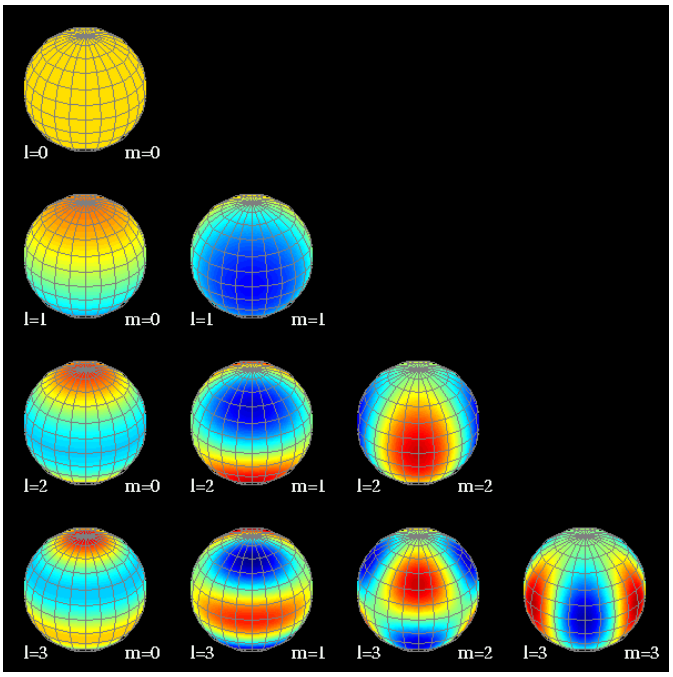

FIGURE 1.4: Low order multipole moments forming elements of the sum of spherical harmonics in 1.2. $l = 0, m = 0$ represents the monopole, $l = 1, m = 0, 1$ the dipole, $l = 2, m = 0, 1, 2$ the quadrupole, etc. [14]

1.4 CMB E & B-mode Polarisation

Aside from the temperature power spectrum of the CMB, another major source of information is polarisation, produced at recombination when CMB photons were Thompson-scattered by free electrons. The resultant field can be decomposed into scalar (non-rotational, or curl-free) *E-modes* and tensor (rotational, or curl-induced) *E-modes* and *B-modes* (named as such to highlight their similarity with the vector nature of electromagnetic fields).

E-modes are created by matter density velocity gradients in the primordial plasma, which also generated the temperature spectrum, so by measuring E-mode polarisation we are reproducing this non-rotational velocity field as it was at recombination. This field is much weaker and therefore more difficult to measure than that of temperature, however due to the intrinsic relationship between temperature and E-mode polarisation, cross power spectra can be generated to refine the expectations of both. Four co- and cross-correlation spectra can be generated, namely $\langle \mathrm{TT} \rangle$, $\langle \mathrm{TE} \rangle$, $\langle \mathrm{EE} \rangle$, and $\langle \mathrm{BB} \rangle$. WMAP provided good measurements of the TE and EE power spectra as shown in figure 1.5. The TE spectrum is understandably easier to quantify owing to the much larger signal-to-noise ratio in temperature and the cancellation of errors in cross-correlation, however the sensitivity of Planck means it was expected to constrain both (figure 1.5).

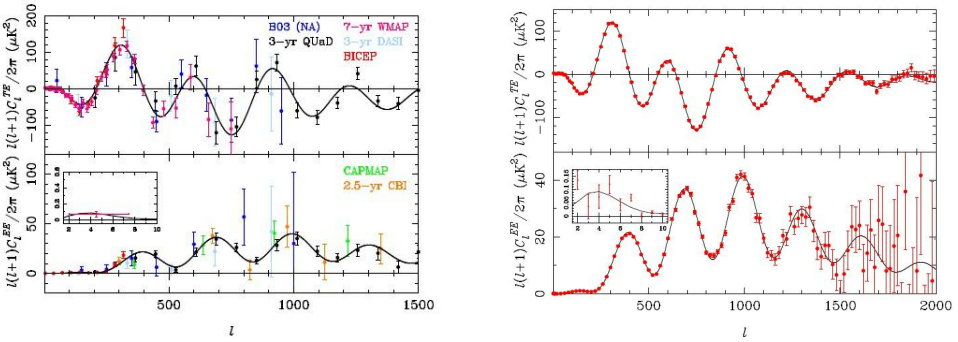

FIGURE 1.5: (**left**) Constraints placed on both ⟨TE⟩ & ⟨EE⟩ power spectra by previous experiments, and (**right**) predictions made circa 2010 on the improvement Planck will make to both. [15]

The second generator of primordial polarisation are tensor perturbations which produce both E and B-modes with roughly equal power, but at significantly weaker levels than those generated by scalar perturbations. There is a decrease in power of roughly five orders of magnitude between temperature and E-mode spectra, and the B-mode spectrum is expected to be another order of magnitude lower. They are yet to be measured by any ground or space-based CMB experiment. It predicts gravitational waves in the early Universe due to large scale structural interactions, and it is these which lead to the tensor perturbations. Successive missions have continued to constrain the level of B-modes, however detection methods sensitive enough to measure these tiny fluctuations in the polarised field have yet to be realised. Their eventually detection will cement inflationary theory as a cornerstone of cosmology, so measurement of B-mode polarisation has become a matter of great importance in the cosmological community. Fluctuations of the order 100 nK or lower are expected, depending on the energy scale of Inflation (see figure 1.6, which shows a comparison between temperature and B-mode intensities).

Using proper analysis methods, however, it is believed that the B-mode inflationary component will eventually be disentangled from the dominant E-mode, opening a unique window to probe the very early Universe and the physics of extremely high energies,($\sim 10^6$ GeV). One contaminant which must be calculated and removed is that of lensed B-modes, produced by gravitational lensing of E-modes around $z \sim 2$ and earlier. This foreground emission is expected to be much greater than that from actual CMB B-modes, as shown in figure 1.7, however rather than being a complete hindrance, it will in itself provide valuable information about density distributions in the earlier Universe, and its correlation with the Cosmic Infrared Background (CIB) may prove useful for lensed B-mode filtering from the Planck data in post-processing (see section 1.6.1).

The real challenge in B-mode detection comes from instrumental systematics mimicking the tiny B-mode signal, which must at the same time be distinguishable from the noise

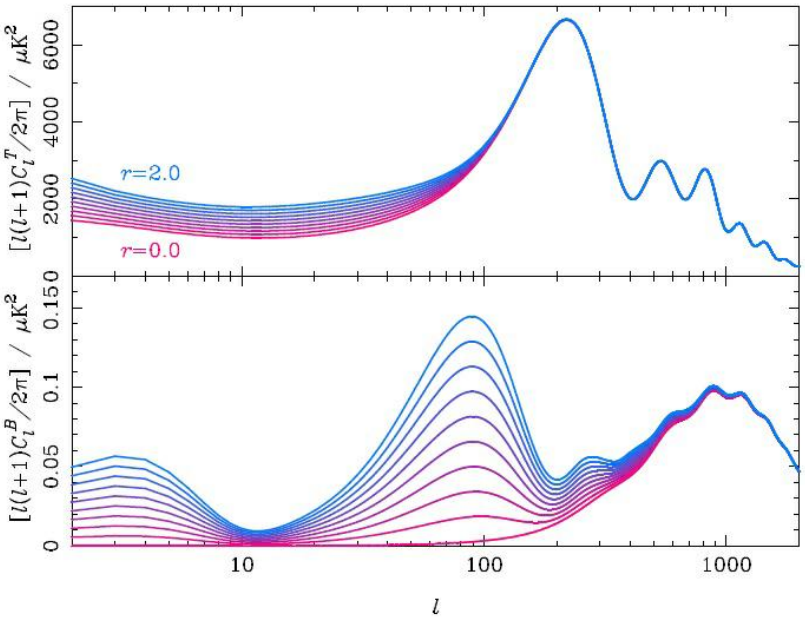

FIGURE 1.6: (top) The scaled temperature $\langle TT \rangle$ and (bottom) predicted B-mode $\langle BB \rangle$ power spectra, showing the extraordinary weakness of B-mode fluctuations with respect to temperature. [15]

in which it is embedded. The ultimate goal in detector engineering is to create an instrument which can detect B-mode signals of the order of 30 nK, but which would produce spurious B-modes no larger than 3 nK, a very challenging task indeed. In an ideal world, the system should also have zero cross-polar response, as its effect would be to convert E-modes into B-modes. As E-modes are present at levels at least 100 times larger than the target B-modes, these effects are controlled with a combination of rotation of the instrument during measurements, and modulation of the polarisation plane via a rotating wave-plate. Using these methods it is reasonable to expect a cross-polar response of $\sim$0.3 % that of the co-polar component.

Sensitivity is also a major issue, as state-of-the-art bolometric detectors have reached a sensitivity limited only by the photon noise of the radiation being measured. To further increase sensitivity these detectors can be replicated in large arrays, thus boosting the mapping speed. However an alternative option is to use multi-moded horns which have much greater sensitivity than single-moded horns, and are a foundation of the work in this thesis. A possible solution to the sensitivity dilemma may be found in research ongoing into the development of superconducting *Transition Edge Sensors* (TES) [16]. These detectors comprise a thin film of superconductive material (e.g. tungsten) held at a transition temperature from the superconducting to normally conductive state. In this particular state there is a very high dependence of resistivity upon temperature, so much so that the absorption of a CMB photon increases the temperature slightly, and the resistance appreciably. This jump is measured via a bias voltage, resulting in

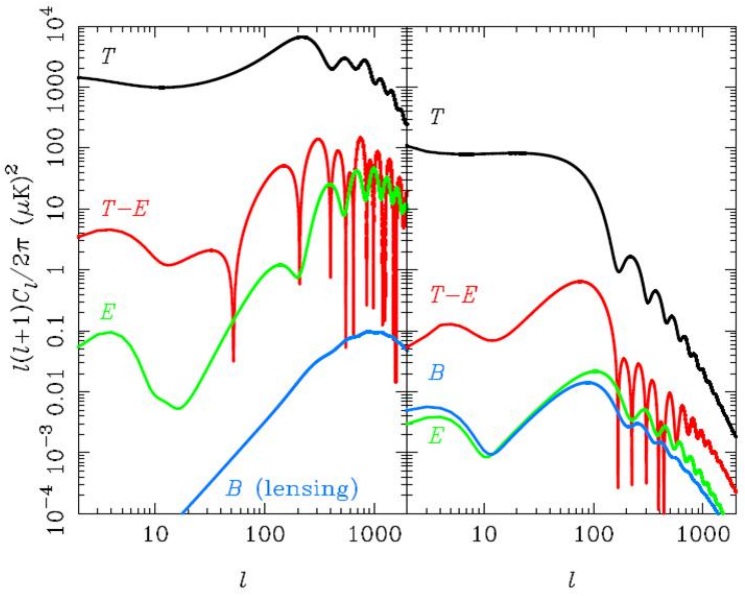

FIGURE 1.7: Scalar (left) and tensor (right) polarisation power spectra, highlighting the contribution of lensed B-modes which hinder the primordial B-mode search. [15]

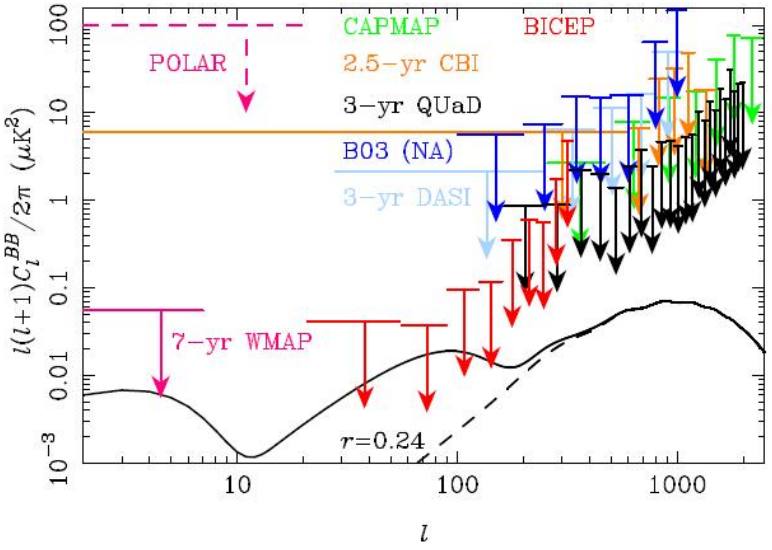

FIGURE 1.8: Constraints placed on B-mode levels by successive experiments in the last 20 years. [15]

upwards of twice the sensitivity of current detectors, and 2000 times faster integration speed. Corrugated feed horns especially, would be very suitable to couple radiation from free space to such detectors. Further discussion on corrugated horns and their implementation in such systems as the Planck telescope will be made throughout this thesis.

1.5 Recent Observations

Since that time a multitude of ground, balloon-borne, and space-based observations have been commissioned to further our knowledge of the CMB, mainly in regard to its temperature and, to a lesser extent, polarisation properties. Following the discovery of the CMB it soon became clear there would be fluctuations (or anisotropies) in the temperature due to inhomogeneities in the early Universe on the scale of $\Delta T/T = 10^{-4}\,\mathrm{K}$ or $10^{-5}\,\mathrm{K}$ [17]. Throughout the 1980s ground-based experiments set increasingly strict limits on the size of the largest CMB fluctuation, that of the dipole due to our motion through the Universe. The first space-based observations were made by a Soviet CMB experiment RELIKT-1, launched in 1983, which gave definitive upper-bounds on the large-scale anisotropy. This was followed soon after by NASA's first space-based CMB mission COBE (Cosmic Microwave Background Explorer) which was launched in November 1989 with a 4-year observing schedule [18]. It not only confirmed the existence of the primary anisotropy [13] but also measured a perfect blackbody distribution of the CMB. Very low-level, large-scale anisotropies were also discovered in the data recovered at the telescope's angular resolution of only 7°. The overall success of the mission then caused a flurry of activity in the field of experimental cosmology over the coming two decades, with various experiments aiming to measure the first acoustic peak of the temperature power spectrum, which COBE had insufficient resolution to detect. In 1998 the BOOMERang (Balloon Observations of Millimetre Extragalactic Radiation and Geomagnetics) experiment took flight over Antarctica, measuring the CMB with $10'$ resolution, a huge improvement on that of COBE. It provided the first successful measurement of CMB anisotropies on scales smaller than the cosmological horizon (i.e. between regions of early Universe casually connected) and accurately measured the first three acoustic peaks predicted beyond 1° [19].

In 2002 ground was broken further as the ground-based mission DASI (Degree Angular Scale Interferometer) became the first to retrieve polarisation data from the CMB signal [20], found to be an order of magnitude weaker than the temperature fluctuations. WMAP (the Wilkinson Microwave Anisotropy Probe), the next space-based CMB mission to be launched late in June 2001, performed a full-sky survey at the same angular resolution as the BOOMERang mission, providing a more detailed map of the CMB temperature anisotropies, and an accurate look at the nature of CMB polarisation [21]. A depiction of the measurement made by Penzias-Wilson, as well as the first full-sky maps, made by COBE and then improved upon by WMAP are shown in figure 1.9.

Since WMAP a number of other experiments have added valuable understanding in

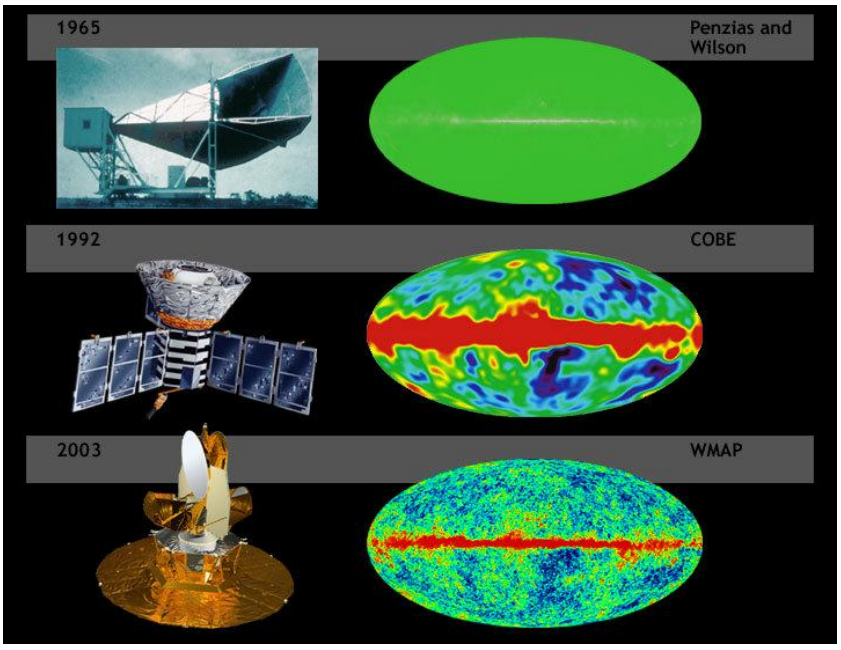

FIGURE 1.9: The first CMB measurement was made by Penzias & Wilson in 1965, measuring an almost perfect blackbody 3 K source in all directions of the sky. Improvements in detection capabilities since have given a much more detailed insight into the nature of the CMB. The vast improvement in resolution from COBE to WMAP over the space of only a decade highlights the boom in CMB interest prompted by COBE's results.

our knowledge of the CMB. The CBI (Cosmic Background Imager) and VSA [22] have proved invaluable to cosmology as higher resolution measurements allow scientists to further constrain the cosmological parameters which govern the evolution and geometry of the Universe (figure 1.3). CBI was the first experiment to measure the fourth and fifth acoustic peaks of the CMB temperature spectrum, verifying predictions that small scale anisotropies are much weaker than large scale anisotropies [23]. The ACBAR (Arcminute Cosmology Bolometer Array Receiver) experiment followed, and returned higher-resolution data on the same angular scale as CBI, noting that the excess at certain angular scales was not as large as previously predicted [24].

Despite the valuable data provided by these missions, the Planck experiment has promised great advancement in all areas of CMB astronomy. Planck is a third-generation space-based experiment which was designed to measure the CMB with unparalleled detail and resolution [25]. Built by the European Space Agency (ESA) and launched in May 2009, Planck's initial aims were to provide three times the resolution and ten times the sensitivity of WMAP, returning high-quality maps of the CMB anisotropy power and polarisation spectra. These goals were made possible by recent advancements in the field of microwave detection, namely the optimal use of horn antennae and bolometers as detectors to which telescopes can efficiently couple radiation. The experimental physics

department at NUIM specialises in the development and optimisation of high-frequency optics, and forms part of the core design team for Planck. The substance of this thesis contains work done modelling the telescope as part of that research group, so an outline of the project goals and a deeper insight into the detection capabilities of the project will be outlined later.

1.6 The Planck Telescope

Following on from the success of NASA's COBE observatory, Planck was first conceived of during an internal meeting at Institute of Space Astrophysics (IAS) in February 1993, where it was pointed out that due to the current rapid advance in bolometric detection techniques the sensitivity of receivers in the millimetre range could see up to three orders of magnitude increase in the near future. This goal was inevitably realised by the development of spider-web bolometers and polarisation sensitive bolometers capable of operation at 100 mK, and an optical design that coupled bolometric and radio detection techniques. Further advancements were also made in understanding sources of systematic noise, while closed-cycle refrigerators removed the need for bulky cryostats isolating varying temperature stages.

The project officially began in 1993 as SAMBA (Satellite for Measurement of Background Anisotropies). The inaugural European space-based mission to measure the CMB set lofty goals of appreciable improvement to the limits set on ΛCDM inflationary parameters by its American predecessors, and in 1994 was merged with another mission COBRAS (Cosmic Background Radiation Anisotropy Satellite) harbouring similar scientific goals and technological requirements. It progressed from competition in 1996 as COBRAS/SAMBA, a dual instrument payload for ESA's 3rd Medium-sized mission (M3) in their Horizon 2000 scientific programme. The original concept design is shown in figure 1.10. In 1998 the project was renamed 'Planck' in keeping with ESA tradition of honouring famous scientists, and the proposal of a High Frequency Instrument (HFI, a.k.a SAMBA) to supplement the design was accepted in 1998. Planck was launched on the 14th of May 2009 and continuously surveyed the sub-millimetre sky since the 12th of August of the same year. It operated perfectly until November of 2011, by which time it had almost completed five all-sky surveys using both instruments.

Planck proposed large gains over its predecessor WMAP, with 2.5 times the angular resolution and 30 times the instantaneous sensitivity. In fact the resolution varies between roughly 30 arcseconds at the lowest frequencies to 5 arcseconds at the highest. The

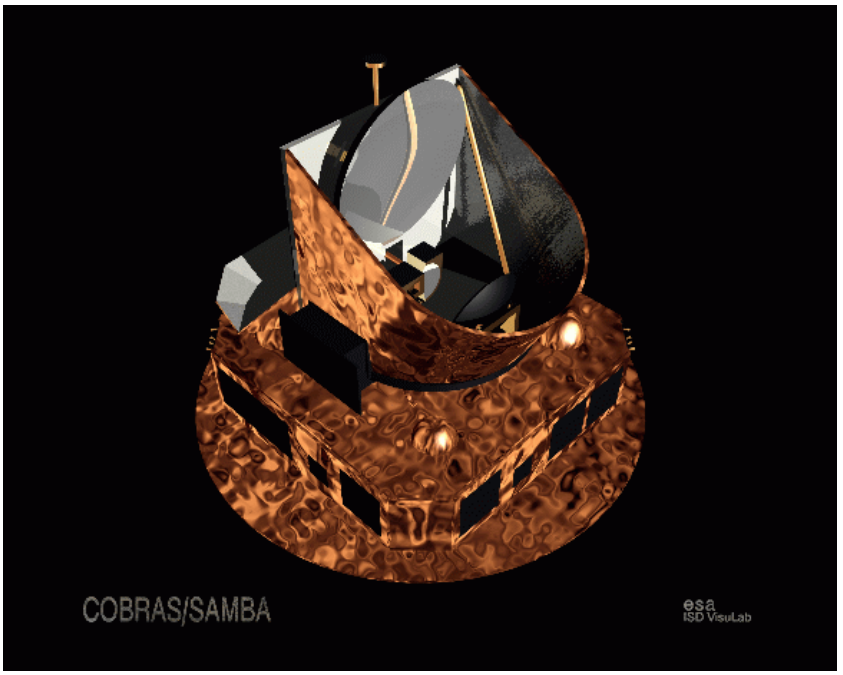

FIGURE 1.10: The original artists impression of COBRAS-SAMBA. Major changes from the original design include the reshaping of baffle structure behind the primary, and the addition of grooves to the underside of the baffles as shown in figure 1.17.

photon-noise limited detectors in the three HFI bands tasked specifically with CMB photon detection (100 GHz, 143 GHz, 217 GHz) give the vast increase in sensitivity. Full description of the CMB temperature spectrum then is limited only by the ability to remove foreground sources from the measurements, and for this reason a very broad range of frequencies are measured across two instruments; the LFI (Low Frequency Instrument) and HFI (High Frequency Instrument), spanning 25 GHz to 1 THz. LFI [26] covers three frequency bands between 30 and 70 GHz while HFI [27] covers six bands between 92 GHz and 1 THz, centred on 100 GHz, 143 GHz, 217 GHz, 353 GHz, 545 GHz, 857 GHz. Covering this range of frequencies allows for measurement of all diffuse and compact "foregrounds" whose emission obscures our image of the CMB.

The defining goal of the Planck mission is to fully characterise the temperature spectrum of the CMB to an accuracy set only by fundamental astrophysical limits. Its design allows extraction of all information regarding temperature fluctuations, while also measuring to the highest accuracy to date the polarisation features of the CMB signal. Though not prioritised, the latter goal of polarisation measurement is crucial for, among other things, understanding the nature of the early Universe, when structure first formed.

1.6.1 Foregrounds

Of further importance is the wealth of information Planck offers on the thermal emission from intermediary foreground sources, both extra-Galactic and closer to home. Though a contaminant to the ultimate goal of CMB measurement, these foreground sources provide significant insight into the composition of our own Galaxy and others, which shall be outlined further below. Figure 1.11 highlights the regions in which emission from various contaminating foreground sources dominate. The greatest contaminants of the LFI signal are synchrotron and free-free radiation which decrease toward the lower end of the HFI band. Thermal dust emission then begins to dominate towards the upper end of the HFI range. There is a window between roughly 30 GHz and 200 GHz in which the CMB dominates over backgrounds. For this reason the three lowest frequency channels of the HFI instrument are known as the 'CMB channels', used primarily for CMB detection. The higher frequency HFI channels and lowest frequency LFI channels are suited to foreground detection and subsequent removal.

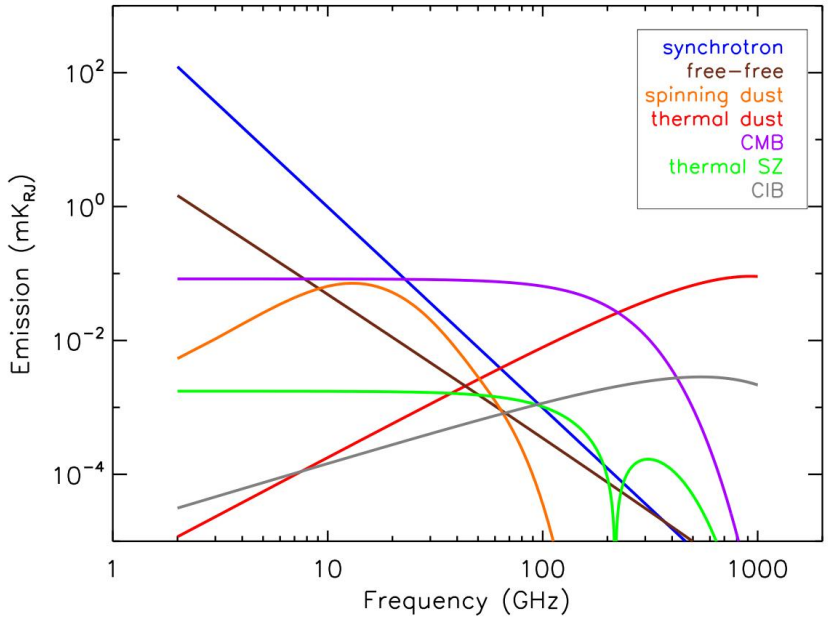

FIGURE 1.11: A plot of the primary foreground contaminants of the CMB anisotropy signal and their contributions at various frequencies.[28]

There are four dominant sources of diffuse Galactic emission which confuse measurement of the CMB; synchrotron, free-free, spinning dust, and thermal dust. Synchrotron radiation arises from the emission of relativistic cosmic ray electrons in supernovae and other shocks, which are subsequently accelerated in interstellar magnetic fields, exciting emission mainly in the Galactic plane [29]. This radiation dominates at lower frequencies, but has a long tapering tail towards THz frequencies where it adds very little to the foreground signal. Free-free (or Bremsstrahlung) emission has similar spectral response,

with a large contaminating component at lower frequencies, and is generated by hot electrons in diffuse interstellar clouds that have been scattered by the Galactic ultra-violet radiation field. Dust emission arises from the re-radiation of absorbed interstellar light, and acts as the greatest source of contamination across all HFI bands, with increased contribution toward THz frequencies. In general, it acts as a very useful thermal tracer of structural evolution, as extinction is greater in molecular clouds than in the diffuse ISM. Spectral observations of HI, HII, and H_2 lines provide insight into this, as well as observations of CO line emissions which effectively trace molecular gas across the ISM. Unfortunately for CMB observation dust is quite a nuisance and dominates the foreground of the highest Planck HFI channels; 353 GHz, 545 GHz, and 857 GHz, which is clearly visible pervading the sky towards the higher end of the spectrum in figure 1.12. The widespread emission is due to the fact that it arises from regions of diffuse matter distribution which are gravitationally bound to the galactic nucleus but can stray far from the Galactic plane. Synchrotron and free-free emission, on the other hand, have high-energy sources which will naturally exist in high-density regions associated with the central Galactic plane, so the region of contamination remains relatively confined. Just like temperature measurements, the polarised component of the foreground signal provides important information. Polarisation arises from dust alignment processes in the Galactic magnetic field, so can tell us a lot about the interplay of this field with the ISM depending on where in the ISM alignment occurs and with what efficiency. Synchrotron radiation also has a polarised component, and although the mechanism of synchrotron emission is well understood, emission within our own Galaxy and from many external sources is not well characterized.

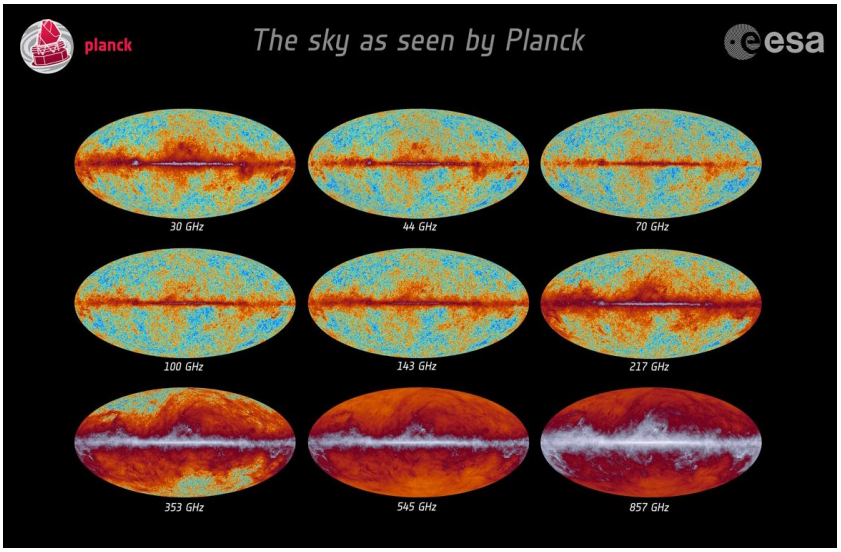

FIGURE 1.12: Full sky maps generated for each of the nine channels of the Planck telescope. The diffuse emission of the local Galaxy and various foreground sources dominates across some bands, while simultaneously the CMB window in which the 44 GHz, 70 GHz, 100 GHz, 143 GHz and 217 GHz bands operate is quite clear.[30]

Another important source of foreground contamination is the Sunyaev-Zeldovich effect, whereby photons are scattered by high-energy electrons in regions of high-density, boosting their energy and misleading measurement of actual CMB temperature. This foreground is observed at lower levels than the diffuse galactic emissions mentioned previously, and similarly tapers off toward regions in which foregrounds become dust-dominated.

Arguably most interesting contaminant of the CMB is Cosmic Infrared Background (CIB), which is in many ways analogous to the CMB. It is produced by the dust within distant galaxies being warmed by the stars forming within it. Its contamination of the CMB signal becomes more prevalent towards higher frequencies in a similar manner to the thermal dust signature (see figure 1.11), and is observable in the 857-GHz map in figure 1.12 as the small scale signal mimicking CMB anisotropic emission in the regions where Galactic dust provides a window. A correlation has been observed between this continuous CIB emission and regions of CMB lensing, since the signal naturally arises from regions of extreme activity and high density. Investigation is currently ongoing into whether it may be possible to use this correlation to provide a more accurate account of gravitationally lensed B-modes when attempting to recover the underlying primordial B-mode signal [31]. This will undoubtedly prove one of the most challenging foregrounds to accurately analyse in future CMB missions.

Spinning dust is a new anomalous source of Galactic foreground emission contaminating the CMB signal, which interferes at wavelengths crucial for analysing CMB recombination lines, so must be better understood. Small dust grains rotating at very high speeds in magnetic fields can undergo so-called "Resonance Relaxation", aligning the dust grains to produce linearly polarised infra-red emission [32]. Polycyclic aromatic hydrocarbons (PAHs) dominate this emission but are not yet fully understood, and naturally interfere with CMB polarisation measurements as they are abundant throughout the Galaxy [33].

Once all foreground contamination had been subtracted from the full-sky maps, they were combined to form an overall image of the CMB, which was released by ESA in March of 2013 to widespread acclaim in the scientific community. It is the most detailed full-sky image of the CMB to date, and incorporates everything we can possibly know about the CMB temperature spectrum across the sky (see figures 1.13 and 1.14). Only when compared with figure 1.15, can the incredible improvement in the quality of data retrieved, spanning two decades from COBE, through WMAP, and finally to Planck, be truly appreciated.

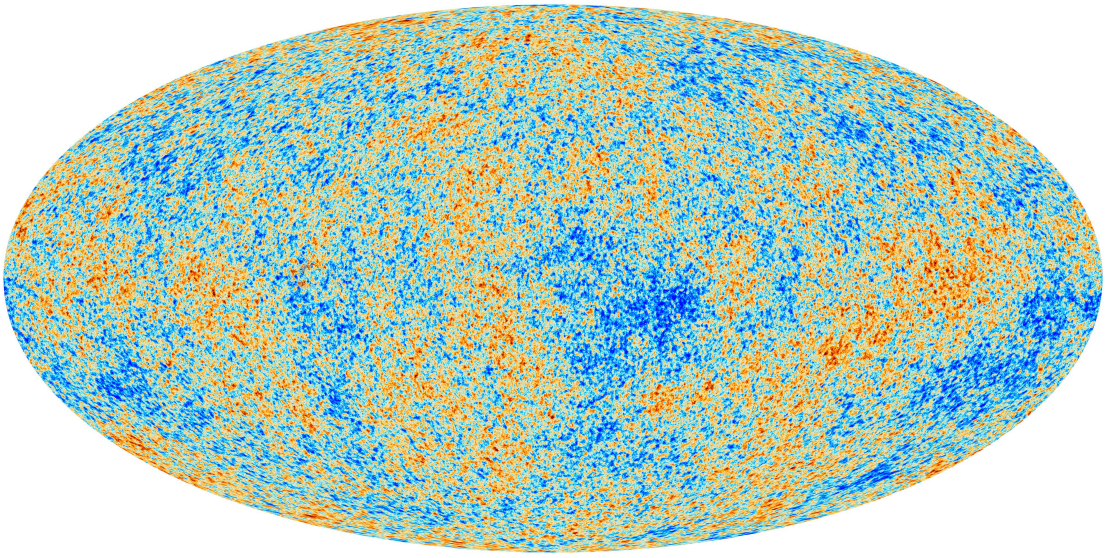

FIGURE 1.13: Full-sky map of the CMB temperature fluctuations, giving essentially all the information we can ever know about CMB temperature.[34]

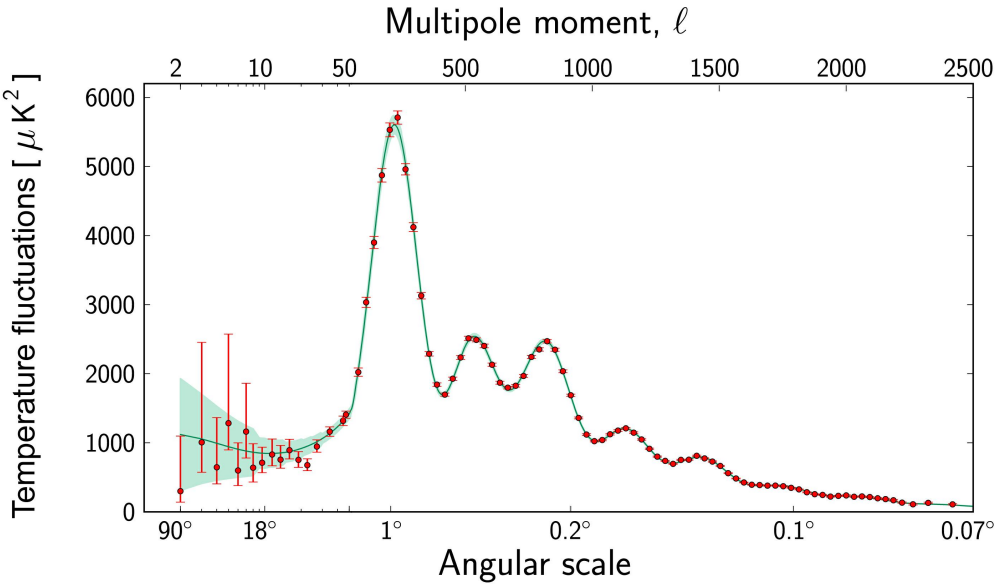

FIGURE 1.14: The angular power spectrum of the CMB as measured by Planck. The unprecedented improvement in accuracy obtained by Planck is clear by comparison with figure 1.3.[34]

Planck Early Results

The ΛCDM model, also known as the standard model of cosmology, is based on a spatially flat, expanding Universe dominated by cold dark matter and a cosmological constant Λ, whose dynamics are governed by the theory of General Relativity. The

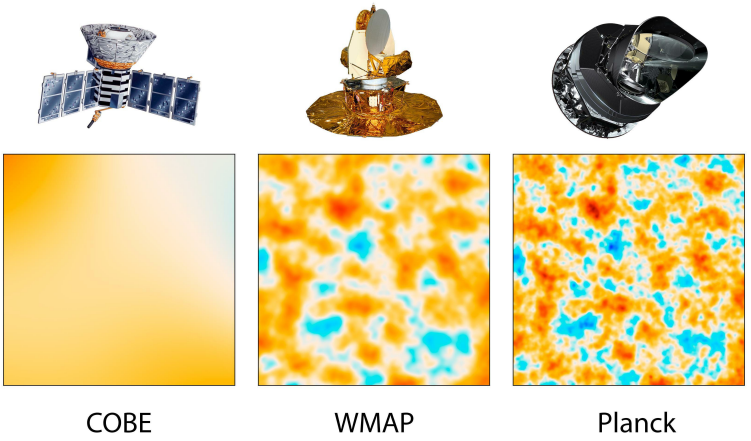

FIGURE 1.15: Contrast in resolution obtained on the CMB anisotropy measurements from COBE (1992) to Planck (2013).[35]

ultimate aim of improving the accuracy of CMB measurements is to constrain the parameters of the ΛCDM model, and to test whether it does in fact provide a correct representation of our Universe. Planck's ability to accurately measure anisotropies on smaller angular scales than previously possible has translated directly into improved constraints on individual parameters, and the breaking of degeneracies between various combinations of others. In this universe the origins of structure are a Gaussian distribution of scale-invariant fluctuations in temperature, and the high multipole temperature spectrum measured by Planck (see figure 1.14) shows excellent correlation with the predictions of this model [34]. Tight constraints have also been placed on deviation from this six parameter model, and are expanded upon by [36]. There are, however, significant differences between the measurements of some parameters when compared with previous WMAP models. For example comparing models formed using CMB data alone, Planck's best fit model gives a 6% drop in dark energy density (Ω_Λ), while baryon density ($\Omega_{baryons}$) and cold dark matter density (Ω_{CDM}) saw increases of 9 % and 18 % respectively when compared with WMAP.

While most of the Planck-derived parameters form good agreement with previous experiments, the value found for the Hubble parameter determining the rate of expansion of the Universe (which arises naturally from the six-parameter model), lies in conflict with previously estimated values. Planck estimates $H_0 = (67.3 \pm 1.2)\,\mathrm{km\,s^{-1}\,Mpc^{-1}}$ [36], which is significantly lower than that measured using traditional techniques. Riess et al. (2011) used the Hubble Space Telescope to measure the redshift of supernovae in distant galaxies, while Freedman et al. (2012) used the Spitzer Space Telescope for mid infra-red observations, both finding values of H_0 well above that calculated by Planck, some of which have since been revised downward. The Planck estimation does lie in agreement with recent WMAP analysis [37] giving $H_0 = (69.7 \pm 2.4)\,\mathrm{km\,s^{-1}\,Mpc^{-1}}$.

In general, however, the Planck results are in good agreement with expectation. Detection of significant levels of CMB lensing by foreground matter has provided strong evidence for dark matter, while the statistics returned from anisotropy measurements show essentially no evidence for non-Gaussianity in the CMB, a topic of previously hot debate among inflationary cosmologists.

1.6.2 The Planck Telescope

The telescope design is an off-axis Gregorian which couples incoming radiation to two receiving instruments, namely the LFI and HFI, sitting on a shared focal plane of 414 mm $\times$ 523 mm. Both instruments can detect the total intensity and polarization of incoming photons, and combined measure over a very broad frequency range as mentioned previously. The more sensitive the photon measurements and the higher the resolution obtained of the primordial CMB anisotropies, the tighter constraints on the cosmological parameters governing the expansion and evolution of the Universe will become.

The off-axis design was chosen to allow for placement of both relatively large instruments in the focal plane of the telescope without incurring significant blockages from intermediary structure. This has been successfully accomplished with the additional advantage that diffraction from the secondary reflector and struts of the telescope are minimised by the design. The line of sight (LOS) of the telescope is titled roughly 3.7 $^\circ$ with respect to the axis of the primary mirror, and a field of view as large as $\pm 5^\circ$ is achieved along this direction, which is rotated 87 $^\circ$ from the spin axis of the telescope. Naturally, this spin axis is also rotated 180 $^\circ$ from the Sun direction to minimise contamination of the signal. The full geometrical description is shown in figure 1.16, where both mirrors are ellipsoidal in shape. The secondary mirror is oversized at approximately 1m diameter to avoid under-illumination of the primary mirror, which has dimensions 1.9 m $\times$ 1.5 m.

Extensive baffling has been mounted to the structure around the mirrors to minimise stray-light in directions away from the LOS of the telescope as shown in figure 1.17. The baffle forms a 360 $^\circ$ casing around the reflectors and focal plane unit (FPU) containing the detectors. This is supplemented by three thermal shields (V-grooves) located between the service module and the telescope, which act as a passive cooling system for the entire assembly, and which minimise coupling to the telescope in the direction of the Sun via baffle edge diffraction. This coupling is further minimised by the 'Sun shield' mounted to the base of the telescope, which prevents heating and subsequent generation of system noise.

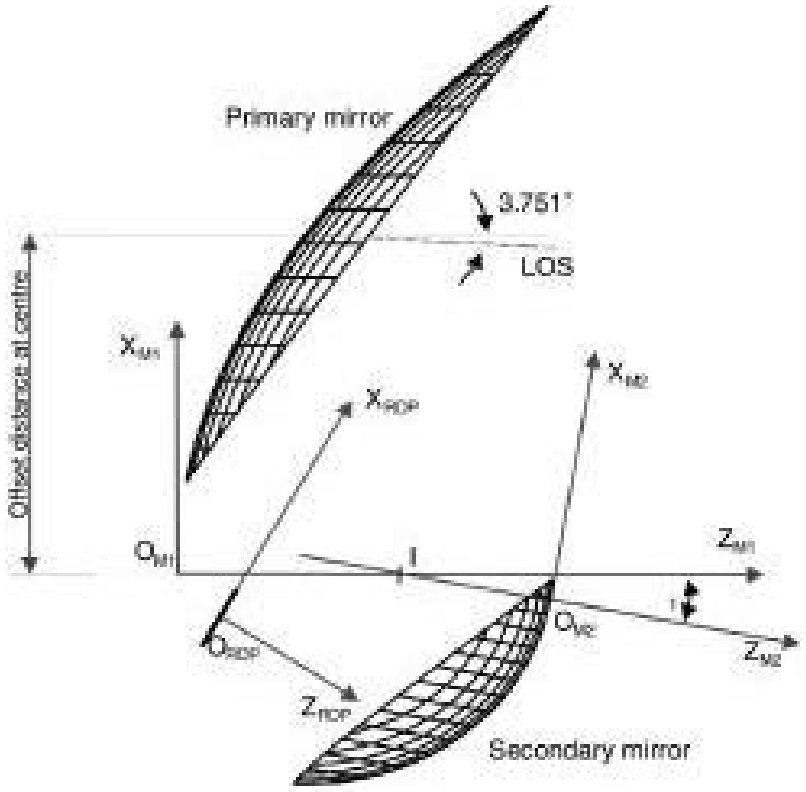

FIGURE 1.16: The main coordinate systems given are those of the primary and secondary reflector frames, the Reference Detector Plane (RDF) which originates at the centre of the focal plane but is tilted 8 ° with respect to it, and the Line of Sight (LOS) coordinate system, tilted 3.781 ° with respect to the primary. Z_{M1} and Z_{M2} represent the rotational axes of the ellipsoids defining the respective reflectors.[38]

1.6.3 The Instruments

The LFI instrument measures the sky across three bands from 30 GHz to 70 GHz using eleven feed horns, which are coupled to highly sensitive microwave amplifiers cryogenically cooled to 20 K. In order to achieve the extraordinary stability required by Planck, the LFI radiometers have a rather complex design called a "pseudo-correlation continuous comparison receiver" which compares the temperature of the CMB to that of a thermally stable "reference load" which is mounted on the 4 K FPU box of the HFI. This allows retrieval of the underlying signal from the sky by removing tiny changes in gain of the cryogenic amplifiers [40]. This coherent detection system of radiometric HEMT-type amplifiers stands in contrast with the bolometric detection methods used on the HFI, the instrument with which the majority of this thesis is concerned. All 22 LFI radiometers remained stable throughout observation, however potential cosmic ray hits caused data loss of $< 0.12\,\%$ averaged over the entire cycle [34].

The HFI comprises six bands covering a frequency range from 85 GHz to 1 THz, the lower

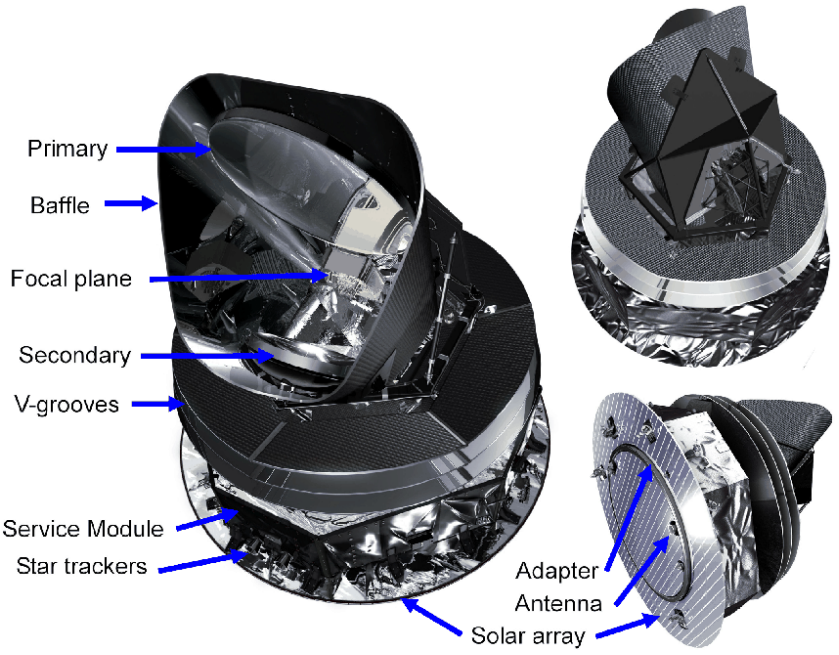

FIGURE 1.17: Multi-angle view of the telescope, with all notable structural components labelled.[39]

end measuring the CMB and the upper end providing full maps of the sub-millimetre sky, featuring mainly extended and point source foregrounds. The centre frequencies of each band are 100 GHz, 143 GHz, 217 GHz, 353 GHz, 545 GHz and 857 GHz, such that a bandwidth of 33 % on each allows coverage of the entire 0.1 - 1 THz range. Figure 1.18 shows the configuration of the detector horns on the focal plane unit, and the respective frequencies at which they operate. There are a total of 36 horns at 4 K, each of which couple radiation to a second set of horns via thermal filter at 1.6 K, as shown in figure 1.19. These feed radiation to the cryostat where spider-web and polarization-sensitive bolometers at 100 mK measure the signal. Modelling of these multimode horns is performed using a rigorous mode-matching technique, in which the horn is fed by a known combination of electromagnetic waveguide modes, which on propagation through the horn scatter power into further higher order modes. On reaching the aperture of the horn, the individual modal contributions to the total power in the horn are summed, returning an accurate description of the horn aperture field. NUI Maynooth has developed in-house software known as "SCATTER" to routinely perform this complex modal analysis, a full description of which is to be found in section 2.3.3. The technique is used throughout this thesis for the modelling of the aperture fields of various multimode horns, commonly in relation to HFI, but in a number of other areas of work also.

A cutaway schematic of the HFI unit is given in figure 1.20, showing the various cooled sections from the 4 K vacuum temperature to the super-cooled 100 mK cryostat containing the bolometers.

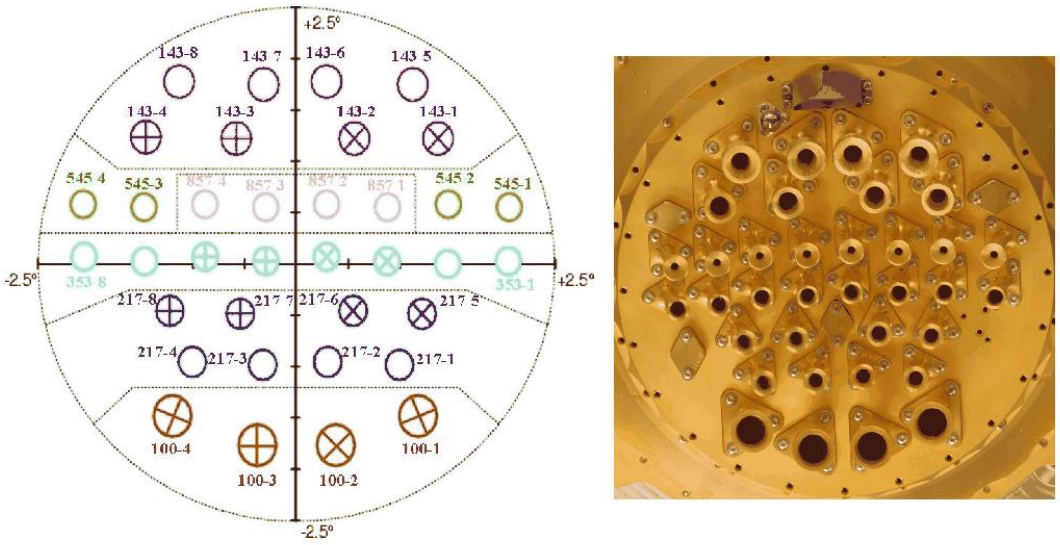

FIGURE 1.18: Configuration of the HFI focal plane unit, and the respective frequencies at which all detector horns operate is illustrated (right).

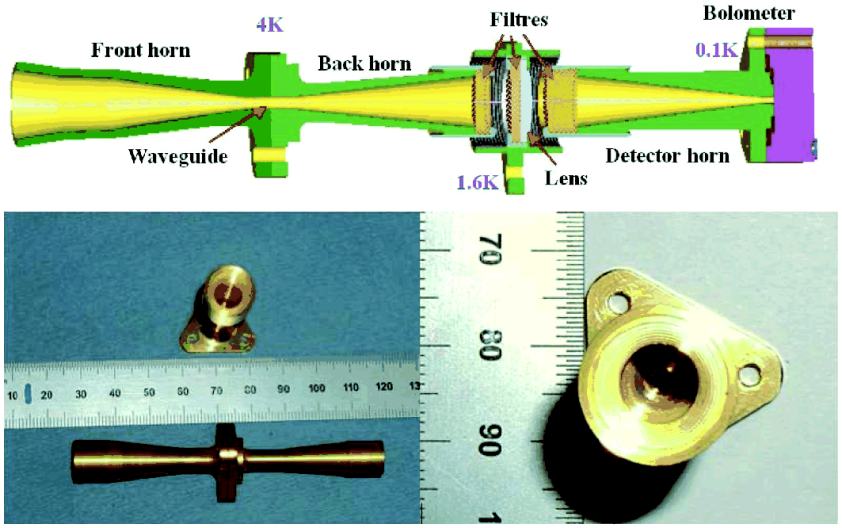

FIGURE 1.19: Complete description of the Planck multimoded pixel (top) and illustrative photo of the back-to-back horns used for HFI and their cross-sectional sizes (bottom).[41]

Two types of bolometer are used on Planck HFI, namely spider-web bolometers (SWBs) and polarisations sensitive bolometers (PSBs). SWBs work by absorbing mm-wave radiation on a web-like surface, and the resulting temperature increase is detected by a tiny thermometer (thermistor) in the centre of the web, which is shown in figure 1.21. Though generally responsive to any source, the SWB design allows long-wavelength thermal radiation to be absorbed, but high-energy cosmic rays pass through, and they are used on the unpolarised channels of the Planck system. It also makes them much lighter and less sensitive to the vibrations such as those occurring in a launch. The spider web consists of a 1 micron thick layer of silicon nitride, coated with gold, and

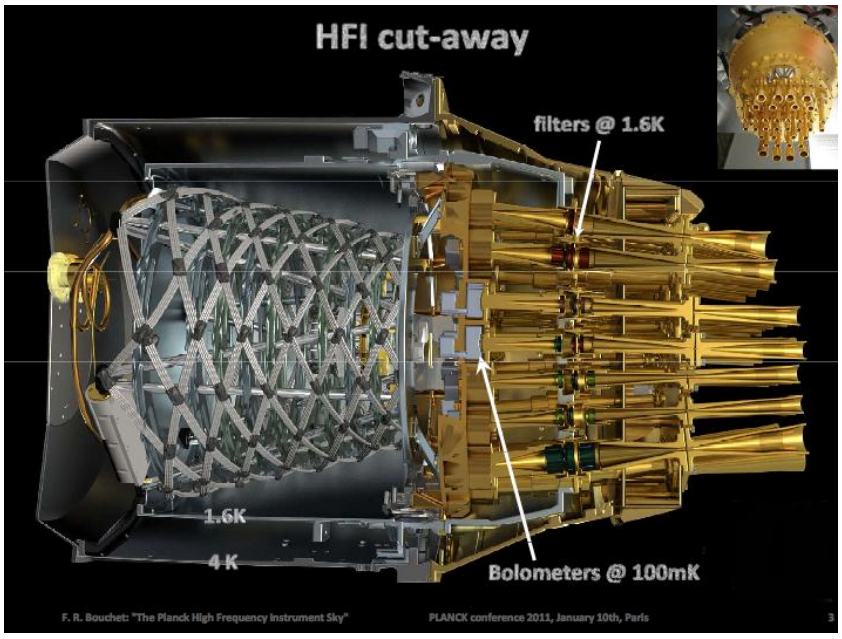

FIGURE 1.20: Cutaway of the HFI assembly.[41]

the thermistor is a $30 \times 100 \times 300\,\mu$m slice of doped germanium connected to the spider web with indium bonds. The spider web diameter and grid spacing varies depending on the frequency of operation of the device, and 20 SWBs are used for four horns on each of the 143 GHz, 217 GHz, 353 GHz, 545 GHz and 857 GHz channels. 16 PSBs are used for four further horns on each of the 100 GHz, 143 GHz, 217 GHz and 353 GHz channels, achieving polarisation purity of between 93 % and 99 % when tested at the 100 GHz band [42]. and are illustrated in figure 1.22. The crosses on HFI horn positions in figure 1.18 denote the PSBs and empty circles denote the SWBs.

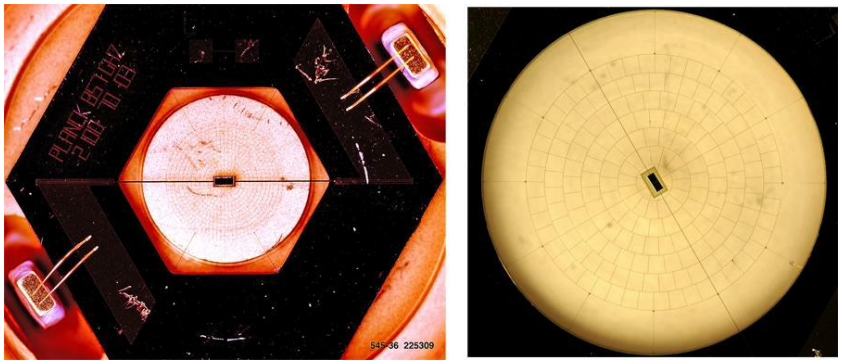

FIGURE 1.21: Planck HFI SWBs, manufactured by the Jet Propulsion Laboratory (JPL), Caltech. Visible is the spider web-like Silicon structure and the central thermistor used across 143 GHz, 217 GHz, 353 GHz, 545 GHz and 857 GHz channels.[43]

The HFI bolometric detector array sits at the centre of the focal plane, indicated by the horns visible on the gold base shown in figure 1.23. The LFI radio receiver array shares the same focal plane and is comprised of eleven larger horns in a ring around the LFI, with the entire focal plane located directly below the primary mirror.

FIGURE 1.22: Planck HFI PSBs, used at 100 GHz, 143 GHz, 217 GHz and 353 GHz channels.[43]

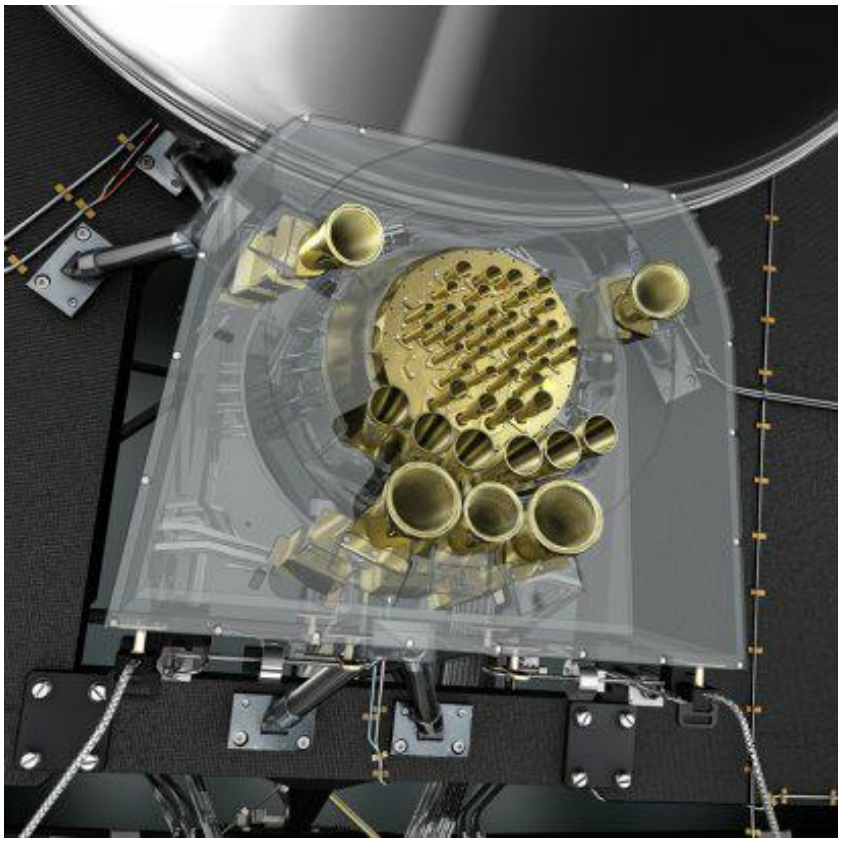

FIGURE 1.23: The Planck focal plane, showing both HFI and LFI instruments in their final configuration.[30]

The HFI also operated smoothly over the duration of the mission, with fluctuations in temperature of the service module due to the eccentricity of the Earth-Sun orbit having insignificant effect on temperature of the HFI electronics. To some degree every horn of HFI (but especially one each at 143 GHz, 545 GHz and 857 GHz), were blighted by "random telegraphic noise" [44]. Use of the two lower frequency horns was discontinued, however usable data was retrieved from the 857 GHz horn.

1.6.4 HFI Beams

One crucial issue with regard the HFI detection chain is spillover, which generally describes the fractional power coupled to the telescope which was not reflected from the antenna reflectors. Due to the finite size of the reflectors in any telescope system, radiation from the sky can pass the edge of the reflectors and couple directly to the feed. Similarly, radiation may enter the telescope but undergo reflections from other surfaces of the instrument and end up coupling to the feed. All of this is deemed spillover, and the spillover efficiency of a telescope is defined as the amount of radiation coupled to the feed antenna which was reflected by the reflector. Spillover is one of the primary concerns of this thesis, and can occur at significant levels when the Galactic plane aligns with one of the elongated far side-lobes of the telescope, either from behind the primary or behind the secondary mirror. The dipole may also impact on FSL levels as it is a large-scale signal which will inevitably couple power to the telescope via the sidelobes. The directions of these sidelobes with respect to the main beam direction are shown in figure 1.24 and it is due to the very high signal in the sub-mm domain that far sidelobe (FSL) pickup is so strong. This coupled with the oversized nature of the mirrors means that power passed the primary can be coupled to the detectors on reflection from the bottom edge of the secondary reflector. The FSL signal is readily visible at both 857 GHz and 545 GHz, which is to be expected due to the sensitivity, however we must model the system accurately in order to explain (and remove) what is actually measured. The sensitivity of these two high frequency channels is due to the multi-moded nature of the detectors, whereby they couple more power to the telescope owing to their larger throughput in modes of radiation higher than just the fundamental. A large portion of this thesis is dedicated to the modelling of these multi-moded horns, so the theory shall be returned to later.

At high frequencies, multi-moded horns are commonly used for detection, however their nature is poorly understood by most of the scientific community. The key issue surrounds their emission of multiple mutually incoherent fields, rather than a single coherent field which is the standard. Adjusting the constituent contributions of each of these modal fields which are incoherent with respect to each other allows increased gain, which improves aperture efficiency. It also provides greater directivity, which improves spillover efficiency. They also boast low cross-polarisation levels, which means less coupling of unwanted to power to the telescope from cross-polar pick-up acting in the same way higher sidelobes which impact spillover pick-up. All of these factors make them a common choice of detector coupling element in modern high frequency systems. Bearing all of this in mind, the significant levels of anomalous power measured by a number of

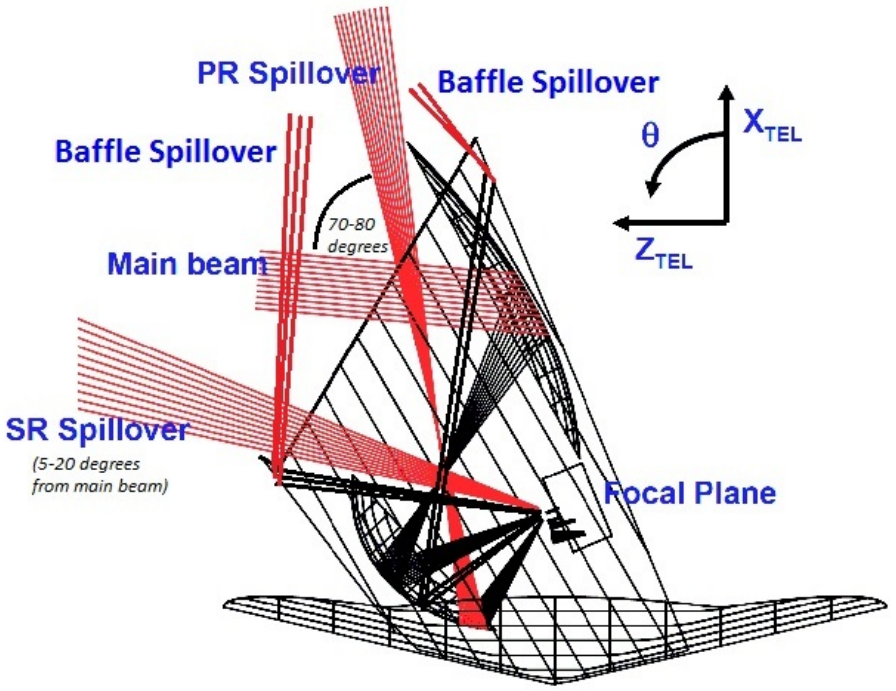

FIGURE 1.24: Diagram of the telescope with associated beams and directions of greatest spillover. The baffle spillover components arise from beams which miss the primary (PR) and secondary (SR) reflectors and strike the small regions of baffle visible along the telescope path.[45]

detectors at the highest frequency channels of HFI caused some concern. Though most likely caused by spillover, this was quite unexpected due to the aforementioned quality of the multi-moded beams, and a thorough investigation of the situation is performed in this thesis.

At the lower frequency channels of HFI very little primary spillover has been detected, while secondary reflector spillover levels are in accordance with predictions from 353 GHz to 857 GHz, but about 2.5 times higher than expected at 100 GHz. A $3\,\sigma$ variation is observed at 217 GHz and 143 GHz. The spillover contribution due to baffle reflected power is minimal due to blockage from the reflectors, and fits the model at 353 GHz and 217 GHz, however it is significantly higher than predicted at 100 GHz [46]. The general direction of these spillover components are shown in figure 1.24 also.

Most of the signals that Planck observes are fixed with respect to the celestial sphere, however the FSL contamination is not. This is due to the "cycloidal" nature of the Planck scanning strategy, which means each time a specific point on the sky is observed with the main beam, the FSL scans a different patch of sky than the previous time. Zodiacal light (ZLE) is the only other non-fixed signal observed, and shall be returned to later. An illustration of the scanning strategy is given in figure 1.25, where Planck

is situated at L2, a so-called "Lagrangian" point about which an object will perform a Lissajous orbit due to the balancing of the gravitational effects of the Earth, Moon and Sun.

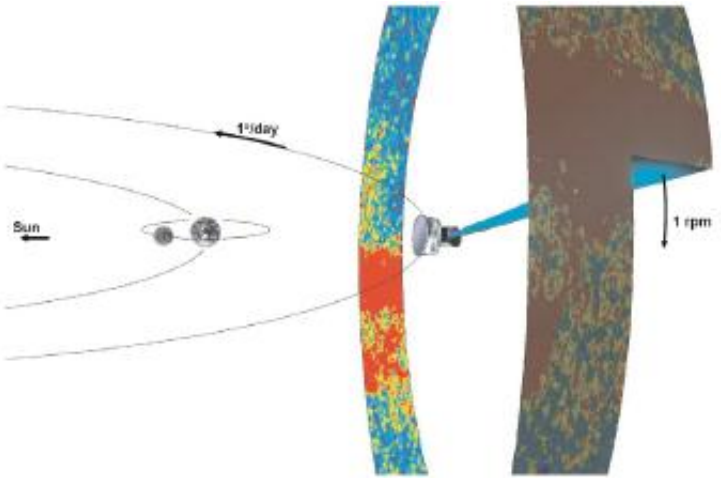

FIGURE 1.25: Planck scans the sky by rotating its Field-of-View at 1 rpm from its orbital location around L2. The spin axis is moved on average by 1 ° per day (in 2 arcmin steps) maintaining a constant aspect angle of 7.5 ° with respect to the Sun.[30]

The secondary reflector spillover sidelobe has two components - direct spillover on the sky between 5 ° and 20 ° from the main beam, and that which reflects on the baffle spreading into a diffuse pattern on the sky. The primary spillover is almost entirely due to direct spillover on the sky past the primary, and is much more strikingly clear in difference maps generated at the two highest frequency bands than that of the secondary spillover. Figure 1.26 shows the survey and difference maps generated for one of the 857-GHz detectors, where the difference map is obtained by subtracting one survey map away from the other. It can be clearly seen that the diffuse emission of the Galaxy is substantially removed by subtraction, however distinct lobes of power appear in regions away from the galactic plane. These "bananas" are residual Galactic emission seen through the primary spillover sidelobes of the telescope when the main beam is pointing in various directions away from the galactic plane. Surveys 1 and 2 were done 6 months apart, covering the same area of sky but with the telescope needing to point at opposite angles due to the rotation of the Earth in orbit about the Sun between scans. This means that although the full sky is observed in each survey, the galactic plane is only observed by the primary sidelobe (labelled as 'PR spillover' direction in figure 1.24) during one of the survey scans. As a result when difference maps are taken the coupled power from the Galactic plane appears as symmetric positive and negative lobes of roughly equal power, in opposing hemispheres.

The level of these so-called "bananas" varies from detector to detector, in some cases disappearing completely. This stands in stark contrast to the secondary reflector spillover,

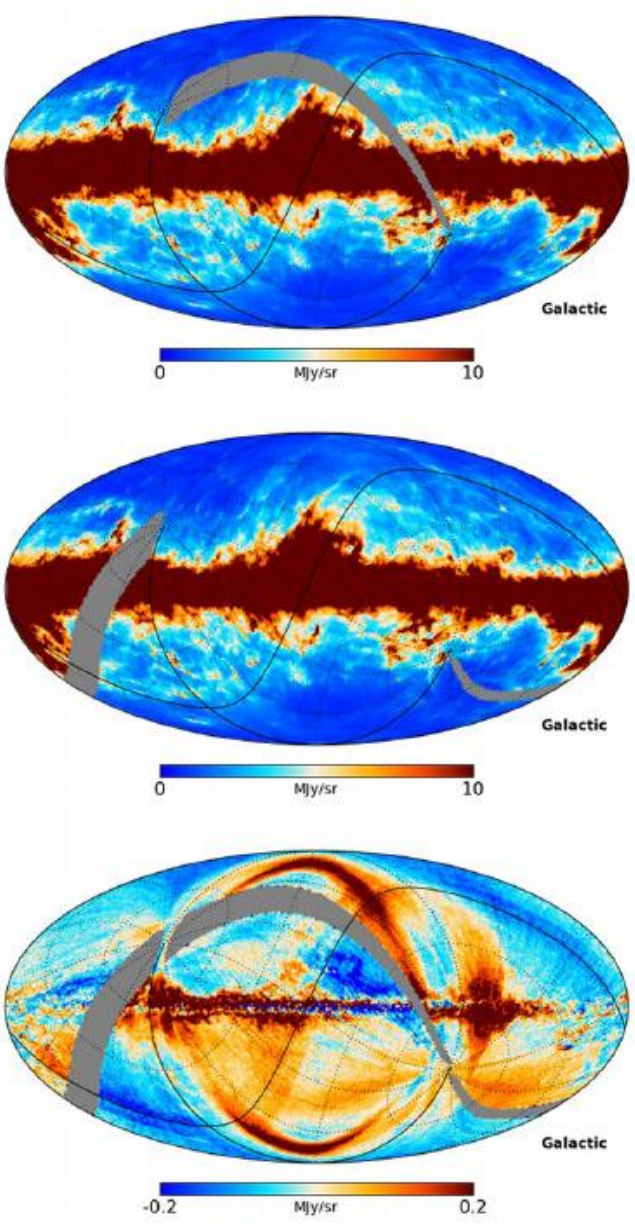

FIGURE 1.26: Top and Centre are the respective single survey 1 and 2 maps in Galactic coordinates, for the 857-1 detector. Bottom is the difference between the two surveys. Undefined pixels (in grey) define regions which were not observed, or were observed during a planetary transit or other event, thus the difference map contains undefined pixels from both maps.[44]

which appears at roughly the level expected by optical modelling across all difference maps. The impact which these sidelobes have on the gain calibration factors of the telescope is of the order 1.3×10^{-3}, however the discrepancy here illustrates the difficulty in predicting spillover levels for the highest frequency channels. We essentially need to know the exact horn beam patterns in order to predict spillover levels, however if beamwidths or sidelobes are increased for any particular horn then spillover will be higher. One potential concern for higher sidelobes surrounds the manufacturing of the

horns, and the difficulty in manufacturing the specified corrugation widths and depths. It stands to reason that small errors in etching of the corrugations could have occurred, which would have significant impact on beam quality, though still within the mechanical tolerances of the process. This would amply account for variation in the levels of the "bananas" from horn to horn, as their beams may vary significantly depending on how smoothly each was etched.

A tantalising hint at this possibility is revealed in the beam pattern measurements of the individual flight horns taken by in-flight observation of Mars, Jupiter and Saturn during transit of the main beam (see figure 1.27). The fitting to data obtained by observation of planets is done by a B-spline method, described in Appendix C of [46]. A B-spline fitting uses a basis set of modes to fit a 2-dimensional surface to time-ordered detection data, and proves superior to a simple 2D binning of data in its ability to capture large signal gradients.

Immediately clear in figure 1.27 is the relative symmetry of the beams across all CMB channels, while at 545 GHz and 857 GHz the beams appear to lose their circular symmetry outside of the main beam region. Time constants play a significant role in this however, as the latency of the detectors leaves a residual imprint away from the main beam in the direction of motion of the telescope pointing. In the worst behaved detectors(857-2 and 857-4), highly asymmetric power distribution in the near-in sidelobes is seen, however this asymmetry varies from horn to horn, resembling the manner in which the "bananas" appeared also to vary across detectors. With no evidence to the contrary this is taken as likely to be a result of horn imperfections, and work on this topic is undertaken in chapter 3.

Zodiacal light emission (ZLE) is the second non-fixed form of contamination observed by the telescope, and forms a diffuse contribution to excess power visible in the difference map of figure 1.26. ZLE is the diffuse glow seen due to the reflection of sunlight from small dust particles in our solar system, which extends up from the vicinity of the Sun along the ecliptic or zodiac. Each time Planck observes a specific point on the sky a different column of local dust is seen due to fact that the satellite has moved with Earth's orbit around the Sun. This leads to different ZLE signal from scan to scan, however the general signature is the "S"-shaped band visible along the ecliptic of the difference map in figure 1.26. These difference maps were originally generated to detect any anomalous features which might arise, such as zodiacal emission. They now have the added benefit of improving our understanding of the FSL features, since the orientation similarly changes as the instrument scans. Figure 1.28 highlights the effect of ZLE on various bands of the HFI instrument, and the improvement to map quality following its

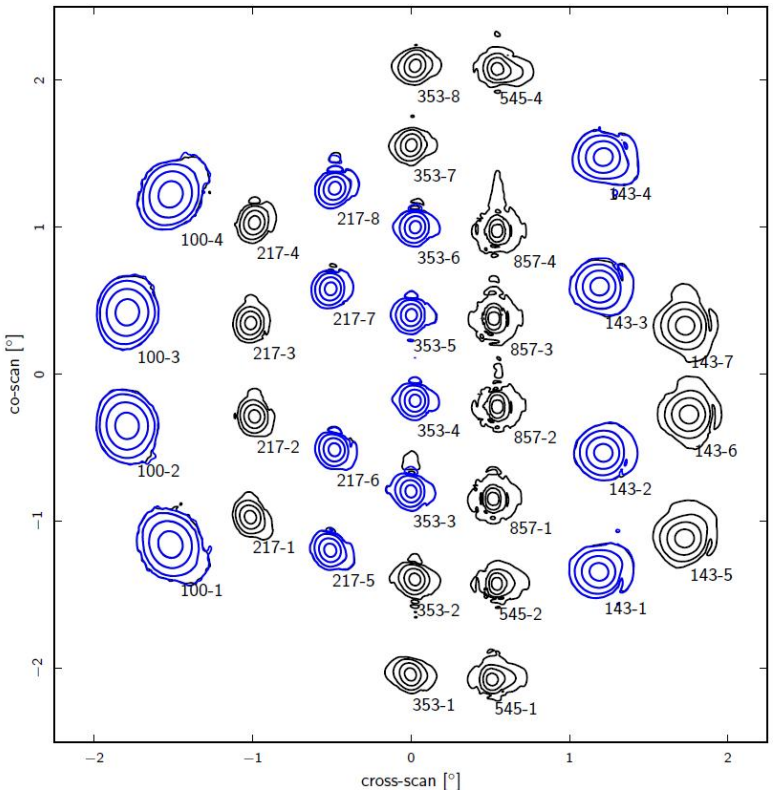

FIGURE 1.27: B-spline fit main beam profiles reconstructed from observations of Mars, Saturn and Jupiter for near-in sidelobe studies. The contours taper from the first contour at the beam FWHM (-3 dB) in decrements of 10 dB. [46]

removal.

We have discussed the physics behind the CMB, the closure obtained on our knowledge of the CMB temperature spectrum from Planck, and the future goals in CMB cosmology, namely the discovery of B-modes, and what they can tell us about the early Universe. Although the measurements have been completed, work will continue on the Planck data for many years to come, with the advent of better techniques for removing unwanted signal from the data. This will allow for direct improvement to λCDM estimates, while study of the various foreground contaminants will yield deeper knowledge of our own Galaxy as well as the greater ISM.

1.7 Thesis Outline

The outline of this thesis will be as follows; we will first examine various methods used for the modelling of horn antenna and telescope systems in Chapter 2, with special consideration given to the GRASP9 software package with which a large part of this work has been performed. We begin with a detailed description of the various numerical

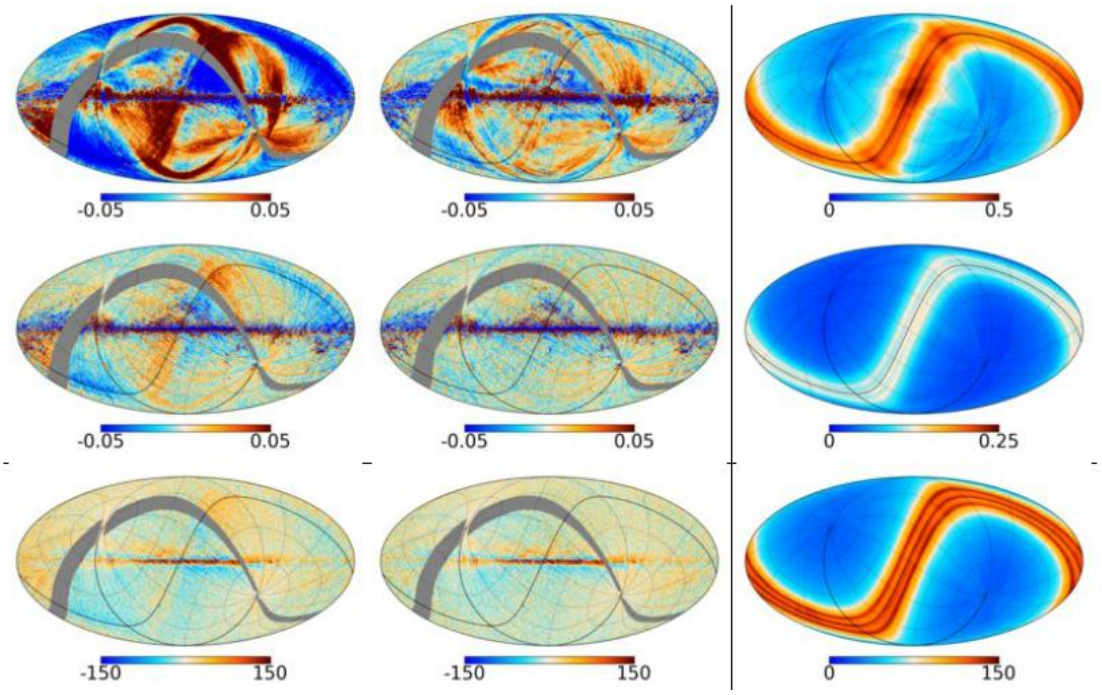

FIGURE 1.28: (Right) is the estimated contribution of ZLE to maps made at 857 GHz (Top), 545 GHz (Centre), and 353 GHz (Bottom), and the survey 1 minus survey 2 difference maps before (left) and after (centre) ZLE removal [47].

techniques used to simulate fields through telescopes and onto the sky, namely physical optics and the geometrical theory of diffraction, as well as the waveguide mode description of field propagation in waveguide structures such as horns. This will lead us conveniently to the modelling of multi-moded horns in the Planck telescope, and the characterisation of features seen in difference maps of the HFI channels in Chapter 3. Various supplementary analytical techniques for modelling telescope systems are outlined in Chapter 4, such as the Projected Aperture and Gaussian beam mode techniques, which assume paraxial lens systems but are useful at frequencies where PO and GTD become inefficient. Following this we will turn our attention to the modelling of additional systems in GRASP9, namely the Planck telescope simulator and FIRI interferometer, which have many unique features the implementation of which is outlined in Chapter 5. We will then conclude in Chapter 6 with analysis of 'ultra-Gaussian' horns to be implemented on the STEAMR radiometer, an atmospheric physics mission in the early stages of development.

Chapter 2

Analysis Methods for Quasi-Optical Systems

Designing systems that operate at terahertz frequencies has for many years been hampered by the inherent difficulty of analysing a region of the EM spectrum which lies sandwiched between the optical regime of shorter wavelength radiation and the radio regime of longer wavelengths. However there is now great interest in the field, as terahertz technology improves and its many applications are being discovered. Cosmology in particular benefits, as successive attempts to measure the Cosmic Microwave Background with higher resolution have proved an increasingly challenging task (see Chapter 1).

Radiation in the visible range is for the most part dealt with via geometrical optics, as systems share the characteristic that the component dimensions are large enough to allow the effects of the relatively small wavelengths (λ) to be ignored. This allows for quite a complete and accurate analysis of optical systems in this range of the electromagnetic spectrum. In the other case, where λ is of the order of the system dimensions, diffraction effects dominate especially in the near-field where the beam diverges rapidly. Here analysis of systems becomes difficult and time-consuming, as the beam behaves in a rather complex fashion.

In the large expanse between these two limiting cases a variety of methods can be implemented to describe the behaviour of radiation when λ is only moderately smaller than the beam radius. Often multiple methods will be used to verify results. In the modelling of telescope systems, methods such as Gaussian beam modes (GBM), physical

optics (PO), geometrical optics (GO), and ray tracing are some of the most common techniques implemented, and their formalisms will be described later.

While methods such as GBM analysis are elegant and quite time-efficient, they are to a certain extent idealistic, as they do not take diffraction effects and other common problems in telescope optics fully into account. This is the forte of more rigorous methods such as PO and the Geometrical Theory of Diffraction (GTD), which make highly accurate calculations of radiation properties on system elements. Accuracy comes at the price of efficiency however, and these methods can be quite time consuming due to the level of sampling required across mirrors or other surfaces which are relatively large compared to λ.

There is of course an inherent necessity for highly accurate models of optical systems at sub-mm wavelengths due to the difficulty of experimental testing in this region of the EM spectrum, and many software packages have been developed to satisfy this need. One such package is the General Reflector Antenna Software Package (GRASP) [48], which boasts a wide variety of tools for the modelling of telescope systems, and shall be described in detail below.

2.1 GRASP9 Software

GRASP9 is a highly specialist software package for analysing general reflector antennas and antenna farms, developed by TICRA [49]. It is written in Fortran 90 source code but can be run in Windows or via the command line in Linux. An object-oriented approach to the design phase allows flexibility in the definition of system elements, as feeds and reflector surfaces are described in terms of objects of various class types. It is regarded as the best optical modelling package available for commercial use, and has been refined over the years by the requirements of industry heavyweights such as ESA. It has been used extensively in the Far Infrared and Sub-millimetre Optics group at NUI Maynooth for modelling Planck, Herschel [50] and ALMA [51], and it will be the principal software package used throughout this thesis for optical modelling, specifically with regard to the Planck telescope.

GRASP9 predicts the radiation patterns of reflector systems (telescopes) by calculating the field from a source feed, then propagating this through the optical system to a detection grid at some location in either the near- or far-field of the telescope. This can be done in a number of ways: by PO and the Physical Theory of Diffraction (PTD), or

if at large enough frequencies that the geometrical limit holds true, by GO and GTD. In PO a source illuminates a scatterer and the currents induced on it are calculated by solving Maxwell's equations. These currents are also considered a source, as they radiate the scattered field to another scatterer, or the sky. In the sub-mm range PO provides the greatest accuracy, however it encounters difficulty with blockages and close spacing between scatterers. Multiple reflections and re-reflections may be present in reality when a blockage or even partial blockage exists in the system, however accounting for these using PO would be extremely time-consuming. PO is best used for idealised systems where currents will only be induced on sub-reflectors, then propagated to a main reflector, then to the sky, and so on. GTD becomes a much more useful tool with regard to blockages, as it performs ray tracing from the source, accounting for the effects of any scattering surface in the model. Each method will be described in more detail in this chapter.

Two distinct files define any system modelled in GRASP9, the TICRA Object Repository (*.tor) and the TICRA Command Input (*.tci) files. The TOR-file contains a list of all defined objects (scatterers, feeds, grids, etc.) and their respective coordinate systems. The TCI-file then contains a list of commands for the generation of fields and currents throughout the system, referencing the TOR-file for information on any of the objects specified for use by the TCI. These commands are readily implemented in the 'Command List' GUI of the package, as shown in figure 2.1

All field storage in GRASP9 (aperture fields, far-fields, or fields on surfaces) is done using grid (.grd) and cut (.cut) files. Both contain specifically formatted header data, from which GRASP9 will know how to read the field data below it. The top of a typical GRASP9 grid-file is shown in figure 2.2. When the field storage object is generated by the GRASP9 software it will automatically write headers to match what has been specified by the user.

2.1.1 GRASP9 Interface

In the Windows operating system the graphical interface can display a 2-dimensional drawing of the system which can be rotated through three projections (xy, xz, and yz) with respect to the basis coordinates of the telescope. This was useful for positioning elements during the design phase. Any objects created will appear transparent if required, and a more versatile 3-dimensional graphical interface is also available. For quickly assessing telescope properties the 3-dimensional 'open-GL' viewer is often preferred, as it

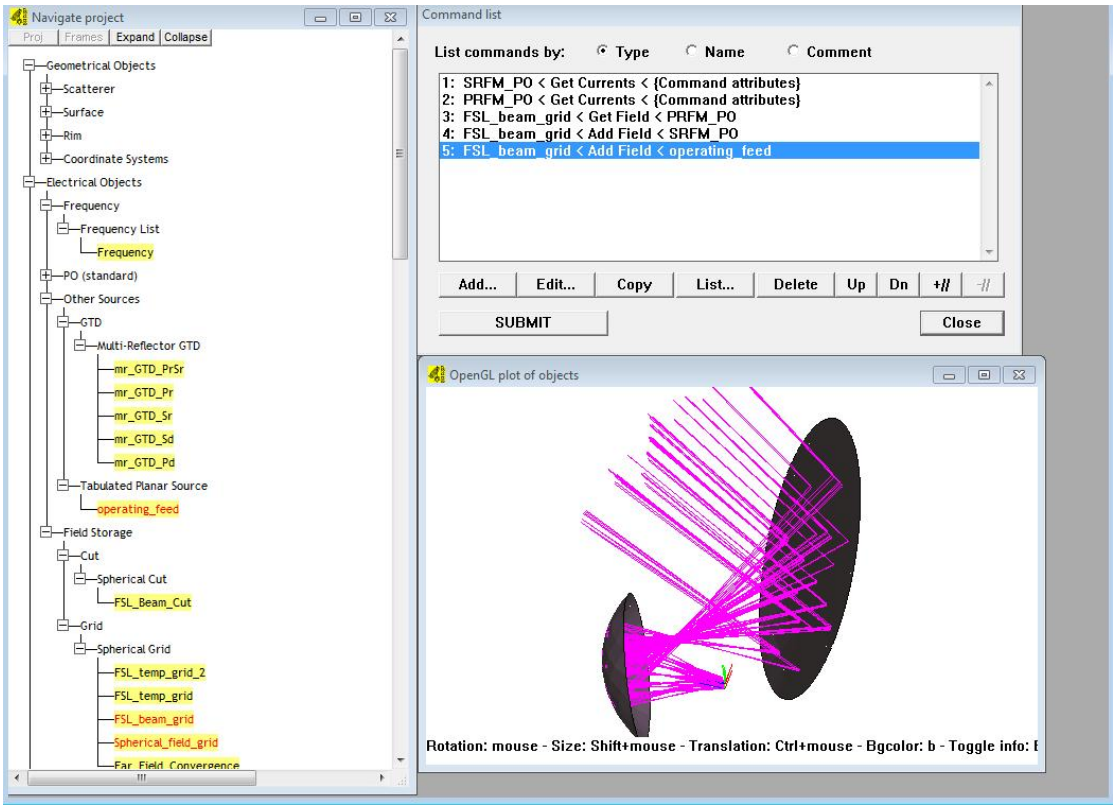

FIGURE 2.1: Standard GRASP9 GUI with tree-list of system objects (from the TOR), and command list (from the TCI).

```
VERSION: TICRA-EM-FIELD-V0.1
Field data in grid
SOURCE_FIELD_NAME: SRFM_PO
FREQUENCY_NAME: Frequency
FREQUENCY:  462.000000000000 GHz,
++++
 1
          1           3           2           7
          0           0
  0.0000000000E+00 -0.5000000000E+02  0.9000000000E+02  0.5000000000E+02
          2         201           0
 -0.9029165970E-02  0.2890334068E-02 -0.2223175528E-13  0.4802022954E-14
 -0.6150467831E-02 -0.9073575331E-02 -0.5264939142E-02  0.2640605952E-02
 -0.9103546958E-02  0.7934418331E-02 -0.3274349536E-14  0.5018325703E-13
 -0.4809664464E-01  0.2251413103E-01  0.1245211059E-01 -0.8291587560E-02
```

FIGURE 2.2: Typical layout of a GRASP9 grid data file (.grd).

allows rotation around any axis. A typical system of two mirrors with rays traced from the aperture location onto the sky is shown in figure 2.3.

The mirrors in figures 2.1 and 2.3 are examples of elements defined by a variety of reflector classes in the GRASP9 repository. Two separate files define any reflector, a surface file (*.sfc) and a rim file (*.rim). Surfaces can be defined as an ellipsoid,

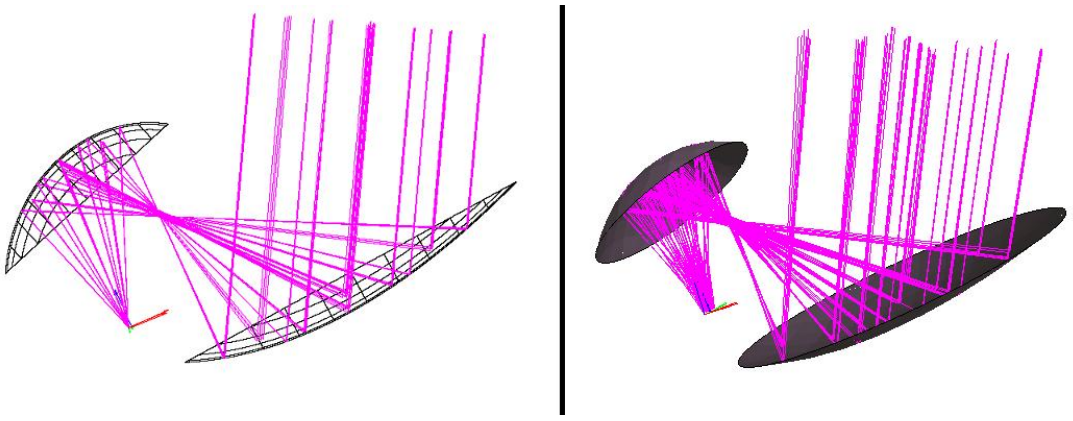

FIGURE 2.3: Typical graphical display of a dual reflector system in GRASP9. 2D plot (left) and 3D 'open-GL' plot (right) with rays traced from a source through the system in both.

hyperboloid, paraboloid, a numerical xy-grid or an irregular xyz-grid, and a general 2nd-order xy-polynomial. The rim is then determined by the intersection of the surface and a cylinder whose cross-section lies in the xy-plane of the coordinate system of the mirror. This allows the rim and surface to be defined independently of each other, with circular or elliptical, super-elliptical, triangular, rectangular and numerically defined rim types available.

Various other planes, conics, pyramidal surfaces and tabulated grids allow for implementation of unusually shaped objects which make up a telescope assembly, some of which are used in the full GRASP9 model of the Planck telescope developed by TICRA, and used for a substantial portion of this thesis.

2.1.2 GRASP9 Sources

Any simulations to be performed in a GRASP9 project must be supplied with a source of radiation. GRASP9 provides a diverse range of options in its object directory, generally representative of sources commonly in use. If the geometry of a source is well known, GRASP9 allows the input of various horn types; conical, rectangular, hexagonal, potter and hybrid-mode horns being among the most useful. In all cases the aperture radius and flare length of the horn are required, and when known, the amplitudes and phases of modes excited in the input waveguide may also be supplied. Based on this information, GRASP9 creates an equivalent aperture field for the desired horn, which may then be propagated. In cases where the aperture field of the horn has already been calculated, such as when one has been generated by NUI Maynooth's in-house software package "SCATTER" (see section 2.3.3), it may be supplied to GRASP9 using the tabulated

source option in the object directory. This requires the input of a standard GRASP9 grid-file, which represents the aperture field of the horn in a planar grid orthogonal to the axis of propagation from the aperture.

Alternatively, it is possible to define a beam pattern fulfilling certain criteria. The aperture field of a typical conical corrugated horn for example, can often be represented by a Gaussian, defining an equivalent beam radius (where the axial intensity drops to $1/e$ of peak value) and beam radius of curvature, which will be infinite if the beam waist is assumed to coincide with the aperture.

Tab Planar Sources

If the aperture field of a horn is known it can be implemented in GRASP9 by means of a tabulated source. This requires that the beam pattern of the horn be specified in a file with appropriate GRASP9 header data describing the dimensions and sampling of the field, as well as the coordinate system used. The user can then specify the level of PO sampling on the desired surface to which the field will be propagated, be it a reflector, near, or far-field grid. This is a useful way of avoiding the lengthy currents convergence process, which will be outlined below, and assumes the user knows the accuracy to which the field should be measured on the surface of interest, as this is determined solely by the PO sampling. Conveniently one can opt to normalise the total power in the beam to the GRASP9 standard of 4π W, however for the purposes of the multi-moded simulations outlined in this thesis, maintaining relative power levels between modes is crucial, and the normalisation is not used.

A version of the 'SCATTER' software was created by the user such that on calculation of the field at the aperture, a .grd file was generated containing a header describing the aperture, and the field data in six columns (real and imaginary for each of the x, y and z components). The z-components of the field are set to 0, as 'SCATTER' provides a complete description of an aperture field in x,y only. This was used to generate hybrid mode aperture fields, and the subsequent tabulated source files were used as input to GRASP9 for the telescope simulations in section 3.4.1.

Gaussian Beams

The Gaussian Beam pattern definition option in GRASP9 is quite useful as a simple representation of the field from a corrugated horn, which will be generally close to Gaussian in shape (the field from a scalar horn is described by a zero-order Bessel function). The required input is simply the taper level (in dB) at a user-defined far-field

angle. This is sufficient to describe a circularly symmetric Gaussian beam, the waist of which lies at the origin of the defined coordinate system. In terms of angle, in the near-field the beam is broader than in the far-field, and the phase front will be ellipsoidal rather than spherical, owing to the taper which generates a more complicated field than that of a simple point source.

Gaussian input provides a useful alternative when a full tabulated description of the field is lacking, however for the purposes of this thesis it was not required. A separate GBM analysis was performed in the early high frequency modelling of the Planck telescope, providing a simplified estimation of sky beams before GRASP9 modelling was undertaken. This will be discussed further in section 2.3.5.

Horns

Both rectangular and conical horn antenna descriptions are also available in GRASP9, and they are sufficient to describe any simple, smooth-walled geometry. For a rectangular horn description the user must supply an aperture width and height, as well as the flare lengths of the horn along both axes 'xz' and 'yz', as shown in figure 2.4. The flare distance is taken from the point at which the orthogonal walls of the horn would meet, which naturally lies some measurable distance behind the waveguide-horn junction. This will in turn determine the phase front of an astigmatic beam at the aperture, whose origin lies at this apex. The modes present at the aperture may also be supplied, naturally in the TE/TM format specific to rectangular waveguides, where for any excited modes, values of amplitude ('amp'), phase ('phase') and rotation ('rot') must be defined. The order of cut-on of modes must also be adhered to for use of this feature the theory of rectangular waveguide modes is outlined in section 2.3).

Uniformly expanding conical horns may also be described using the aperture radius and flare length, which again is taken from the apex of the walls behind the entrance to the waveguide, as shown in figure 2.5. The mode content of the horn can also be defined, where cylindrical TE/TM modes are the appropriate choice for the standard conical horn (the theory behind which is also outlined in section 2.3). Modes for which the cut-off is lower than the operating frequency cannot be included. Any modes for which 'phase' is left at the default value of zero will be in phase at the aperture. The value 'rot' defines the rotation of mode from the axis x_f towards y_f in figure 2.5, such that any TE mode will be linearly polarised along y_f and any TM mode will be linearly polarised along x_f when defaults of zero are maintained.

Hybrid mode conical horns can be defined in the same way as regular conical horns, the

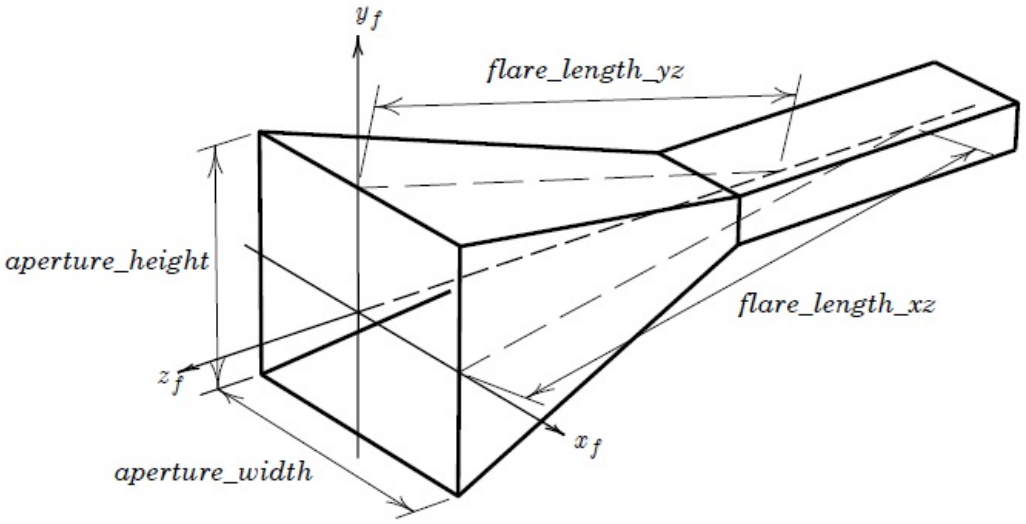

FIGURE 2.4: Geometrical description of a rectangular horn in GRASP9 where rectangular TM and TE waveguide mode are polarised along x_f and y_f respectively. [52]

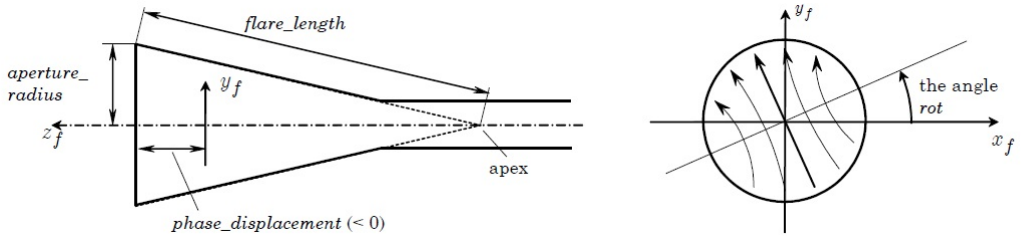

FIGURE 2.5: (Left) Outline of the geometry of a standard conical horn, as defined in GRASP9, and (right) the rotation of a TE_{11} mode away from linear polarisation symmetric with y_f. [52]

only difference being the definition of the mode set used - hybrid modes rather than cylindrical waveguide modes. This can be extremely useful for horn optimisation in particular, as modifying the amplitude of the smaller number of hybrid modes present allows much more efficient optimisation of horn characteristics. Work undertaken by the author in the modelling of ultra-Gaussian horns for the STEAMR project makes use of this GRASP9 tool, and is outlined further in chapter 6.

2.2 Analysis Methods

Having detailed a range of field storage options (grids, and cuts) available in GRASP9 some insight into the methods used to calculate these fields would be prudent at this stage. The two most relevant methods used are PO and GO, both of which deal with scattering problems, but in different ways. PO is generally used in the mm/sub-mm

range, while at shorter wavelengths GO can provide a more practical approximation, owing to the quicker calculation time for wavelengths where current calculations on surfaces become large. Both methods were used for the Planck HFI modelling in this thesis, and for this reason the theory behind each will be detailed below.

2.2.1 Physical Optics

As already mentioned, GRASP9 can perform scattering simulations using a number of methods, of which PO is the most commonly used. It is an approximation to the classical solutions of Maxwell's equations describing the behaviour of electric and magnetic fields, and is widely used in optics as a middle-ground between the regime of GO which ignores wave effects, and the full electromagnetic wave regime used at lower frequencies. The term 'physical' arises from the fact that it is a more physical approach to optics than ray tracing by geometrical optics.

For any scattering problem the ultimate aim is to calculate the radiated field, which can be done knowing only the incident field and the properties of the scatterer in question. Induced electric and magnetic currents on a surface, $\mathbf{J}$ and $\mathbf{M}$ respectively, give rise to an electric vector potential $\mathbf{F}$ and a magnetic vector potential $\mathbf{A}$. Using these, the electric and magnetic fields can be quite easily generated. The electric vector potential function $\mathbf{F}$ arising from the magnetic current distribution $\mathbf{M}$ is given by [53]

$$\mathbf{F} = \frac{\mu}{4\pi} \int \int_S \mathbf{M} \frac{e^{-ikR}}{R} dS, \tag{2.1}$$

and the magnetic vector potential function $\mathbf{A}$ due to the electric current distribution $\mathbf{J}$ is given by

$$\mathbf{A} = \frac{\varepsilon_0}{4\pi} \int \int_S \mathbf{J} \frac{e^{-ikR}}{R} dS, \tag{2.2}$$

where integration is taken over the region, S, containing the source distribution which varies as e^{-ikR}, and R is the radial distance from a point in that source distribution to the point of observation. ε_0 is the permeability of free space and μ is the magnetic permittivity of the surface.

To begin, let us take Maxwell's fundamental curl relationship between electric and magnetic fields $\nabla \times \mathbf{E} = -i\omega\mu\mathbf{H}$, where ω represents the frequency of radiation. Using the secondary relationship between magnetic field and magnetic vector potential

$$\mathbf{H}_A = \frac{1}{\mu} \nabla \times \mathbf{A}, \tag{2.3}$$

where $\mathbf{A}$ denotes the magnetic vector potential giving rise to magnetic field $\mathbf{H}_A$, a relationship for the electric field is found

$$\mathbf{E}_A = -i\omega\mathbf{A} - i\frac{1}{\omega\mu\varepsilon_0}\nabla(\nabla\cdot\mathbf{A}), \tag{2.4}$$

where the magnetic vector potential satisfies the Helmholtz equation $\nabla^2\mathbf{A}+k^2\mathbf{A} = -\mu\mathbf{J}$. The divergence term incorporates a scalar magnetic potential term which is a function of position.

Now taking the electric field due to the electric vector potential $\mathbf{F}$

$$\mathbf{E}_F = \frac{1}{\varepsilon_0}\nabla\times\mathbf{F}, \tag{2.5}$$

an equation for the magnetic field due to the electric vector potential is derived in a similar manner as before, such that

$$\mathbf{H}_F = -i\omega\mathbf{F} - i\frac{1}{\omega\mu\varepsilon_0}\nabla(\nabla\cdot\mathbf{F}). \tag{2.6}$$

So assuming the current distribution on any surface is known, the complete radiated field can thus be found by combining equations 2.3, 2.4, 2.5, and 2.6.

$$\begin{aligned}\mathbf{E} = \mathbf{E}_A + \mathbf{E}_F &= -i\omega\mathbf{A} - i\frac{1}{\omega\mu\varepsilon_0}\nabla(\nabla\cdot\mathbf{A}) - \frac{1}{\varepsilon_0}\nabla\times\mathbf{F}\\ \mathbf{H} = \mathbf{H}_A + \mathbf{H}_F &= \frac{1}{\mu}\nabla\times\mathbf{A} - i\omega\mathbf{F} - i\frac{1}{\omega\mu\varepsilon_0}\nabla(\nabla\cdot\mathbf{F}).\end{aligned} \tag{2.7}$$

By integrating over the scatterer surface (varying the value of R, and thus the distance between source distribution and point of observation in equations 2.1 and 2.2), the appropriate approximation to the radiated fields in the near- or far-fields of the scatterer can be easily found.

The total radiated electric field E_t from a scatterer may now be considered as the PO approximate solution to a scattering problem, and is defined by the sum of the scattered electric field E_s and the incident electric field E_i [52] as:

$$\mathbf{E}_t = \mathbf{E}_i + \mathbf{E}_s. \tag{2.8}$$

An ideal conducting surface will radiate a scattered field based on the induced surface currents, thus a three step-process describes the solution to a scattering problem:

1. calculate the induced currents on a scatterer's surface, which under the PO regime requires an incident electromagnetic field to excite both electric and magnetic

currents,

2. calculate the radiated field based on the previously described currents, equations 2.1, 2.2, 2.4, 2.6, and 2.7,

3. sum the incident field with the scattered field to find the total field distribution 2.8

The first step is by far the most complex. For non-ideal surfaces the method-of-moments (MoM) technique is commonly used, however for scatterers which are large in terms of wavelength this proves extremely time-consuming. PO however provides a good approximation to the fields by assuming a perfectly conducting scatterer for which calculations can be significantly reduced.

One subtle issue with regard to the PO calculation done by GRASP9 is that when the total reflected and diffracted field from a surface has been calculated, the portion of the incident field which strikes the scatterer is added to it, and the two propagated. This incident field is phase-inverted by 180 ° on contact with the scatterer, but will continue along its original axis of propagation. As this field in the rear of the reflector is non-physical (ignoring any currents excited on the back of the scatterer which will generate a very weak field) it is cancelled by adding the field from the source to the total field. It is the 180 ° phase shift between both contributions in the rear of the scatterer that allow this complete cancellation, while simultaneously retrieving the spillover passed the edges of the reflector by inclusion of the original field. This will prove crucial in PO modelling of the Planck HFI far sidelobe structure, which shall be discussed in chapter 3.

In the PO approximation we assume that the induced current at a specific point on a curved scatterer's surface is equivalent to the current which would be induced on a perfectly conducting infinite planar surface tangential to the scatterer's surface at that point. The PO approximation may then be mathematically written as [54]:

$$\mathbf{J} = 2\hat{n} \times \mathbf{H}_i \tag{2.9}$$

where $\mathbf{J}$ is the induced electric current, $\mathbf{H}_i$ the incident magnetic field and $\hat{n}$ the unit normal to the surface at that specific point. The approximation is good for conductors if their dimensions and radius of curvature are large when measured in terms of wavelength. The surface currents are then computed and the electric and magnetic radiated fields determined by integrating these currents over a two dimensional surface defined by the rim dimensions [52]. The form of these integrals will vary depending on whether a near-

or far-field is to be calculated. The accuracy of the integration is wholly determined by the degree of sampling on the scatterer's surface, and this is chosen by GRASP9's PO convergence tool described next.

PO convergence

Two variables define the PO integration grid on any surface, those are referred to as *po1* and *po2* (each referring to sampling along one of two coordinate directions). Although it is possible to set these values prior to the initiation of a scattering calculation, inappropriate values will lead to inaccurate representation of the radiated field. Thus it is usually best to allow GRASP9 to calculate these values automatically. Taking the natural example of a dual-reflector system, the auto-convergence starts by setting *po1*=*po2*=10 on both sub- and main-reflector, and calculating the field on the main reflector. The value of *po1* on the sub-reflector (i.e the level of sampling across the surface) is then doubled and the field on the main reflector recalculated. This doubling continues until a point is reached where the field on the main reflector differs by $< 10^{\frac{Field\ \ Accuracy}{20}}$ between successive doubling of the *po1* value [52]. This routine is repeated on the main reflector for convergence of the output field at the number of output points specified in the field grid or cut. GRASP9 automatically sets the value of field accuracy to -80 dB, meaning the surface integral will be re-computed with finer sampling until changes of less than 1 dB are observed at the -60 dB level. For PO calculations performed throughout this thesis the field accuracy is set to -80 dB unless otherwise stated. If the user has recorded the values of *po1* and *po2* based on a previous auto-convergence by GRASP, they can be entered into the GRASP 'PO-object' which contains a reference to the surface on which PO is to be used, and (optionally) the *po1* and *po2* sampling required. This object is then referenced in any commands requiring reflection from the given surface. The input of *po1* and *po2* can help avoid the computation time involved in the convergence procedure, however this is assuming frequency, source file and other important factors stay the same. It is essential that the number of integration points be sufficiently large that the integration will be correct, however if the values are too high this may result in an unacceptably long processing time.

The values *po1* and *po2* are entirely dependent on the scatterer being analysed, and the position of the field points to be mapped with respect to the scatterer. Thus, if the target PO object on which currents are being calculated illuminates one or more scatterers (from which the scattering shall be determined in a following step) then these must be specified for the convergence procedure. Correspondingly, if the field due to the induced currents is to be calculated at specified points on the sky, then convergence must take place on the given output sky cut or grid.

Taking the general case of a scatterer with a circular rim, and a polar integration grid projected onto the scatterer's surface, *po1* defines the number of integration points, N_r, along the radial direction, and *po2* defines the number of points, N_ϕ, along the azimuthal direction [52], as shown in figure 2.6, such that

$$\begin{aligned} po2 &= z \\ po1 &= po2/2.4, \end{aligned} \tag{2.10}$$

where the values are rounded to the nearest integer, and

$$z = 1.09\pi\frac{D}{\lambda}\sin\theta_0 + 10 \tag{2.11}$$

D is the scatterer diameter, λ the wavelength and θ_0 the maximum angle away from beam centre which the reflector subtends when viewed from the source. In the worst cases of illumination at a high angle of incidence the value of z may need to be increased to $z = 2\pi D/\lambda$. It is worth noting here that the value of *po2* can also be used to represent the number of physical theory of diffraction (PTD) points along the outer rim.

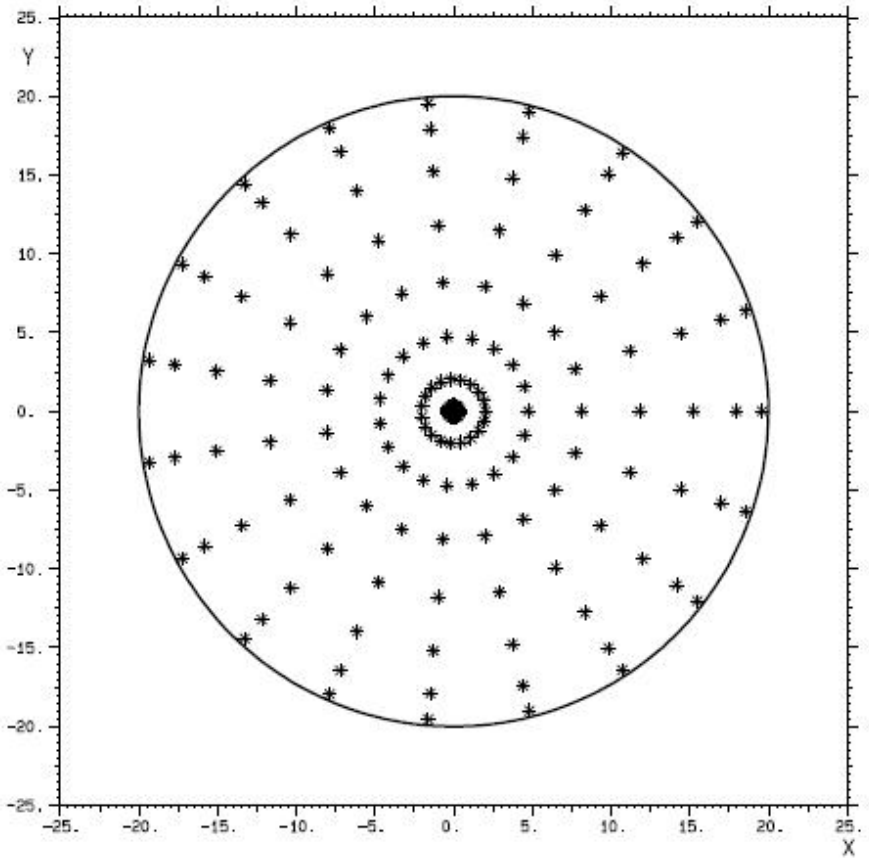

FIGURE 2.6: The integration grid used on a circular reflector for which N_r=*po1*=8 (radially out from the centre), and N_ϕ=*po2*=19 (in a circle around the surface). The total number of integration points on the grid is 152, with the central part of the mirror sampled more than the outer regions for obvious reasons [52].

Taking, for example, the modelling of the Planck telescope undertaken in this thesis, at 730 GHz (the lower end of the 857 GHz band) the total number of PO points required to correctly sample the primary mirror to -80 dB field accuracy is of the order of 26 million. The smaller secondary mirror requires 7 to 8 million points, which means when propagating from one mirror to another, the number of pairs of points which must be considered is extremely high. This massively impacts computation time, requiring use of the 66 strong cluster of processors available in the NUI Maynooth physics department. Were this not available, calculations such as these would be near impossible.

Physical Theory of Diffraction

PO describes the currents induced on a scatterer assuming scattering from an infinite planar surface, however this will not correctly account for currents near the edge of a reflector, for which another method must be used. This is the forte of the physical theory of diffraction (PTD), which integrates so-called 'equivalent edge' currents along the edge of the reflector surface. These are found by considering the currents arising from a plane wave incident on an infinite perfectly conducting half-plane, and then integrating the difference between these currents and the equivalent PO currents which would have been calculated assuming an infinite plane at this point. Thus, PTD act as a correction to PO, such that the total scattered field from any point on the edge is given by

$$\bar{E}^S = \bar{E}^{PO} + \bar{E}^{PTD}. \tag{2.12}$$

The incremental strips along which the currents are integrated can be either finite or infinite in length, however for the purposes of reflector analysis GRASP9 assumes infinite strips, based on the equations governing the implementation of PTD [55].

2.2.2 Geometrical Optics & Geometrical Theory of Diffraction

The PO approach described in the previous section is extremely accurate in modelling all regions around the telescope, however in dual-reflector antenna systems the density of the integration grids grows with the 4th power of frequency. This means that as the frequency gets higher the computation time will inevitably increase, because the grids must get finer to maintain the same accuracy over a given angular region. For this reason a separate approach is necessary when structures become quite large relative to wavelength, and GO solves this problem.

Three steps define any GO calculation, beginning with the selection of significant rays required for the desired field computation. If one wishes to calculate the field behind a reflector, it should be clear that calculation of the reflected field will be of no use, as it does not exist behind the reflector. By omitting such unnecessary calculations computation time can be significantly optimised.

The second task involves tracing each of the chosen rays through the system, determining all reflection points from surfaces and diffraction points from surface edges. This is generally quite difficult, however once complete leaves only the third step of field calculation at the output plane, which is relatively straightforward.

Multiple ray types are considered in a GO model, defined by the sequence of interactions of the ray with intermediary structures en route to the desired field point. The number of interactions can be chosen by the user, and is defined as the order of the rays. Taking a standard dual-reflector system the direct ray onto the sky has order $n = 0$. If a ray undergoes a single reflection or diffraction from a surface en route to the field point of interest it has order $n = 1$. A single diffraction in a sub-reflector followed by reflection from the main reflector defines a ray of order $n = 2$ and so on. In this manner the paths computed for the propagation of a ray grows in complexity with each increase in order, as shown in figure 2.7. This will inevitably impact upon computation time as for each added order all paths computed in the previous order must now individually undergo an entire range of possible interactions defined by the system properties. Depending on the location of a given field point the number of possible ray types which will carry power to it could be small, making computation of higher order reflections unnecessary. In most cases only the main beam and spillover regions will contain a large numbers of rays, and though forming only a small relative area of the entire sky, computation of all possible rays to these points will be quite time-consuming.

In some cases the number of rays converging on the same point can be so high that a "caustic" is found, usually visible as a spike or null in power in the field pattern across a very small angular scale. This is usually due to the reflecting surface focussing all rays incoming on it to a specific field point on the sky, determined solely by the reflector shape. This location on the sky will be along a 'caustic hyperboloid' which intersects the reflector, and can be seen in figure 2.8. Here the interval A_1A_2 represent the major axis of the rim ellipse, and E_1 and E_2 are focal points of the rim. However one can define a hyperbola, at any point along which the reflector appears circular. This hyperbola passes through the focal points of the reflector, F and F$'$, with vertices at E_1 and E_2, and focal points A_1 and A_2. Crucially, the distance from any point along one leg of the hyperbola, via the reflector, to any point on the opposite leg of the hyperbola, will

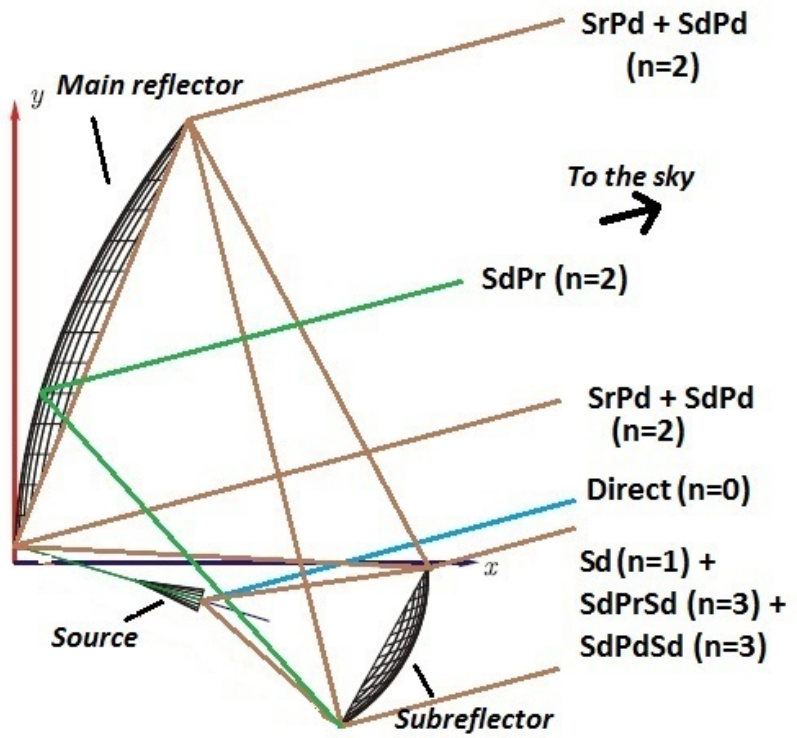

FIGURE 2.7: Standard dual reflector telescope, with a number of possible rays of different orders contributing to the overall field on the sky. The abbreviations used to define various ray paths are secondary reflection ('Sr'), secondary diffraction ('Sd'), primary reflection ('Pr') and primary diffraction ('Pd'). Multiple combinations of these define higher order rays ('SdPrSd' for example), which will only be traced once the user specifies an order, 'n'.

always be equal in length. Given this fact, when a feed is naturally placed at either focal point of the reflector, all field points along the opposite leg of the hyperbola will be caustics. The hyperboloid is asymptotic with the direction of boresight in the far-field of the paraboloid reflector, and for this reason a caustic in the main beam will be observed whenever a far field is required using GTD. Similarly an ellipsoidal reflector will have a hyperbola intersecting the angle of boresight, and the focal points of the reflector, along which it appears circular, thus producing caustics at either focal point of the reflector.

Note also that a caustic will be found in the region behind the reflector, which may become an issue when modelling far-out sidelobe structure, outlined later in this thesis. The caustic hyperbola is naturally aligned with the plane of symmetry of the reflector in question, thus the caustic field point in the rear of the telescope can always be found taking a far-field cut around the sphere along the plane of symmetry. This may ease automated removal of caustics by accurate prediction of the finite region over which they will appear.

Numerically, the diffracted field from the edge of a curved surface is given by [56]

$$\bar{E}^d = \bar{E}^i \bar{D} A \frac{e^{-jkz}}{s} \tag{2.13}$$

where $\bar{D}$ is known as the constant Dyadic diffraction coefficient, $\bar{E}^i$ is the incident field, and A is given by

$$A = \sqrt{s\rho/(\rho + s)}. \tag{2.14}$$

Here s is the distance from the diffraction point to the field point, and ρ is the caustic distance. Naturally, when a feed intersects one arm of the caustic hyperbola, and a field point on the sky intersects the other leg, it is found that $\rho = s$, and $A \to \infty$. Thus the GTD formulism breaks down, producing erroneous field results in the caustic region. An example is shown in figure 2.9, where GTD is implemented for main beam calculations. A PO comparison highlights the caustic produced by the GTD approach in the main beam region. Where this occurs a PO approach is best implemented to obtain the correct field. Examples of caustics in FSL regions will be highlighted in Planck modelling performed in chapter 3.

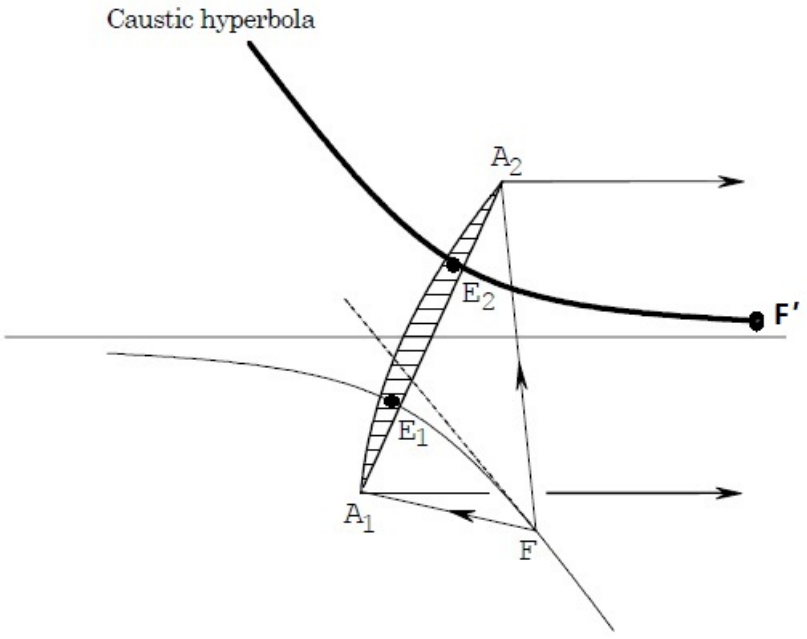

FIGURE 2.8: A caustic hyperbola for a parabolic reflector with focal points of the rim at E_1 and E_2. The feed is located at F, caustics occur at F′, and the angle of boresight is outlined by rays from A_1 and A_2 [52].

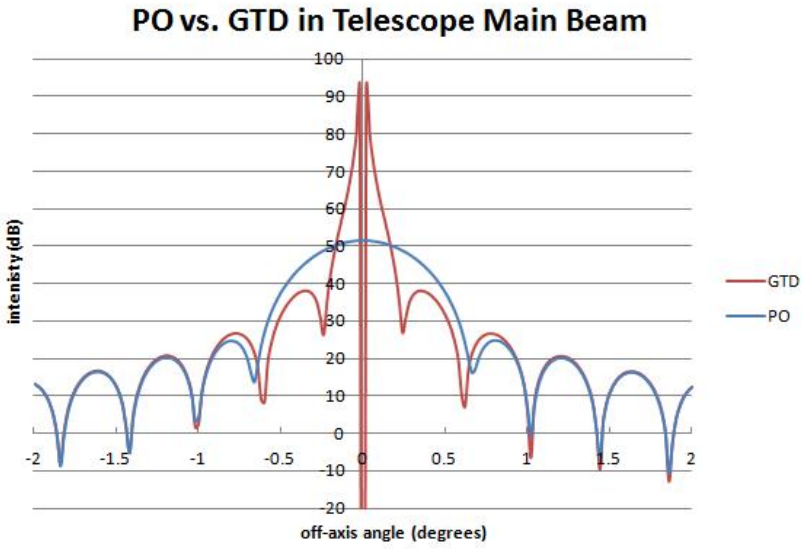

FIGURE 2.9: Comparison between PO and GTD in modelling of the main beam at 100 GHz, showing the caustic which blights the main beam region calculated using GTD.

2.3 Modal Solutions to EM Wave Propagation

The modal modelling of quasi-optical systems is based on finding modal solutions to the wave equation which, depending on the medium in which radiation is being propagated, take on a variety of forms. Transverse Electric (TE) and Transverse Magnetic (TM) waveguide modes can be used to describe the field at any point in waveguide structures such as horn antennas, and can be obtained in either cylindrical or rectangular form, for conical or pyramidal shaped horns, respectively. Hybrid modes, denoted HE/EH, can be used to efficiently describe the field in corrugated waveguide structures. These hybrid modes are of particular use in the modelling of multi-moded horns, as describing a field using a smaller set of modes dramatically reduces the time required to compute the total field on propagation through a system of reflectors. This shall be returned to later when discussion of the multi-moded HFI horns is undertaken. In free-space, solutions to the wave equation take the form of Gaussian beam modes, however transition from one mode set to another (at the aperture of a guide structure to free space, for example) is easily performed by overlap integrals between the modes of the two regimes. In all cases the evolution of a beam through a quasi-optical system can be readily derived by propagation of the individual modes which constitute the overall field. These individual modes maintain their original shape on propagation, however their phase varies, and the resulting phase difference between the modes at any chosen output plane will determine the form of the overall field.

Herein the theoretical basis behind various modal solutions shall be outlined, with a view to understanding their implementation in quasi-optical systems such as the Planck telescope. Beginning with the fields inside waveguide structures, we shall first describe the modelling of conical horns by means of cylindrical waveguide modes appropriate to smooth-walled structures, and follow this with a description of rectangular waveguide modes. This can be extended to the description of corrugated structures in which there are many corrugations per wavelength. To provide a helpful illustration, the manner in which rectangular modes propagate is shown in figure 2.10.

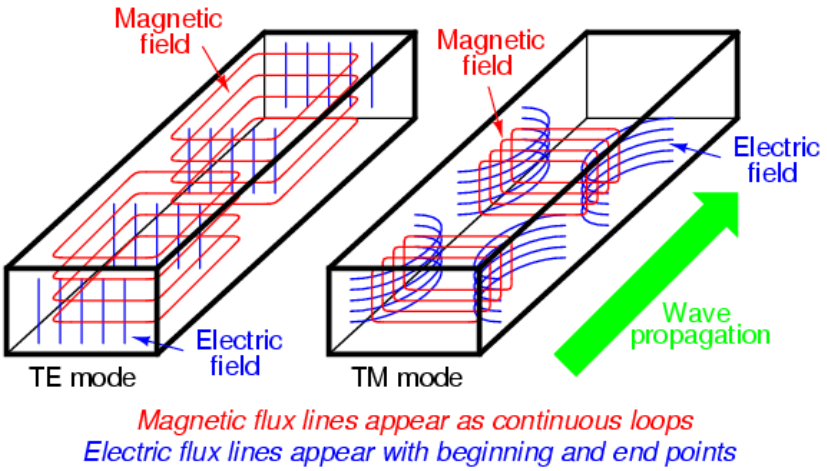

FIGURE 2.10: Electric and magnetic fields of TE and TM modes in smooth-walled waveguides [57].

2.3.1 Cylindrical Waveguide Modes

Two orthogonal mode sets exist in any smooth-walled waveguide with uniform cross-section, namely the TE and TM modes mentioned previously. TE modes obey the condition that the electric field component along the direction of travel is zero ($E_z = 0$), while for TM modes the corresponding magnetic field is zero ($H_z = 0$). Applying these boundary conditions to the wave equation allows expressions for the modal fields to be derived, where the total number of existing modes in a waveguide section depends solely on the radius of the guide. The 2D EM-wave Helmholtz equations are given as [53]:

$$\begin{aligned} \nabla^2 E + k^2 E = 0 \\ \nabla^2 H + k^2 H = 0 \end{aligned} \tag{2.15}$$

where k, the wavenumber, is generally given by $k = \omega\sqrt{\mu\varepsilon}$ and $\omega = 2\pi/\lambda$ where λ is the wavelength of the radiation, ε and μ are the permittivity and permeability of free space.

The cutoff wavenumber for any mode in a waveguide can be written as

$$K^2 = k^2 - \beta^2 \tag{2.16}$$

where β is known as the propagation constant of the wave in the waveguide, and any wave travelling along the axis of propagation will vary as $e^{-\beta z}$. This constant also allows us to determine properties such as the degree of attenuation within the structure, and the phase velocities between modes.

The Laplacian operator ∇^2 can be rewritten as the sum of the differential of axial and transverse field components:

$$\nabla^2 E = \nabla_t^2 E + \frac{\partial^2 E}{\partial z^2}. \tag{2.17}$$

Letting $E = e^{-\beta z}$ in 2.17 and substituting back into 2.15, the Helmholtz equation for the electric field is given by

$$\nabla_t^2 E = -(\beta^2 + k^2)E = -K^2 E \tag{2.18}$$

and similarly for the magnetic field $\nabla_t^2 H = -(\beta^2 + k^2)H = -K^2 H$. The transverse components of the field are sufficient to describe the field at any plane, and they are derived from Maxwell's equations in cylindrical coordinates as [58];

$$\begin{aligned}
E_r &= -\frac{j}{K^2}\left(\beta\frac{\partial E_z}{\partial r} + \frac{\omega\mu}{r}\frac{\partial H_z}{\partial \phi}\right) \\
E_\phi &= \frac{j}{K^2}\left(\frac{\beta}{r}\frac{\partial E_z}{\partial \phi} + \omega\mu\frac{\partial H_z}{\partial r}\right) \\
H_r &= \frac{j}{K^2}\left(\frac{\omega\mu}{r}\frac{\partial E_z}{\partial \phi} - \beta\frac{\partial H_z}{\partial r}\right) \\
H_\phi &= -\frac{j}{K^2}\left(\omega\mu\frac{\partial E_z}{\partial r} + \frac{\beta}{r}\frac{\partial H_z}{\partial \phi}\right),
\end{aligned} \tag{2.19}$$

where the relationship between components can also be written as

$$\begin{aligned}
E_r &= H_\phi Z \\
E_\phi &= -H_r Z
\end{aligned} \tag{2.20}$$

Here Z is the ratio of the transverse electric field to the transverse magnetic field for a given mode, and is known as the waveguide impedance. It is given by $Z = \beta/(\omega\mu)$. The longitudinal components of the field, E_z and H_z are themselves determined by a separation of variables technique [53], such that transverse electric (TE) and transverse magnetic (TM) solutions to the Helmholtz equations arise, sufficient to provide a modal description of the internal field. The derivation of the TE and TM fields follows that in

[59].

Transverse Magnetic (TM_{nl}) Modes

Expanding the Laplacian operating on the transverse component of the electric field in cylindrical coordinates gives:

$$\nabla_t^2 E_z = \frac{1}{r}\frac{\partial}{\partial r}(r\frac{\partial E_z}{\partial r}) + \frac{1}{r^2}r\frac{\partial^2 E_z}{\partial \phi^2} = -K^2 E_z, \tag{2.21}$$

which on application of a separation of variables technique [53] returns modal solutions of the form

$$E_{nl,z} = A_{nl} J_n(Kr) \begin{pmatrix} \cos n\phi \\ \sin n\phi \end{pmatrix} e^{j(\omega t - \beta z)}, \tag{2.22}$$

where A_{nl} is a constant and J_n is a Bessel function of the first kind, and of order n. The $\cos n\phi$ and $\sin n\phi$ terms describe the azimuthal variation of E_z for two orthogonal and degenerate modes, both of which exist for a given combination on K and n. They exhibit the same radial variation, and exist only in incoherent detector systems with no preferred polarisation sensitivity.

Taking the waveguide to be a perfect conductor, it can be assumed that the electric field on the walls of the waveguide will always equal zero, always varying orthogonally with respect to the conductor boundary. This means $E_z(r = a) = E_\phi(r = a) = 0$, where a is the radius of the waveguide. However for equation 2.22 to go to zero, it must be true that $J_n(Ka) = 0$. Thus, Ka is found to be a root of the Bessel function, where K is unique to each mode. We can thus write

$$Ka = \frac{2\pi a}{\lambda_c} = p_{nl}, \tag{2.23}$$

where p_{nl} is the l^{th} root of $J_n(z)$. For a given n, an infinite number of roots of $J_n(Ka)$ exist, equivalent to a two infinite sets of orthogonal modes denoted TM_{nl}, where n is the azimuthal order and l the radial variation. Usefully, the cut-off frequency for any TM mode can now be found via the simple relationship $K = p_{nl}/a$. Further, the characteristic waveguide impedance for any TM mode can now be rewritten as [59]

$$Z_{TM_{nl}} = \frac{\beta}{\omega\mu} = \frac{\sqrt{1 - K^2/k^2}}{\omega\mu} = Z_0\sqrt{1 - \left(\frac{p_{nl}\lambda}{2\pi a n}\right)}. \tag{2.24}$$

Using 2.20, we can rewrite 2.19 in the form

$$\begin{aligned} E_{nl,r} &= C_{nl} J_n'(Kr) \begin{pmatrix} \cos n\phi \\ \sin n\phi \end{pmatrix} e^{j(\omega t - \beta z)} \\ E_{nl,\phi} &= C_{nl} \frac{n J_n(Kr)}{Kr} \begin{pmatrix} -\sin n\phi \\ \cos n\phi \end{pmatrix} e^{j(\omega t - \beta z)} \\ H_{nl,r} &= -\frac{E_{nl,\phi}}{Z_{TM_{nl}}} \\ H_{nl,\phi} &= -\frac{E_{nl,r}}{Z_{TM_{nl}}} \end{aligned} \tag{2.25}$$

where $C_{nl} = (-j\beta A_{nl})/K$. Taking $\mathbf{E}_{nl} = \mathbf{e}_{nl}(r,\phi)e^{j(\omega t-\beta z)}$ and $\mathbf{H}_{nl} = \mathbf{h}_{nl}(r,\phi)e^{j(\omega t-\beta z)}$ the total field of two identical but orthogonal modes is normalised such that

$$\int_0^{2\pi}\int_0^{a} \left(|e_{nl,r}|^2 + |e_{nl,\phi}|^2\right) r dr d\phi = 1, \tag{2.26}$$

which after integration returns $C_{nl} = \sqrt{(2-(1/n-1)/\pi a^2 J_{n+1}^2(p_{nl})}$. The full orthogonal modal equations in cylindrical coordinates, ignoring the propagation term, can be written as [59]

$$\begin{aligned} \mathbf{e}_{nl} &= C_{nl}\left(J_n'(p_{nl}r/a) \begin{pmatrix} \cos n\phi \\ \sin n\phi \end{pmatrix} \hat{r} + \frac{n J_n(p_{nl}r/a)}{p_{nl}r/a} \begin{pmatrix} -\sin n\phi \\ \cos n\phi \end{pmatrix} \hat{\phi} \right) \\ \mathbf{h}_{nl} &= C_{nl}\left(-\frac{n J_n(p_{nl}r/a)}{p_{nl}r/a} \begin{pmatrix} -\sin n\phi \\ \cos n\phi \end{pmatrix} \hat{r} + J_n'(p_{nl}r/a) \begin{pmatrix} \cos n\phi \\ \sin n\phi \end{pmatrix} \hat{\phi} \right). \end{aligned} \tag{2.27}$$

For implementation in the modal matching technique of horn modelling used later in this thesis, it is useful to obtain the equations in equivalent cartesian coordinates. Using the relationships $E_x = E_r\cos\phi - E_\phi \sin\phi$ and $E_y = E_r \sin\phi + E_\phi\cos\phi$ the final expressions for the two orthogonal mode sets are written as

$$\begin{aligned} e_{nl}^{TM}{}_{x} &= C_{nl}\left(J_{n-1}(p_{nl}r/a) \begin{pmatrix} \cos(n-1)\phi \\ -\sin(n-1)\phi \end{pmatrix} - J_{n+1}(p_{nl}r/a) \begin{pmatrix} \cos(n+1)\phi \\ -\sin(n+1)\phi \end{pmatrix} \right) \\ e_{nl}^{TM}{}_{y} &= C_{nl}\left(J_{n-1}(p_{nl}r/a) \begin{pmatrix} \sin(n-1)\phi \\ \cos(n-1)\phi \end{pmatrix} + J_{n+1}(p_{nl}r/a) \begin{pmatrix} \sin(n+1)\phi \\ \cos(n+1)\phi \end{pmatrix} \right) \\ h_{nl}^{TM}{}_{x} &= \frac{C_{nl}}{Z_{TM_{nl}}}\left(J_{n-1}(p_{nl}r/a) \begin{pmatrix} \sin(n-1)\phi \\ \cos(n-1)\phi \end{pmatrix} + J_{n+1}(p_{nl}r/a) \begin{pmatrix} \sin(n+1)\phi \\ \cos(n+1)\phi \end{pmatrix} \right) \\ h_{nl}^{TM}{}_{y} &= \frac{C_{nl}}{Z_{TM_{nl}}}\left(J_{n-1}(p_{nl}r/a) \begin{pmatrix} \cos(n-1)\phi \\ -\sin(n-1)\phi \end{pmatrix} - J_{n+1}(p_{nl}r/a) \begin{pmatrix} \cos(n+1)\phi \\ -\sin(n+1)\phi \end{pmatrix} \right). \end{aligned} \tag{2.28}$$

Transverse Electric (TE_{nl}) modes

In a similar fashion to before, and following [59], we will now outline the derivation of field equations for all TE modes. The transverse Laplacian operating on H_z will give solutions of the form

$$H_{nl,z} = B_{nl} J_n(Kr) \begin{pmatrix} \sin n\phi \\ \cos n\phi \end{pmatrix} e^{j(\omega t - \beta z)} \tag{2.29}$$

where B_{nl} is another constant. Thus, on applying the relationships in 2.19, the impedance of a TE mode is found to be

$$Z_{TE_{nl}} = Z_0 / \sqrt{1 - (q_{nl}\lambda / 2\pi a n)^2} \tag{2.30}$$

where q_{nl} is the l^{th} root of $J'_{nl}(z)$, the derivative of the Bessel function $J_n(z)$. As before, we arrive at two infinite sets of orthogonal modal solutions, which differ from the TM solution in only their azimuthal dependencies by $\cos n\phi$ and $\sin n\phi$, and are given by [59]

$$\begin{aligned} E_{nl,r} &= -D_{nl} \frac{n J_n(Kr)}{Kr} \begin{pmatrix} \cos n\phi \\ -\sin n\phi \end{pmatrix} e^{j(\omega t - \beta z)} \\ E_{nl,\phi} &= D_{nl} J'_n(Kr) \begin{pmatrix} \sin n\phi \\ \cos n\phi \end{pmatrix} e^{j(\omega t - \beta z)} \\ H_{nl,r} &= -\frac{E_{nl,\phi}}{Z_{TE_{nl}}} \\ H_{nl,\phi} &= -\frac{E_{nl,r}}{Z_{TE_{nl}}} \end{aligned} \tag{2.31}$$

where the constant $D_{nl} = -j\omega\mu\beta/K$. It is found that since $E_z(r=a) = E_\phi(r=a) = 0$, $J'_n(Ka) = 0$, and thus the cut-off for a TE mode can be found by $K = q_{nl}/a$. Normalising the orthogonal TE mode sets and integrating in the same way as before for TM modes, we obtain

$$D_{nl} = \sqrt{(2 - (1/n - 1)/\pi a^2 (1 - (n/q_{nl})^2) J^2_{n+1}(q_{nl})} \tag{2.32}$$

and the full field equations for the transverse component of electric and magnetic fields for TE modes can be written as [59]

$$\begin{aligned} \mathbf{e}_{nl} &= D_{nl} \left(\frac{n J_n(q_{nl} r/a)}{q_{nl} r/a} \begin{pmatrix} \cos n\phi \\ \sin n\phi \end{pmatrix} \hat{r} - J'_n(q_{nl} r/a) \begin{pmatrix} \sin n\phi \\ \cos n\phi \end{pmatrix} \hat{\phi} \right) \\ \mathbf{h}_{nl} &= D_{nl} \left(J'_n(q_{nl} r/a) \begin{pmatrix} \sin n\phi \\ \cos n\phi \end{pmatrix} \hat{r} + \frac{n J_n(q_{nl} r/a)}{q_{nl} r/a} \begin{pmatrix} \cos n\phi \\ -\sin n\phi \end{pmatrix} \hat{\phi} \right) \end{aligned} \tag{2.33}$$

and in cartesian coordinates they are given by [59]

$$
\begin{aligned}
e_{nl}^{TE}{}_{x} &= D_{nl}\left(J_{n-1}(q_{nl}r/a)\begin{pmatrix}\cos(n-1)\phi\\ -\sin(n-1)\phi\end{pmatrix} + J_{n+1}(q_{nl}r/a)\begin{pmatrix}\cos(n+1)\phi\\ -\sin(n+1)\phi\end{pmatrix}\right)\\
e_{nl}^{TE}{}_{y} &= D_{nl}\left(J_{n-1}(q_{nl}r/a)\begin{pmatrix}\sin(n-1)\phi\\ \cos(n-1)\phi\end{pmatrix} - J_{n+1}(q_{nl}r/a)\begin{pmatrix}\sin(n+1)\phi\\ \cos(n+1)\phi\end{pmatrix}\right)\\
h_{nl}^{TE}{}_{x} &= \frac{D_{nl}}{Z_{TM_{nl}}}\left(J_{n-1}(q_{nl}r/a)\begin{pmatrix}\sin(n-1)\phi\\ \cos(n-1)\phi\end{pmatrix} - J_{n+1}(q_{nl}r/a)\begin{pmatrix}\sin(n+1)\phi\\ \cos(n+1)\phi\end{pmatrix}\right)\\
h_{nl}^{TE}{}_{y} &= \frac{D_{nl}}{Z_{TM_{nl}}}\left(J_{n-1}(q_{nl}r/a)\begin{pmatrix}\cos(n-1)\phi\\ -\sin(n-1)\phi\end{pmatrix} + J_{n+1}(q_{nl}r/a)\begin{pmatrix}\cos(n+1)\phi\\ -\sin(n+1)\phi\end{pmatrix}\right).
\end{aligned}
\tag{2.34}
$$

The roots of the Bessel function and its derivative define the order in which modes can be excited within a horn. As the value of the root in 2.23 increases, the cut-off frequency below which a mode becomes evanescent, increases also. In this manner the modal content of any waveguide structure can easily be determined and optimised based on operating frequency and waveguide dimensions. Modes which share the same root are degenerate, however their field distributions will be uniquely defined by the $\sin n\phi$ and $\cos n\phi$ variations in the modal field equations. Waveguide systems are generally designed to be single moded, transmitting radiation via the fundamental mode (the TE_{11}) only. This forms the basis for a coherent system, however incoherent systems transmit power via multiple higher order modes, and are known as "over-moded structures. These are particularly common in bolometric systems which have no polarisation discrimination. In these cases both orthogonal mode sets also exist simultaneously. In over-moded systems modes are not coherent with respect to each other and the total field at any point is found by adding the modes in quadrature. Modes must be treated as distinct and separate on propagation at all times. This will be returned to in chapter 3, where modelling of the Planck multi-moded channels requires consideration of the partially coherent nature of the horn fields.

2.3.2 Rectangular Waveguide Modes

Where cylindrical waveguide modes were described using cylindrical coordinates, it is naturally useful to define rectangular waveguide modes in cartesian coordinates. To this

end we can take the cartesian form of the Helmholtz equations originally shown in 2.19

$$\begin{aligned} E_x &= -\frac{j}{K^2}\left(\beta\frac{\partial E_z}{\partial x} + \frac{\omega\mu}{r}\frac{\partial H_z}{\partial y}\right) \\ E_y &= \frac{j}{K^2}\left(\frac{\beta}{r}\frac{\partial E_z}{\partial y} + \omega\mu\frac{\partial H_z}{\partial x}\right) \\ H_x &= \frac{j}{K^2}\left(\frac{\omega\mu}{r}\frac{\partial E_z}{\partial x} - \beta\frac{\partial H_z}{\partial y}\right) \\ H_y &= -\frac{j}{K^2}\left(\omega\mu\frac{\partial E_z}{\partial y} + \frac{\beta}{r}\frac{\partial H_z}{\partial x}\right). \end{aligned} \tag{2.35}$$

Performing a similar analysis as for the cylindrical waveguide modes, a separation of variables technique and implementation of the condition that $E_z = 0$ along the walls of the conductor, the transverse field components of TM modes are given as [60]

$$\begin{aligned} E_{TM_{mn}\ x} &= -\frac{j\beta m\pi}{K^2 a}B_{mn}\begin{pmatrix} \cos(m\pi x/a)\sin(n\pi y/b) \\ -\sin(m\pi x/a)\cos(n\pi y/b)\end{pmatrix} e^{j(\omega t-\beta z)} \\ E_{TM_{mn}\ y} &= -\frac{j\beta n\pi}{K^2 b}B_{mn}\begin{pmatrix} \sin(m\pi x/a)\cos(n\pi y/b) \\ -\cos(m\pi x/a)\sin(n\pi y/b)\end{pmatrix} e^{j(\omega t-\beta z)} \\ H_{TM_{mn}\ x} &= \frac{j\omega\varepsilon_0 n\pi}{K^2 b}B_{mn}\begin{pmatrix} \sin(m\pi x/a)\cos(n\pi y/b) \\ -\cos(m\pi x/a)\sin(n\pi y/b)\end{pmatrix} e^{j(\omega t-\beta z)} \\ H_{TM_{mn}\ y} &= -\frac{j\omega\varepsilon_0 m\pi}{K^2 a}B_{mn}\begin{pmatrix} \cos(m\pi x/a)\sin(n\pi y/b) \\ -\sin(m\pi x/a)\cos(n\pi y/b)\end{pmatrix} e^{j(\omega t-\beta z)} \end{aligned} \tag{2.36}$$

where it is assumed that

$$E_{mn,z} = A_{mn}\begin{pmatrix} \sin(m\pi x/a)\sin(n\pi y/b) \\ \cos(m\pi x/a)\cos(n\pi y/b)\end{pmatrix} e^{j(\omega t-\beta z)} \tag{2.37}$$

and the dimensions of the waveguide are given by a and b, where $a \geq b$. m and n are integers $(m, n \geq 1)$. As before $\beta = \sqrt{k^2 - K^2}$, however in this case the waveguide cutoff is given by

$$K = \sqrt{\left(\frac{m\pi}{a}\right)^2 + \left(\frac{n\pi}{b}\right)^2}. \tag{2.38}$$

As with cylindrical waveguides, the cutoff frequency determines what modes can be excited, and it depends on the waveguide dimensions a and b. Expressions for the modal fields of TE modes can also be obtained by the same process, such that by assuming

$$H_{mn,z} = A_{mn}\begin{pmatrix} \cos(m\pi x/a)\cos(n\pi y/b) \\ \sin(m\pi x/a)\sin(n\pi y/b)\end{pmatrix} e^{j(\omega t-\beta z)} \tag{2.39}$$

we obtain

$$\begin{aligned}
E_{TE_{mn}\ x} &= \frac{j\omega\mu n\pi}{K^2 b} A_{mn} \begin{pmatrix} \cos(m\pi x/a)\sin(n\pi y/b) \\ -\sin(m\pi x/a)\cos(n\pi y/b) \end{pmatrix} e^{j(\omega t-\beta z)} \\
E_{TE_{mn}\ y} &= -\frac{j\omega\mu m\pi}{K^2 a} A_{mn} \begin{pmatrix} \sin(m\pi x/a)\cos(n\pi y/b) \\ -\cos(m\pi x/a)\sin(n\pi y/b) \end{pmatrix} e^{j(\omega t-\beta z)} \\
H_{TE_{mn}\ x} &= -\frac{j\beta m\pi}{K^2 a} A_{mn} \begin{pmatrix} \sin(m\pi x/a)\cos(n\pi y/b) \\ -\cos(m\pi x/a)\sin(n\pi y/b) \end{pmatrix} e^{j(\omega t-\beta z)} \\
H_{TE_{mn}\ y} &= -\frac{j\beta n\pi}{K^2 b} A_{mn} \begin{pmatrix} \cos(m\pi x/a)\sin(n\pi y/b) \\ -\sin(m\pi x/a)\cos(n\pi y/b) \end{pmatrix} e^{j(\omega t-\beta z)}.
\end{aligned} \tag{2.40}$$

Once again, orthogonal modes are normalised to unity on integration over any plane of dimensions $a \times b$ where $\mathbf{E}_{mn} = \mathbf{e}_{mn}(x,y)e^{j(\omega t-\beta z)}$ and $\mathbf{H}_{mn} = \mathbf{h}_{mn}(x,y)e^{j(\omega t-\beta z)}$, returning equations for the constants A_{mn} and B_{mn}

$$\begin{aligned}
|A_{mn}| &= \frac{K^2}{\omega\mu\pi}\sqrt{\frac{4ab}{n^2a^2+m^2b^2}} \\
|B_{mn}| &= \frac{K^2}{\beta\pi}\sqrt{\frac{4ab}{n^2a^2+m^2b^2}}.
\end{aligned} \tag{2.41}$$

In a rectangular waveguide no modes of order $n = 0, m = 0$ can exist, and the fundamental mode is the TE_{10}. All TM modes of order $n = 0$ or $m = 0$ are also zero. Higher modes will be excited with increased frequency, such that a rectangular horn can operate as a multi-mode horn but with different constituent modal fields making up the overall partially coherent field.

2.3.3 Mode-Matching Technique for Modelling a Corrugated Feed

The modal-matching technique is a powerful tool for modeling corrugated feed horns, whose derivation here follows that of [59]. Although it was developed in the late 1960s by [61], it was only used in a very limited capacity until the advent of high-power computing in latter years in which it was developed upon by [62]. It is now used extensively due to the simplicity and flexibility of the method. This allows relatively complicated structures to be easily modelled in a short time. To begin, the physical horn is broken down into a number of waveguide sections which matches the number of corrugations present in the horn. Each corrugation is thus represented as a single continuous cylindrical waveguide section in which the modal composition of a prorogating electric field can be calculated. At each junction between continuous sections the mode-matching technique is used to conserve total power by transforming one modal field to another

via a scattering matrix. Each scattering matrix contains the amplitude of a certain number of modes, which may or may not be present at that particular junction, and each junction has its own scattering matrix. Thus by cascading them along the length of the horn one all-encompassing scattering matrix can be arrived at, which will form a general description of the horn.

The mode-matching technique is essentially a method of obtaining the overall transmission and reflection properties of a horn, where the output transmission and input reflection coefficients are described by the complete scattering matrix $[S]$, which may be represented as a box as in figure 2.11. Thorough analysis of both corrugated and smooth-walled horns was undertaken by [63], leading to the development of the software package SCATTER, now regularly used in NUI Maynooth for the modelling of corrugated feeds [59].

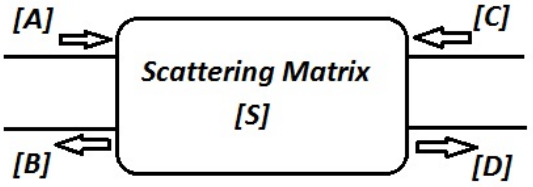

FIGURE 2.11: The scattering matrix representation of a horn, with input and output coefficients.

Column matrices $[C]$ and $[D]$ represent the respective forward and reflected coefficients of all modes looking into the aperture of the horn from outside. $[A]$ and $[B]$ contain the respective transmission and reflection coefficients of these same modes at the waveguide-fed end of the horn, such that:

$$\begin{bmatrix} [B] \\ [D] \end{bmatrix} = [S] \begin{bmatrix} [A] \\ [C] \end{bmatrix} \tag{2.42}$$

The horn is described by the scattering matrix, $[S]$:

$$[S] = \begin{bmatrix} [S_{11}] & [S_{12}] \\ [S_{21}] & [S_{22}] \end{bmatrix}. \tag{2.43}$$

$[S]$ is made up of four $n \times n$ square matrices containing the power coupling between all n number of TE and TM modes in the horn. By combining equations 2.42 and 2.43 we obtain:

$$\begin{bmatrix} [B] \\ [D] \end{bmatrix} = \begin{bmatrix} [S_{11}] & [S_{12}] \\ [S_{21}] & [S_{22}] \end{bmatrix} \begin{bmatrix} [A] \\ [C] \end{bmatrix} \tag{2.44}$$

When matrix multiplication is performed:

$$\begin{aligned}[B] &= [S_{11}]\,[A] + [S_{12}]\,[C] \\ [D] &= [S_{21}]\,[A] + [S_{22}]\,[C]\end{aligned} \tag{2.45}$$

However under the assumption that there is no reflection back into the system at the aperture, the column matric $[C]$ will simply become zero, and the transmission/reflection coefficients of the horn are then given by:

$$\begin{aligned}[D] &= [S_{21}]\,[A] \\ [B] &= [S_{11}]\,[A]\end{aligned} \tag{2.46}$$

The length of the column matrices A, B, C and D are defined by the number of modes present at the horn aperture, however since most horns will be fed by only a single fundamental waveguide mode of azimuthal order 1, either TE_{10} or TE_{11}, the column matrix A will fully describe mode content at this section with only one non-zero entry:

$$[A] = \begin{bmatrix} 1 \\ 0 \\ 0 \\ .. \\ .. \end{bmatrix} \tag{2.47}$$

The horn is now separated into a number of continuous sections and junctions, each represented by its own scattering matrix as in (2.42). Thus the horn can be represented as a series of scattering matrices, where if any two matrices contain the elements:

$$\begin{aligned}[S^a] &= \begin{bmatrix} [S^a_{11}] & [S^a_{12}] \\ [S^a_{21}] & [S^a_{22}] \end{bmatrix} \\ &\& \\ \left[S^b\right] &= \begin{bmatrix} [S^b_{11}] & [S^b_{12}] \\ [S^b_{21}] & [S^b_{22}] \end{bmatrix}\end{aligned} \tag{2.48}$$

cascading them will result in the matrix:

$$[S^c] = \begin{bmatrix} [S^c_{11}] & [S^c_{12}] \\ [S^c_{21}] & [S^c_{22}] \end{bmatrix} \tag{2.49}$$

where:

$$\begin{aligned}
[S_{11}^c] &= [S_{12}^a]\left[[I] - \left[S_{11}^b\right][S_{22}^a]\right]^{-1}\left[S_{11}^b\right][S_{21}^a] + [S_{11}^a] \\
[S_{12}^c] &= [S_{12}^a]\left[[I] - \left[S_{11}^b\right][S_{22}^a]\right]^{-1}\left[S_{12}^b\right] \\
[S_{21}^c] &= \left[S_{21}^b\right]\left[[I] - [S_{22}^a]\left[S_{11}^b\right]\right]^{-1}[S_{21}^a] \\
[S_{22}^c] &= \left[S_{21}^b\right]\left[[I] - [S_{22}^a]\left[S_{11}^b\right]\right]^{-1}[S_{22}^a]\left[S_{12}^b\right] + \left[S_{22}^b\right]
\end{aligned} \tag{2.50}$$

. Here $[I]$ is a unit matrix and $[\,]^{-1}$ an inverse matrix. The four calculations in (2.50) are repeated in a linear fashion from one section to the next. This provides an advantage in that the exact number of sections and junctions need not be known before calculation begins, since the calculation will proceed logically from the back to the front of the horn.

The scattering matrices of each separate section must now be determined, be it junction or continuous waveguide, such that cascading can be implemented, as highlighted in figure 2.12.

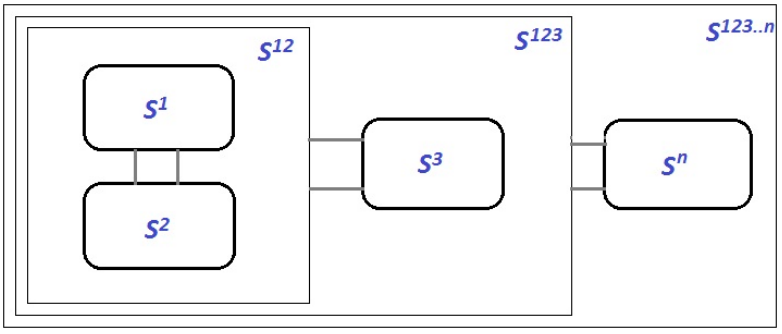

FIGURE 2.12: Iterative process of cascading adjacent matrices, each of which represents a modular section.

In a continuous waveguide section the scattering matrix elements are defined solely by the length of the section, l, and the propagation coefficient of all modes in the waveguide, γ_n, neglecting any complex component arising from loss in the material. Rather simply:

$$\begin{aligned}
[S_{11}] = [S_{22}] = [0] \\
[S_{12}] = [S_{21}] = [V]
\end{aligned} \tag{2.51}$$

where $[V]$ is an N×N diagonal matrix such that $V_{nn} = e^{-\gamma_n l}$, $1 < n < N$. By ignoring losses, the propagation constant will be either purely real ($\gamma_n = \alpha_n$) for all evanescent modes or alternatively imaginary for all prorogating modes ($\gamma_n = j\beta_n$). The elements of the matrices will always be real. As the amplitude of the decaying wave is usually still significant by the time it has travelled from one junction to the next, due to the short length of each section, a large number of evanescent modes must be included in any calculation.

At a junction the scattering matrix derivation is slightly more complex due to the total power in all modes present on both sides of the junction having to be matched [64]. However keeping the number of modes, N, the same on both sides does significantly decrease computation time. The transverse electric fields in any continuous section of guide can thus be represented as a combination of N modes, such that the electric and magnetic fields at a junction on the left-hand side of a junction may be written as:

$$\begin{aligned} E_L &= \sum_{n=1}^{N} (A_n e^{-\gamma_n z} + B_n e^{\gamma_n z}) e_{n_L} \\ H_L &= \sum_{n=1}^{N} (A_n e^{-\gamma_n z} - B_n e^{\gamma_n z}) h_{n_L} \end{aligned} \tag{2.52}$$

and the fields on the right-hand side are:

$$\begin{aligned} E_R &= \sum_{n=1}^{N} (C_n e^{-\gamma_n z} + D_n e^{\gamma_n z}) e_{n_R} \\ H_R &= \sum_{n=1}^{N} (C_n e^{-\gamma_n z} - D_n e^{\gamma_n z}) h_{n_R} \end{aligned} \tag{2.53}$$

where subscripts R and L represent right-hand and left-hand sides of the junction, such that the electric and magnetic modal functions on the right hand side are given by e_{n_R} and h_{n_R} respectively. As before, A_n, B_n, C_n and D_n are simply the forward and reflected amplitude coefficients of mode n on both sides of the junction.

Since the total transverse field must match on both sides of the junction we obtain:

$$\begin{aligned} \sum_{n=1}^{N} (A_n + B_n) e_{nL} &= \sum_{n=1}^{N} (C_n + D_n) e_{n_R} \\ \sum_{n=1}^{N} (A_n - B_n) h_{nL} &= \sum_{n=1}^{N} (C_n - D_n) h_{n_R} \end{aligned} \tag{2.54}$$

assuming the junction is located at $z = 0$.

Now if s_L and s_R represent the cross-sectional areas of left and right-hand sides of the junction respectively, we can assume the transverse fields over the region $s_R - s_L$ will always equal zero (taking $s_R > s_L$), and the fields over s_L will be continuous, such that a pair of simultaneous equations are arrived at [59]:

$$\begin{aligned} [P]\,[[A] + [B]] &= [Q]\,[[C] + [D]] \\ [P]^T\,[[D] - [C]] &= [R]\,[[A] - [B]] \end{aligned} \tag{2.55}$$

where $[A]$ and $[B]$ are N-element column matrices containing the modal coefficients A_1 to A_N, and B_1 to B_N respectively for the left-hand side of the junction. $[C]$ and $[D]$ similarly contain unknown coefficients of the right-hand side. Also this assumes $s_R > s_L$, for which the description of $[S]$ in equation 2.43 holds, however if $s_R < s_L$ the elements in $[S]$ are instead given by:

$$[S] = \begin{bmatrix} [S_{22}] & [S_{21}] \\ [S_{12}] & [S_{11}] \end{bmatrix} \tag{2.56}$$

. The matrices $[P]$, $[Q]$ and $[R]$ are $N \times N$ dimensional square matrices containing integrals used to couple power between modes. The integral elements of $[P]$ return mutual coupled power between mode n on the left and m on the right, such that:

$$P_{nm} = \int_{s_L} (e_{nL} \times h_{mR}) \cdot ds_L \tag{2.57}$$

and $[P]^T$ represents the transpose of $[P]$. The integration is performed over the cross-sectional area on the left-hand side of the junction under the assumption modal power transfer is completed before entering the new continuous waveguide section.

Matrix $[Q]$ is an $N \times N$ diagonal matrix representing the self-coupled power between two modes on the right hand-side of the junction, and in a similar fashion $[R]$ describes self-coupled power between modes on the left, giving;

$$Q_{mm} = \int_{s_R} (e_{mR} \times h_{mR}) \cdot ds_R \tag{2.58}$$

and

$$R_{nn} = \int_{s_L} (e_{nL} \times h_{nL}) \cdot ds_L \tag{2.59}$$

These power-coupling integrals can be solved analytically or numerically depending on the case, however SCATTER does both. It works out analytical solutions to the integrals first, and then evaluates these numerically during computation. This does have the downside of increasing computation time, since all combinations of modes at each junction must be evaluated.

Finally, rearranging equation 2.55 to again obtain a scattering matrix formalism:

$$\begin{aligned} [S_{11}] &= \left[[R] + [P]^T [Q]^{-1} [P]\right]^{-1} \left[[R] - [P]^T [Q]^{-1} [P]\right] \\ [S_{12}] &= 2\left[[R] + [P]^T [Q]^{-1} [P]\right]^{-1} [P]^T \\ [S_{21}] &= 2\left[[Q] + [P] [R]^{-1} [P]^T\right]^{-1} [P] \\ [S_{22}] &= -\left[[Q] + [P] [R]^{-1} [P]^T\right]^{-1} \left[[Q] - [P] [R]^{-1} [P]^T\right] \end{aligned} \tag{2.60}$$

The overall theory described above can be visualised by a procedural diagram, as shown in figure 2.13, where the bulk of the computational work is in calculating the coupling coefficients and wavenumber. This has to be done for each section and for every mode in that section.

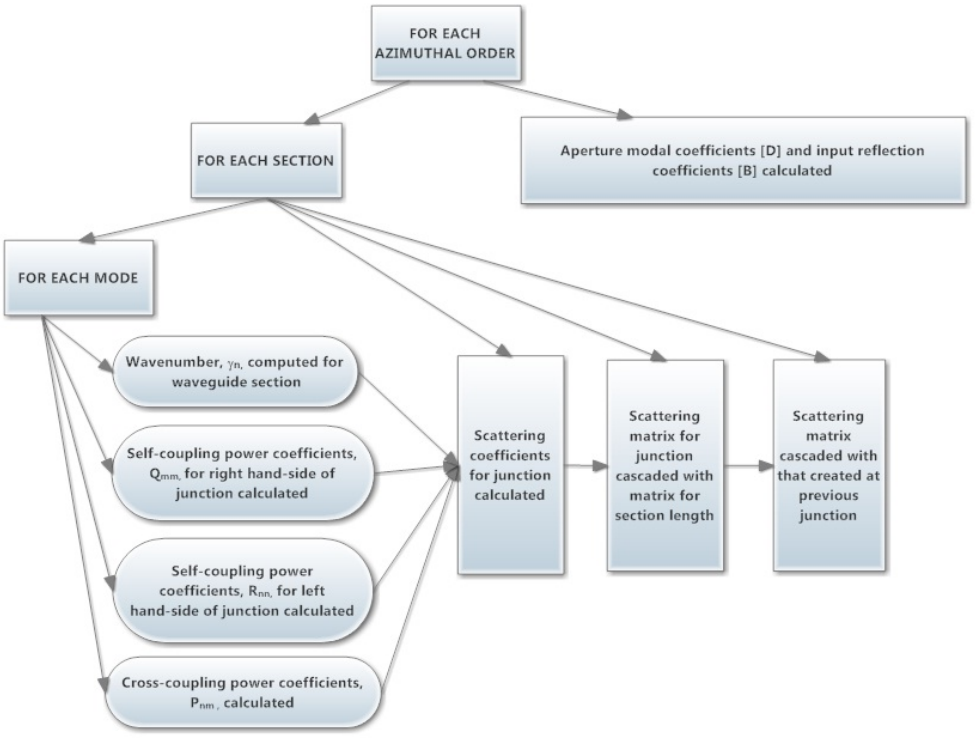

FIGURE 2.13: The procedure implemented by the mode-matching technique across the length of a horn, with the properties to be calculated for section, and for every mode inside each section.

For the most part, horns will be fed either by a circular waveguide propagating the TE_{11} mode or a rectangular waveguide propagating the TE_{01} mode into a rectangular-to-circular section. In an ideally symmetric structure all modes will have an azimuthal dependance of unity, such that only TE_{1m} and TM_{1m} modes will be created at a junction.

2.3.4 SVD-based Hybrid Mode Generation

While waveguide modes suffice to describe the internal field of a horn, at the aperture these modal fields can be combined to produce one coherent field, which can then be propagated through free space. This single field represents the fundamental hybrid mode, a combination of all the waveguide modal fields at the aperture. Thus, hybrid modes form a different basis set of modes with which to represent the field of any horn. Generally at low frequency a horn will be 'single-moded', meaning only one coherent field suffices to describe the total aperture field arising from all waveguide modes in

the horn. At higher frequencies, however, higher and higher orders of waveguide modes are required to describe the field, not all of which are coherent with respect to each other, and which couple to hybrid modes other than the fundamental. Once more than one hybrid mode is required to fully describe the radiation pattern of the horn it is now be referred to as 'multi-moded', and each of the hybrid mode fields generated by the horn are incoherent with respect to each other, meaning they cannot be combined at the aperture and propagated to the sky as one coherent field. These hybrid mode fields are a useful basis set with which to describe the aperture field of a multi-moded horn, however, as the modal constituents of whatever basis set is used must be treated as distinct and separate on propagation into free space. Doing this with waveguide modes would create a very large number of independent modal fields, however with fully equivalent hybrid modes the number of independent fields which must be propagated is considerably reduced.

To create the modal fields a singular value decomposition of the S21 at the aperture of the horn is performed, given by $S21 = UWV^{\star}$, where S21 is $m \times n$ in size. U then is an $m \times m$ matrix, containing all of the left hand singular vectors of the matrix S21, which in this case represents the power in each input mode at the junction. V on the other hand is an $n \times n$ matrix describing the power in all of the output modes at the junction. W is an $m \times n$ diagonal matrix containing the singular values of S21 along the diagonal and zeros elsewhere. The number of columns of $V^{\star}$ containing non-zero entries, represents the reduced number of eigenmodes by which the field can be defined. These are a basis set of hybrid modes, and all of the waveguide modes originally used to propagate power through the horn will couple their power to one or more of these eigenmodes. Figure 2.14 illustrates the SVD of a 3×5 matrix, labelled A.

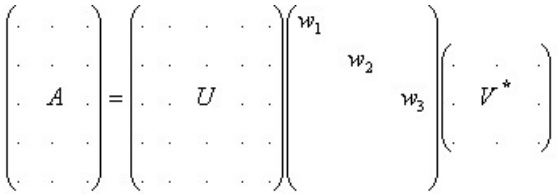

FIGURE 2.14: Illustration of the three matrices U, W and $V^{\star}$ arising from an SVD performed on the matrix A, of dimensions 3×5.

This is a very powerful tool for high frequency optical modelling of telescope systems, as feed horns used in modern detector arrays are often multi-moded. This means rather than propagating a single coherent field from the aperture, which is a sum of all the waveguide modal contributions, these horns are only partially coherent, described by multiple incoherent fields at the aperture, each of which must remain independent on propagation to the sky. A significant issue arises, however, as accurately definition the field at the aperture of any feed horn requires a large number of waveguide modes.

Propagation of each of these modal fields to the sky would take considerable time, more so at high frequencies, as outlined in section 2.2.1. Thus it is extremely convenient to describe the field in terms of a much smaller number of eigenmodes and propagate these instead. In the case of the Planck back-to-back 857-GHz horn, for example, five azimuthal orders of higher order modes are required to accurately define the total field. Accurately calculating the power through the horn in terms of 20 TE and 20 TM modes per azimuthal order would mean 200 modal individual modal fields at the aperture. However by performing an SVD of the S21 matrix at each azimuthal order, in fact only ten eigenmodes (and their 10 orthogonal modes) fully describes the field at the lowest end of the band, 730-GHz (see Chapter 3). This constitutes 5% the number of incoherent fields, and thus only 5% of the computation time, vastly increasing the efficiency of simulations, and affording the author the ability to perform highly accurate models at such high frequencies.

2.3.5 Gaussian Beam Modes

Another quasi-optical approach to modelling can be done using Gaussian beam modes (GBM), so long as beams diverge only slowly relative to distance from the source. This mode set is especially useful due to the fact that many mm-wave devices emit radiation that is nearly Gaussian in form. As such, this emitted radiation can be represented as originating at a beam waist location somewhere inside the device. This can provide a useful alternative to the lengthy EM calculations associated with a PO approach to modelling. The propagation of a Gaussian beam from its waist location is illustrated in figure 2.15.

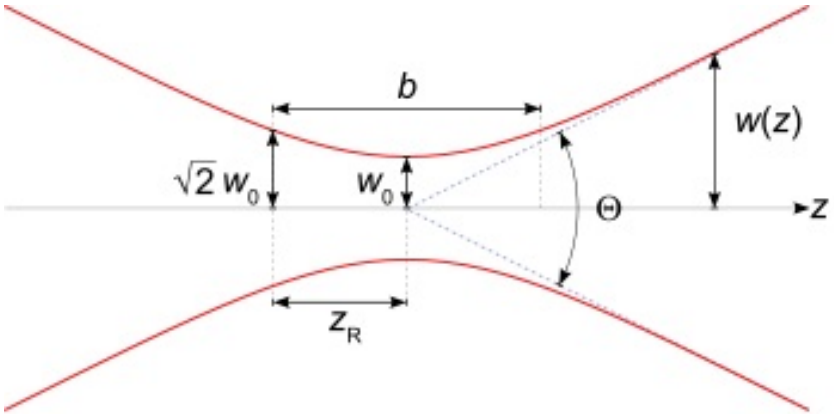

FIGURE 2.15: A Gaussian beam propagating from its waist location, where z_r denotes the confocal distance separating near and far-fields. θ is known as the viewing angle, and $w(z)$ is the beam width at any point along the axis of propagation.

Herein the fundamental equations governing GBM theory shall be derived, following [65], and their power illustrated by implementation in beam modelling.

Paraxial Wave Equation

The paraxial wave equation describes a beam of radiation which is largely collimated in the direction of travel, however the beam has some transverse variation as it naturally diffracts. Gaussian beam modes are simply solutions to the paraxial wave equation. Here solutions shall be derived in cylindrical coordinates, appropriate for cylindrically symmetric systems.

Following the derivation in [65], we first assume a wave that is travelling along the z-axis, so the field distribution in rectangular coordinates is given as:

$$E(x, y, z) = u(x, y, z)e^{-jkz}. \tag{2.61}$$

To transform from cartesian to cylindrical coordinates (r, φ, z), we use:

$$\begin{aligned} r^2 &= x^2 + y^2 \\ \varphi &= \arcsin(y/x) \\ z &= z \end{aligned} \tag{2.62}$$

where z is the direction of propagation, r is the radial distance from the axis of propagation to any point in space, P, at which the field is to be calculated, and φ is angle between the axis of propagation and the line connecting the origin to P. Alternatively the relationship between the two coordinate systems can be written as;

$$\begin{aligned} x &= r\cos\varphi \\ y &= r\sin\varphi \\ z &= z \end{aligned} \tag{2.63}$$

so,

$$E(x, y, z) = u(r[x, y], \varphi[x, y], z[z])e^{-jkz}. \tag{2.64}$$

The Helmholtz Equation $\nabla^2 + k^2 E$ can conveniently be used to derive the wave equation [65]. To find the field component along the x direction, solutions of $\nabla^2 E_x$ or $\frac{\partial^2 E}{\partial x^2}$ must be found, where:

$$\frac{dE}{dx} = \frac{\partial u}{\partial x}e^{-jkz} \tag{2.65}$$

and

$$\frac{d^2E}{dx^2} = \frac{\partial^2 u}{\partial x^2} e^{-jkz}. \tag{2.66}$$

$\frac{\partial u}{\partial x}$ can then be split into partial derivatives such that;

$$\frac{\partial u}{\partial x} = \frac{\partial u}{\partial r}\left(\frac{\partial r}{\partial x}\right) + \frac{\partial u}{\partial \varphi}\left(\frac{\partial \varphi}{\partial x}\right) \tag{2.67}$$

and thus:

$$\frac{\partial^2 u}{\partial x^2} = \frac{\partial}{\partial x}\left(\frac{\partial u}{\partial x}\right) = \frac{\partial}{\partial x}\left(\frac{\partial u}{\partial r}\left(\frac{\partial r}{\partial x}\right) + \frac{\partial u}{\partial \varphi}\left(\frac{\partial \varphi}{\partial x}\right)\right) \tag{2.68}$$

Using the chain rule then on $\frac{\partial u}{\partial r}$ and $\frac{\partial u}{\partial \varphi}$ (which are of course functions of r and φ), $\frac{\partial^2 u}{\partial x^2}$ can be written as:

$$\begin{aligned}\frac{\partial^2 u}{\partial x^2} = \frac{\partial^2 u}{\partial r^2}\left(\frac{\partial r}{\partial x}\right)^2 + \frac{\partial^2 u}{\partial \varphi \partial r^2}\left(\frac{\partial \varphi}{\partial x}\right)\frac{\partial r}{\partial x} + \frac{\partial u}{\partial r}\left(\frac{\partial^2 r}{\partial x^2}\right) + \frac{\partial^2 u}{\partial \varphi^2}\left(\frac{\partial \varphi}{\partial x}\right)^2 \\ + \frac{\partial^2 u}{\partial r \partial \varphi^2}\left(\frac{\partial r}{\partial x}\right)\frac{\partial \varphi}{\partial x} + \frac{\partial u}{\partial \varphi}\left(\frac{\partial^2 \varphi}{\partial x^2}\right).\end{aligned} \tag{2.69}$$

The dependance on cartesian coordinate x in the partial derivatives above must be replaced with an equivalent cylindrical dependency by solving w.r.t. x using the relationships in 2.62. Substituting with the relationships in 2.63 then gives;

$$\begin{aligned}\frac{\partial r}{\partial x} &= x\left(x^2+y^2\right)^{-\frac{1}{2}} = \cos\varphi \\ \frac{\partial^2 r}{\partial x^2} &= -x\left(x^2+y^2\right)^{-2} = \frac{\sin^2\varphi}{r}\end{aligned} \tag{2.70}$$

and

$$\begin{aligned}\frac{\partial \varphi}{\partial x} &= \frac{-\frac{y}{x^2}}{1+\left(\frac{y}{x}^2\right)} = -\frac{\sin\varphi}{r} \\ \frac{\partial^2 \varphi}{\partial x^2} &= 2xy\left(x^2+y^2\right)^{-2} = \frac{2\sin\varphi\cos\varphi}{r^2}.\end{aligned} \tag{2.71}$$

Substituting these results back into 2.69, and rewriting in a similar fashion, $\frac{\partial^2 u}{\partial y^2}$, it is found after considerable simplification that

$$\frac{\partial^2 u}{\partial x^2} + \frac{\partial^2 u}{\partial y^2} = \frac{\partial^2 u}{\partial r^2} + \frac{1}{r}\frac{\partial u}{\partial r} + \frac{1}{r^2}\frac{\partial^2 u}{\partial \varphi^2}. \tag{2.72}$$

And for z also

$$\frac{dE}{dz} = \frac{\partial u}{\partial z} e^{-jkz} - jkue^{-jkz} \tag{2.73}$$

and thus

$$\frac{d^2E}{dz^2} = \left(\frac{\partial^2 u}{\partial z^2} - 2jk\frac{\partial u}{\partial z} - k^2 u\right) e^{-jkz}. \tag{2.74}$$

So, since the Helmholtz Equation for $E(x, y, z)$ can be expanded as

$$\frac{\partial^2 E}{\partial x^2} + \frac{\partial^2 E}{\partial y^2} + \frac{\partial^2 E}{\partial z^2} + k^2 u = 0 \tag{2.75}$$

by summing all terms and dividing across by u, it is found that:

$$\frac{\partial^2 u}{\partial r^2} + \frac{1}{r}\frac{\partial u}{\partial r} + \frac{1}{r^2}\frac{\partial^2 u}{\partial \varphi^2} + \frac{\partial^2 u}{\partial z^2} - 2jk\frac{\partial u}{\partial z} - k^2 u + k^2 u = 0. \tag{2.76}$$

And finally, since for paraxial behaviour u changes slowly w.r.t. z, i.e. $\frac{\partial^2 u}{\partial z^2} << \frac{\partial u}{\partial z}$;

$$\frac{\partial^2 u}{\partial r^2} + \frac{1}{r}\frac{\partial u}{\partial r} + \frac{1}{r^2}\frac{\partial^2 u}{\partial \varphi^2} - 2jk\frac{\partial u}{\partial z} = 0 \tag{2.77}$$

which is the paraxial wave equation in cylindrical coordinates.

Fundamental Gaussian Beam Mode

Having derived the paraxial wave equation, finding a solution to it which describes the behaviour of a propagating Gaussian beam is the next task. We begin by assuming that the simplest solution to the paraxial wave equation can be written as [65]:

$$u(r, z) = A(z) exp\left(\frac{-jkr^2}{2q(z)}\right) \tag{2.78}$$

where *A(z)* and *q(z)* are undetermined complex functions. In order to find these unknowns a substitution of (2.78) into the paraxial wave equation must be done, where on solving it is found that

$$\begin{aligned} \frac{\partial q}{\partial z} &= 1 \\ \frac{\partial A}{\partial z} &= -\frac{A}{q} \end{aligned} \tag{2.79}$$

so that $q(z) = q(0) + z$. This is quantity is known as the complex beam parameter. It can be rewritten as:

$$\frac{1}{q} = \left(\frac{1}{q}\right)_r - j\left(\frac{1}{q}\right)_i. \tag{2.80}$$

Substituting this into (2.78) and solving it is found that

$$\frac{1}{q} = \frac{1}{R(z)} - j\frac{\lambda}{\pi w(z)^2} \tag{2.81}$$

where $R(z)$ is the beam phase radius of curvature, and $w(z)$ the beam radius at a given distance z from the origin. Another equation for q can be written:

$$q = j\frac{\pi w_0^2}{\lambda} + z \tag{2.82}$$

where w_0 is defined as the beam waist. The beam waist location is where the beam radius is smallest and the beam is perfectly collimated in z.

Now putting the two equations for q together, formulae for the beam radius and phase radius of curvature as a function of distance along z can be obtained:

$$\begin{aligned} R &= z + \frac{1}{z}\left(\frac{\pi w_0^2}{\lambda}\right)^2 \\ w &= w_0\left[1 + \left(\frac{\lambda z}{\pi w_0^2}\right)^2\right]^{0.5}. \end{aligned} \tag{2.83}$$

With these two equations alone, the propagation of a fundamental Gaussian beam through any optical system can be modelled.

To complete the analysis of the fundamental Gaussian beam (2.79) can be rewritten as $\frac{\partial A}{A} = -\frac{\partial z}{q}$ and from (2.79) $\partial z = \partial q$, so $\frac{\partial A}{A} = -\frac{\partial q}{q}$. Hence, $\frac{A(z)}{A(0)} = \frac{q(0)}{q(z)}$ and substituting q from 2.82;

$$\frac{A(z)}{A(0)} = \frac{1 + j\lambda z/\pi w_0^2}{1 + \lambda z/(\pi w_0^2)^2}. \tag{2.84}$$

Then defining;

$$\tan(\phi_0) = \frac{\lambda z}{\pi w_0^2} \tag{2.85}$$

it is found that:

$$\frac{A(z)}{A(0)} = \frac{w_0}{w}e^{j\phi_0} \tag{2.86}$$

where ϕ_0 is known as the Gaussian beam phase shift. By taking the on-axis beam amplitude to be unity at the waist, a final complete term for the fundamental Gaussian is obtained:

$$u(r,z) = \frac{w_0}{w}exp\left(-\frac{r^2}{w^2} - j\frac{\pi r^2}{\lambda R^2} + j\phi_0\right). \tag{2.87}$$

The expression for the electric field is then found by $E(r,z) = u(r,z)e^{-jkz}$, such that, finally;

$$E(r,z) = \left(\frac{w_0}{w}\right)exp\left(-\frac{r^2}{w^2} - jkz - j\frac{\pi r^2}{\lambda R} + j\phi_0\right). \tag{2.88}$$

2.3.6 Ray Matrices & Gaussian Beam Parameters

As seen earlier in equation 2.81, a complex beam parameter, q can be written as

$$\frac{1}{q} = \frac{1}{R(z)} - j\frac{\lambda}{\pi w(z)^2}. \tag{2.89}$$

This q specifies the state of the wave at the start of the region through which it will propagate a distance, L(equivalent to z). To discover the properties of the wave (i.e. w or R) at the end of the region through which it propagates, one can very simply use ray ('ABCD') matrices [65]. This ABCD matrix formalism is very useful and widely used in paraxial system design to trace geometrical rays through various system components i.e. mirrors, lens, etc. One simply needs to know the beam properties at the system origin, and the properties at the end of the region are readily deduced. Matrix elements vary for different components and media, so if a system consists, say, of a free space element, after which the beam is focused by a lens element, and then propagates again through another free space region, three separate matrices must be used, given by:

"Free space": refractive index $n_0 = 1$ and length, L

$$\begin{pmatrix} 1 & L/n_0 \\ 0 & 1 \end{pmatrix}$$

thin lens: focal length, f;

$$\begin{pmatrix} 1 & 0 \\ -1/f & 1 \end{pmatrix}$$

followed by a second free-space matrix. A useful expression exists [65] allowing one to recover the beam width and radius or curvature at the end of any region, namely:

$$q_{out} = \frac{Aq_{in} + B}{Cq_{in} + D} \tag{2.90}$$

where q_{in} is the value of q calculated at the beginning of the region. Now q_{out} can be substituted back into 2.89, so that the output beam radius can be found by:

$$w = -\sqrt{\frac{\lambda}{\pi Im\left(\frac{1}{q_{out}}\right)}}. \tag{2.91}$$

The phase radius of curvature can also be recovered from q_{out} by:

$$R = \frac{1}{Re(\frac{1}{q_{out}})}. \tag{2.92}$$

Take for example a system of three lenses, as shown in figure 2.16, with a distance f_1 separating all planes and lenses, whose focal lengths are given as either f_1, f_2 or f_3. Ray matrices can be used to propagate the beam through the system, returning the beam width and radius of curvature at the output plane.

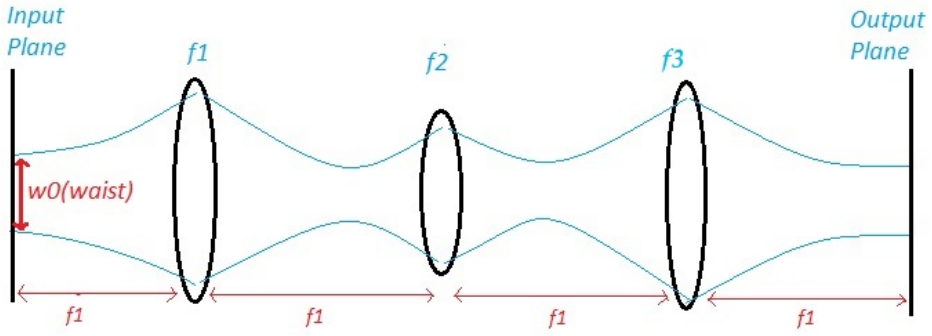

FIGURE 2.16: Paraxial optical system of three lenses with given focal lengths and separations. The ray matrix formulism allows propagation of a Gaussian beam through the system.

As the system consists of four free space elements and three lens elements, the combined ABCD matrix of the system can be written as a combination of free-space and thin lens matrices

$$M = \begin{pmatrix} 1 & f_1 \\ 0 & 1 \end{pmatrix} \begin{pmatrix} 1 & 0 \\ -\frac{1}{f_3} & 1 \end{pmatrix} \begin{pmatrix} 1 & f_1 \\ 0 & 1 \end{pmatrix} \begin{pmatrix} 1 & 0 \\ -\frac{1}{f_2} & 1 \end{pmatrix} \times \begin{pmatrix} 1 & f_1 \\ 0 & 1 \end{pmatrix} \begin{pmatrix} 1 & 0 \\ -\frac{1}{f_1} & 1 \end{pmatrix} \begin{pmatrix} 1 & f_1 \\ 0 & 1 \end{pmatrix} \tag{2.93}$$

and performing matrix multiplication the calculated ABCD matrix of the full system, in terms of f_1 and f_2 where for ease of simplification we assume $f_1 = f_3$, is given as:

$$M = \begin{pmatrix} -1 & -f_1^2/f_2 \\ 0 & -1 \end{pmatrix} \tag{2.94}$$

This quick and relatively simple calculation shows the power of the ray matrix and complex beam parameter formalisms, as they allows one to quickly assess how a beam will propagate in a multiple component system.

2.3.7 Higher Order Gaussian Beam Modes

Up to this point it has been assumed that the fundamental mode of electromagnetic propagation was all that was of interest. Often, there are multiple modes which contribute to the total power of a beam. Higher-order modes are often described in rectangular

coordinates in the form of Hermite-Gaussian modes, or in cylindrical coordinates in the form of Laguerre-Gaussian modes.

Working again in cylindrical coordinates to derive the expression for higher-order modes, a solution such as that in (2.78), but which isn't limited to a purely Gaussian form, is taken [65]. Thus

$$u(r,\varphi,z) = A(z)exp\left(-\frac{jkr^2}{2q(z)}\right)S(r)exp\left(jm\varphi\right) \tag{2.95}$$

where, again, A and q depend only on propagation distance z and a new factor S depends upon radial distance r. Implementing the trial solution as previously for the fundamental mode solution, the paraxial wave equation returns an equation in S, namely;

$$S(r) = \left(\frac{\sqrt{2}r}{w^2}\right)^m L_{pm}\left(\frac{2r^2}{w^2}\right) \tag{2.96}$$

where m is an integer and L_{pm} is the general Laguerre polynomial (i.e. $L_{pm}(u)$ are solutions to Laguerre differential equation). Solving for all variables as before, the normalized electric field distribution in cylindrical coordinates is:

$$\begin{aligned} E_{pm}\left(r,\varphi,z\right) = &\left(\frac{2p!}{\pi(p+m)!}\right)\frac{1}{w(z)}\left(\frac{\sqrt{2}r}{w^2}\right)^m L_{pm}\left(\frac{2r^2}{w^2}\right) \\ &exp\left(-\frac{r^2}{w^2(z)} - jkz - \frac{j\pi r^2}{\lambda R(z)} - j(2p+m+1)\phi_0(z)\right)exp\left(jm\varphi\right). \end{aligned} \tag{2.97}$$

As for the fundamental mode w represents beam width, R represents radius of curvature, and $(2p+m+1)\phi_0$ is the phase shift. In this case the phase shift depends on the mode indices p and m. The only other differences between the fundamental and higher-order field are the angular and radial dependence of the mode amplitude.

2.4 Comparison of GBM Model, GRASP9 model, and Laboratory Measurements of a Rectangular Horn

At mm-wave and THz frequencies, radiation is typically transmitted through free-space and coupled to detectors via an antenna structure. Horn antennas are most often used, as they provide good rejection of stray light over reasonably large bandwidths. Their behaviour is also easily characterised resulting in well understood beam patterns, a trait which has made them useful in applications such as CMB telescopes. These experiments require good beam symmetry and well-defined behaviour, low cross-polarization,

low side-lobe levels, and bandwidths of up to 30%, standards for which single-moded corrugated conical horns have sufficed.

The next generation of telescopes, however, will require even greater sensitivity. There is now much interest in rectangular-aperture horns that can be packed closely for use in array detectors. In particular there is interest in using multi-moded horns which are less well understood. The investigation of the beam characteristics of a typical multi-moded rectangular horn are outlined here. We first perform an analytical model of the beam from a rectangular horn and see how well that can be reconstructed from Gaussian beam modes. This model is then compared against measurements of a rectangular horn made in NUI Maynooth.

The rectangular horn used for the purpose of this work was a smooth walled pyramidal feed horn produced by Farran Technology Ltd. It had WR-10 waveguide dimensions, thus allowing it to operate optimally over a bandwidth from 75 to 110 GHz. The aperture width measured 24.6 mm horizontally, and 18.8 mm vertically, while the flare length from waveguide entrance to aperture plane measured 49.3 mm.

Here, beam patterns of the rectangular horn will be predicted using the GBM approach, and also modelling using GRASP9. Laboratory measurements of the beam pattern from a real horn of the same dimensions will then be shown, supporting the accuracy of both GBM and GRASP9 modelling routines. It should be noted that in all cases only quadrants of the overall beam pattern are shown, owing to the scanning restrictions of the laboratory set-up.

2.4.1 GBM Construction of a Rectangular Horn Beam

Unlike the Laguerre-Gaussian modes used primarily for circularly symmetric systems, and outlined previously, Hermite-Gaussian modes are generally used for systems with cartesian symmetry such as the rectangular horn. The Hermite-Gaussian mode coefficients for a modal expansion of a rectangular horn antenna field are derived herein, and the horn beam pattern reconstructed at various distances from the aperture to compare

with measurement. The Hermite-Gaussian modal field is given by:

$$E_{mn}\left(x, y, w_x(z), w_y(z), R(z), \phi_0(z)\right) = \left(\frac{1}{\pi w^2(z) 2^{m+n+1} m! n!}\right)^{0.5} H_m\left(\frac{\sqrt{2}x}{w_x}\right) H_n\left(\frac{\sqrt{2}y}{w_y}\right) \times \exp\left(-\frac{(x^2+y^2)}{w^2} - jk\left[z + \frac{(x^2+y^2)}{2R}\right] + j(m+n+1)\phi_0\right) \tag{2.98}$$

and the fundamental mode Gaussian is illustrated in figure 2.17. The field at the aperture of the rectangular horn of length L_{axial} given by [65]:

$$E_{horn}(x, y) = \sin\left(\frac{\pi x}{a}\right) \exp\left(i\frac{\pi(x^2+y^2)}{\lambda L_{axial}}\right) \tag{2.99}$$

for $0 < x < a$ and $0 < y < b$. This aperture field looks rather akin to a 'shed-roof', varying sinusoidally along the longest axis and as a top-hat along the shorter axis. This is shown in figure 2.17, where radiation intensity is normalised and the axis of propagation, z, is perpendicular to the plane shown.

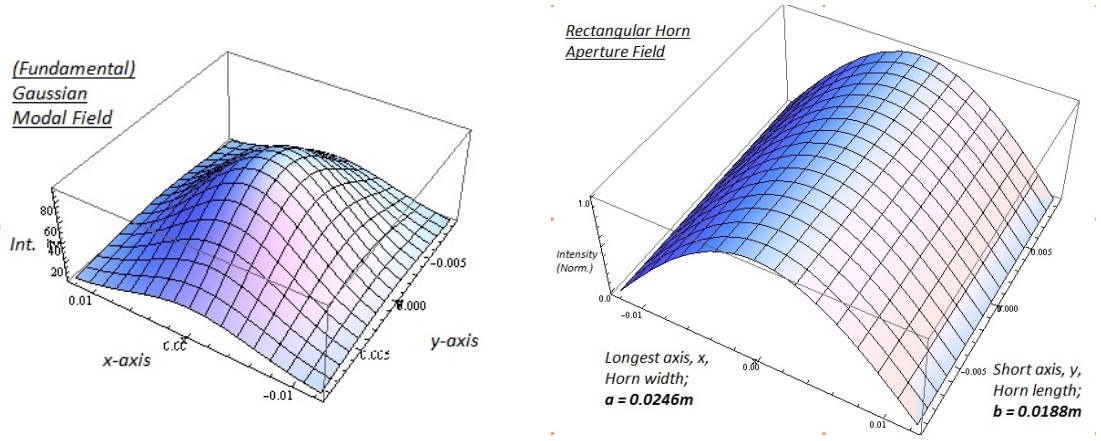

FIGURE 2.17: (**left**) Gaussian Beam modal field, E_{00}, showing power in the fundamental mode, and (**right**) the Rectangular Horn aperture field, E_{horn}, modelled in *Mathematica*.

Now, given a set of Gaussian beam modes E_m any function f can be expanded as:

$$f(u) = \sum_{m=0}^{\infty} a_m E_m(u) \tag{2.100}$$

where $f(u)$ represents the aperture field and a_m are the expansion coefficients to be derived. Thus, an overlap integral of the aperture and modal fields must be performed to extract these coefficients, as below:

$$a_m = \int E_m^*(u) f(u) du \tag{2.101}$$

This represents only a one-dimensional example, however in two dimensions coefficients must be derived in m and n. Taking $R = \infty$ for the mode set and starting with all modes, in this case the overlap integral can be written as:

$$a_{mn} = \int_{-a/2}^{a/2} \int_{-b/2}^{b/2} E_{mn}(x, y, w_{x0}, w_{y0}, \infty, 0) E_{horn}(x, y) dx dy \tag{2.102}$$

where $z = 0$ at the aperture, a is the width and b the height of the rectangular horn aperture, representing the limits of the field. The Gaussian beam widths of the mode set were taken as $w_x = w_y = 0.35a$, as this gives the best coupling between a rectangular horn and the fundamental mode Gaussian for $R = \infty$.

The coefficients represent the fraction of total power contained in each individual mode, such that when combined, they return the summed total power in the field at the aperture. One can now elegantly reconstruct the beam at any distance, z, along the axis of propagation, by simply propagating each mode independently and recombining them at z. To do this one must include the changed beam radius of curvature, R, beam widths w_x and w_y, and the phase shift, ϕ_0. Defining a confocal parameter, $z_c = \pi w_x / \lambda$, which represents the border between near and far-fields, the three beam parameters can be written as;

$$\begin{aligned} w_y = w_x &= w_{x0} \left(1 + \left(\frac{z}{z_c}\right)^2\right)^{0.5} \\ R &= z + \frac{z_c^2}{z} \\ \phi_0 &= \tan^{-1}\left(\frac{z}{z_c}\right) \end{aligned} \tag{2.103}$$

which allows calculation of the beam in the near- or far-field by summing the product of each mode coefficient coefficient, (2.102), and its field, (2.98), i.e.:

$$E_{near-/far-field}(x, y, z) = \sum_m \sum_n a_{mn} E_{mn}\left(x, y, w_x(z), w_y(z), R(z), \phi_0(z)\right) \tag{2.104}$$

and is illustrated in figure 2.18, where the field is constructed using 20 modes and at 75 GHz.

The rectangular horn was then modelled in GRASP9, which uses the SWE technique as outlined earlier. To model this type of feed in GRASP9 one can use the 'Rectangular Horn' object, which requires definition of the aperture size, horn length, and frequency of operation. A simple set-up to measure the far-field from the horn is shown in figure 2.19.

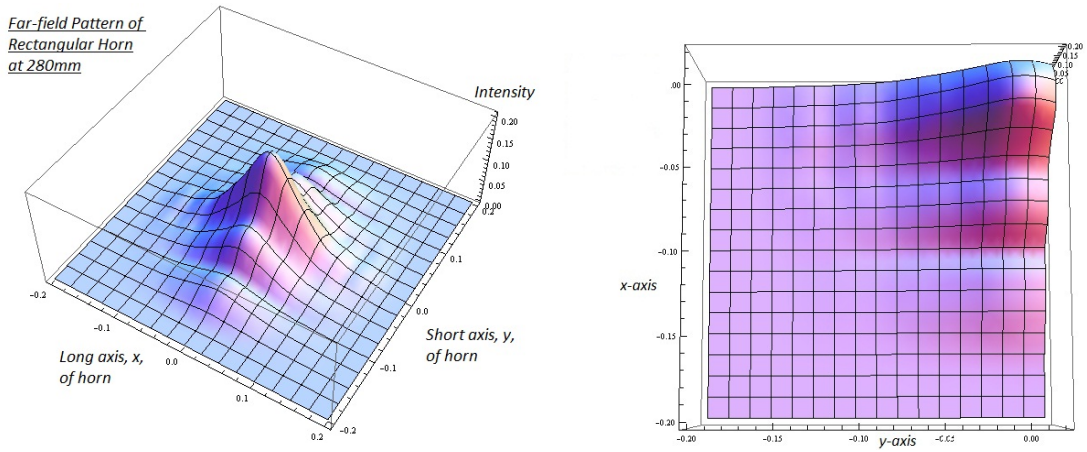

FIGURE 2.18: Constructed theoretical far-field pattern of the rectangular horn at 75 GHz, viewed from 2 angles ('height' of intensity is just for illustration purposes, it is not along the z-axis).

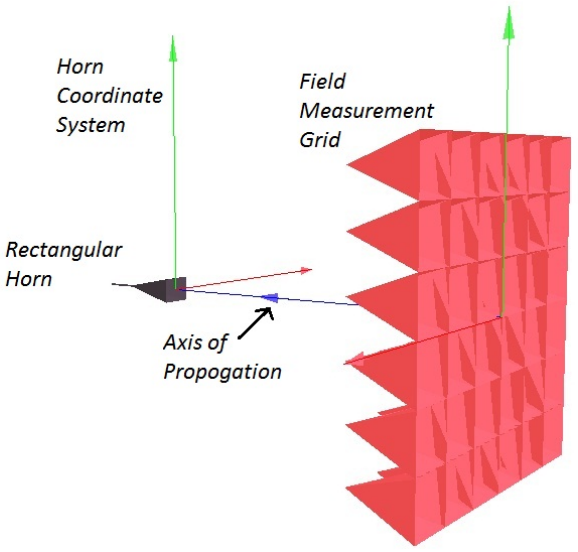

FIGURE 2.19: Simple Horn set-up with measurement grid at a distance, $z = 280\,mm$, from the aperture.

As the field measurements were over a quadrant of the horn beam profile, a similar field grid was created in GRASP9 so that comparisons could be easily drawn. Simulations were performed at three frequencies within the allowed range of the Vector Network Analyser (VNA); namely 75, 92.5 & 101 GHz. Far-field beam profiles were then calculated for each frequency, a distance of 280 mm from the aperture. This particular distance was chosen as it was calculated to be four times the confocal distance, z_c, which defines the distinction between near and far-field. The results are depicted in figure 2.20, and there is reasonable agreement between the general shape of the beam pattern produced using GBM, and shown in figure 2.18.

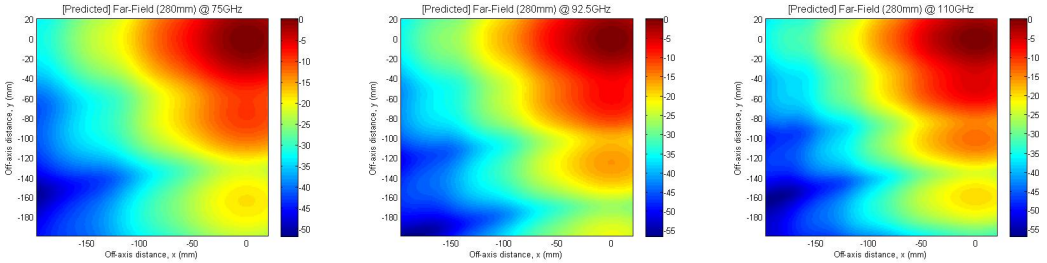

FIGURE 2.20: Horn far-field at (**left**) 75 GHz, (**centre**) 92.5 GHz, and (**right**) 110 GHz, as predicted by GRASP9.

2.4.2 Measured Rectangular Horn Beam Patterns

All measurements performed on the rectangular horn involved using a *Rohde & Schwarz* VNA acquired by NUI Maynooth to support a wide range of high frequency optical measurements. This device allows the real-time measurement of electric field amplitude and phase in the high frequency bandwidth 75 GHz to 110 GHz. It is attached via fibre optic cables to two THz emitting converter heads, which can be set up in any required arrangement, such that both are capable of emitting/detecting the radiation through a system. For the purpose of this experiment a rectangular horn was attached to the waveguide aperture of one of the heads, and a simple WR-10 waveguide transition element attached to the other which is connected to port 1 of the VNA. The two heads were then set up directly facing each other at various distances from horn to receiver and 2-dimensional scans were performed by moving the head attached to port 1 (the receiver), to build up both near and far-field beam profiles. Figure 2.21 shows the general setup. The restriction on beam profile measurements was due to the scanning rig being unable to utilise its entire range at the time of measurements.

Two-dimensional scans were taken of the radiation pattern, in this case at a distance of 280 mm from the aperture. This lies well into the far-field, at approximately four times the confocal distance, z_c. As the beam diverges significantly by this point, larger field scans must be taken. It was decided that quadrant grids would be again used, in this case across x/y ranges of 200 mm,-200 mm. The number of points were also increased to 177 $\times$ 177 such that much more accurate scans were obtained. The predicted and measured fields at 75 GHz and 110 GHz are shown in figure 2.22.

Clear similarity is visible when comparing the two fields at a particular wavelength, however standing wave artifacts are somewhat noticeable due to the inherent difficulty in eliminating reflections from a system with many reflective surfaces. Normalised cuts through the modelled and measured main beams are shown in figure 2.23. In the case of horizontal beam cuts, the predicted and measured off-axis intensities matched very well,

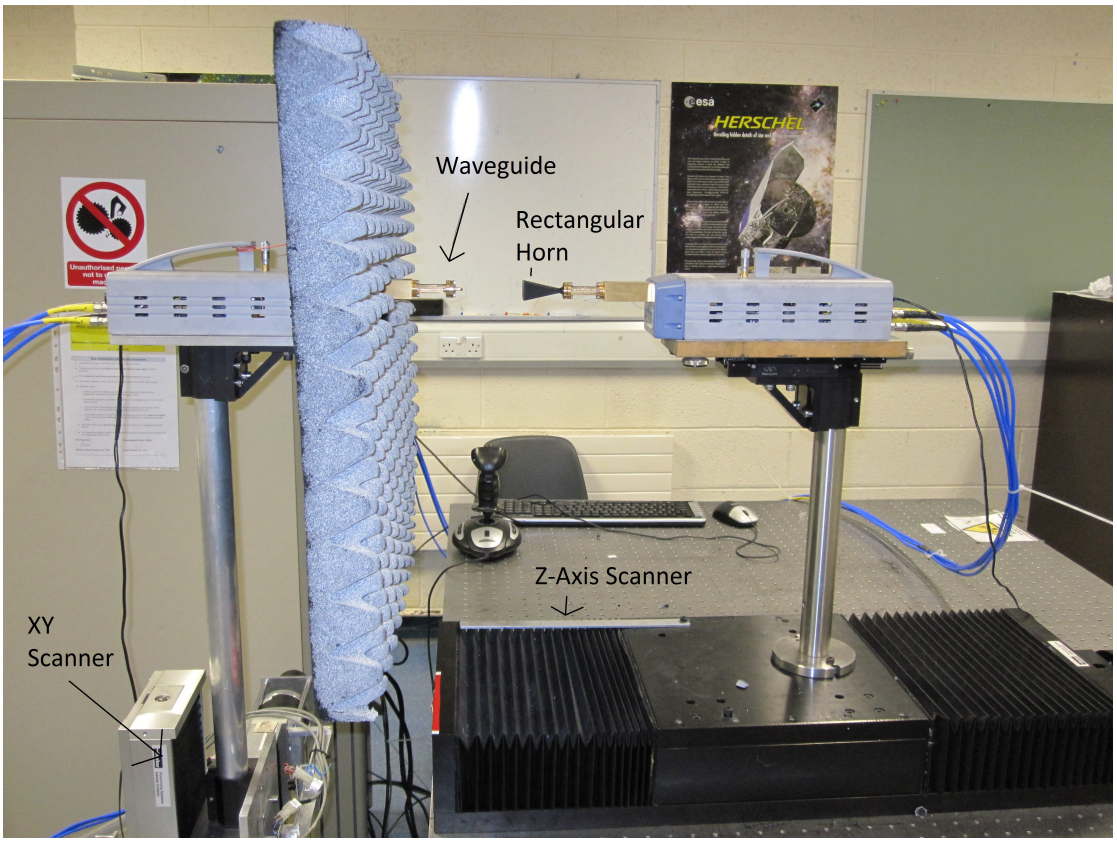

FIGURE 2.21: The XY-scanner, Z-scanner, and two emitter heads in measurement configuration on the optical bench. The rectangular horn is attached to head 1, and a WR-10 waveguide transition to head 2, with a distance of $z = 280\,\text{mm}$ between them. Corrugated 'egg-carton' Ecosorb material is placed around the experimental setup to absorb stray light and minimise reflections in the system.

down to approximately -25 dB, where power is predicted to be higher than was actually found. Some moderate standing wave effects can be seen in the intensity pattern below -30 dB.

In comparison along the vertical axis, predicted and measured intensities were well matched around 75 GHz. At 110 GHz, however, the measured intensity is significantly larger than predicted, from roughly -3 dB normalised power, down to -20 dB. The difference of approximately 3 dB is maintained as the off-axis intensity falls, and both never really match until the second off-axis lobe at -20 dB. This discrepancy is the result of higher-order mode excitation at the furthest reach of the band, which is not fully accounted for in the GRASP9 model. The cut-on frequency of various TE/TM_{mn} modes in this rectangular horn are given in figure 2.24, and it can be seen that a number of higher-order modes above the fundamental cut-on across the band. Multi-moded horns will be discussed further in the coming chapters, where modelling of the multi-moded Planck channels is undertaken.

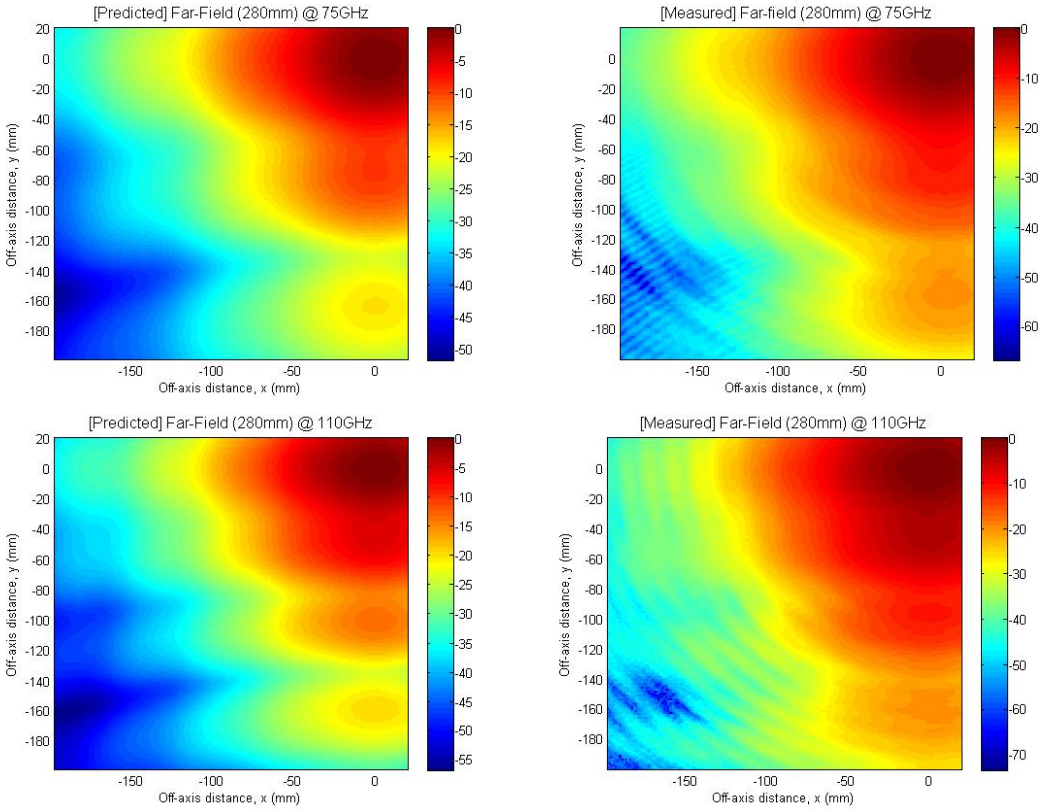

FIGURE 2.22: At 75 GHz (**top**) & 110 GHz (**bottom**); Predicted far-field patterns (**left**), and measurements after reduction of standing wave artifacts (**right**).

2.5 Conclusion

In this chapter the various techniques used for the modelling of horn antenna and telescope systems were outlined, alongside an overview of the GRASP9 software which implements some of these techniques. We first detailed various features of the software, which was followed by a concise overview of the mathematical theory governing the implementation of PO and GTD techniques. We then outlined the various modal solutions to the wave equation which can be implemented in waveguide structures and free space. This included a detailed outline of waveguide mode theory, as well as Gaussian beam mode theory and the ray matrix formalism. This was followed by a model of a the field from a rectangular horn, performed numerically in GRASP9, and analytically using GBM. Good agreement was found between both models, and laboratory measurement of the horn were in good agreement with the model also. In the next Chapter we will investigate the implementation of some of the techniques already outlined, and advance from modelling a simple single-reflector system to the much more complex Planck telescope Radio Frequency Flight Model (RFFM), with the aim of replicating the features seen in the HFI difference maps.

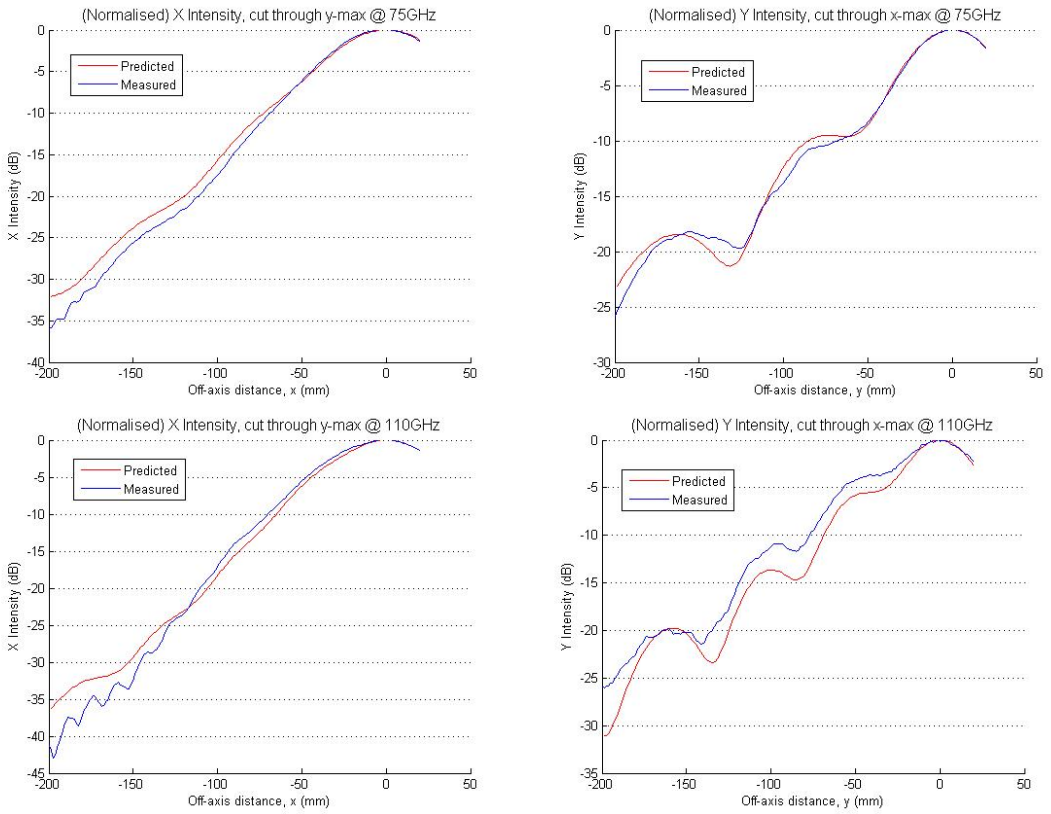

FIGURE 2.23: Comparisons between measured and predicted horizontal cuts (**left**), and vertical cuts (**right**) through the main beams at the points of maximum intensity at 75 GHz (**top**) & 110 GHz (**bottom**).

Mode	Cut-on Freq (GHz)
TE01	50.13
TE02	100.26
TE10	38.31
TE11/TM11	63.10
TE12/TM12	107.33
TE13/TM13	155.20
TE20	76.62
TE21/TM21	91.57
TE22/TM22	126.19
TE30	114.94
TE31/TM31	125.39

FIGURE 2.24: Cut-on frequencies of various higher-order rectangular waveguide modes, calculated using equation 2.38 for aperture dimensions of a=24.6 mm and b=18.8 mm.

Chapter 3

Modelling of the Planck Telescope in GRASP9

In the previous chapter we saw an outline of the various quasi-optical modelling techniques available in the GRASP9 package, namely physical optics (PO) and geometrical optics (GO) with the geometrical theory of diffraction (GTD). In this chapter we shall implement these techniques and investigate their merits, as well as their limitations. Beginning with an arbitrary single reflector system the various subtleties of PO will be investigated, after which a basic dual reflector model of the Planck system will be implemented to compare the PO and GTD techniques. This will lead on to a full description of the Planck system, which shall then be modelled for the purposes of far sidelobe (FSL) investigation in the high frequency channels of HFI. This will involve the complex analysis of reflected power from baffles and reflector edges, which contribute to the overall FSL structure of the beam on the sky, however a full GTD analysis of the Planck system will only be performed for only the 857-1 horn location. Separate GTD simulation for all four horn locations would prove quite time-consuming, and show little difference in FSL structure from one sky beam to another due to the close proximity and orientation of the 857-GHz horns on the focal plane.

3.1 Simple Example: Single Reflector System

To provide a better understanding of the theory of PO and GTD outlined previously, they will now be implemented for a simple geometrical telescope system, consisting of a feed propagating a field to a single off-axis reflector, from which the field on the sky

will be determined using a variety of methods in GRASP9. Performing a comparative study, the benefits of one method over another in different situations will become readily apparent.

The 'Single reflector' option in GRASP9 allows a simple system to be described in 2D by a number of parameters. Such a system can form the fundamental building block of much more complicated systems the user may wish to implement (see figure 3.1). A single reflector system is very useful and also trivial to optimise using a simple paraboloid mirror. Along with the definition of a project frequency (100 GHz was used here as it is relevant to the modelling in sections 3.2 and 3.3) values for the reflector size, focal length, off-axis tilt and distance between feed and reflector allow the complete description of a simple paraboloid telescope system, as shown in figure 3.1. Once formed, 3D imaging of the system is done using the 'Open-Gl' command in GRASP9, and a purely illustrative ray trace from feed to sky implemented for better visualisation of how changes to the system will affect the feed radiation pattern, as shown in figure 3.2. This is performed using the 'Ray Plot' function in GRASP9. This is a purely illustrative technique rather than qualitatively describing the nature of the beam. The angular extent and sampling in θ,ϕ spherical coordinates defines the region in which the beam cone is formed. In this case we have taken a standard parabolic mirror with our detector at the focus resulting in parallel rays on reflection to the sky, simulating the radiation from distant sources. Mathematically a parabola is a mere extension of an ellipse, where a fundamental elliptical mirror will have two focii in the near field of the mirror, but a parabolic mirror has only one.

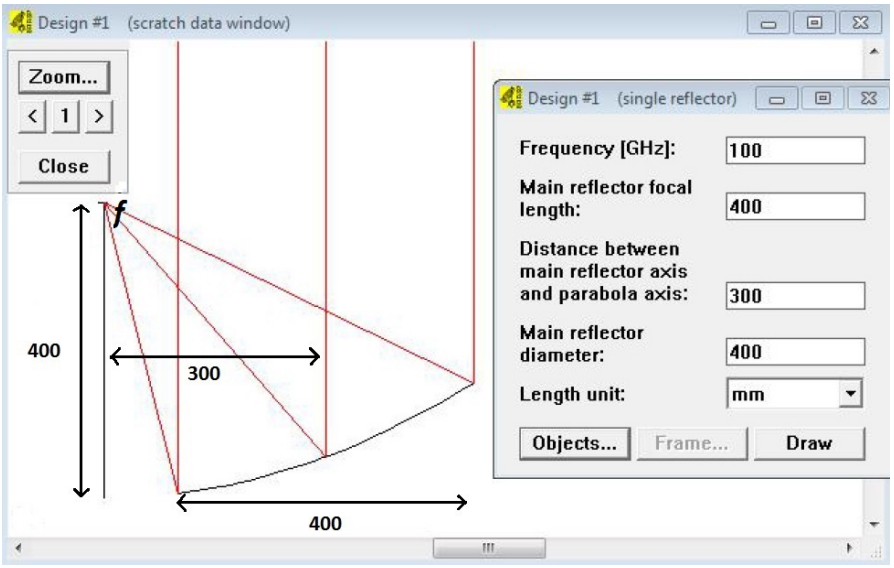

FIGURE 3.1: Typical 2-dimensional rendering of a basic off-axis single reflector system in GRASP9 (left) with appropriate values of system parameters (right). The reflector in this case is a section of a parent parabola centred on 'f'.

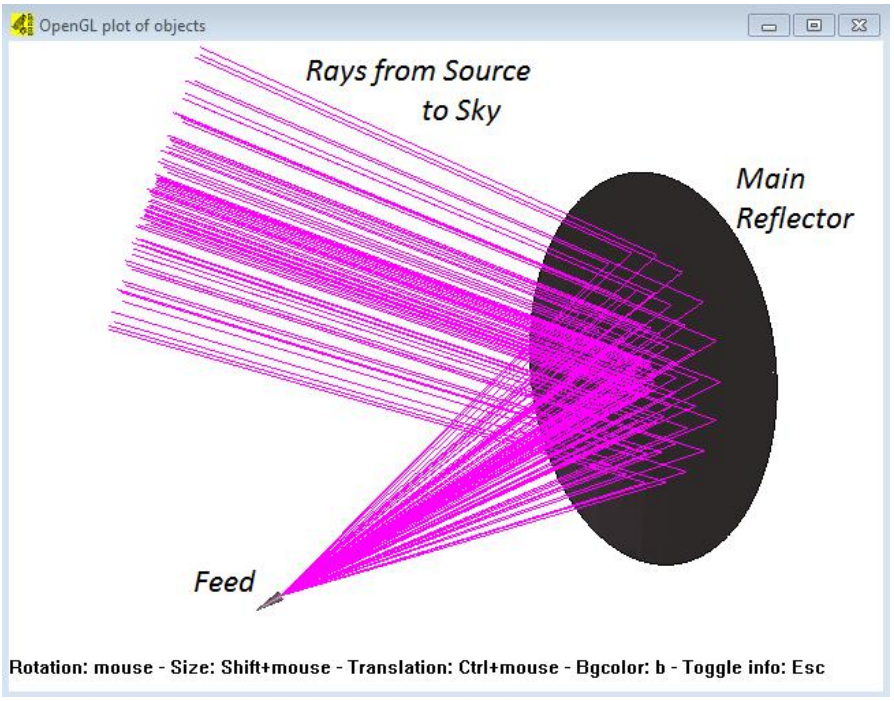

FIGURE 3.2: 3-dimensional rendering of the telescope system using the 'Open-Gl' function in GRASP9 where rays have been traced from the centre of the feed aperture for illustration of beam path. The divergence angle of the cone here is defined by a 30 ° span in θ and a 360 ° span in ϕ, sampled every 3.75 ° in θ and 18 ° in ϕ.

Various sources can be chosen in the GRASP9 directory. To keep the model as simple as possible a fundamental Gaussian with an edge taper of -12 dB at a taper angle of 25 ° is defined using the 'Gaussian Beam, Pattern Def' option in GRASP9. The actual edge taper of the Planck HFI horns on the reflectors is considerably lower than this estimate. The total power is standardised to 4π W by GRASP9, however if the user wishes to alter this, a 'factor' in dB may be defined, by which the standard 4π will be multiplied.

This source object in GRASP9 provides a good approximation to the aperture field of modern horn antennas, whose beam patterns are generally Gaussian in nature. The beam produced by propagating a Gaussian beam into the far-field of the horn itself is shown in figure 3.3, with an on-axis intensity of 20 dB tapering smoothly off-axis. Though we can of course couple radiation directly to our detector from a large range of angles, if resolution is important we only wish to observe a very small angular portion of the sky at any one time, and from this direction couple as much radiation to the detector as possible. To this end, focussing mirror systems become extremely useful, capturing much more radiation onto the large surface area reflectors, which couple the signal to the much smaller detector at the focus of the system. The improvement is obvious from comparison of figures 3.3 and 3.4, where the latter shows the main beam propagated into the far-field of the telescope after reflection, maintaining circular symmetry about the axis. The on-axis intensity in the main beam increases by over 30 dB and the beam is

much narrower in angular width, thus coupling much more radiation from a smaller area of the sky. Of course to improve upon this and increase the gain of the telescope, one must also attempt to minimise unwanted signal coupling to the telescope from directions away from the main beam, the main focus being the near-in sidelobes which form past the first null in the main beam. In figure 3.4 the first sidelobe forms at beyond half a degree, and 25 dB to 30 dB below peak, indicating it will couple very little radiation to the telescope in comparison to the main beam.

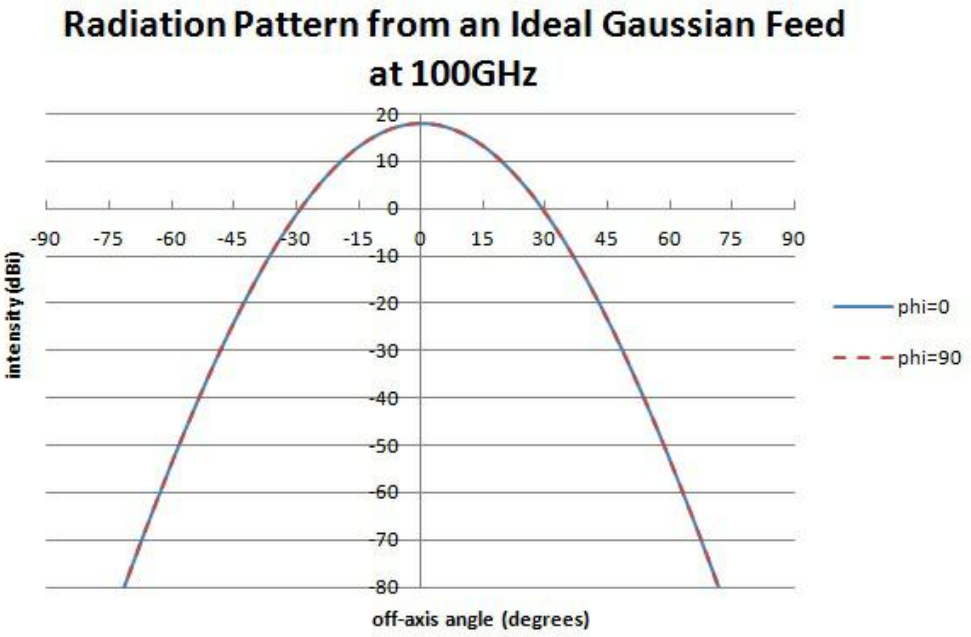

FIGURE 3.3: Far-field of a Gaussian beam defined by -12 dB taper at 25 ° taper angle at 100 GHz.

Diffraction effects from the edges of surfaces must often be accounted for in reflector systems. However in the region around the main beam there is little contribution from diffraction effects. This is the domain of PO, and figure 3.5 highlights that only PO is necessary to estimate correct levels and structure in the main beam region, while physical theory of diffraction (PTD) adds very little information, while simultaneously increasing computation time. For this reason when calculating main beams it should generally be switched off.

Though the results in figure 3.5 were obtained using PO, another modelling method often used toward the higher end of the THz spectrum is geometrical optics (GO) and the geometrical theory of diffraction (GTD) whose physical principles are explained in chapter 2. While GTD is very effective in modelling sidelobe structure, as shall be seen later, PO does much better in the main beam region, providing correct expectations of gain and beamwidth as illustrated in figure 3.6. GTD on the other hand encounters

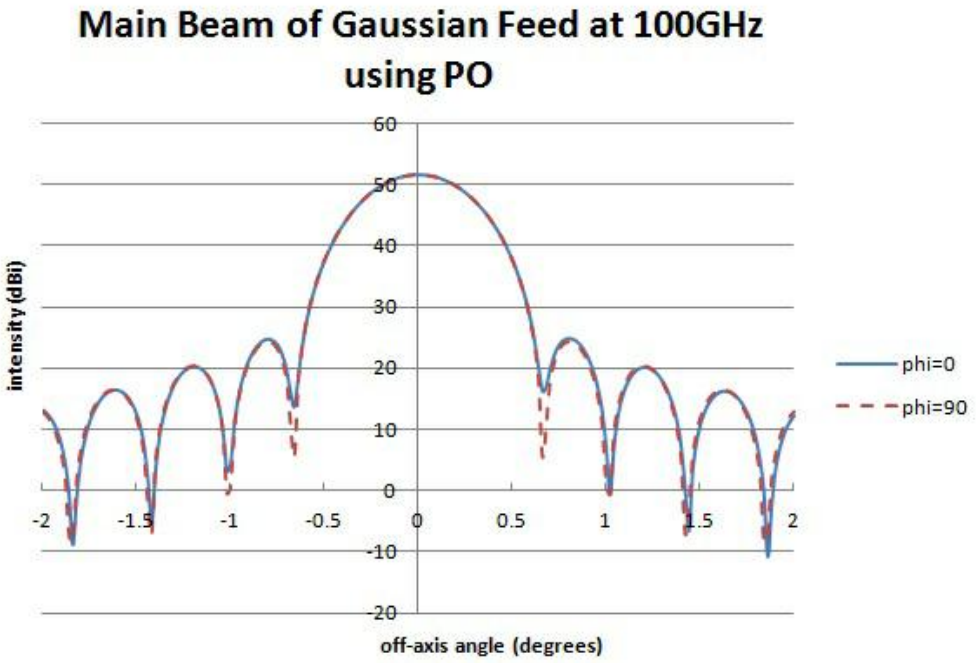

FIGURE 3.4: Gaussian beam of figure 3.3 propagated through the telescope of figure 3.2 and into the far-field at 100 GHz and using a field accuracy (F.A.) of -120 dB.

severe caustics in the same region, which can be seen as the infinite central trough in the main beam surrounded by extremely high peaks. This renders useless any information inferred about the telescope's directive power, making PO the preferred option for this task. Both methods do however converge to the same accuracy beyond roughly 1 °, in the near-in sidelobe region of the telescope.

Let us now consider modelling the radiation pattern of the telescope in regions beyond the main beam, namely the far-out sidelobes, which can be a significant source of unwanted power. Taking a cut along the axis of symmetry of this simple system (conveniently described by ϕ=0 °), and expanding from -180 ° to 180 ° around the sphere the far-out sidelobe structure can be observed. Figure 3.7 illustrates the spherical coordinates in which the radiation pattern on the sky is obtained, with the axis of symmetry of the system clearly aligned along ϕ=0 °.

Beginning with a PO approach, the far-field main beam and far sidelobe structure was obtained by calculating the currents induced on the reflector, and propagating the surface field which arises from these currents to the sky. PTD was then incorporated on the edges to supplement the PO calculation, and the radiation pattern was simulated over the same range. The small but noticeable contribution of PTD can be seen in the low level regions of figure 3.8, as PTD contributes power diffracted from the edge of the reflector into directions away from the main beam. Though some diffracted power will

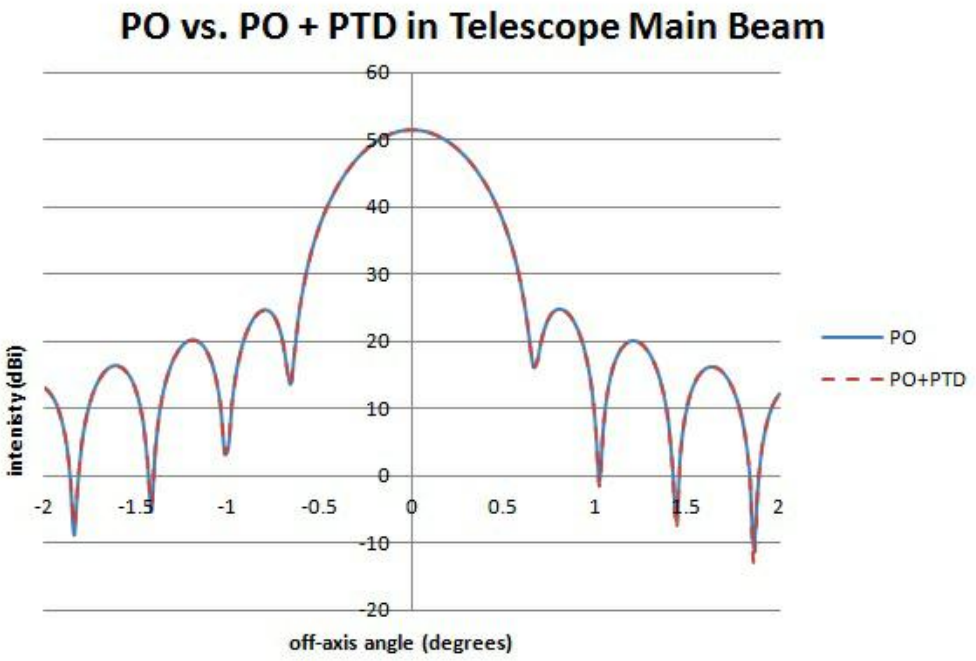

FIGURE 3.5: Gaussian propagated through the single reflector system onto the sky comparing the techniques of PO, and PO with PTD at 100 GHz (FA = -120 dB).

also end up in the main beam direction, the contribution is minimal with respect to the main beam reflected power, and thus the main beam appears identical to the main beam generated by PO alone.

One concern arising from the PO-modelled far-field in figure 3.8 is the broad lobe structure beyond 120 °, which peaks a mere 30 dB below the main beam. It is replicated in the PO with PTD model, and one might expect it was due to spillover from the reflector because of the region in which it is seen. Indeed there will be spillover into the region behind the reflector, however this is not the cause of the distinct peak. Returning to equation 2.8 the total field is described by the sum of scattered field (that which is reflected and/or diffracted off the reflector) and incident field (that which has been propagated from the source). Thus far we have calculated only the scattered field with PO and PTD, however to obtain the correct field on the sky we must now add the radiated field from the source to cancel the 180 ° inverted contribution included in the field propagated from the scatterer. The difference between physical models with and without inclusion of the direct radiation from source can be seen in figure 3.9. The broad lobe is removed by cancellation with the scattered field contribution bringing the sidelobe level down by over 20 dB to between 50 dB and 60 dB below peak in the region where the lobe was originally largest. A smaller, sharper peak is now observed at 140 ° which arises from rays diffracted from the primary edge and converging on the same region behind the reflector. The two small ridge-like peaks at 115 ° and 170 ° are

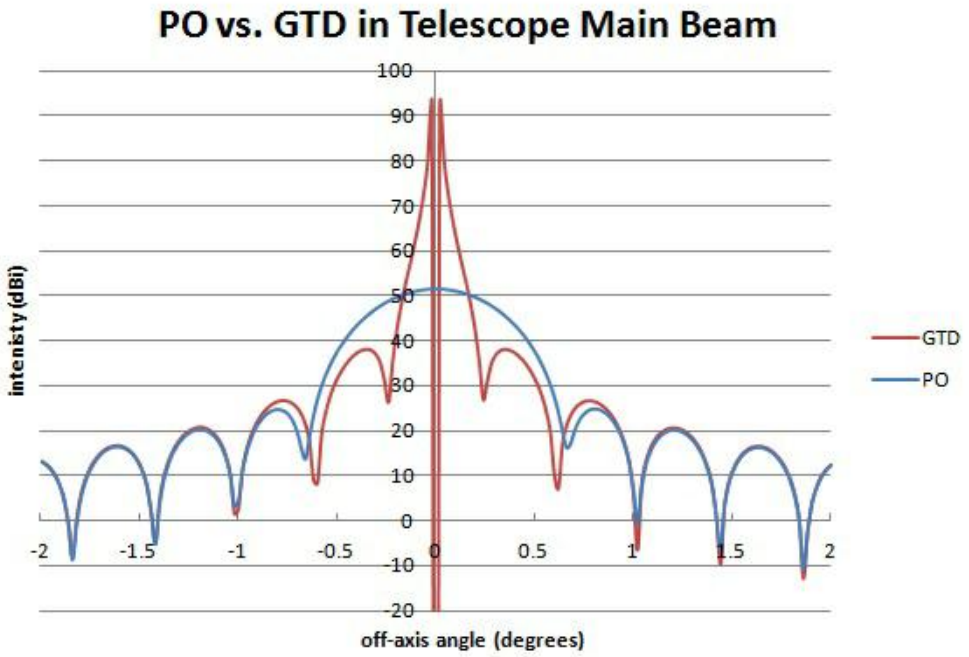

FIGURE 3.6: Comparison between PO and GTD in modelling of the Gaussian main beam at 100 GHz (FA = -120 dB).

caused by power spillover beyond the rim of the scatterer directly from the feed, and thus would not have been included in the scattered field component of the total field. This is of course a real effect so provides relevant information pertaining to any stray light concerns the designer may have.

Having fully described a PO approach to modelling a simple system, let us now look at the same system modelled using the GO and associated GTD framework. Here we approach the matter from a less physical perspective. Where PO used fundamental EM theory to perform surface approximations of induced currents and so forth, with GTD a more schematic ray-tracing technique is used. Treating the feed as a source of rays, these are propagated through the telescope to the sky, accounting for any reflections, diffractions and blockages encountered en route. As mentioned previously, in the PO approximation all scattering and/or blocking elements must be treated as sources of fields generated by incident currents. In a simple single reflector system this is fine, but for a more complicated system of reflectors and blockages, calculation of multiple reflected fields, and of increased orders of reflection, will be exhaustive. To this end GTD proves superior to PO, however in the single reflector case and for the majority of simplified telescope models both are useful.

Using GTD to find the field on the sky at an arbitrary point, the only rays which must be accounted for are those either reflected from a scatterer, diffracted off a scatterer's edge,

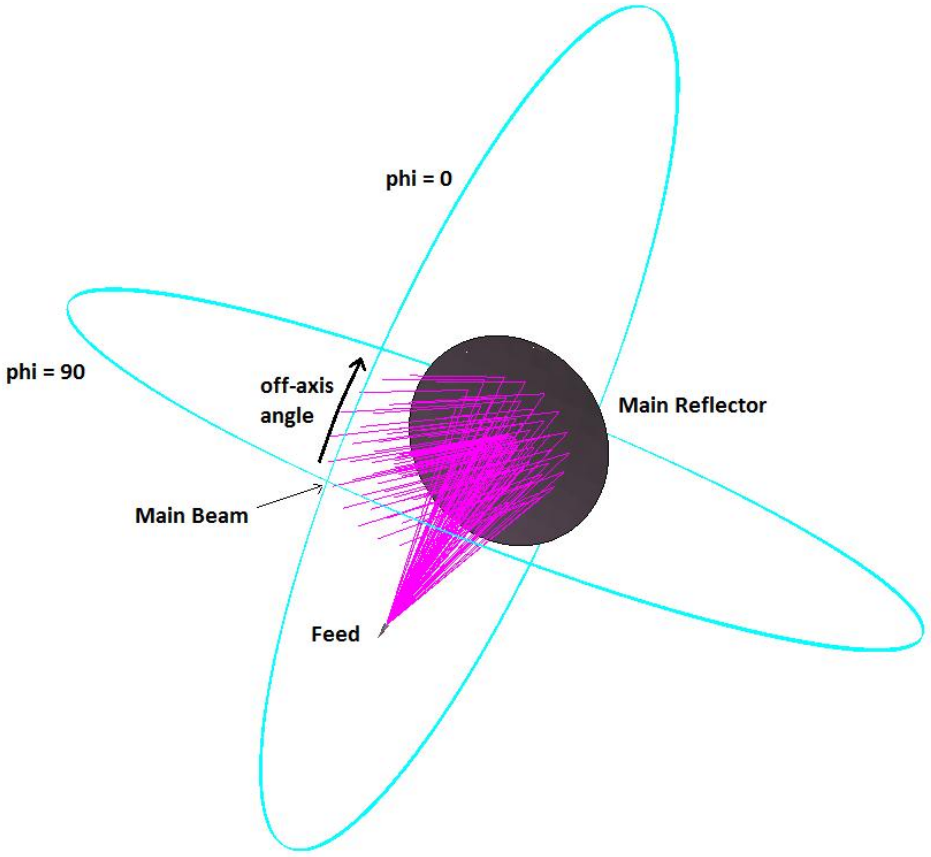

FIGURE 3.7: Illustration of the single reflector telescope and the θ,ϕ spherical coordinate cuts of the radiation pattern which are taken around the sphere.

or traced directly from feed to the particular location on the sky. If the point we choose is somewhat close to the line-of-sight (LOS) of the telescope, it becomes immediately clear that direct rays will contribute almost nothing to the field at this point, as illustrated in figure 3.10.

The reflected rays will contribute almost all of the power, whereas diffracted rays and direct rays generate the majority of the sidelobe power. The GRASP9 GTD object allows choice of which of these three components are to be included in a field calculation; labelled 'GO', 'GTD' and 'Direct'. As GO and GTD must be used, two cases with and without the contribution of direct radiation from the feed were modelled and compared, as shown in figure 3.11. Comparing with 3.9, it becomes immediately clear that GTD better estimates appropriate sidelobe levels, even before inclusion of the direct feed contribution. This is due to the incorporation of blockages which the user simply named in the GTD object, and proves much easier than having to account for them by the complex process of cancelling fields using PO. The blockage due to the scatterer is accounted for in the GTD calculation, so no lobe is seen in the backward direction, while the subsequent inclusion of direct radiation adds power due to spillover from rays

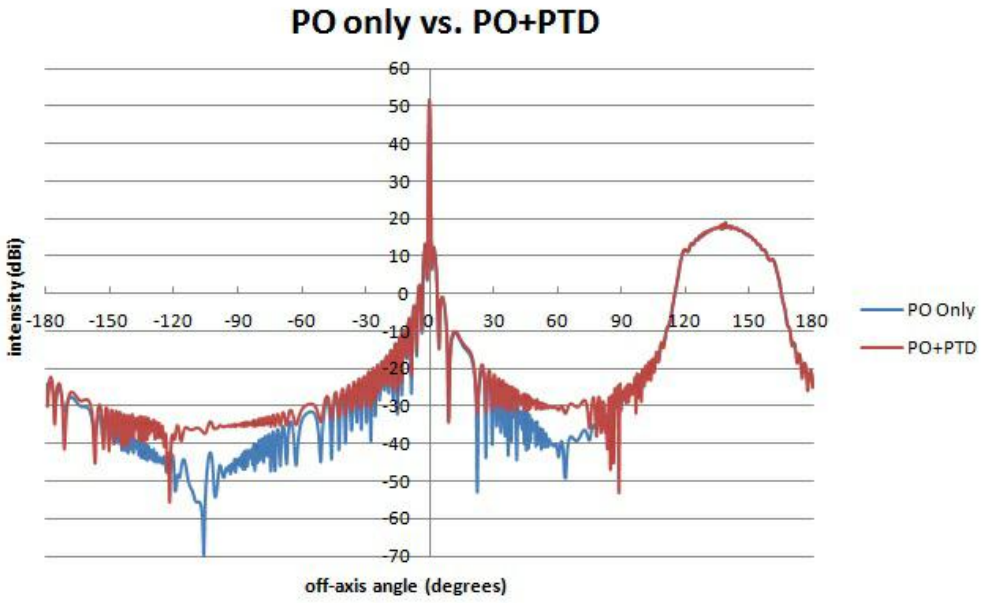

FIGURE 3.8: Comparison between the PO and PO+PTD modelling of the FSL structure of reflector in figure 3.2 at 100 GHz (FA = -120 dB).

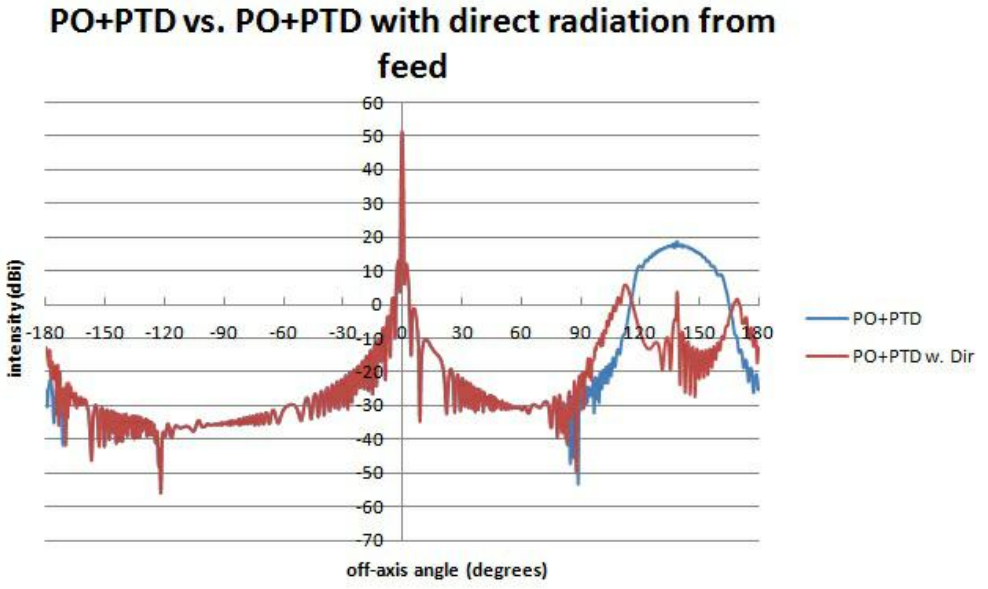

FIGURE 3.9: Comparison between PO+PTD modelling of the FSL structure with (w. Dir) and without inclusion of the field from the source in the sky beam calculation at 100 GHz (FA = -120 dB).

from the feed which are unimpeded by the blockage.

A comparison between PO and GTD techniques with inclusion of all fields is given in figure 3.12, showing excellent agreement between models in the near-in and far sidelobe regions. In this regard both prove useful for spillover calculations, however when effects due to diffracted and re-reflected radiation are taken into account for more complicated

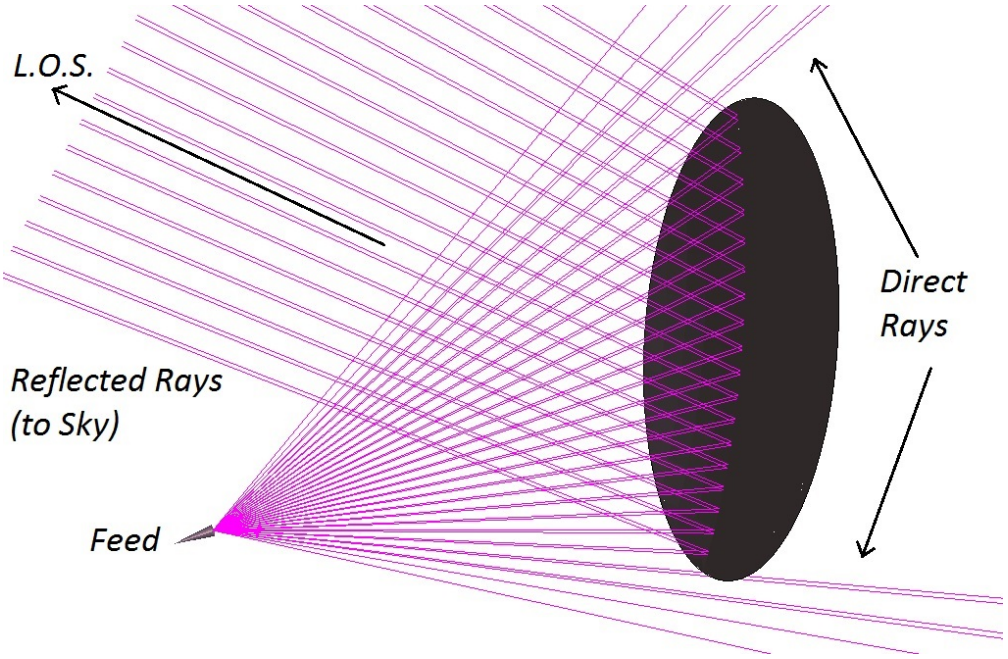

FIGURE 3.10: Various rays traced from feed to sky, both direct (i.e. no scattering) and reflected along the line of sight of the telescope (FA = -120 dB).

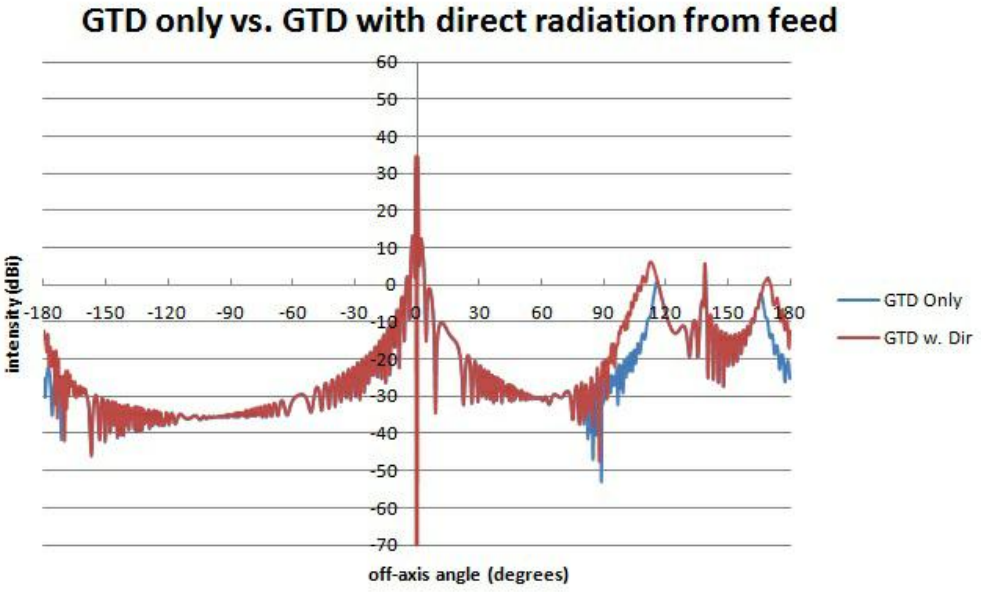

FIGURE 3.11: Comparison between GTD modelling of the FSL structure with and without inclusion of the field from the source in the sky beam calculation at 100 GHz (FA = -120 dB).

systems the qualitative difference in results will become apparent. The only discrepancy between the models occurs in the main beam region where the caustic due to focussed rays in the GTD model gives erroneous results. This region will henceforth be modelled using only PO so the GTD effects here can be ignored.

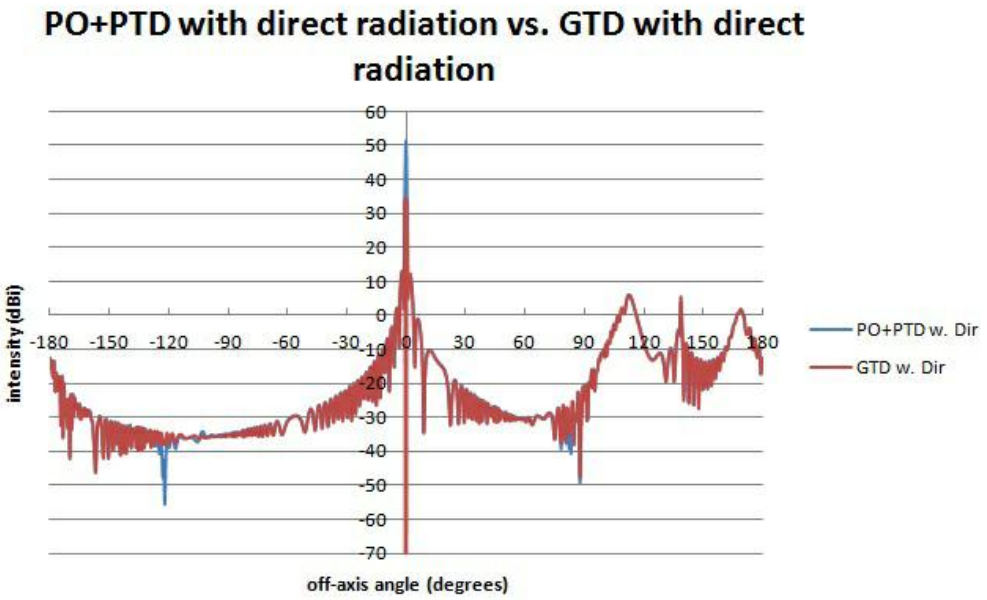

FIGURE 3.12: Comparison between PO+PTD and GTD modelling of the FSL structure with inclusion of the field from the source in the sky beam calculation of both at 100 GHz (FA = -120 dB).

3.2 Planck Basic Model: Dual-Reflector System

Having investigated the effects of PO and GTD on a simple single reflector model, let us now move to the more complex dual-reflector system of the Planck telescope. Here the modelling of spillover into off-axis regions behind the telescope will be performed first using PO, and for the purposes of this section alone, no structural components such as the baffles, Sun shield, or FPU box are included in the model. The telescope has been designed to take into account many complex issues surrounding multi-beam detection across a very wide bandwidth. Minimising off-axis aberration is crucial in this regard, as the mapping nature of the experiment requires that all beam patterns remain relatively uniform in shape across all bands.

The telescope is a tilted off-axis Gregorian design, meeting a requirement for compactness while also minimising blockage of the very large focal plane array. The secondary reflector is an off-axis ellipsoid of focal length of 0.514 m and dimensions 1.1 m by 1.05 m, while the primary reflector is an off-axis paraboloid with dimensions 1.7 m by 1.5 m and a focal length of 0.72 m. The surface accuracy on each mirror is well below 10 μm with roughness sub-1 μm. The secondary reflector is tilted by an average 34 $^\circ$ with respect to the focal plane array, and 14 $^\circ$ with respect to the axis of the primary. This, combined with the eccentricity of the secondary allows the telescope to obey the

Dragone-Mizuguchi condition [66], minimizing any cross-polarisation effects, and avoiding degradation of beam quality over what is a relatively large focal plane array. The GRASP9 3-dimensional representation of the model is shown in figure 3.13.

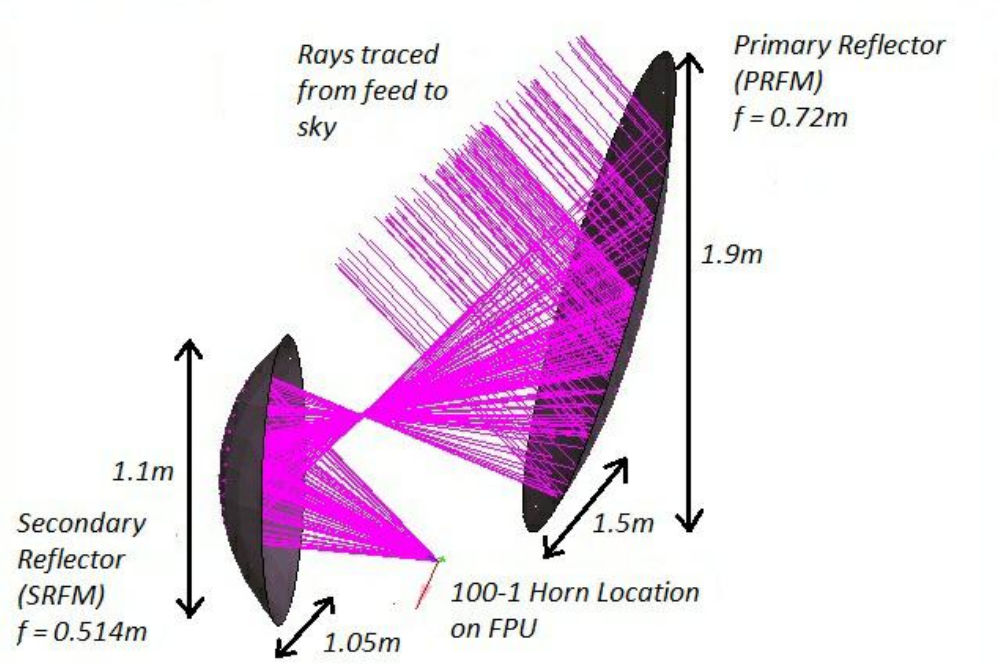

FIGURE 3.13: GRASP9 'Open-GL' visual depiction of the Planck dual reflector system with rays traced from the aperture location of the 100-1 horn location on the FPU. The focus between secondary and primary is indicative of a Gregorian system, but in reality a waist forms here varying in size and location depending on the source location of the FPU.

The 100-GHz channel is of primary use in direct CMB detection. The 100-GHz channels make use of single-moded conical corrugated horns whose beam patterns are highly symmetric around the axis of propagation, as shown by the horn far-field in figure 3.14. Immediately obvious is the vast increase in on-axis intensity afforded by the optimised design of a single-moded horn profile compared with the fundamental Gaussian used in the previous section. The modelling and optimisation of these horns is done using the rigorous electromagnetic mode-matching technique described in Section 2.3.3, which provides diffraction limited performance with very high throughput. The reduced angular diameter of the main beam at 9° FWHM means greater gain and sensitivity, while sidelobes peaking beyond 30° off-axis and at roughly 35dB below peak signifies very little coupling to power away from the main beam, ideal for high-resolution imaging.

The 100-GHz horns are the largest of the HFI, and thus spread over a wider area of the FPU than horns at other bands (see figure 1.18). The beam patterns generated by propagating the aperture field of an ideal 100-GHz horn to the sky from all four FPU locations are shown in figure 3.15. The slight variation from one beam to the next, and

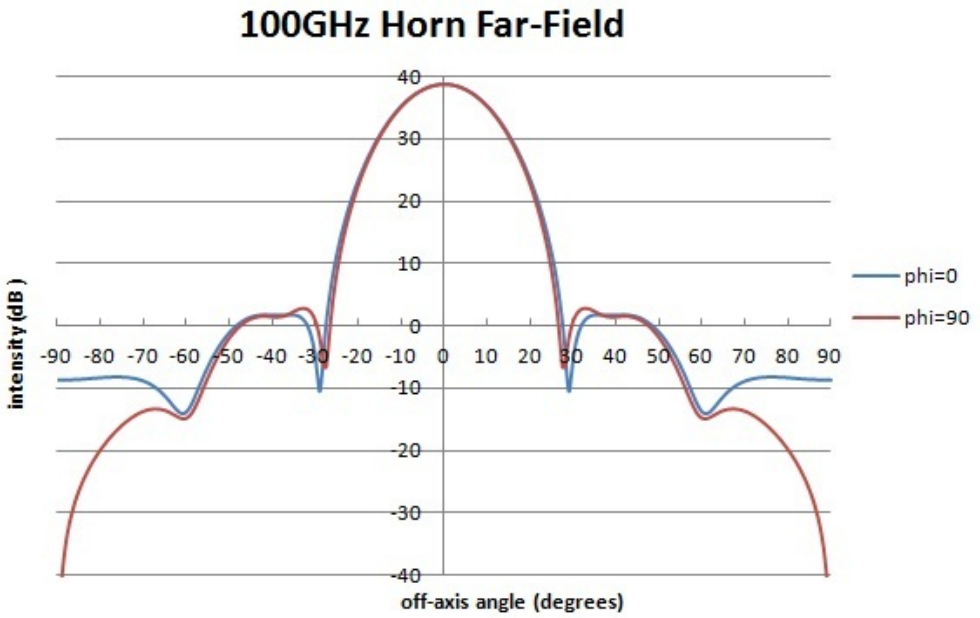

FIGURE 3.14: Far-field beam pattern of a 100-GHz conical corrugated horn, displaying distinct symmetry in orthogonal planes.

the asymmetry between cuts across orthogonal planes of what was a highly circularly symmetric beam indicates the impact on beam properties of horn location in the FPU. The various locations of each detector on the FPU and consequentially the different angles at which they strike the reflector surfaces impact upon beam patterns of the horns. This is most clear for the 100-2 beam, where sidelobes arise asymmetrically at much higher levels than for the other three locations; 30 dB below peak compared with the average 35 dB down. After propagation through the optics of the telescope, the more efficient beam shape generated using corrugated horns means the main beam intensity reaches almost 80 dB, confined within a $15'$ width. The average near-in sidelobe level of well below 40 dB gives these channels their excellent on-axis angular sensitivity and off-axis stray-light rejection.

Having highlighted the various main beam characteristics let us now consider the far sidelobe structure with which the majority of this chapter is concerned. In the single reflector system regions of spillover were highlighted, and shall similarly be considered here. The regions of interest were briefly discussed in chapter 1 and a somewhat similar GRASP9 plot of these regions is shown in figure 3.16

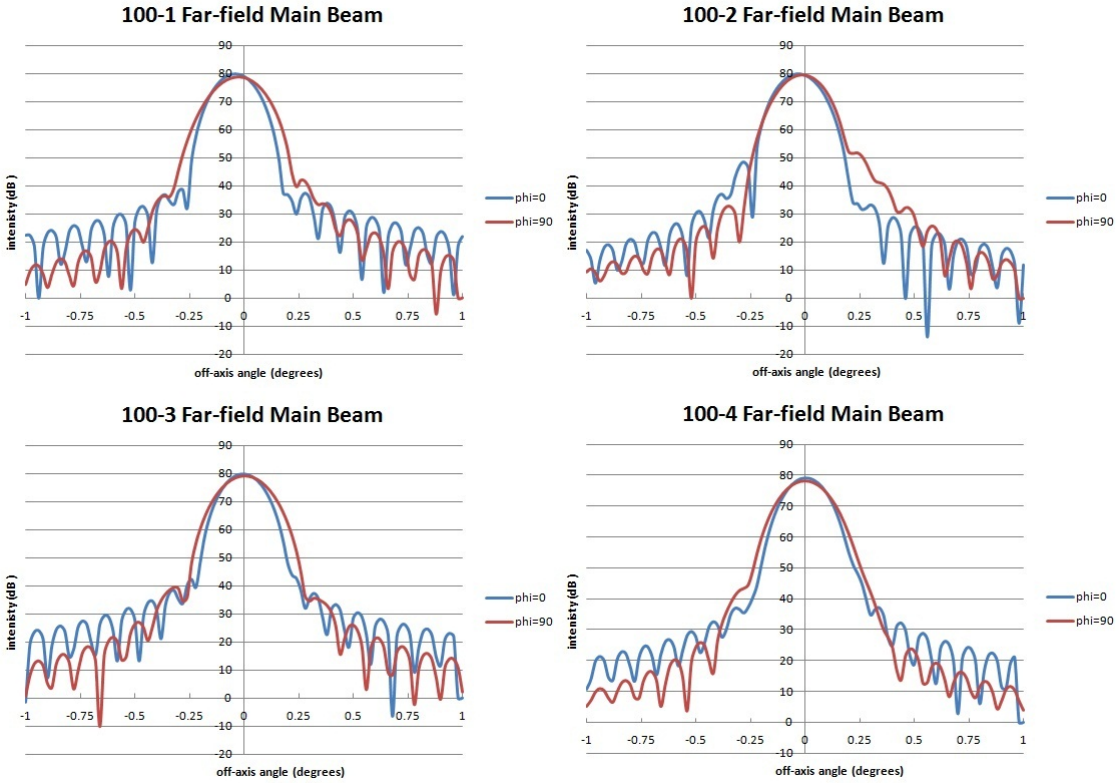

FIGURE 3.15: Orthogonal cuts across the main beam on the sky generated from all four 100 GHz horn locations (FA = -120 dB).

3.2.1 Addition of Relevant Fields

In Chapter 2 and also in Section 3.1 the importance of summing the direct radiation from feed to the reflected field onto the sky for a single reflector system was extensively discussed. Generalising to multi-reflector systems the same principle holds for any PO calculation with GRASP9. Returning to equation 2.8, the total output field from any reflector is a sum of the scattered field and the incident field. Keeping this in mind, a slightly more complicated problem involving the total sky field from a dual reflector system will now be investigated.

A generic PO beam propagation through a dual reflector system entails propagation of radiation from the feed via a spherical wave expansion, and computation of the induced currents on the secondary reflector. The field generated by these currents induces further currents on the primary reflector, and they give rise to the final field on the sky. While for a single reflector system the computation time for current calculations is relatively fast, a dual reflector system sees a vast increase due almost entirely to the coupling of currents between reflectors. The convergence routine in this case can be quite memory-intensive, increasing rapidly with frequency, as the number of PO points required to

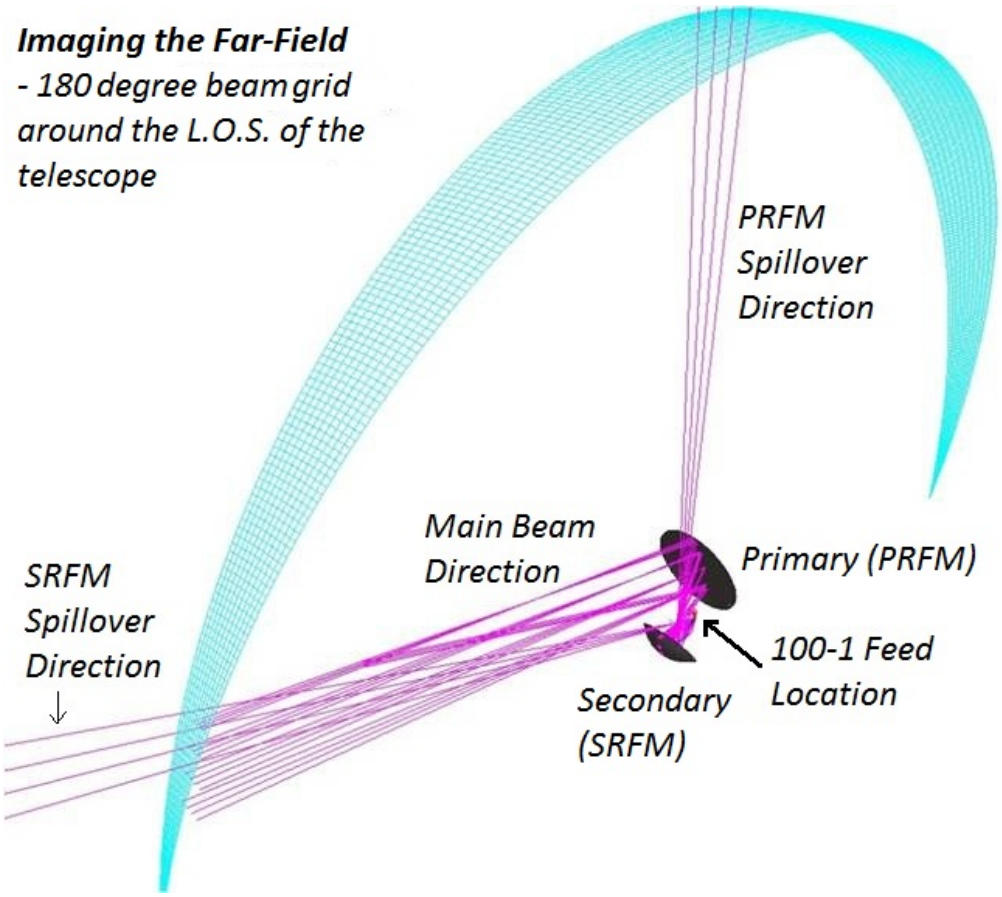

FIGURE 3.16: 3-dimensional 'open-GL' plot of the directions in which spillover from the telescope is most important. Both directions (labelled 'PRFM (Primary) Spillover Direction' and 'SRFM (Secondary) Spillover Direction') lie in the plane of symmetry of the telescope, with spillover in other directions largely irrelevant due to the baffle blockages. Their omission here is to allow better visualisation of the beam propagation in the telescope system.

describe the field on a mirror follows a D/λ relationship (as seen in equation 2.11). In moving between 100 GHz and 1000 GHz, for example, the order of magnitude increase in frequency results in a comparative order of magnitude increase in the values of po1 and po2 required to sample a reflector. The total number of PO points then increases by two orders of magnitude (po1 $\times$ po2). In a dual reflector system where the same will occur on the subsequent reflector, this means the total number of po points which must be calculated across the system increases of the order 10^2. At 100 GHz the routine takes a relatively short amount of time (of the order of an hour on a single CPU with 3 GB of RAM, and the order of minutes on a 66 CPU cluster), however modelling Planck at 857 GHz, the PO routines grows to the order of days in computation time for the reasons outlined above.

Following the routine outlined for this dual reflector system, the resulting field on the sky is shown in figure 3.17. Immediately clear is the resemblance with figure 3.8 in which

a large lobe of power arises far off-axis behind the main beam. In this case, having propagated the field from primary to sky, the lobe spans almost 90 ° and peaks at a non-negligible 45 dB below the main beam. It arises due to inclusion of the incident field from the secondary in the total field generated by the primary, in accordance with equation 2.8, so is solely an artefact of the PO field calculation process. Removing this feature can be achieved in the same manner as for a single reflector system. The field radiated from the secondary is added to that radiated by the primary, cancelling their identical but 180 ° out of phase contributions to the region behind the primary. The result of this summation is shown in figure 3.18.

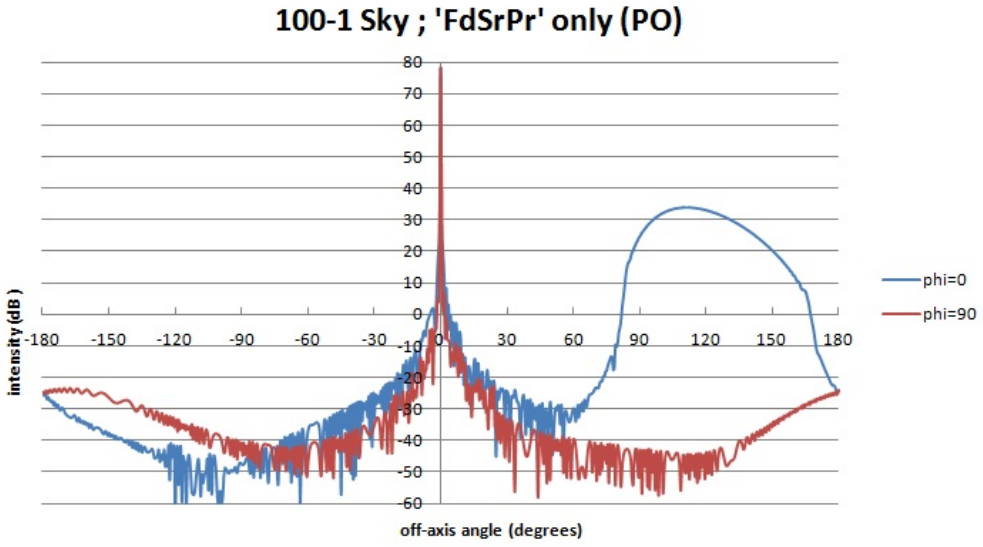

FIGURE 3.17: Orthogonal full sphere cuts through the sky beam at 100 GHz, where phi=0 represents the plane of symmetry of the telescope, and consequentially intersects the regions of greatest spillover. 'FdSrPr' implies use of the field generated by feed radiation ('Fd') reflected on the secondary ('Sr'), and finally reflected on the primary ('Pr') (FA = -120 dB).

Having incorporated the field from the secondary, the broad lobe of power behind the primary disappears completely as expected from our previous single reflector example. More importantly however, the sidelobe due to power from the secondary missing the primary arises in a 15 ° region roughly 70 ° away from the main beam. This is the region of spillover with which this work is primarily concerned, and for the 100-GHz band rises to no more than 70 dB below peak due to the slow divergence of beams at low frequencies. The extremely low level of the FSL's generally, is due to the -120 dB field accuracy which is used for the 100 GHz modelling At 857 GHz there are considerable limitations to the accuracy with which fields can be converged based on the size of the reflectors, and thus a lower field accuracy of 80 dB will be used throughout modelling at 857 GHz. The sidelobe curiously does not have a central peak or gentle taper indicative of beam fall-off, rather a central null. It is in fact the region surrounding the first null in the beam at

roughly 30 ° in figure 3.14, which on reflection from the secondary misses the primary and appears inverted on the sky. The broad angular region containing the original lobe (∼90 ° - 150 °) is replaced by a deep null, indicative of primary blockage of the beam in that direction. A smaller peak appears at almost 180 ° behind the main beam, however this and the majority of the structure beyond -120 ° in figure 3.18 would not arise in reality. Baffling structure, the telescope base and the large instrument housing are all sources of blockage eliminating any potential spillover power in these directions. They are unaccounted for in this model and thus no blockage exists in these directions.

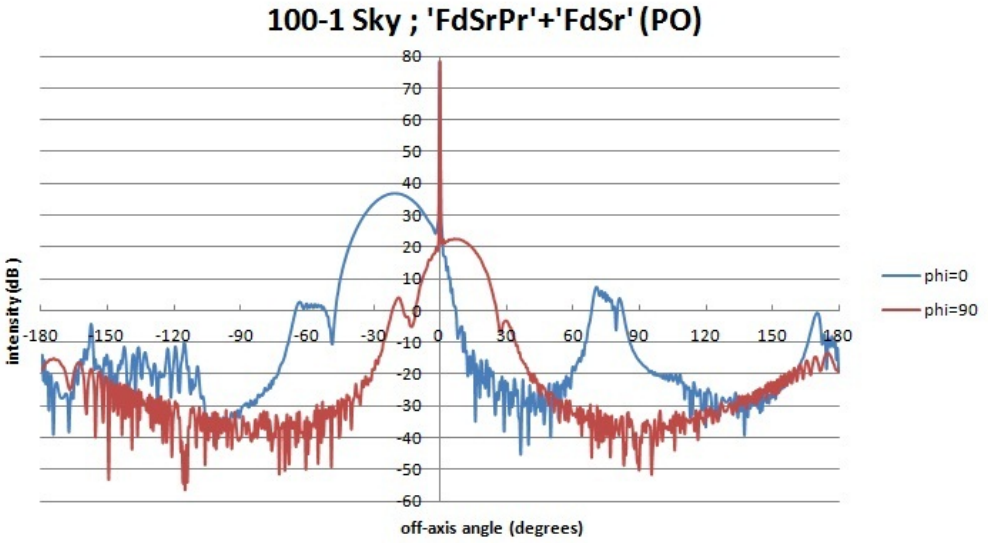

FIGURE 3.18: Orthogonal full sphere cuts through the sky beam at 100 GHz, where phi=0 represents the plane of symmetry of the telescope, and consequentially intersects the regions of greatest spillover. 'FdSr' implies use of the field generated by feed radiation ('Fd') reflected on the secondary ('Sr') (FA = -120 dB).

Though the problem of unwanted power in the rear of the telescope (shown in figure 3.17) has been solved by addition of the field due to the secondary, it is clear in figures 3.18 and 3.19 that further issues have arisen as a consequence. At ϕ=0 ° and ϕ=90 ° a lobe of power can be seen to intersect the main beam, almost equal in peak intensity to the lobe removed by the previous summation. It was shown that the primary field on the sky contained the incident field from the secondary; in a similar manner the total field produced by the secondary (which was propagated to the sky and summed with the primary field) contains the incident field from the feed. This is simply the far-field of the horn, which is easily recognisable on comparison of figures 3.18 and 3.14, and since the 100-1 beam direction is only marginally misaligned with the LOS of the telescope, it appears on the sky slightly off-axis from the main beam.

Removal of this unwanted power is done in a similar manner to before, such that now the total field on the sky is found by summation of total field from the primary, the total

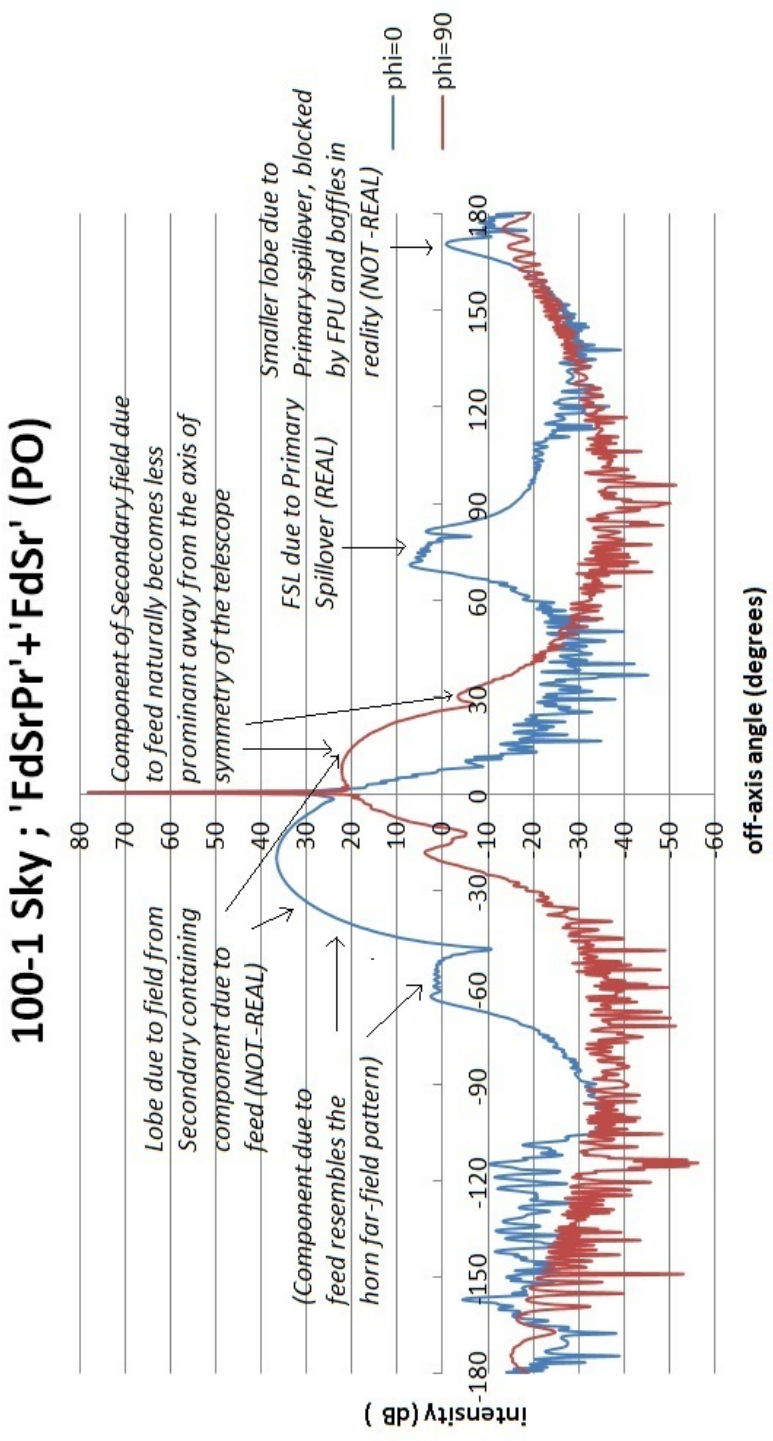

FIGURE 3.19: Replica of figure 3.18 where all areas of interest are labelled for greater clarity. The field component due to the feed becomes obvious on comparison of the beam and sidelobe shape with figure 3.14. This feed component of the secondary field can be seen peaking at 5 ° off-axis in the ϕ=90 ° cut, and 15 dB lower than at ϕ=0 ° due to the shift away from axial symmetry of the telescope, and thus away from the centre of the beam.

field from the secondary, and the aperture field radiated by the feed. The resulting field on the sky is shown in figures 3.20 and 3.21, where it is immediately obvious that all significant lobes of power have been removed from the main beam region and beyond. A small lobe of power rises between 10 ° and 30 ° off-axis, a real effect due to spillover from the secondary mirror. This is the second important region of spillover which must be factored into accurate understanding of the Planck HFI beam features, and its impact on Planck results will be investigated later.

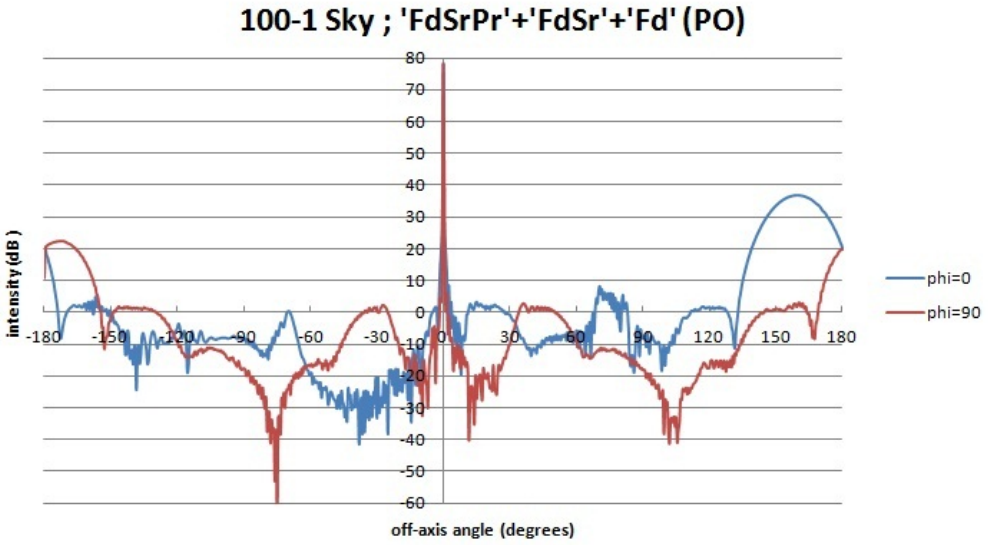

FIGURE 3.20: Orthogonal full sphere cuts through the sky beam at 100 GHz, where ϕ=0 ° is the plane of symmetry of the telescope, and consequentially intersects the regions of greatest spillover (FA = -120 dB).

One anomalous feature arising from summation of the aperture field of the feed occurs almost 180 ° from the main beam, due to the field from the feed being propagated to the sky in opposite directions aligned with the axis of propagation from the feed. This can be verified by comparison with the beam pattern of the 100 GHz feed modelled in figure 3.14, and is an unfortunate hindrance to accurate depiction of the entire 360 ° sky. However as the effect is simply a feature of the GRASP9 code, and in every regard not real, it may be ignored for the purposes of this discussion. A more detailed inspection of the various sidelobe effects visible in figure 3.20 is shown in figure 3.21.

The symmetric nulls either side of the main beam in the ϕ=90 ° cut, represent the blockage due to the secondary reflector, which also contributes to the deep null in the direction of negative off-axis angle for the ϕ=0 ° cut. Again, the gradual increase in power moving beyond the mirrors in negative off-axis angle is an unreal effect negated by realistic payload and baffle blockage. A comparison between the beams at each stage of field addition is shown in figure 3.22. In this figure the beam pattern of the feed can be discerned in the difference between the red and green in the main beam region, and

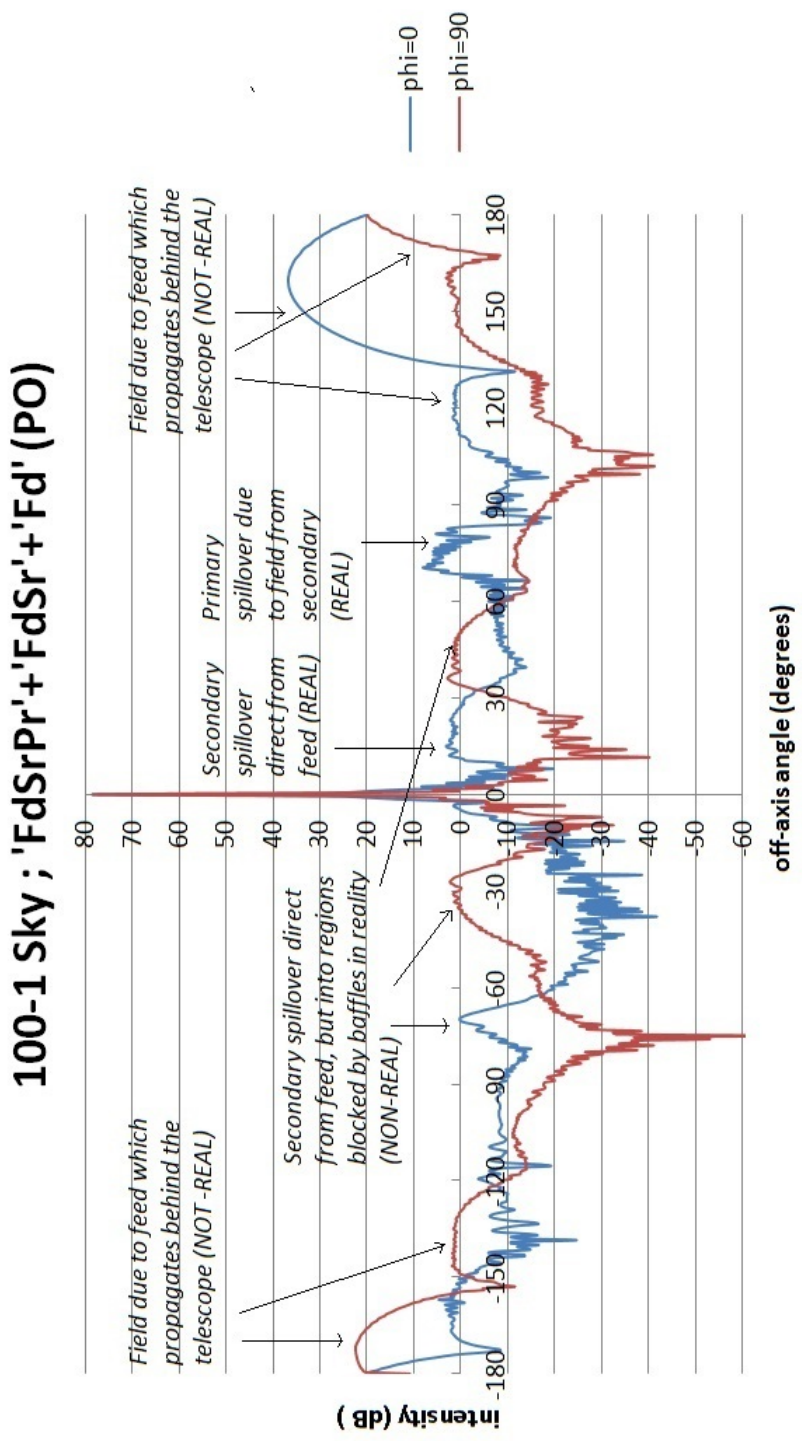

FIGURE 3.21: Replica of figure 3.20 where all areas of interest are labelled for greater clarity. The feed component of the secondary field is completely removed from the main beam and near-in sidelobe region by addition of the 'Fd' field, while at the same time the real lobe due to direct secondary spillover is seen to rise between 10 ° and 30 ° off-axis, and by comparison with the figure 3.19 it can be seen that the lobe takes the shape of the missing first sidelobe of the horn far-field beam pattern.

in the blue plot in the backward direction. Removal of this artefact from the forward direction is of greatest concern for retrieval of accurate far sidelobe levels, so ignoring it in the sidelobe-free backward region of the telescope is permissable.

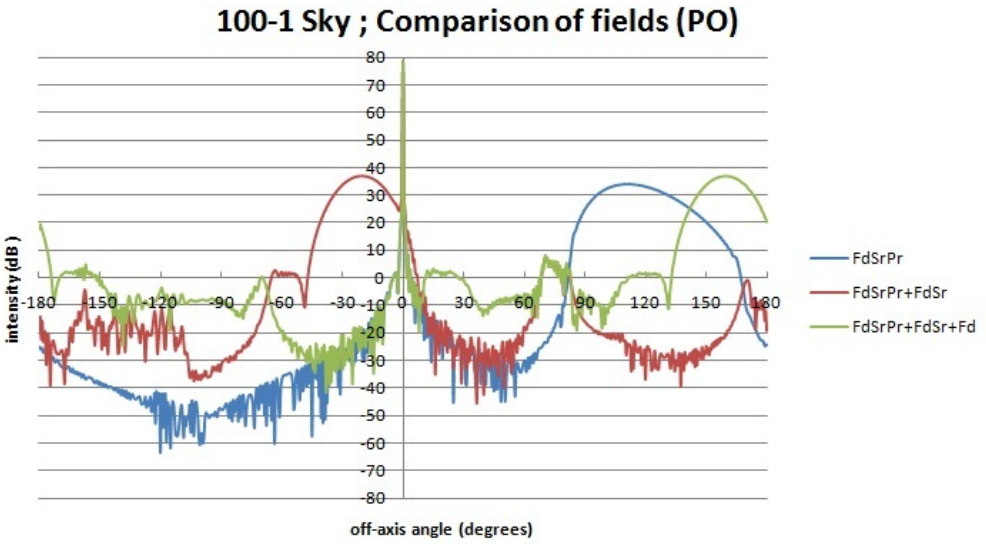

FIGURE 3.22: Cuts through the sky beam at ϕ=0 ° and 100 GHz, highlighting the difference in beam pattern after each field summation (FA = -120 dB).

At this time it is perhaps pertinent to take a brief detour and investigate the convergence procedure implemented by GRASP9. The theory behind the procedure was outlined in section 2.2.1, and described here is an example illustrating its importance to the determination of PO fields obtained on the sky. As explained in section 2.2.1, the objects in the model on which fields are converged are critical to the convergence returning accurate results. This is trivial when one requires simply the main beam from the telescope, as calculated in the dual reflector system above. In that case spillover power is not considered so the radiated feed pattern generates currents on the secondary, which are simply converged on the primary (as this is where all significant power contributing to the main beam will collect). The currents generated on the primary reflector are then converged on the main beam output grid, and the field is calculated. When FSL considerations become important this does not suffice, as the currents generated on the secondary contribute both to the main beam, and the FSL due to primary spillover. In this case the convergence routine must be performed on both the primary reflector and the output grid simultaneously. Failure to do this may prevent the PO calculation from achieving the required field accuracy in regions of importance to the model, as depicted in figure 3.23. While spillover and primary reflector blockage is well described by the field obtained on convergence of the secondary reflector PO, the same cannot be said for the field obtained by convergence on the primary alone. Although spillover is accurately depicted around 70 ° off-axis, the model becomes unreliable in the regions shadowed by the primary and secondary from roughly 130 ° to 300 ° (which depicted as -60 ° in figure

3.23), giving levels even larger than those of the real sidelobe. Similarly, after inclusion of all necessary fields a large extent of the off-axis regions see noise at levels which peak above the real sidelobes, due to the field accuracy not being obtained in these regions. This is shown in figure 3.24.

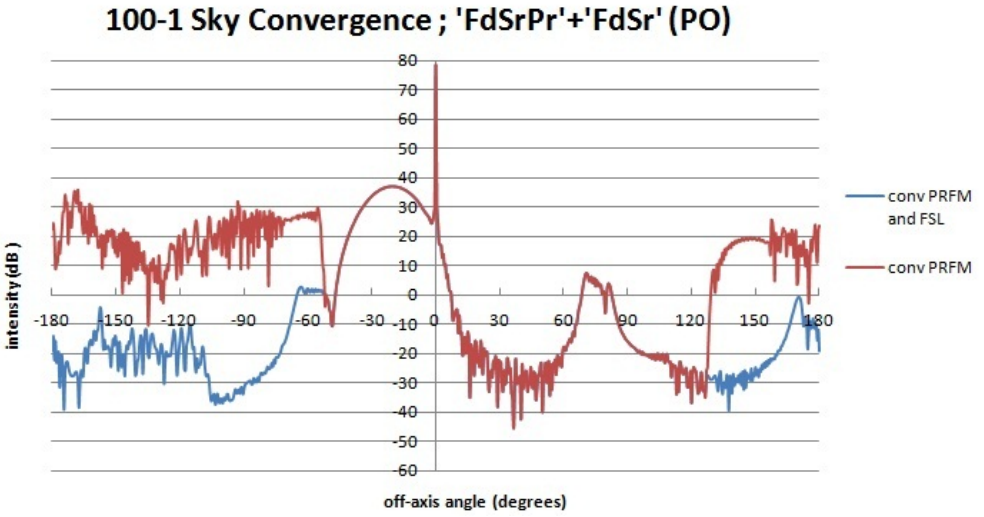

FIGURE 3.23: 360 ° FSL cut along ϕ=0 ° at 100 GHz (originally seen in figure 3.18), which highlights the difference between results when PO convergence is accurately and inaccurately considered.

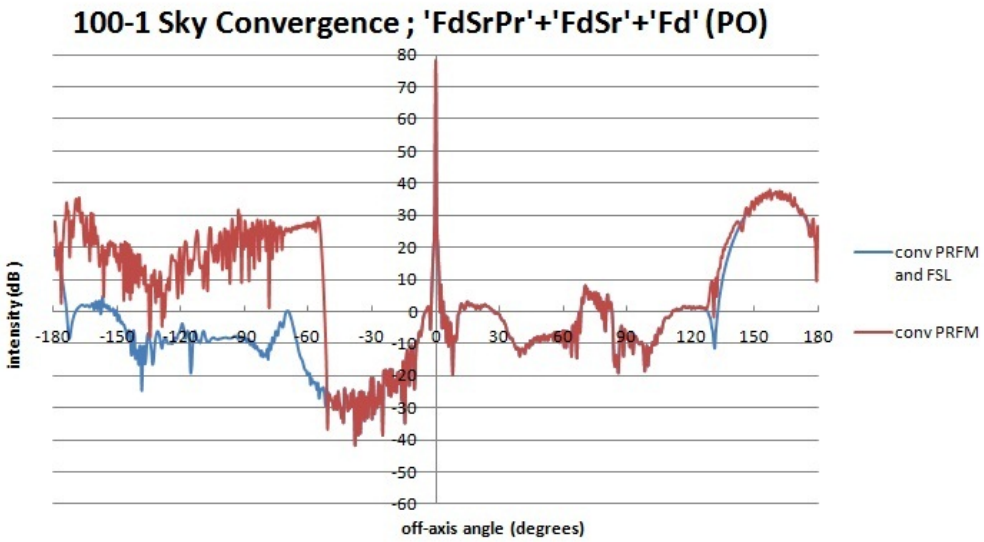

FIGURE 3.24: 360 ° FSL cut along ϕ=0 ° at 100 GHz (the blue trace is the one originally seen in figure 3.20), highlighting the difference between results when PO convergence is accurately and inaccurately considered.

Not considered in any of the above was the inclusion of PTD alongside PO, so for completeness it will be touched on here. Although useful in many regards, for the purposes of depicting the sidelobe levels due to spillover, it adds very little in accuracy. At the same time it adds significantly to computation time, and for this reason it has been omitted. A significant amount of power is in fact diffracted from structural rims

in the system, however it is distributed across large angular scales on the sky and falls to much lower levels than those of the more concentrated regions of direct spillover. This coupled with the diminishing returns from PO-based modelling with increasing reflections means accurately depicting its effect becomes quite difficult. A comparison between fields generated with and without PTD inclusion is shown in figure 3.25 (where in this case convergence of the secondary currents was performed on the primary only, leading to the inaccurate levels in far off-axis regions). As expected there is very little gained by including PTD for the specific task of FSL calculation, however it is worth mentioning here as we will return to more accurately depicting the effects of diffracted power on the sky later using GTD.

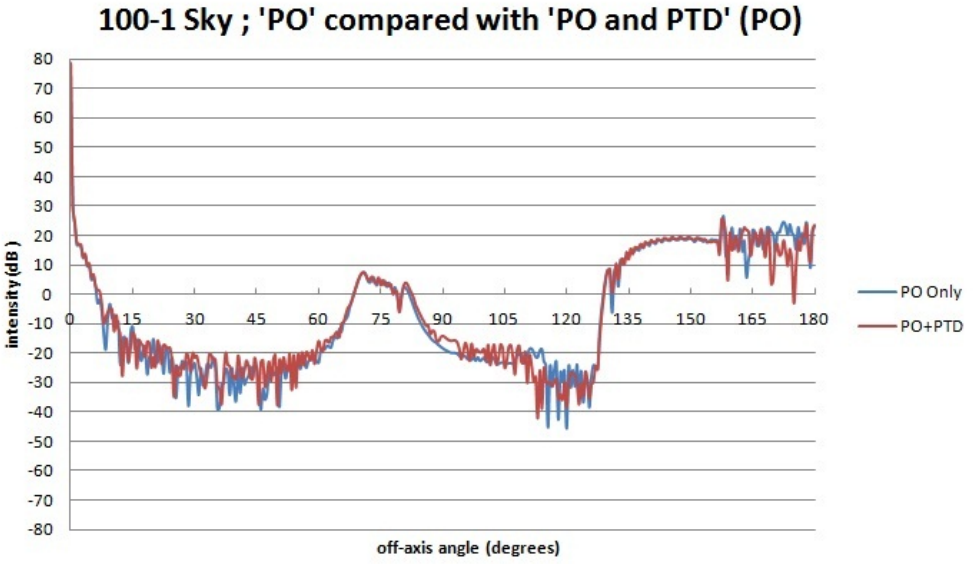

FIGURE 3.25: Comparison between models performed with and without the inclusion of PTD at 100 GHz, where the field is convergence is with respect to the primary only (FA = -120 dB).

3.3 Planck Full Model

The model above was simplified by exclusion of all payload blockages such as the baffle structure surrounding the mirrors, the focal plane unit, the sun shield, and multiple other structural components. Their addition to the model adds significant complexity to an already sizeable dual reflector system, and the greater the number of reflections accounted for in a system, the closer one approaches the point of diminishing returns with regard to accuracy. In the interest of completeness however various baffle contributions to the PO model will now be investigated.

Figure 3.26 displays the full GRASP9 model of the Planck telescope, containing all structural components relevant to modelling of the system, all of which are generated as tabulated surfaces [67], [49]. The baffle surrounding the telescope is split into eight segments, four flat and four curved, labelled baffles A - H in figure 3.26. While each of these will contribute some reflected and diffracted power to the sky, the segments of greatest concern are those which intercept direct spillover from the primary, namely baffles A, G and H. These will thus clearly have the greatest impact on the FSLs, so a check on whether the sidelobe is tapered by their presence was undertaken. It is worth noting then that contributions due to the less relevant baffle segments, as well as any possible diffracted power from components such as the focal plane unit (FPU) and grooves will be ignored, as they will contribute mostly to internal reflections. In a PO model of the system any attempt to incorporate effects due to these components is of little use, since the contributions will be minimal compared with the FSL contribution, and certainly not worth the trade-off in calculation time required to accurately model them. To this end then, only three baffle components will be added to illustrate the diminishing returns from PO with increased number of reflected contributions.

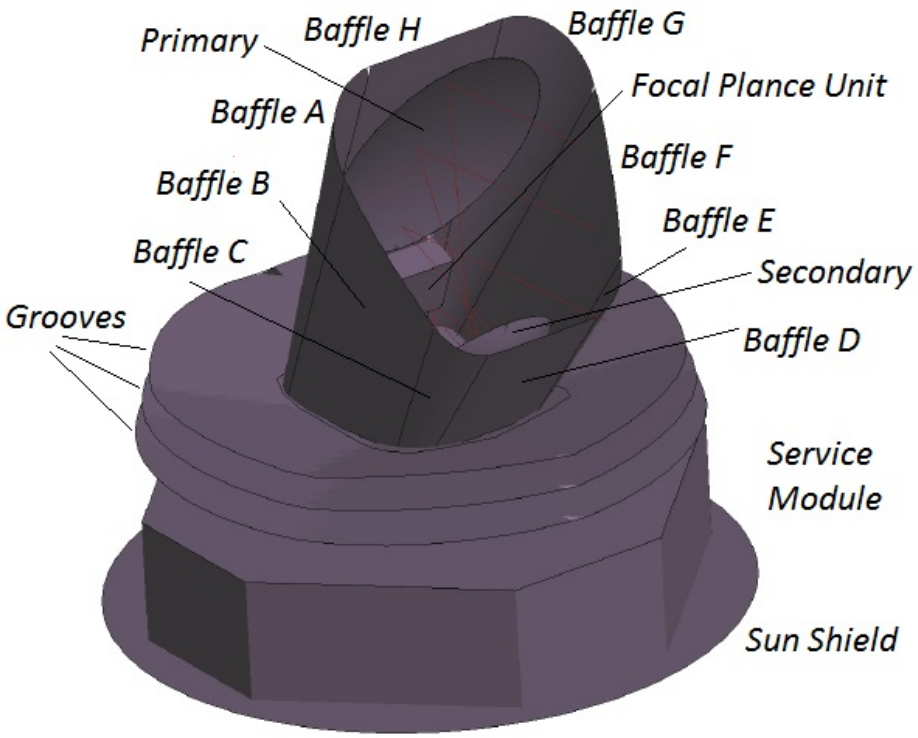

FIGURE 3.26: Complete model of the Planck telescope in GRASP9 with structural components labelled appropriately. Notice the segmentation of the baffle for simplified geometrical descriptions. [68]

3.3.1 PO Analysis

As can be seen from figure 3.27 the beam quality deteriorates rapidly with addition of reflections from each baffle segment. The process of PO field addition, outlined in sections 3.1 and 3.2, is inherently complicated by the input of additional elements to the system. While field additions (resulting in the cancellation of unwanted power) were manageable for the ideal dual reflector system, once further structures such as baffle H are added behind the primary (and in the same direction as the beam from the secondary), adding only the reflected power from the part of the baffle surface not shadowed by the reflector becomes extremely difficult. The only way to do this using PO is outlined below, taking as an example the blockage due to Baffle H;

- Calculate the field at the surface of the baffle segment (which is treated as an ideal smooth reflective surface), arising from currents generated on the secondary (and assuming non-existent primary i.e. no blockage en-route).
- Add to this the field arising from currents generated on the primary (i.e. the imaginary phase-inverted field propagated behind the primary which was outlined previously).
- The cancellation of field components will leave only the field which passed the primary and reached the baffle by spillover, and using this alone currents can be generated on the baffle.
- Generate the field on the sky due to these baffle currents and sum with the total field to take account of power reflected from this segment.

Though rigorous, implementing this procedure on all baffle segments proves extremely time-consuming, and the possibilities of re-reflections in the system remain undetermined. To consider these additional effects would take accurate knowledge of all possible beam paths within the system, which is extremely difficult for a system as complex as Planck. This is the forte of the GO and GTD packages in GRASP9, which accurately account for any number of re-reflections in a system depending on the accuracy required. With this in mind modelling of the blockage and reflection effects of all important structural components will be done using GTD.

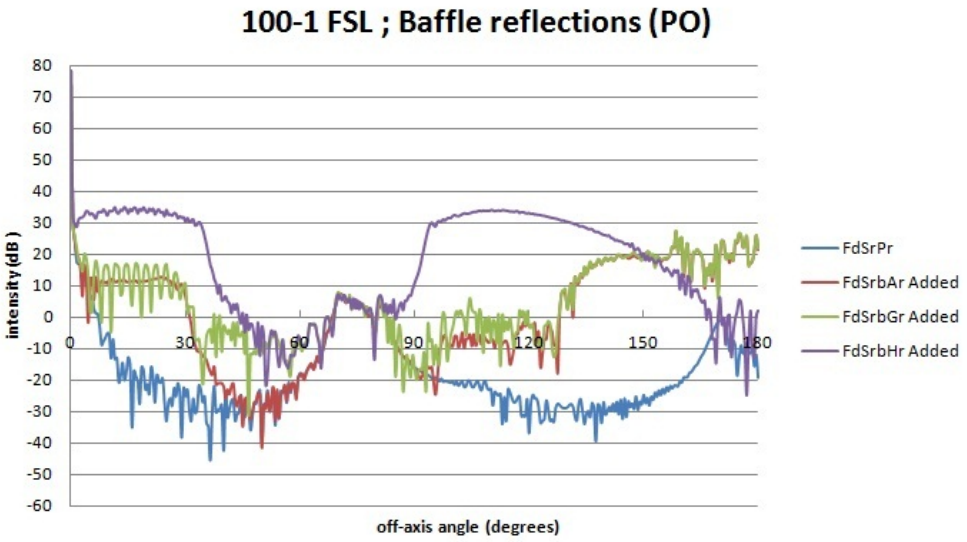

FIGURE 3.27: FSL beams after addition of successive reflections from various baffle segments. 'FdSrPr' represents the beam travelling along the path Feed ('Fd') → Secondary reflection ('Sr') → Primary reflection ('Pr'). Similarly 'FdSrbAr' represents the beam travelling along the path Feed ('Fd') → Secondary reflection ('Sr') → baffle A reflection ('bAr'), and subsequent baffle segments are denoted 'bGr' and 'bHr' (FA = -80 dB).

3.3.2 GTD Analysis

While multiple reflections and blockages in the full Planck system prove problematic with PO modelling, the GTD regime allows full account to be taken of such factors. A 'Multi-GTD' object in GRASP9 requiring operating frequency, operating feed, and any number of scatterers from which power will be reflected or diffracted can fully describe the field on the sky. This is done by referencing all objects in the project file as potential blockages, such that when a GTD calculation is performed any candidate ray, traced from source to sky, can be disposed of on interaction with a blocking object. In this manner any number of ray paths can be defined, and rays traced along these paths will reach the sky only if they are not intercepted by a blockage.

The gradual summation of beams propagated along various ray paths is shown below in figure 3.28. The first plot shows the gradual shaping of the FSL due to spillover from the primary. It occurs at the correct angular distance from the main beam, however it reaches almost 30 dB at the peak, 20 dB greater than that calculated using PO. Though PO failed with increased complexity in the system, it was shown to be stable and accurate in predicting the FSL levels due to spillover. GTD encounters issues accurately predicting the FSL in this case. However, this is due to theoretical instability in GTD implementation at the given frequency. The sharp sidelobe feature from roughly 80 ° to 90 ° arises from a caustic due to reflections from the primary reflector edge, leading

to inaccurate representation of the FSL level in that region. At the higher frequency channels of Planck HFI GTD provides a much more accurate description of all off-axis features as shall be seen later.

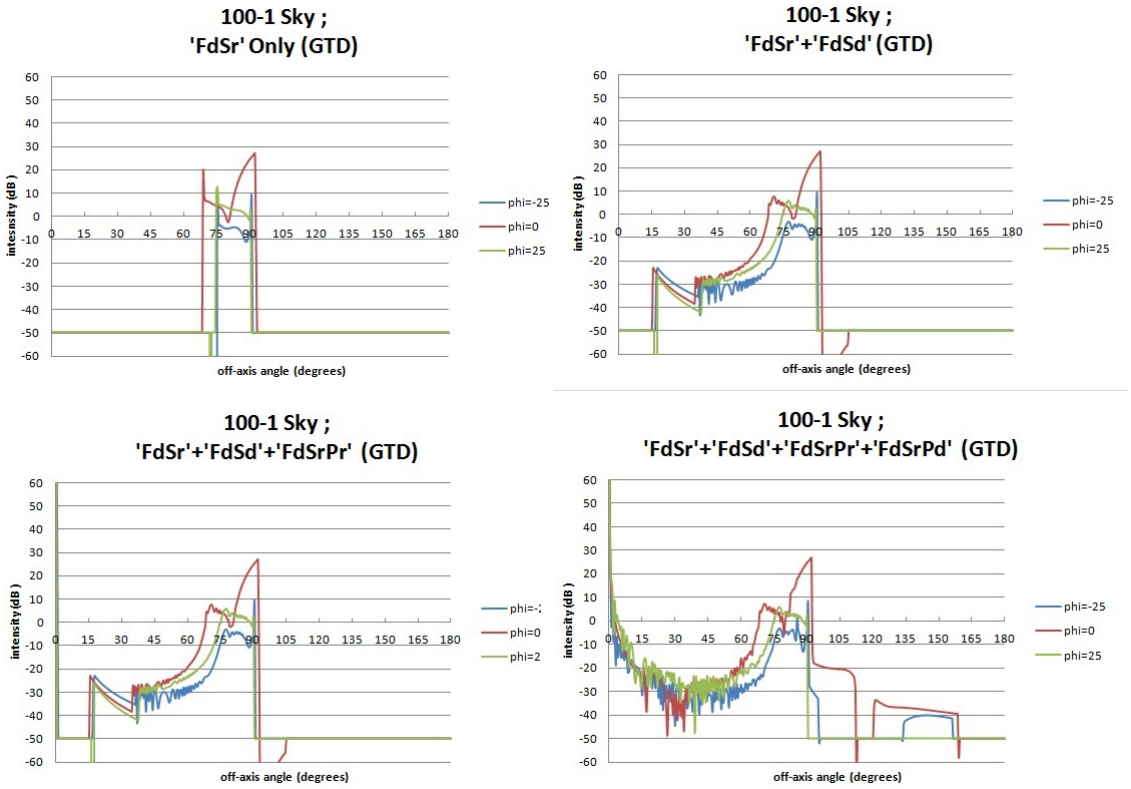

FIGURE 3.28: Summation of fields from various ray paths contributing to the overall field on the sky, successfully incorporating the spillover and blockages which contribute to the FSL structure seen at large angles. The ray paths included are those from the feed reflected on the secondary ('FdSr'), diffracted on the secondary ('FdSd'), reflected on secondary and then primary ('FdSrPr') and diffracted on primary ('FdSrPd'). In regions where no power was modelled the lower limit threshold on dB power was set to -50 dB.

A comparison between the PO and GTD models of the FSL region is shown in figure 3.29. It can be seen that the benefit from use of PO over GTD in the near-in regions is somewhat counterbalanced by PO's inability to correctly account for blockages in regions of the sky shadowed from the reflectors.

3.3.3 Planck 353-GHz Band Modelling

Until now we have considered the modelling of single-moded systems, requiring just one coherent field to describe the aperture field of our feed horn. In the case of the three coherent frequency bands of Planck (100, 143, 217-GHz) this field can be propagated to the sky and the field at any point recovered. 353-GHz is generally considered a coherent

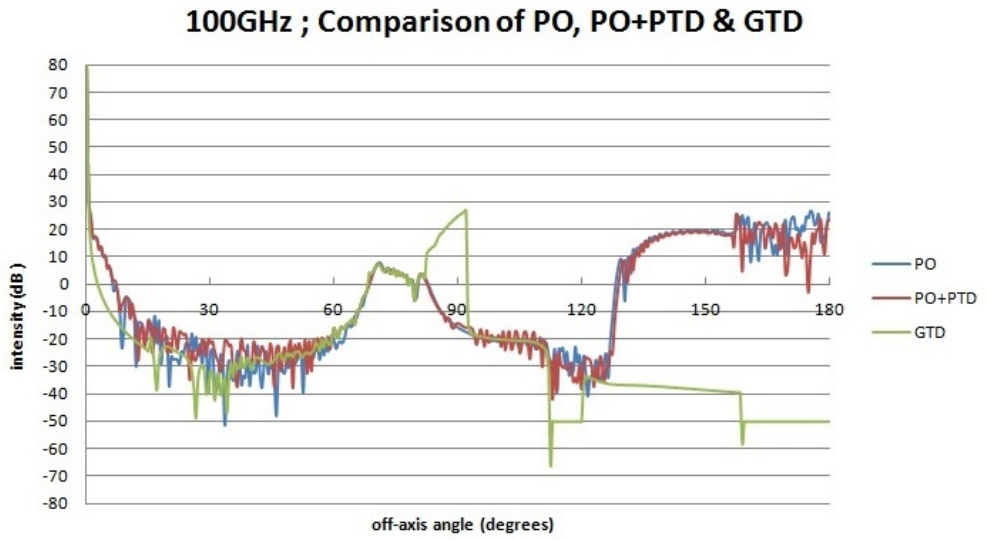

FIGURE 3.29: Comparison between PO and GTD in modelling of the FSL structure of the 100-GHz horn beam on the sky. The sharp increase in power beyond 80° is due to instability in the GTD technique at low frequencies, where PO does a better job of modelling this lobe correctly. The large lobe beyond 120° in the PO and PO+PTD traces (shown originally in figure 3.25) arises from inaccurate field calculation in the region behind the primary . The primary acts as a blockage to this region, modelled much more effectively by GTD.

band also, however it has been shown [69] that modal cut-on occurs at the highest frequency end of the band due to the back-to-back set-up of the horns and cavities. The band-centre 353-GHz aperture field can be simply described by the fundamental HE_{11} mode and its orthogonal, and the aperture modal fields generated using the SCATTER software (see Section 2.3.3) are shown in figure 3.30, where the amplitude patterns in orthogonal polarisations are shown for both the HE_{11} mode and its orthogonal. The co-polar beam is dominated by the hybrid mode, with the orthogonal mode contributing contributing very little power.

Starting at the focal plane location of the 353-1 horn in the GRASP9 model of the Planck system (see figure 1.18), the simulated main beam and FSL structure is shown in figure 3.31, where due to the more central location of the 353-horns on the focal plane, spillover from the primary mirror is minimal, rising no higher than 70 dB below the peak. To speed up simulations the spillover passed the secondary is not included here as it was for the 100-GHz model, nor are the secondary reflector currents converged simultaneously on the output grid and primary. For this reason a significant amount of signal is simulated beyond 130 ° in figure 3.31 which in reality does not exist due to blockage from the primary, so can be ignored.

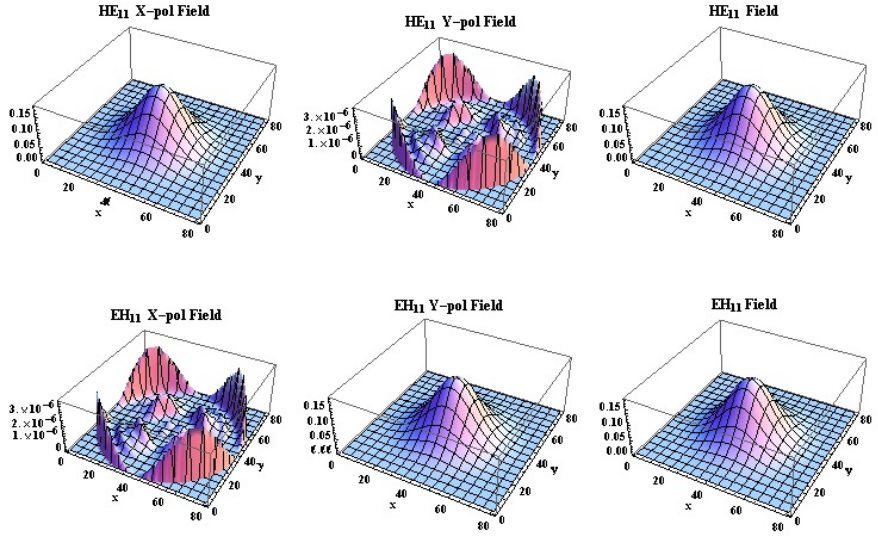

FIGURE 3.30: Aperture field amplitude profiles of both HE_{11} and it's orthogonal mode for the profiled 353-GHz horns of the Planck HFI at the band centre.

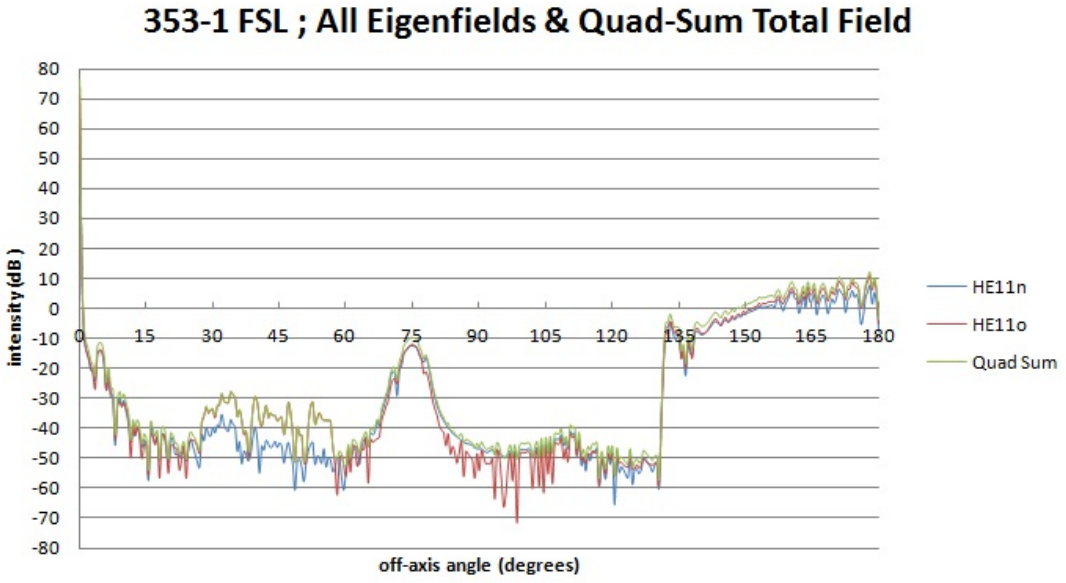

FIGURE 3.31: Cut around the sphere in the direction of greatest Primary spillover for the 353-GHz sky beam, where two orthogonal modes are summed to fully describe the sidelobe level expected of the 353-GHz band.

3.4 Multi-Moded Model

Moving to higher frequency channels, the HFI horns become multi-moded, with more than just the fundamental HE_{11} mode excited in the horn structure. Each higher order mode generated in the horn will behave differently, however none of the higher order modes will couple power to each other. Rather, they remain completely incoherent with respect to each other, and the total aperture field becomes an incoherent combination

of multiple independent modal fields. Each of these so-called 'eigenfields' will also propagate independently through the telescope, so must be considered in isolation. This means that rather than propagating one field to the sky when modelling, one must now propagate multiple fields, and recombine them in quadrature on the sky to determine the correct field level at any point. One obvious issue with this is the time required for field calculation, which increases with every additional eigenfield to be considered. This becomes more significant a problem at the highest frequency channel of the Planck HFI. As detector horns become more multi-moded the number of eigenfields required to define a given aperture field increases quickly. This coupled with an increased integration time for PO/GTD estimates due to higher sampling (which depends on frequency) makes modelling quite difficult. With this in mind we will now consider the appropriate procedure for modelling multi-moded systems, briefly investigating the lowest multi-moded channel, 353-GHz, after which we will move onto a full model of the 857-GHz sky.

3.4.1 Planck 857-GHz Band Modelling

Due to the over-moded nature of the feed horns, and the greater computation time required at higher frequencies, the majority of the time taken in GRASP9 modelling of the Planck system was spent around 857 GHz. This is the highest frequency band of HFI, and it is with this that we will now concern ourselves. Initially a model was attempted with an operating frequency of 860 GHz, as the best estimation of the full sky beams would be made by observation of the effects at band centre. Early on, however, it became quite obvious that this would be a sub-optimal approach, and a frequency of 730 GHz (the lower end of the band) was decided upon. The reason for this was the lengthy integration time required for calculation of currents at these frequencies using a PO approach, due to the size of the telescope structures compared to wavelength. Taking the lowest possible frequency in the band is therefore an advantage. As previously mentioned the most time consuming calculation in a PO approach of a dual-reflector system is that done in taking the currents generated on the secondary mirror and, from there, generating new currents on the larger primary mirror. The first task is the convergence of the currents integral, during which the number of PO points to be taken is estimated. Then the currents must be calculated at each point.

In general the PO integral is easiest to calculate for focused reflectors and close to the main lobe because the integrand in the PO integral is then a slowly varying function of the integration variables. As the observation point moves into the side-lobe region the integrand becomes increasingly oscillatory which requires a finer integration grid resulting in longer computation time. As the purpose of this chapter is far sidelobe

modelling, it should be immediately obvious that this will have a profound impact on our simulations. The requirement of a full 360 ° sky field means that the integration time will be appreciably lengthened, without yet considering the finer sampling required across all surfaces at higher frequencies. For this reason many of the figures which appear subsequent to this introduction are in fact single beam cuts across the sky, rather than being taken from a full 4π sky field description. Taking a single beam cut around the sphere allows for a significant saving in time, while at the same time returning enough information to qualitatively assess the model. This was done by taking a cut which passed precisely through the centre of both regions of greatest axial spillover, thus providing a decent indication of the integrity of the model without having to commit to a full 4π simulation.

At 860 GHz, the coupling of PO points from the feed to secondary is relatively straightforward; taking a 101×101 PO point description of the aperture field, this will quickly couple to ≈ 1 million PO points converged on the secondary, based on equation 2.11, and a task time ≈ 3 to 4 minutes is observed. Since the larger primary requires a greater number of points for the same level of sampling, after propagation the secondary field must now be coupled to upwards of 6 million points on the primary. This is a truly exhaustive calculation which takes up to 10 days to complete on a cluster of 66 processors, built in-house for the purposes of memory intensive simulations such as these. On a single processer the simulation would be next to impossible, as when the author attempted this first the simulation ran for a week without converging currents.

So we have seen how the PO integration time, while already lengthy, can be made prohibitive by requirement of modelling away from the main lobe. This issue is compounded by another, which is the multi-moded nature of the horns used at these frequencies. At 860 GHz, 10 hybrid modes and their orthogonal counterparts are present at the aperture, increasing towards the top of the band as further modes switch on, as shown in figure 3.32. This equates to 20 incoherent aperture fields, each of which must prorogate in isolation through the system to the sky, at which point they will be combined. Given the already lengthy computation time required for the generation of even one field on the sky, the added requirement for 20 individual fields meant that modelling at this frequency was simply too difficult.

Instead 730 GHz was chosen, where only 5 hybrid modes (and their orthogonal modes) exist at the aperture (due to most of the higher order modes not yet having switched on), meaning only half the number of fields, and a lower integration time due to the lower frequency. Figure 3.33 shows the number of modes in existence at each frequency across the 857 GHz band, where the total power contained in all modal fields is included

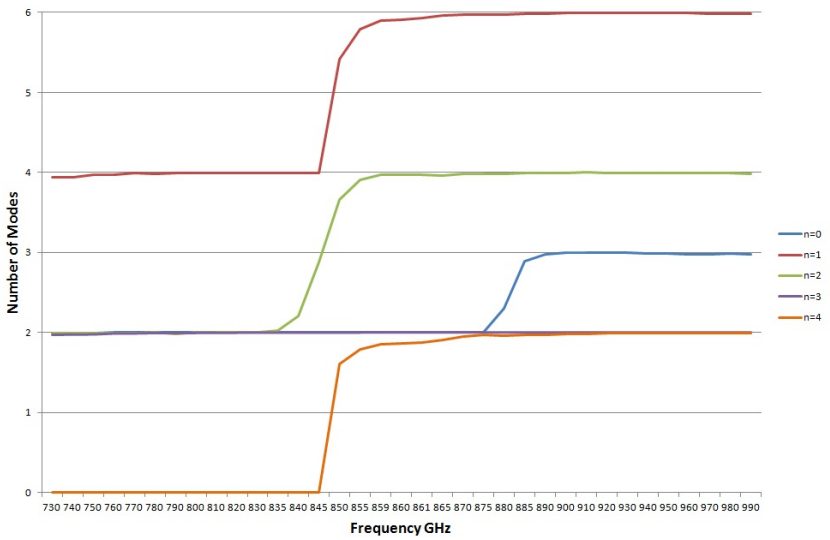

FIGURE 3.32: Plot of the cut-on of modes at each azimuthal order as a function of frequency across the band. Clearly visible are points where modes spontaneously cut-off and on and again, unfortunately due to numerical instability in the software. (Credit Ian McAuley, NUIM)

to highlight how much more power can be coupled to the detectors at they approach maximum efficiency at higher frequency. One might notice immediately that 6 independent modes seem to be present at the lowest end of the band, rather than the 5 previously stated. Each mode at n=0 gives rise to a polarised field in one direction only, dependent on whether the mode-number is odd or even. This is due to cancellation of orthogonal oscillatory terms in the modal equations (see Chapter 2). The odd and even numbered n=0 modes which do exist at 730 GHz (HE_{01}, and HE_{02}) are essentially orthogonal representations of the same modal field, and can be considered as such. This being the case the zero azimuthal order contains two modal fields which can be considered orthogonal, and which must be combined with the other four modes and their orthogonals to generate the total field of 10 modes.

The field amplitude profiles of all ten modes existing at the aperture of an ideal unaltered 857 GHz horn operating at 730 GHz are shown in figure 3.34. The fundamental HE_{11} mode and its orthogonal contribute all of the main beam power, while all higher order modes contain a central null, and provide greater weighting to sidelobe structure. In altered horns the shape of the modes can be quite divergent from the simple symmetric shapes seen in figure 3.34, due to the impact of corrugation imperfections on modal excitation. An example of this is given in figure 3.36, where although the resemblance in profile is clear, the rotational symmetry of the field has deteriorated.

	n=0			n=1			n=2		n=3	n=4	
Freq	HE01	HE02	HE03	HE11	HE12	HE13	HE21	HE22	HE31	HE41	Total Power
730	0.997	0.995		0.9996	0.9633		0.998		0.945		9.8038
740	0.999	0.993		1	0.972		0.9953		0.986		9.8986
750	0.999	0.998		1	0.9875		0.9929		0.9871		9.932
760	0.999	0.999		1	0.9886		0.9923		0.9929		9.9456
770	0.9997	0.9866		1	0.9946		0.9917		0.9928		9.9445
780	0.9994	0.9984		1	0.9938		0.9994		0.9956		9.9754
790	0.9996	0.9994		0.9999	0.9963		0.9993		0.9955		9.981
800	0.9998	0.9997		0.9978	0.992		0.9869		0.9904		9.9337
810	0.9999	0.9998		1	0.9967		0.9877		0.926		9.8205
820	0.9999	0.9998		1	0.9992		0.9998		0.9917		9.9811
830	0.9999	0.9855		0.9999	0.9989		0.9906		0.9623		9.8888
840	0.9998	0.988		0.9998	0.9986		0.9999	0.103	0.9979		10.1862
850	0.9977	0.9914		0.9999	0.999	0.72	0.9999	0.83	0.9893	0.8062	14.6777
860	1	0.9999		1	0.9998	0.9557	0.9838		0.9989	0.8572	13.5907
870	1	0.9957		0.9999	0.9923	0.9848	0.9995	0.9775	0.9872	0.9747	15.8275
880	1	0.9998	0.3012	0.9999	0.9996	0.9885	0.9988	0.9812	0.999	0.9831	16.2012
890	0.9999	0.9998	0.9811	1	0.9996	0.9936	0.9995	0.9925	0.9994	0.9857	16.9214
900	0.9997	0.9991	0.9796	0.9994	0.9993	0.9943	1	0.9982	0.9857	0.9326	16.7974
910	0.9998	0.9997	0.9977	1	0.9991	0.9975	1	0.9998	0.9981	0.9905	16.9672
920	0.9997	0.9986	0.9898	0.9999	0.9973	0.9982	0.9997	0.9853	0.9998	0.9931	16.9347
930	0.9999	0.9999	0.994	0.996	0.9931	0.9325	0.9997	0.9984	0.9999	0.9965	16.826
940	0.9999	0.9995	0.9902	0.9999	0.9987	0.998	0.9997	0.9995	0.9999	0.9583	16.8976
950	0.9999	0.9996	0.9875	0.9999	0.9983	0.9982	0.9995	0.9981	0.9999	0.9975	16.9698
960	0.9999	0.999	0.9823	0.9999	0.9983	0.9966	1	0.9959	1	0.9978	16.9582
970	0.9999	0.9895	0.9728	0.9998	0.9979	0.9953	0.9998	0.9959	0.9983	0.9982	16.9326
980	0.9998	0.9996	0.9841	0.9999	0.9985	0.9948	0.9999	0.9966	1	0.9988	16.9605
990	0.9999	0.9998	0.9816	0.9998	0.999	0.9906	0.9998	0.9937	0.9999	0.9987	16.9443

FIGURE 3.33: Table outlining the percentage of power retained by all modes and the points at which they switch on toward higher frequency. (Credit Ian McAuley, NUIM)

Effects of Manufacturing Tolerances

To simulate the FSL observed by a detector operating at 730 GHz, one must prorogate the constituent incoherent fields of the horn to the sky. This, however, may not give us a complete understanding of telescope behaviour. If the unexpected power seen in off-axis measurements (outlined in Section 1.6.4) cannot be accounted for by assuming a perfectly symmetric horn, then it stands to reason that internal defects may be the root cause.

The manufacture of corrugated horns is most commonly done by electroforming, and it was in this manner that the Planck HFI horns were manufactured. In this technique an aluminium mandrel is milled in the negative shape of the horn design, and is then placed into an electrolytic bath, wherein copper electrochemically deposits onto the mandrel over time. The aluminium mandrel is then dissolved leaving the completed copper horn antenna, which is thoroughly washed of any residual aluminium by the chemical etching process. Although the milling process is very precise in generating the negative of the horn, the electroplating process cannot boast the same precision. It is almost impossible to distribute the copper evenly across the mandrel, and although not usually an issue, when the corrugation (also labelled 'fin' in some diagrams to follow) size becomes extremely small precision becomes even more important. The potential for unformed or malformed corrugation fins becomes a lot higher as a result.

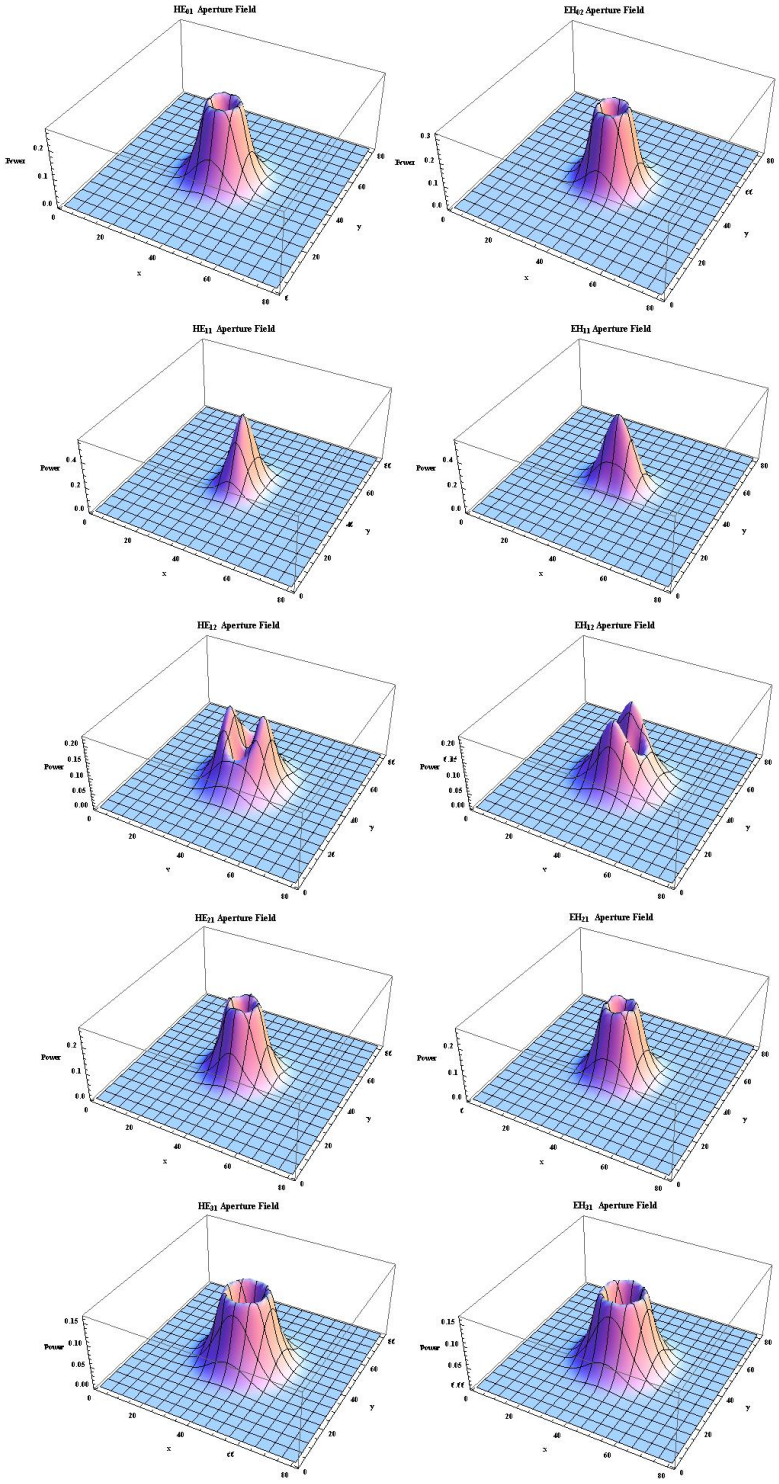

FIGURE 3.34: Amplitude profiles of all 5 modes excited at 730 GHz (left) and their orthogonal modes (right).

Another issue surrounds the chemical etching process after the mandrel has been dissolved. Again, the kind of precision attained during etching cannot be obtained here, and not all of the metal from the dissolved mandrel may be properly removed. If this occurs corrugations can be left partially or even completely filled, drastically affecting

the performance of the horn. One region of the horn which is notoriously difficult to etch is the throat (see figure 3.35), which unfortunately is also the most important region for multi-moded applications, as it is in this region, generally, that all higher order modes are excited. Should etching fail to remove all material from the corrugation depths it can have a detrimental impact on beam quality, as not all of the power input at the back of the horn will couple to higher order modes correctly as it passes through the horn. The ultimate result of this is a less efficient beam where the higher order modal fields which contribute mostly in off-axis sidelobe regions become less well behaved than under ideal circumstances. Thus, sidelobes rise, and contribute more power to regions of spillover from the telescope. To investigate the effects of this, three different horn geometries were created, one ideal horn geometry and two containing plausible defects in a region of the horn which is notoriously difficult to etch perfectly. These two would have the greatest effect on sidelobe level, but at the same allow for the likelihood of these defects going undetected in pre-launch testing (see Section 5.1). The altered horns had five corrugations filled in different sections of the horn throat, imitating a smooth-walled horn across a distance of appreciable length compared to wavelength. This causes the internal fields to behave quite differently, resulting in an impedance mismatch whereby waveguide modes will not efficiently couple power to a parent hybrid mode. This has a serious effect on the overall structure of a hybrid mode as it propagates in the horn, and figure 3.36 highlights the deterioration in beam quality at the aperture as a result of this.

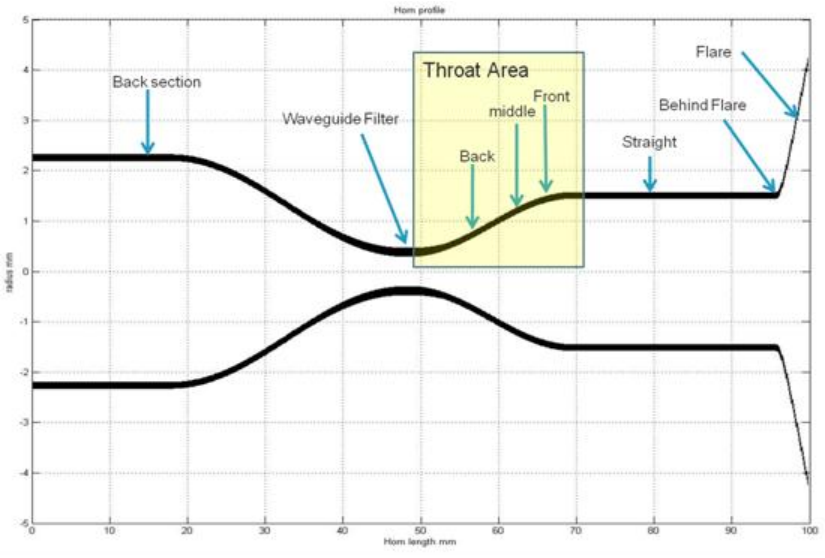

FIGURE 3.35: Profile of the 857 GHz back-to-back horn. Regions in which corrugations were filled or removed to test the horn response are highlighted [69].

The two altered horns were carefully chosen such that the alterations would have the most significant effect on the FSL levels, but would at the same time prove quite plausible in reality. Two potential issues with the horn manufacturing were tested by simulation.

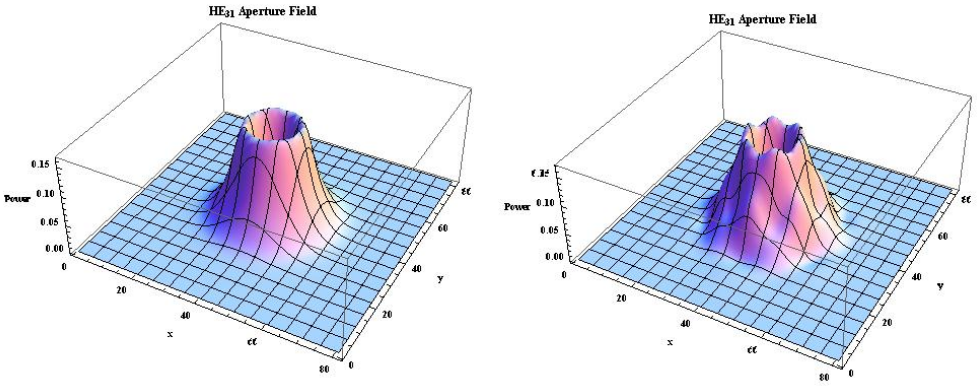

FIGURE 3.36: Comparison between the amplitude profiles of the HE31 mode at the aperture for a perfect unaltered horn (left) and a horn with five corrugations filled in the back of the throat section (right).

The first issue surrounded the size of the corrugated fins etched inside the horn. As the frequency gets higher and the wavelength shorter, the width of the corrugations must be reduced also. In general, three to four corrugations per wavelength is sufficient for the horn to operate optimally. At 857 GHz, equivalent to 0.35 mm wavelength, it becomes clear that these corrugations must be very thin indeed, of the order of 100 microns in width. This pushes the limits of manufacturing capabilities, and although they can be successfully etched, the long term integrity of the wafer-thin fins is still unknown. One potential issue, then, was that some of these fragile fins may have broken or become dislodged in launch due to intense strain and vibration. To model this, various numbers of corrugations were removed from the simulated horn geometries, at various locations throughout the horn, noting their effect on beam quality produced by SCATTER. It was found that removing corrugations from the flare and profiled sections had the least impact on beam quality, while removing them from regions close to the waveguide, the throat specifically, had the largest effect. The effects on beam quality after the removal of various number of corrugations from the throat section is shown in figure 3.37.

Another potential issue surrounded the etching process is the possibility of some residual aluminium remaining lodged in the corrugations as mentioned previously. Though inspections of the horns are always performed after etching, the size of the 857-GHz horns is extremely limiting in this regard. Inspection of the near-aperture corrugations are easily performed, however it is difficult to check regions such as the throat, and incomplete scraping of a region such as this would have an effect on beam quality. This was tested in a similar manner to before, by filling different numbers of corrugations at various locations throughout the horn, and measuring the far-fields using SCATTER, as shown in figure 3.38. Again it was found that the most detrimental effect on beam quality was obtained by filling in the throat, which greatly impacted sidelobe levels of

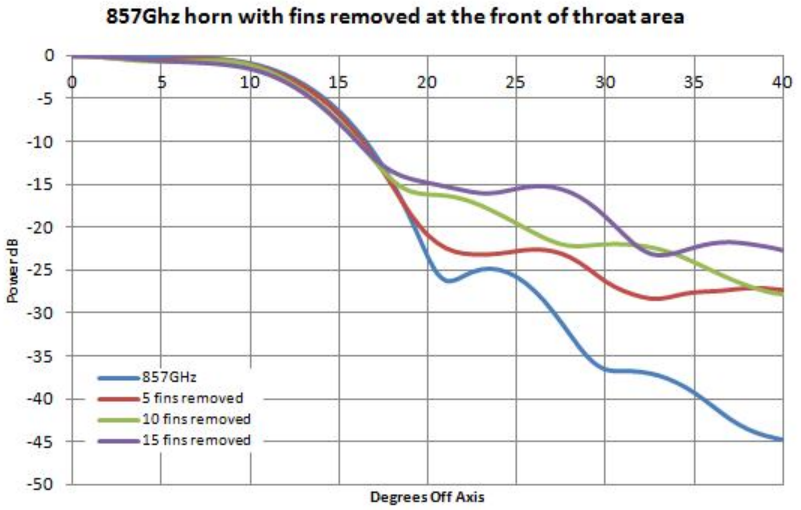

FIGURE 3.37: Comparison between the beam patterns of horns with various numbers of corrugations removed from the front of the throat section [69].

the far-field beam. Crucially, filling of corrugations in the throat had a more detrimental effect than removing corrugations in the same location. Thus it was decided that the two altered horns picked for the full system model would have corrugations filled, as they would have a more profound effect on beam quality.

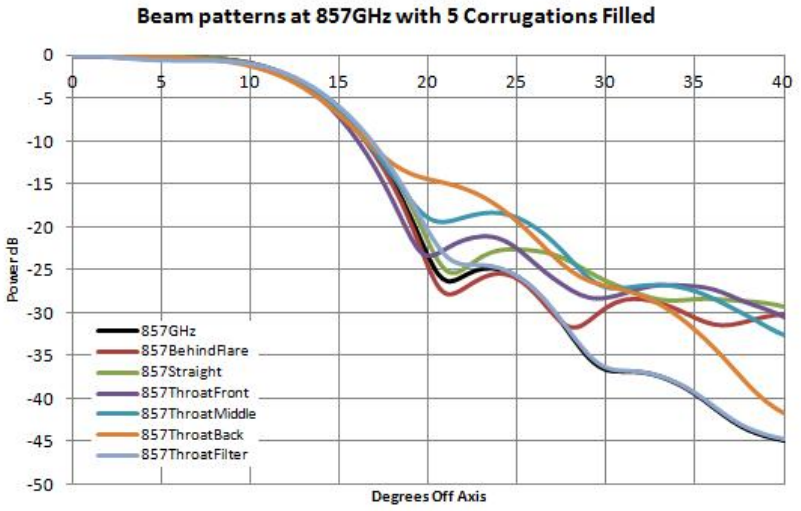

FIGURE 3.38: Comparison between the beam patterns of six altered horns at 857 GHz, showing the effects on main beam shape and sidelobe levels when corrugations at various horn locations are filled [69].

Also, filling of corrugations was the most plausible scenario in which the horns could have been altered, as the horns could not be thoroughly checked after etching. The removal of corrugations was somewhat less plausible as they underwent lengthy vibration testing pre-launch to assess their integrity, and no noticeable deterioration in beam quality was noted. That said, recent work [69] has revealed that even if corrugations in the throat

had broken in testing, the increased sidelobe levels resulting from this would have gone un-measured, due to the noise floor of the test-bed simulations lying roughly 10 dB above base sidelobe levels. The only noticeable effects would have been in the main beam, however corrugation removal has the greatest effect on higher order modes, which contribute predominantly to sidelobe power.

The number of corrugations to be filled had to be carefully decided, as it was crucial that the altered horn represented a plausible scenario for which full sky modelling would be worthwhile. A balance was struck between the beam effects resulting from the removal of 'n' corrugations, weighed against the likelihood of that number of corrugations remaining filled and at the same time going unnoticed in manufacture or pre-launch testing. This testing of the Planck multi-moded flight horns was performed in Cardiff, however it was performed at 460 GHz, much lower than operational frequency of the flight horns, and thus may not have shown signs of imperfection in the measured beam patterns. The telescope simulator used for measurement of the horn beams is modelled by the author in Section 5.1, where the test campaign will be described further. Figure 3.39 shows the impact on beam quality of filling various number of corrugations in the throat section specifically. While the difference between beams when two corrugations are filled is almost negligible in respect of main sidelobe considerations, filling five corrugations shows a significant increase in sidelobe level. At ten filled the sidelobes have risen further, however not as dramatically as before. The main effect is on the spread of the main beam and slower taper of the sidelobes, which sees further deterioration with 20 corrugations filled. These two scenarios seem somewhat unlikely to go unnoticed in examination of the horns themselves, or in testing, so the more plausible scenario of five corrugations being filled, which still shows a significant effect on beam quality, was chosen.

It was found in testing that filling corrugations in the front of the throat (i.e. nearer the aperture) had a lesser effect than filling then in the back, as shown in figure 3.40. This is due to most of the higher order modes having already switched on fully by the time they reach the front of the throat, whereas at the back they may still not couple any power, and disruption of the surface impedance due to filling of corrugations would prevent them from doing so optimally.

Bearing all this in mind, the three horns chosen to be tested were:

- Perfect Horn with no alterations to the corrugations.
- Bad Horn with five corrugations filled in the front of the throat section.
- Worst Case Horn with five corrugations filled in the back of the throat section.

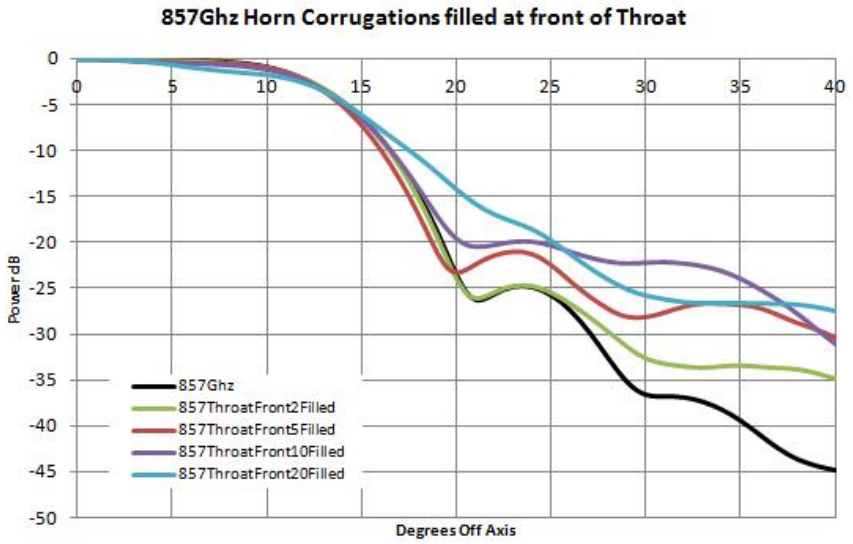

FIGURE 3.39: Comparison between the beam patterns of horns with various numbers of corrugations filled in the throat (front) section [69].

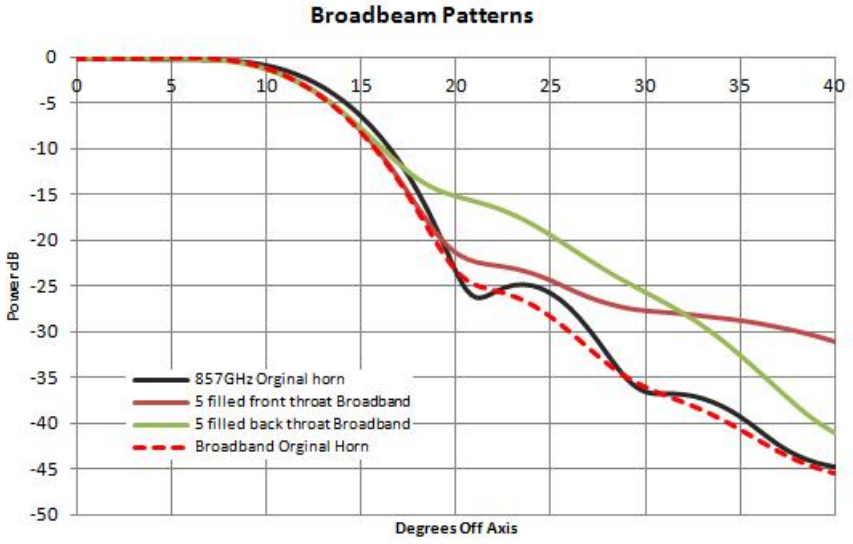

FIGURE 3.40: Broadband far-fields of the altered 857 GHz horns showing the gradual deterioration of beam quality from a perfect unaltered horn, to one with 5 corrugations removed at the front of the throat, and one with 5 removed in the back of the throat [69].

A comparison between the component modal fields produced by the three horns at 730 GHz is shown in figure 3.41, where the far-field has been taken for each. Immediately obvious is the sizable contribution to sidelobe power from all higher-order modes present, while the main beam power arises almost exclusively from the fundamental HE11 mode. It is clear also that the secondary sidelobes are brought up considerably for the 'worst case' horn, when compared with those of the 'perfect' horn, and even the intermediary 'bad' horn. The sidelobe differences between the 'perfect' and 'bad' horns are less critical

but still discernable with up to 5 dB gains for some modes, and generally wider taper in the sidelobe regions.

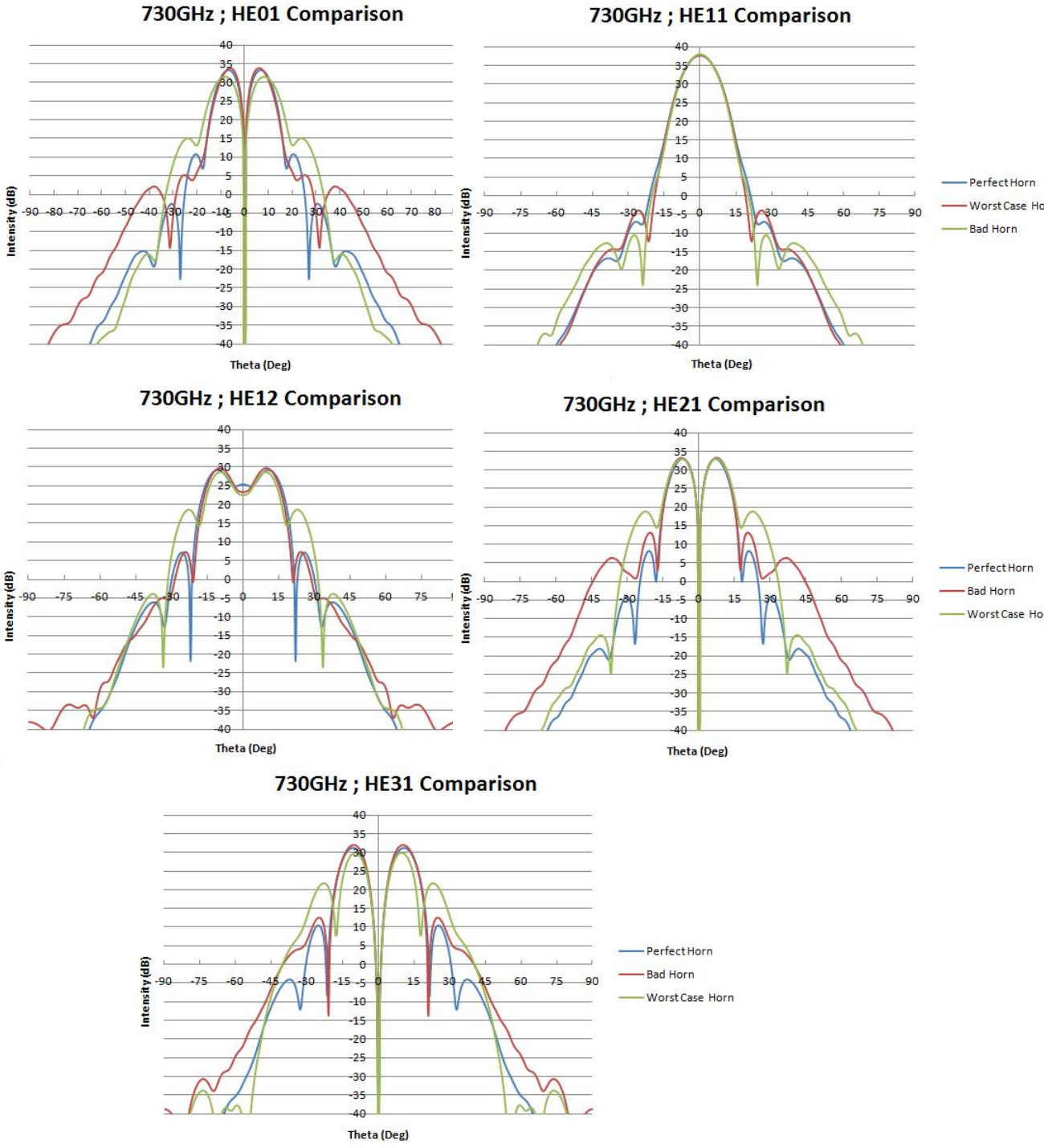

FIGURE 3.41: Comparison between the far-fields of each component modal field making up the sum of power in the 857 GHz horn operating at 730 GHz. Orthogonal modes have been omitted as they display almost identical properties.

The total far-field produced by combining all modes in quadrature for all three horns at 730 GHz is shown in figure 3.42. Although the main beams remain quite similar, the

increase in sidelobe level going from 'perfect' to 'worst case' horns is clearly significant. On implementation in the Planck system in GRASP9 these differences should be evident in FSL levels due to spillover from the mirrors, which shall be discussed shortly.

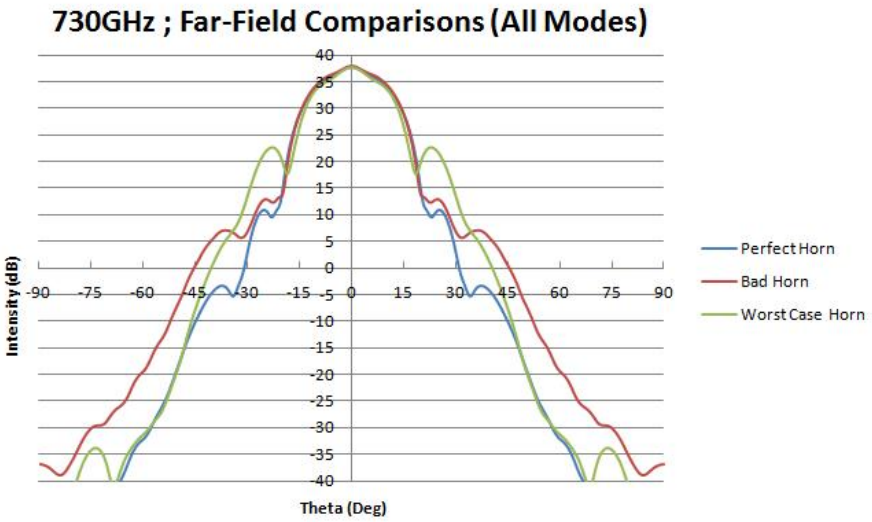

FIGURE 3.42: Intensity plot of the three 730 GHz test horns, obtained by propagating each hybrid mode and combining them in quadrature in the far-field.

Next we shall discuss the modelling of all three horns for the purpose of a full-sky beam description, which can be fed into the Planck pipeline to try and recreate the "bananas" seen in the Planck maps. Two techniques were attempted to simulate FSL structure due to spillover, first PO which we will touch on only briefly, and then GTD. Each will be considered in turn with their associated merits and results outlined.

PO Modelling of the 857-GHz Band

As mentioned previously, PO calculation of the full sky at such high frequency is extremely challenging, especially for a system as complex as Planck. At 100 GHz it was possible to test the effects of adding fields due to partial reflection from the baffles behind the reflectors, in an attempt to accurately describe FSL structure. At 857 GHz, and even 730 GHz, this is next to impossible given the processing capabilities available. The computation time required to calculate currents on the primary reflector are already quite daunting, however an attempt to calculate currents on the sizable baffles behind the reflector would prove next to impossible. This is due to the proximity of the two surfaces, as the convergence integrals becomes almost unsolvable when using a current distribution in the near-field of the surface on which induced currents are to be calculated.

For this reason the field on the sky was taken from a combination of the three fields noted as critical for cancellation of secondary effects in section 3.2. Simplifying the model to this level, however, would prove insufficient if the field accuracy on the reflectors is to be set to 80 dB, as propagating a single mode to the sky would take roughly 10 days. With ten individual modal fields to propagate, for each of three separate horns, the overall computation time would approach one year given the processing power available. This was obviously not considered feasible, and a more accurate and efficient description by GTD, which will be discussed later, was developed.

An attempt to calculate the entire field by cutting the field accuracy from 80 dB to 40 dB reduced the computation time for each modal field to roughly 3 days. The HE11 mode of the worst-case horn was propagated to the sky, and the resulting field along the axis of greatest spillover is shown in figure 3.43. Unfortunately at this low level of surface field accuracy the convergence of surface currents from the secondary on the output grid is not accurate enough to see the low level spillover from the primary, and the signal does not rise above the noise floor of the simulation. Near-in, a peak is seen roughly 8 ° off-axis, which is almost indistinguishable from the noise floor. It is in fact direct spillover from the horn passing the secondary onto the sky, which is calculated independently of the convergence on the reflectors, and thus is not nullified by the field accuracy used in current calculations.

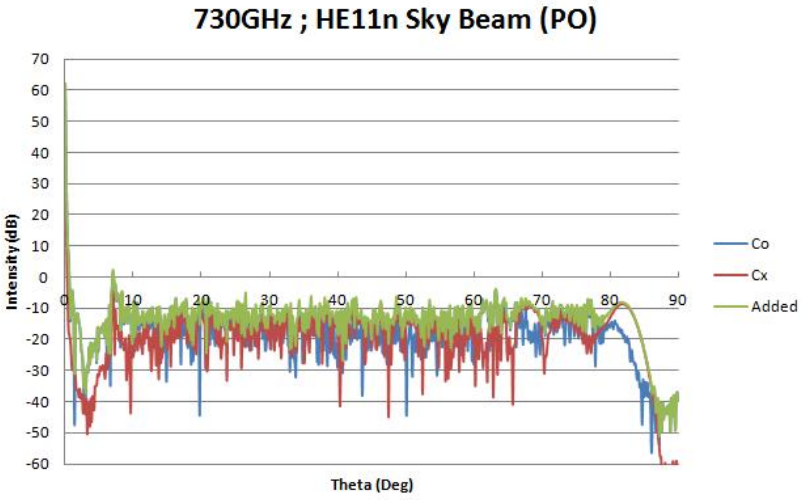

FIGURE 3.43: Sky beam obtained using PO for the worst case 730 GHz horn, along the directions of greatest spillover. At 40 dB field accuracy the noise floor of the simulation dominates the relatively small signal due to spillover which was expected 70 ° off axis.

With this in mind it was concluded that a field accuracy of 80 dB would almost certainly be required to detect any FSL structure. Although computationally intensive, it was decided to test the accuracy of the PO prediction using the HE01 and it's orthogonal eigenfield, the HE02, which were propagated to the sky and combined. This was done

for higher order modes rather than for the fundamental mode, since the sidelobe contributions from the higher order modes are quite significant and must be detectable for the technique to be useful. The resulting cut across direction of greatest spillover is shown in figure 3.44, with the primary FSL clearly visible past 70 ° off-axis. The field due to the feed was not added for this simulation which was done exclusively to test for the dominant primary FSL level, hence spillover from the secondary is not included. Even so, the large off-axis effect seen along the ϕ=90 ° cut in regions which would in reality be shadowed by baffles and payload structures shows the major shortcoming of a PO approach to full sky modelling. Although it may accurately model FSL regions with direct lines of sight into the FPA, accounting for blockages in all regions shadowed from the detectors is limited by the excessive computation time required. For this reason, alongside the already lengthy computation time required for a basic FSL description, the PO approach was abandoned in favour of a GTD approach.

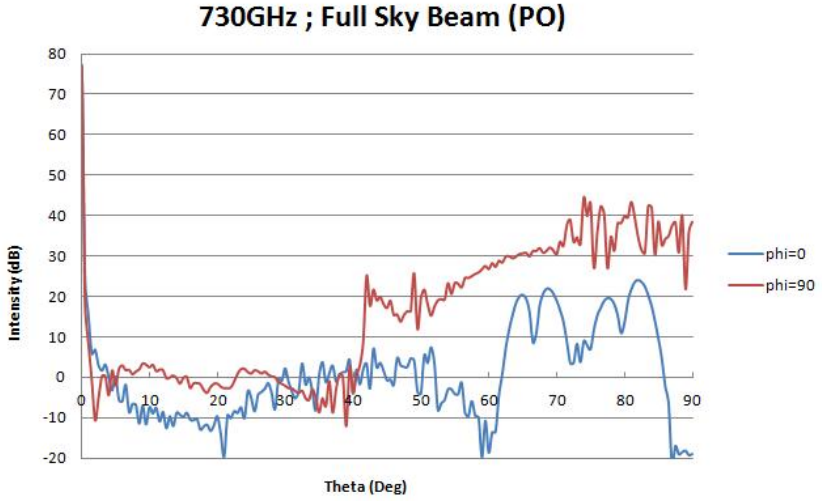

FIGURE 3.44: Sky beam obtained using PO for the worst case 730 GHz horn, along the directions of greatest spillover. At 40 dB field accuracy the noise floor of the simulation dominates the relatively small signal due to spillover which was expected 70 ° off axis.

GTD Modelling of the 857-GHz Band

At the highest frequencies GTD proves a more useful approach than PO, since blockages are better accounted for, and electromagnetic current calculations on surfaces are unnecessary. At 730 GHz, each of the incoherent hybrid mode fields which constitute the total beam are propagated to the sky using GTD and their fields combined to return the sidelobe pattern. The same key issue still surrounds the field generation, that is although the method of GTD modelling is much more efficient, the larger the field grid the more time it will take to accurately calculate. $\{\theta, \phi\}$ coordinates are used for representation of the sky beam grid. In this coordinate space the main beam is centred

on θ=0 ° and moving radially in θ will perform a lap of the sphere. Rotating around ϕ then extends the single arc to cover the entire sphere. This is illustrated in figure 3.45. Sampling the entire sky at 1 ° increments in theta and ϕ thus requires 361 points along one coordinate direction and 181 in the other, a combined total of 65,431 points on the sphere. This size of field grid spanning such a large area requires a much larger number of rays to be traced across all surfaces than would otherwise be necessary, and while this will be required for final production of the full sky Planck beams, much smaller grids are taken during the intermediate trials. These comprise highly sampled arcs in θ, taken at only a few values of ϕ which are of interest, namely the ones which intersects the regions of spillover. In doing this any anomalous features arising from the simulation could be observed and corrected for without having to perform a lengthy full sky calculation first. A graphical representation of the cuts to be taken is shown in figure 3.46

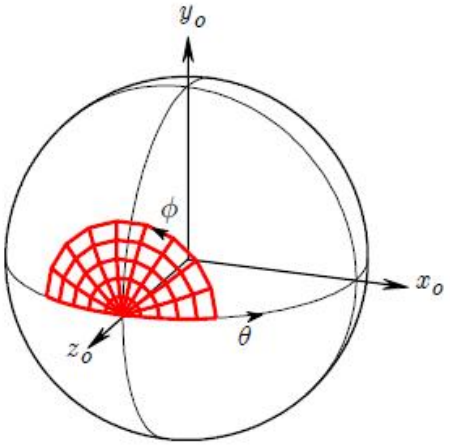

FIGURE 3.45: The grid is drawn for 0⩽ θ ⩽30 and 0⩽ ϕ ⩽180 with a spacing of 6 ° in θ and 20 ° in ϕ [52].

Some of the rays required to give an accurate description of the sky beam were described in the GTD overview, and an illustration can be seen of various rays which contribute to the total field on the sky in figure 2.7. Further rays unique to the Planck system strike baffle surfaces. Some are illustrated in figure 1.24, and were included in figure 3.28 with the appropriate naming scheme outlined. As the 857-GHz model was to be rigourous, the ray paths chosen to be included needed careful consideration. While all reflective surfaces surrounding the telescope inevitably contribute fractional power to the overall sky, not all of their contributions are of sufficiently high levels to merit the added calculation time required to model them. The grooves (illustrated in figure 3.26) for example will couple power to the telescope, however it will be extremely low level, as only rays which are first diffracted off the secondary, then diffracted at large angles off the baffle edge can possibly strike the grooved surface. In this case a minimum ray order of $n = 3$ will be required, and the time needed to evaluate every possible path along which the groove may couple power to the telescope will yield disproportionately little

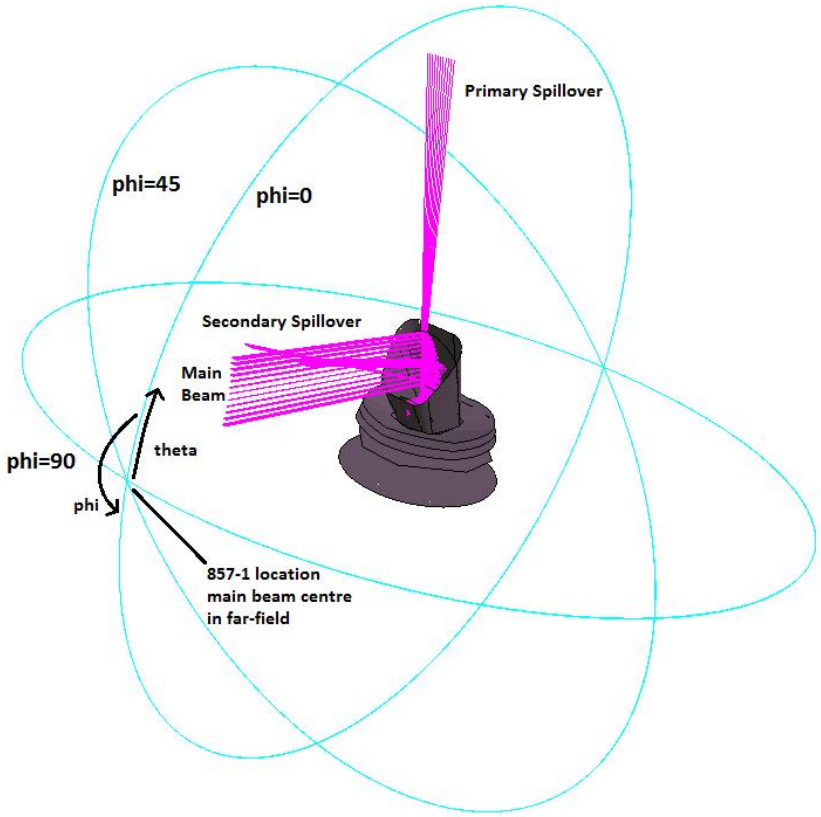

FIGURE 3.46: GRASP9 description of the Planck system with prominent rays and cuts around the sphere taken for illustration of GTD effects in various directions.

extra information about the sky beam. For this reason only rays deemed to contribute significant sidelobe power have been carefully considered for inclusion.

The most important rays chosen for inclusion in the model were as follows;

1. direct rays from horn to sky (labelled 'Direct' in figure 2.7 but 'D' here; order n=0),
2. diffraction from the secondary ('Sd'; n=1),
3. diffraction from the secondary followed by reflection from the primary ('SdPr'; n=2),
4. reflection in the secondary followed by diffraction from the primary ('SrPd'; n=2),
5. reflection from the secondary followed by diffraction from baffle A ('SrbAd; n=2)
6. reflection from the secondary followed by diffraction from baffle B ('SrbGd'; n=2)
7. reflection from the secondary followed by diffraction from baffle H ('SrbHd'; n=2)
8. reflection from the secondary ('Sr'; n=1)

The critical rays are 'D' and 'Sr', which contribute to the vast majority of spillover seen in regions away from the main beam. The baffle-diffracted rays also provide information in the regions of interest. Unfortunately, the nature of testing by three cuts around the sphere means that minor effects due to other potential rays of interest may not be seen, and therefore ignored in the final model. Herein lies another trade-off between complete analysis of all effects and the limited computational power available. A full analysis of 'SrbHd' rays alone, for example, when applied to the full sphere final model takes 12 hours on 66 machines. If all reflected and diffracted rays of various orders from each baffle segment were to be included the time required for full sky analysis would become too large, and diminishing returns for the time allocated would inevitably result. With this in mind most baffle reflected rays have been ignored as they are almost completely shadowed by the reflectors in front of them along the line of sight of the 857-1 beam. For the same reason analysis of baffles B and F have been ignored, as they contribute a minimal amount of reflected power to the system when compared the more troublesome baffles behind each reflector.

Rays reflected from the secondary and then from the primary ('SrPr'; n=2) are not included either, as this constitutes the main beam. Rays along this path converge in the far-field and will give a caustic, inaccurately representing the main beam while also providing little additional information about sidelobe structure. Instead, the main beam peak will be obtained using the PO approach and shall be returned to later in construction of the final sky beams. In the plots to come the main beam has not been accurately calculated, however in this case the purpose is merely to demonstrate the sidelobe response to various factors, so the main beam may be ignored.

Each of the ray paths mentioned above are individually represented by a 'multi-GTD' source element in GRASP9. This is an extremely useful element of GRASP9, as it contains all the information required to perform a ray calculation. The element requires input of the source (in this case our 730-GHz modal aperture field), a list of the 'GTD Scatterers' with which the generated rays will interact (so for 'SrPr' this would be the primary and secondary mirrors), and a list of blockages which will kill any rays that hit them ('all' should be specified here, meaning any surface other than those listed as scatterers will act as a blockage). The final important attribute of this element is 'combinations', which requires the user to define the order of reflections to be accounted for in the model. Two variables must be carefully defined here, namely 'from order' and 'to order', representing the minimum and maximum order of reflections. The ray path 'SrPr' naturally contains reflections of order n=2, as outlined previously, and this is acknowledged by GRASP9 once 'GTD scatterers' has been defined. If 'from order' and 'to order' are defined as 0 and 1 respectively then, only one additional reflection or

diffraction to those specified will ever be accounted for.

The number of diffraction points to be used on any reflector's surface must also be taken into consideration when performing a GTD simulation, and is specified as 'sample points' in the GRASP9 object class 'GTD Scatterer'. The numerical ray tracing process uses these as starting points for trial ray traces, and the total number of trial ray traces for a given ray type is found as the product of the specified values of 'sample points' for all scatterers along the ray trace. The less likely it is for radiation to propagate along a chosen route, the larger the sampling should be on every surface. The ray traces chosen to be modelled were only those along which the largest proportion of scattered power would travel, thus level of sampling had very little effect on the overall quality of the beam.

Taking only the fundamental HE11 mode, a GTD estimation of sidelobe structure was performed, and the gradual emergence of structure on the sky with addition of various GTD rays of interest is shown in figure 3.47. Due to the nature of ray tracing there exist regions of the sky in which zero field is measured, and thus an intensity of 0 will be returned, logarithmically -∞ dB. To avoid this the threshold has been set at -80 dB at all points for which zero field was measured in all plots.

The increase in power at almost 180 ° around the sphere and 45 ° away from the axis of symmetry of the telescope arises only after addition of the field due to diffraction from the baffle A edge. This is due to diffracted rays from the curved edge of the surface becoming focussed on the sky, generating a peak in this direction. This will naturally occur on the opposite side of the sphere for reflections from baffle G, however having only taken three cuts around the sphere in the directions illustrated by figure 3.46 this is not visible.

With regard to the near-in sidelobe, almost all of the power arises from the direct rays passing the secondary to the sky, as can be seen in the first plot in figure 3.47. The sharp peak at roughly 50 ° has no real origin, as the direct rays of order n=0 will naturally undergo no interaction with surfaces en route. It is a non-physical peak arising from instability in the GRASP9 GTD simulation around this point.

Three components collectively contribute to the far-out sidelobe beyond 70 °, the greatest of which arises from 'Sr'. This generates a broad 10 ° lobe with a finger at the furthest angular extent. This is a fractional part of the horn main beam, approximately half a degree in extent, which on reflection from the secondary misses the edge of the primary, along with a portion of the first sidelobe. Further smaller contribution arise from both

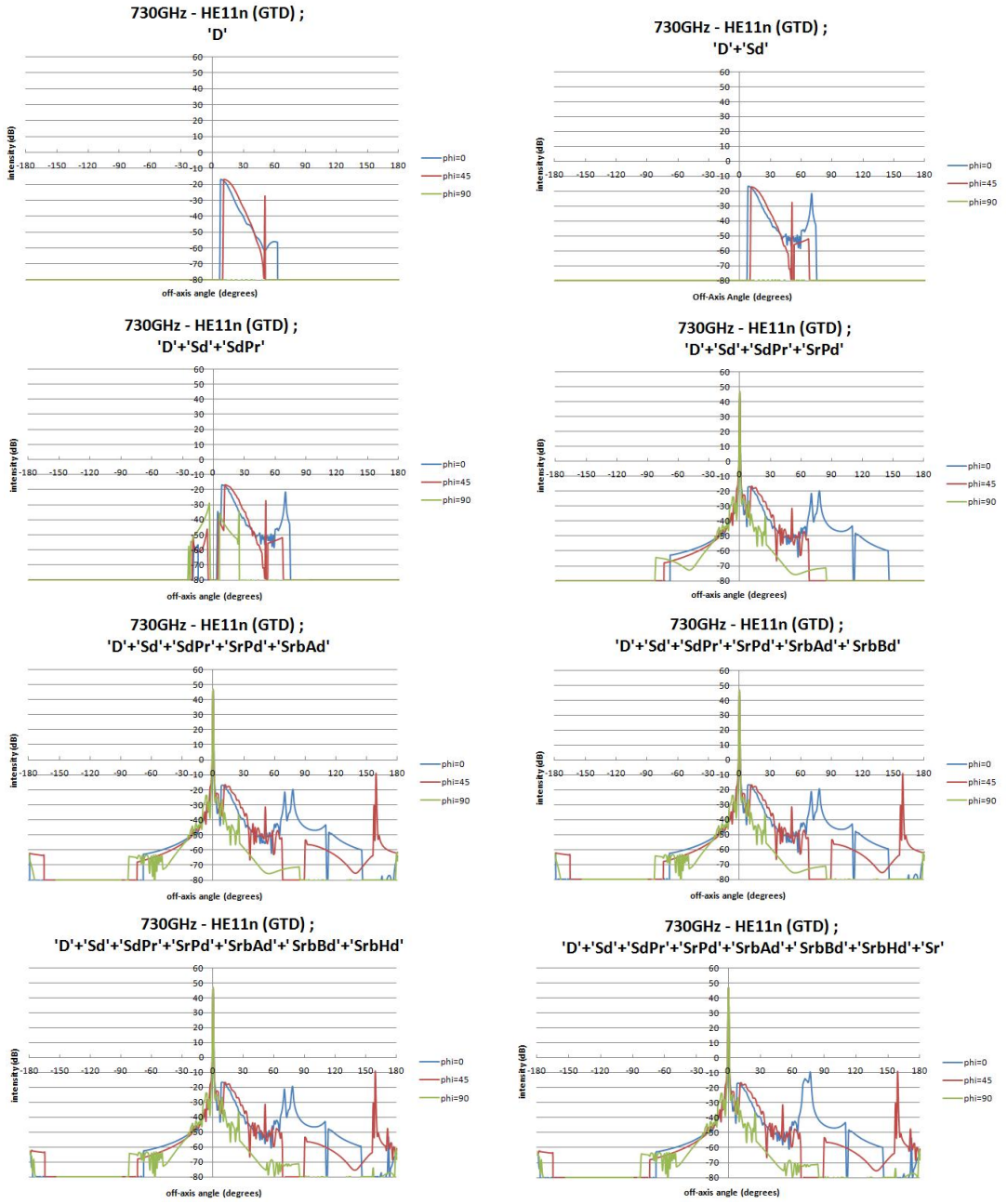

FIGURE 3.47: Multiple GTD rays traced through the system for the fundamental HE11n mode (where 'n' is for normal as opposed to orthogonal) at 730 GHz, and summed to gradually build a representation of the FSL structure at three cuts around the sphere. The sidelobe beyond 80 ° has the largest contribution from 'Sr' rays as can be seen by the final summation.

'SdPr' and 'SrPd', as can be seen in the two plots making up the second row of figure 3.47.

A full GTD calculation of all ray contributions to the field takes roughly 50 hours on a cluster of 66 CPUs, however this must be done for each of the modal fields which contribute to the overall beam. As mentioned previously, the lower number of modes

at 730 GHz made it the ideal choice of frequency at which to model the 857-GHz horns, however even the ten individual modal fields at 730 GHz meant a total computation time of roughly three weeks for a full sky grid of each of the three horns.

Taking an ideal horn at 730 GHz and summing all GTD effects, the contribution of each modal component to the overall field is illustrated below in figures 3.48 to 3.52.

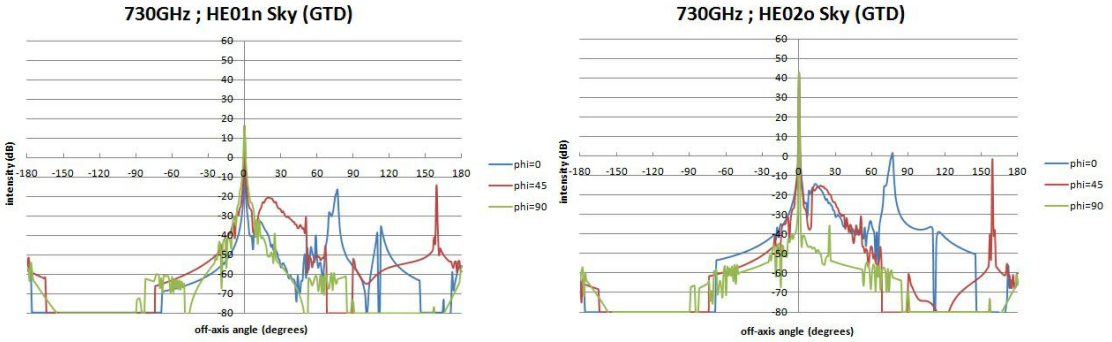

FIGURE 3.48: Complete beams on the sky for both zero-azimuthal order modes.

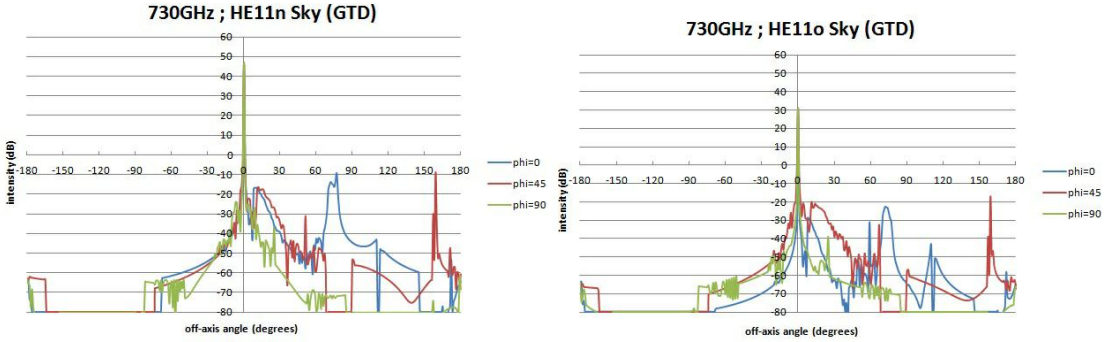

FIGURE 3.49: Complete beams on the sky for the fundamental mode, HE11 and its orthogonal mode, labelled HE11n and HE11o respectively.

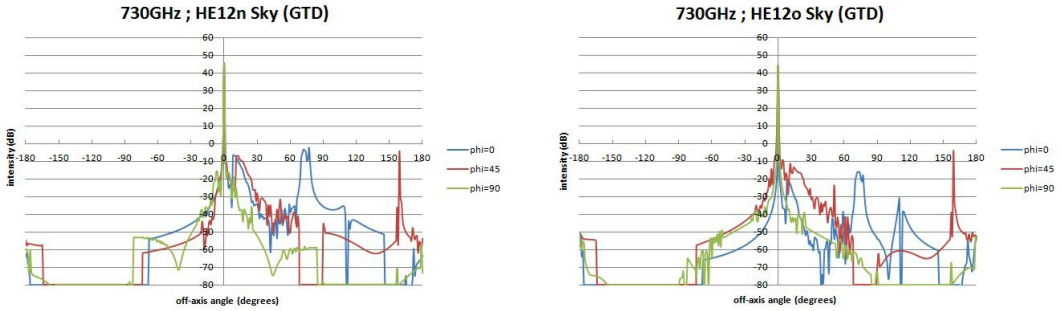

FIGURE 3.50: Complete beams on the sky for the second mode of azimuthal order n=1, labelled HE12n here, and it's orthogonal labelled HE12o.

Immediately obvious from the cuts above are the varying contributions to sidelobe level of each mode. Critically, while the fundamental HE11 mode contains the vast majority of the power radiated from the aperture of the horn, it is by no means the dominant source of primary spillover. The peak sidelobe level is observed in contributions from the weaker

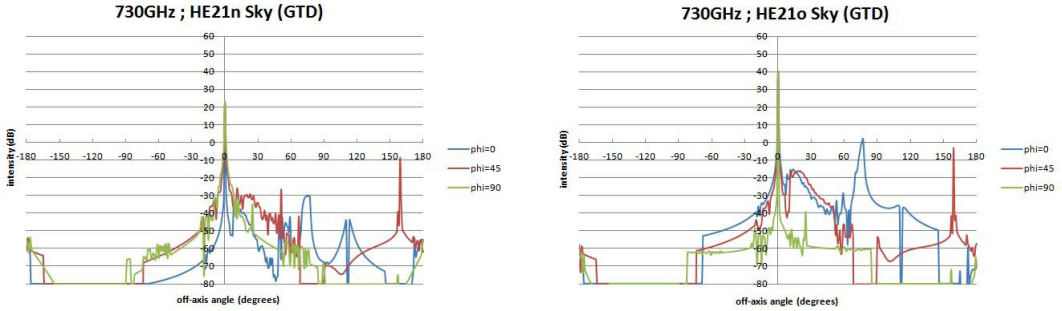

FIGURE 3.51: Complete beams on the sky for the second azimuthal order mode (n=2), labelled HE21n here, and it's orthogonal labelled HE21o.

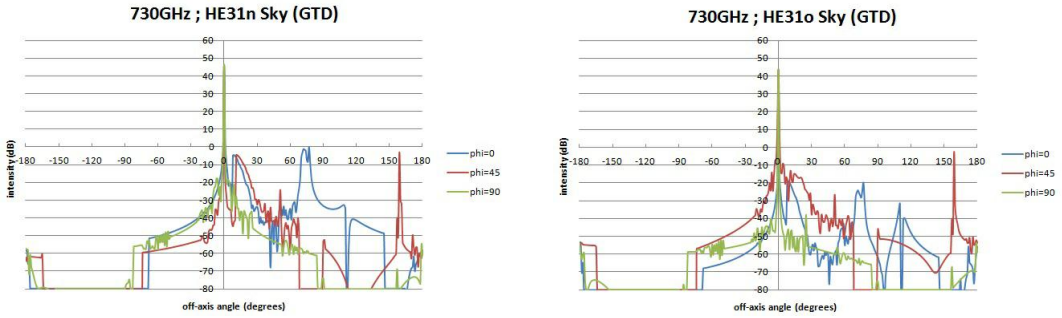

FIGURE 3.52: Complete beams on the sky for the third azimuthal order mode (n=3), labelled HE31n here, and it's orthogonal labelled HE31o.

zero-order orthogonal (HE02o) and second order orthogonal (HE21o) modes, while a plateau of just below 0 dB is maintained across a region of 10 °. The HE12n displays very similar features to that of the HE21o, albeit at slightly lower levels, owing to the similarity in structure of their modal fields. The HE11n contribution to sidelobe power is 10 dB lower than the largest contributions of other modes, which bears some significance to a general issue regarding modelling of multi-moded fields, described further below. The spike in the beam pattern visible in all modal fields at 160 ° off-axis is a second caustic, which arises as a result of the path followed by the caustic hyperbola of the reflector, as outlined in section 2.2.2. It only contributes minor inconsistency to the beam, as blockage due to the baffles results in, much fewer rays reaching this field point than would focus to the main beam field point. It has however, alongside the main beam, been corrected for by PO modelling in the small angular region over which it occurs.

With regard to secondary spillover, the dominant contribution again arises from both the HE12n and HE31n modes, whose sidelobe levels reach over 10 dB higher than for all other modes. The level of secondary spillover is consistently well below that of the primary spillover, which is expected since reflection from the secondary compounds the beam divergence and results in much greater subsequent spillover passed the primary.

Noticeably, however, the effect of this secondary spillover is generally higher at $\phi = 45^\circ$ than at $\phi = 0^\circ$. In some cases the spillover along the 0° axis of symmetry of the telescope is almost negligible, while off-axis the contribution is much higher. This is most noticeable among the orthogonal modes, and generally a 10 dB difference between sidelobe levels at these different angles is observed.

At this point it would be prudent to mention a common error made in the modelling of multi-moded horns. This is to take the aperture field of the horn and to fit a Gaussian to it. This Gaussian is then propagated to the sky in an attempt to simulate the multi-moded beam. While a similar level to that of the true main beam may be approached, the incoherent nature of the component fields means the single-mode Gaussian will fail to replicate the full effects of propagation of all modes through the telescope, especially into regions off-axis. The predominant source of power to which the Gaussian will couple is the fundamental HE11 mode, itself a Gaussian, which is far from the largest contributor to sidelobe power, but at the same time contributes much of the main beam power. Thus, in simulation of the full sky, sidelobes will very likely fail to approach levels even close to those seen using a truly correct multi-moded approach. This subtlety is quite often overlooked in the modelling of multi-moded horns, as taking a best-fit Gaussian yields quick results and is often assumed to be of negligible difference from what a true depiction of the decomposed multi-mode field.

The complete beam on the sky is calculated by quadrature summation of all modal field components which in turn have been generated by a summation of all GTD effects for the particular mode. The final beam on the sky for an ideal 857-GHz horn propagated from the 857-1 horn location of the FPA is shown below in figure 3.53. While the main beam due to GTD will produce a caustic, as explained in section 2.2.2, this has been corrected for by modelling of the main beam using PO. This is relatively simple and quick compared with the PO analysis performed previously, due to the smaller number of PO samples required on the primary reflector when measuring over small angular scales on the sky. It has been calculated here and replaces the GTD main beam out to 1° in the full sky beam in order to give a true representation of the FSL levels w.r.t. the main beam.

Of immediate note is the sharpness of the sidelobe around 80° off-axis, which on first appraisal appears similar to the instability seen in the 100 GHz GTD model of the FSL region. This however is not the case, as a comparison of the angular regions in which both occur can verify (see figure 3.29). In fact, the sharpness of the FSL here is due to a smaller angular region of the main beam missing the primary, alongside the first sidelobe, which is seen as the smaller peak at 72°. The beam is of course inverted

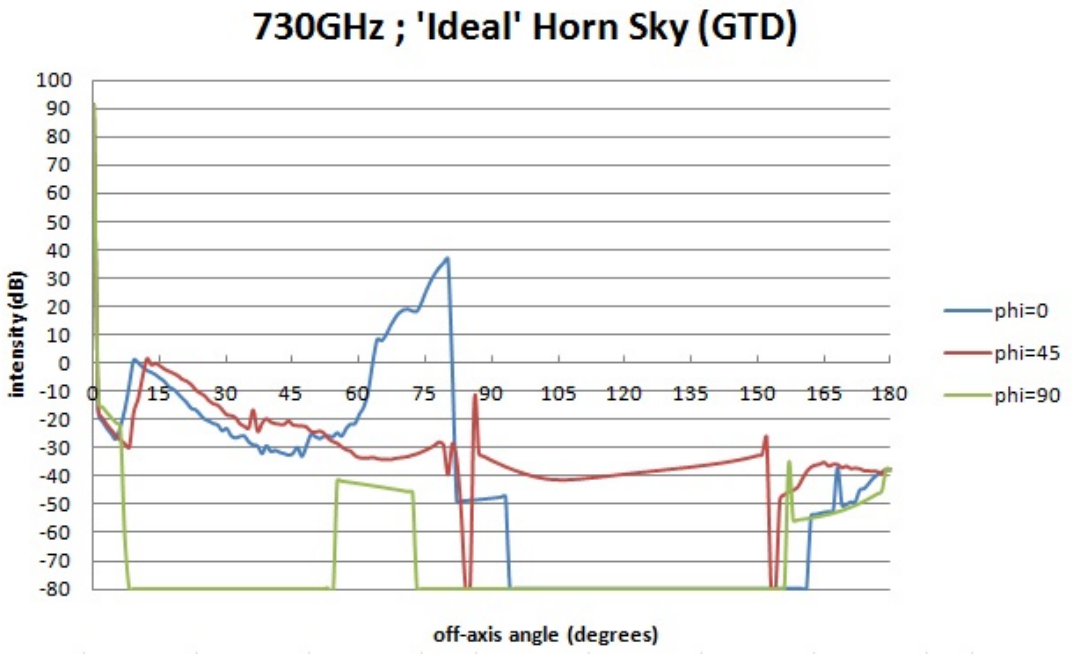

FIGURE 3.53: Full beam on the sky for an ideal 857 back-to-back horn situated at the 857-1 horn location, modelled at 730 GHz using GTD. The main beam is calculated using PO.

on reflection from the secondary with respect to the detection grid along the primary spillover line of sight, so the sidelobe is now closest to the line of sight of the main beam, when viewed on the sky.

Similar full sky beams for the 'bad' and 'worst' case horns are shown in figures 3.54 and 3.55, respectively.

It was originally believed, based on modelling of the telescope outlined in chapter 4, that all three horns would exhibit varying sidelobe level. This was based entirely on the assumption that only the first sidelobe of the horn far-field beam pattern would miss the primary on reflection from the secondary. While a difference in sidelobe pattern is obvious on comparison of the 'ideal' 'bad' and 'worst' beam patterns, their peak levels are very similar. This is due to the fact that a small portion of the horn far-field main beam misses the primary, along with the first sidelobe. The alterations to horn integrity performed for the three cases had very little effect on the main beam size or taper, so the same peak levels of approximately 35 dB are observed across all examples. Differences between the sky sidelobe patterns arises instead from varying levels of the horn far-field first sidelobe, which was known to be broadly affected by imperfections in the horn. The taper from peak for the ideal horn is quite rapid, falling below 10 dB at approximately 65 ° off-axis. Both 'bad' and 'worst' case horn sidelobes taper to only 20 dB at the same distance off-axis, highlighting the effect of imperfections. While the 'ideal' horn tapers

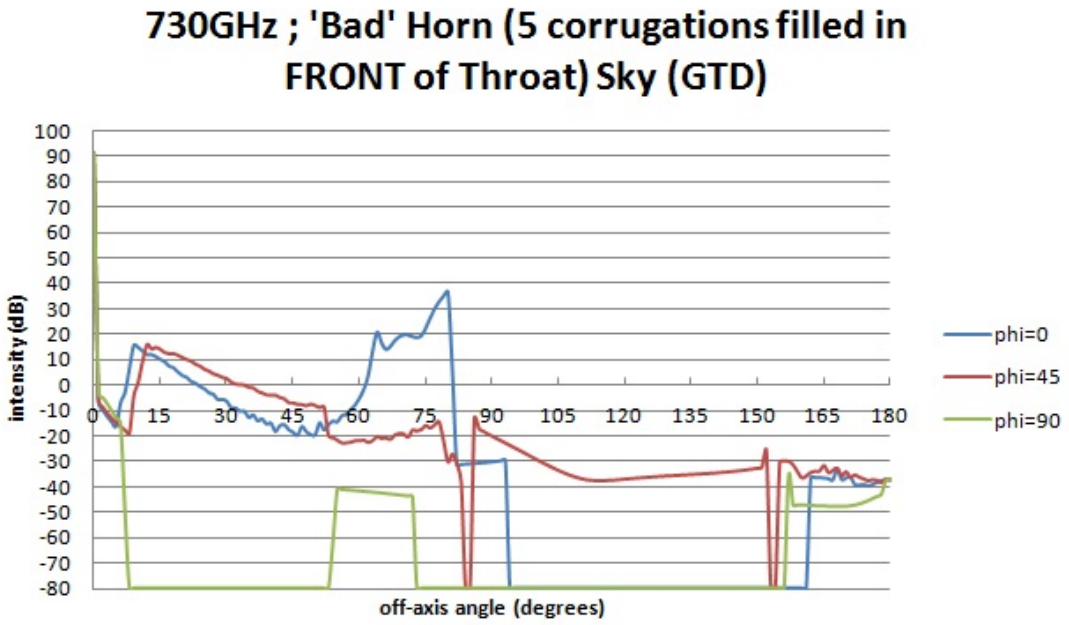

FIGURE 3.54: Full beam on the sky for a 'bad' 857 back-to-back horn situated at the 857-1 horn location, modelled at 730 GHz using GTD. The main beam is calculated using PO.

quite quickly, the 'worst' horn maintains lobe strength in the region of 30 dB across a considerable angular extent of the sidelobe, clearly highlighting the difference in sidelobe power contributions which would be expected with deterioration of horn quality.

3.5 Conclusion

In this chapter we outlined the implementation of the full Planck telescope model in GRASP9, with specific use in numerical FSL modelling of the HFI 857-GHz band. This was done using both PO and GTD, and various examples of increasing complexity illustrated the key issues that need to be understood for accurate off-axis modelling. We began with a simple single reflector telescope, outlining the method of field summation required to obtain correct beam patterns around the sphere. We then moved to a simplified dual-reflector model of Planck, again performing PO calculation of the FSL structure, before finally moving to a full model of the telescope. This included all baffle components which act as blockages to stray light, and thus have significant impact on FSL concerns. Finally, a GTD model was performed and a comparison with PO made, highlighting the superiority of GTD in simulation at such high frequency. We also made predictions about the spillover sidelobe levels expected for the ideal horn, and the two cases of horn imperfection. There was little difference between the peak sidelobe

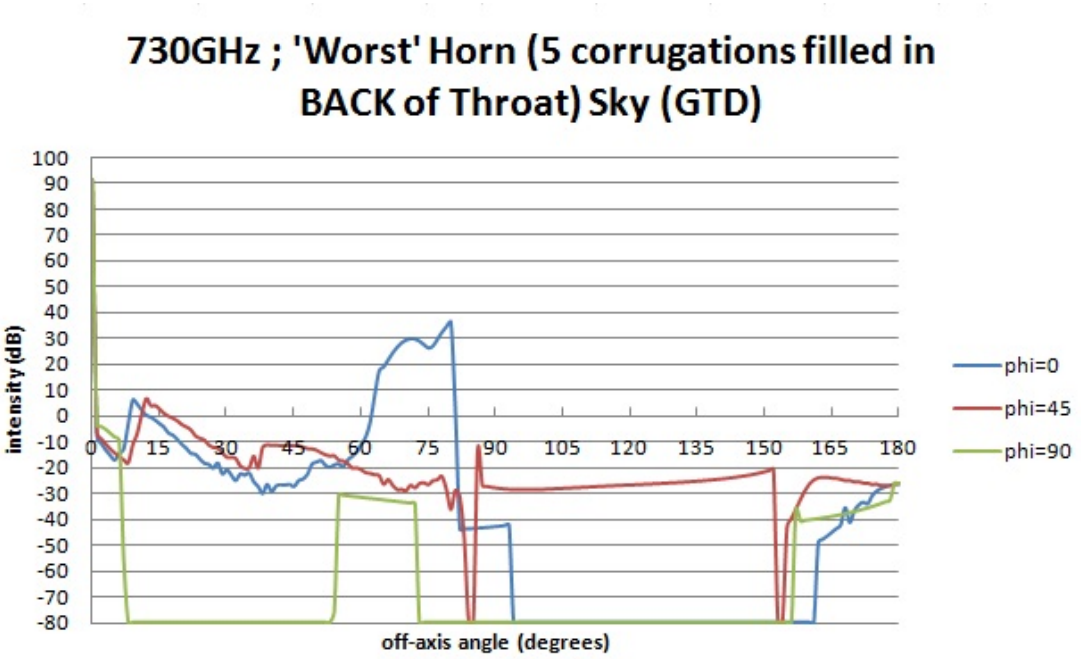

FIGURE 3.55: Full beam on the sky for a 'bad' 857 back-to-back horn situated at the 857-1 horn location, modelled at 730 GHz using GTD. The main beam is calculated using PO.

level of all three cases, however the sidelobe coupled more power to the telescope with deterioration in quality of the horn. This allows for the possibility that the 'bananas' seen in the difference maps of the 857-GHz band could indeed arise from imperfections in horn etching, raising the beam pattern sidelobes, which in turn add power to the primary spillover FSL.

This will be reinforced in the following chapter, where two further techniques will be demonstrated, with which the FSL structure of the telescope can be quickly modelled. These are the projected aperture technique, and the GBM technique, both of which assume a paraxial system of reflector-equivalent lenses. Using these two methods the aperture field of a horn antenna can be transformed from aperture to sky, and FSL levels measured to compare with the standard GTD model of this chapter. We will then investigate the effect of reflector surface deformations on the Planck HFI beams, with specific interest in regular dimpling due to print through of the reflector supports onto the surface.

Chapter 4

Modelling of the Planck System including Broadband Multi-moded Beams

In the previous chapter, high-performance PO and GTD modelling of the Planck telescope was performed in GRASP9, with a view to accurate modelling of the "bananas" observed in difference maps of the HFI 857-GHz channels, and outlined in section 1.6.4. Both techniques, however, proved to be quite time-consuming, so in this chapter two simplified models of the Planck system will be implemented which have the benefit of much reduced computation time, while still providing important information about the FSL levels.

We will first implement the projected aperture technique, whereby the telescope is modelled as a paraxial single-lens system, and the aperture fields of the multi-moded horn undergo Fresnel transformation through the system. This is either done from source to lens and from lens to sky, simulating the telescope main beam, or directly from source to sky simulating FSL spillover.

The second technique implemented is an elegant GBM approach to telescope modelling, whereby the telescope is once again modelled a paraxial lens system, but with two lenses simulating each of the primary and secondary reflectors. In this case, however, the aperture field of the multi-moded horn is decomposed into an associated set of Gauss-Laguerre modes, which under a ray matrix formalism can be propagated from source to sky and provide a good approximation to main beam and spillover levels expected in

the actual system.

Finally, an investigation of the effects of mirror distortions on the multi-moded 857-GHz main beams will be performed, with a view to replicating the "grating lobes" seen in main beam measurements, and which are believed to arise from periodic surface deformations due to print-through of the mirror supports on to the reflector surfaces. Work on this topic was originally done using only a single-moded source at 857 GHz, however the band is distinctly multi-moded, so herein we perform more accurate simulations using a multi-moded beam. The work is performed using a distortion modelling capability in GRASP9, and will conclude the work of this author on the Planck system.

4.1 Planck 857-GHz Sidelobe Modelling

Spanning 730-990 GHz, the highest frequency channel of Planck HFI gathers light from relatively high energy sources, usually dust and gas in the vicinity of our own Galaxy. The optical chain assembly of this channel is composed of a so-called 'back-to-back' (B2B) horn feeding a bolometric detector via a filter section, the dimensions of which can be seen in figure 4.1. A typical example of the optical chain used on all HFI channels is shown with further description in figure 4.2, however the back-to-back illustrated here is not the same horn used on the 857-channel.

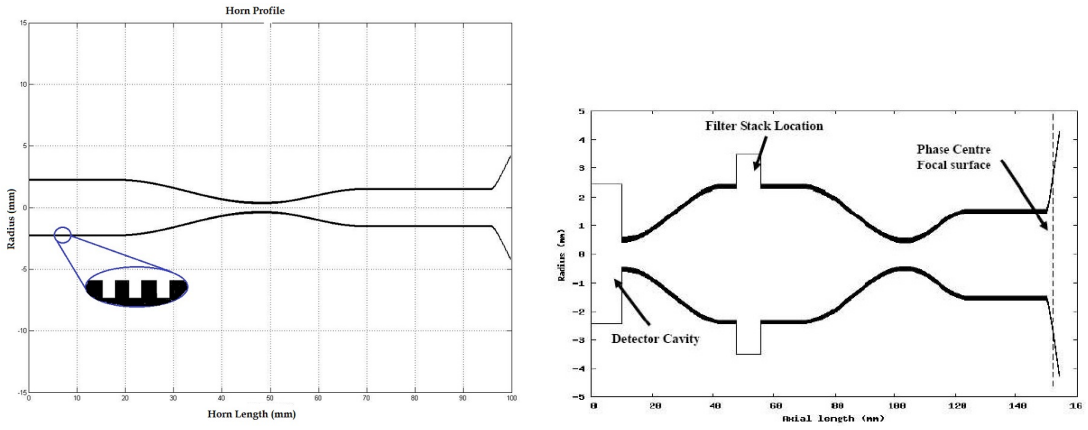

FIGURE 4.1: (left) The size and shape of the 857 horn, and (right) The B2B horn couples radiation from sky onto the bolometric detector in the rear, which, via a filter stack, is super-cooled to minimise instrument noise interfering with the incoming signal.

The multi-moded horns used on the Planck 857-GHz channel are extremely small, thus the corrugations etched in manufacturing had to be very thin indeed. They pushed the boundaries of acceptable tolerances providing a challenge for the suppliers, however once successfully manufactured they behaved very well throughout testing. However

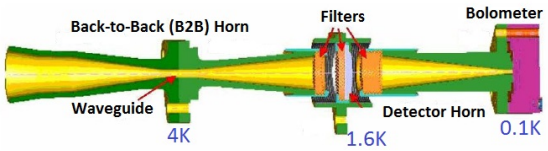

FIGURE 4.2: Schematic of a typical HFI detector assembly. The front horn collects radiation from the telescope optics with good stray-light rejection, and by means of a thin waveguide section couples only a precise number of modes to the back horn, all at roughly 4 K. This in turn sends the radiation through a series of filters to the 0.1 K bolometer in the detector cavity.

these tests were performed at around 460 GHz (a much lower frequency than the horns were designed for) due to the unavailability of sources as high as 857 GHz. Testing a horn away from its design frequency is not usually an issue, however the depth and width of corrugations inside corrugated horns have been designed specifically for operation at that design frequency. Use at a frequency significantly different from this operating band will clearly then lead to the horn behaving differently, and as the width of a corrugation approaches the wavelength of operation the horn will effectively operate as if it were smooth-walled. Thus, any damage to the horn's fragile corrugations during vibration testing may not show up in measurements at a frequency where the corrugations are essentially ignored anyway.

The purpose of this section is to test the sensitivity of the 857 GHz horn sidelobes to any damage done to the corrugations inside the horn, and to see if they could vary significantly from the ideal case in which the horn is undamaged and the sidelobes are extremely low. To perform this research a number of analytical techniques were implemented, some of which have been described previously.

In previous parts of this thesis modelling of telescopes was undertaken in software packages such as GRASP9, which propagates radiation from a source first by spherical wave expansion and then calculates fields and currents on scatterers where appropriate. Though quite useful and extremely reliable, this electromagnetic modelling technique can prove computationally intensive as frequencies get quite high. This is due to the software's application of physical optics and physical theory of diffraction in modelling the fields produced on surfaces (mirrors, etc) due to currents excited by incoming radiation. The higher the frequency the smaller the wavelength, and the larger the number of points on a surface which must be sampled to provide meaningful data. In projects such as Planck the size of these mirrors, and thus the extremely large number of points at which currents and fields must be generated can strain the limits of computing power and time available. The Planck HFI 857-channel horns prove a significant challenge, as the incoherent nature of multi-moded horns requires that many individually coherent

modal fields must be propagated separately through the telescope, and combined in quadrature on the sky to form the overall beam pattern of an individual horn. Generation of one mode's full beam on the sky is quite a lengthy calculation, even with the aid of a computer cluster, so a multi-moded horn is even more challenging. Previous work in NUI Maynooth by Tully Peacocke [70], involved the modelling of the broadband main beam of a Planck 857-GHz multi-moded horn. This was done in GRASP9, however modelling just 0.25 ° either side of the main beam proved an exhaustive calculation. The final broadband beam resulting from this is shown in figure 4.3, and will be used later for normalisation of the Planck 857-GHz main beam in this work.

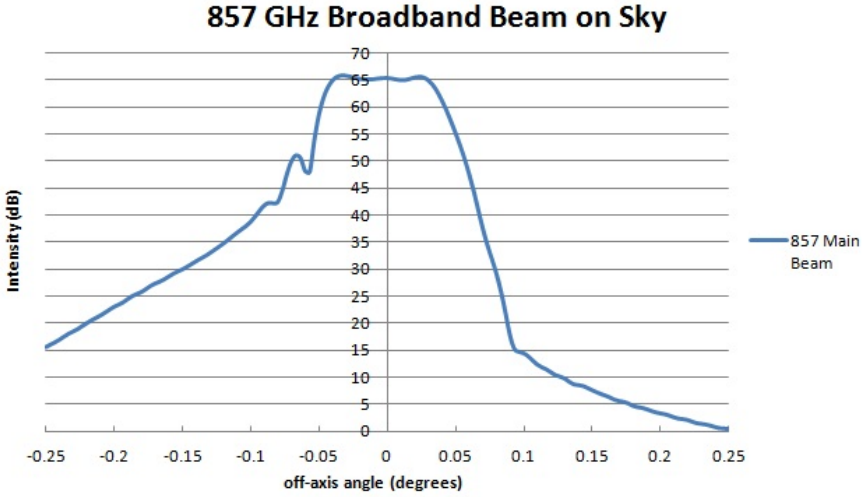

FIGURE 4.3: Modelled Planck HFI broadband multi-moded beam on the sky for an 857 GHz horn at the 857-1 location on the focal plane. Courtesy of Tully Peacocke.

An alternative approach which can considerably decrease computation time, is the use of ray optics rather than physical optics. Ray tracing itself has limitations in the computation time required, as it requires an extremely large number of rays to accurately predict the beam on the sky after reflection from mirrors which are extremely large relative to wavelength.

When only rough information is required about the main beam on the sky, such as sidelobe levels as compared with that of the main beam, an alternative technique discussed next can prove useful.

4.1.1 Projected-Aperture Technique for Modelling 857-GHz Sidelobes

The projected aperture technique is an elegant yet powerful approach to telescope modelling, which can be used at high frequencies that are difficult to model using the more rigorous PO or GTD approaches mentioned previously. The technique is, however,

restricted to paraxial systems, meaning that the off-axis Gregorian description of the Planck system will not be of use. Instead, the telescope reflectors are modelled as one large lens of effective focal length, f_{eff}, which suffices to describe an on-axis equivalent system, the geometry for which is shown in figure 4.4.

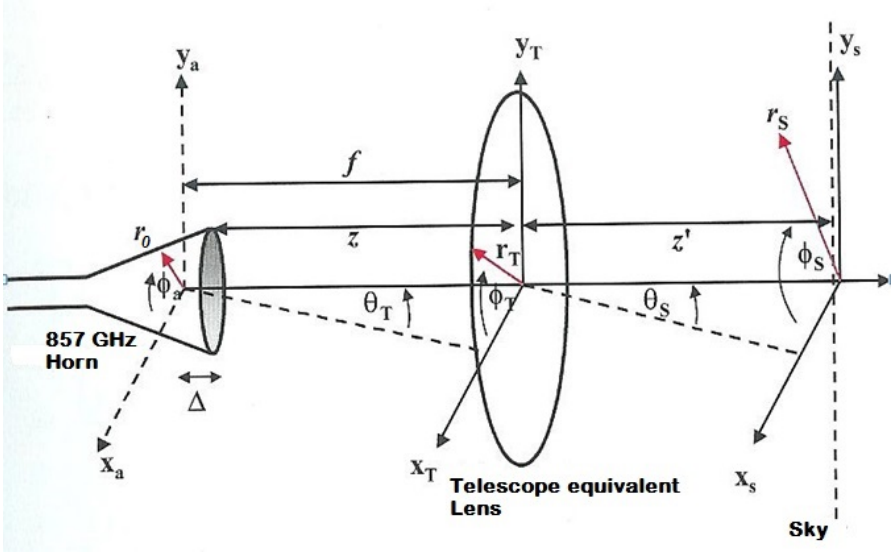

FIGURE 4.4: Geometrical description of the paraxial projected aperture telescope, with telescope-equivalent lens between source and sky. All important angles and distances are labelled.

Herein, the technique will be used to deduce the expected levels of Planck telescope sidelobes due to spillover, with a view to verifying the effects seen in the 857 GHz difference maps generated by HFI from the results of the Planck all-sky survey. One obvious difficulty with this procedure is the correct deduction of sidelobe levels in an off-axis system, which is instead being modelled paraxially. To account for this, the projected angular width of the secondary as viewed from the horn aperture was determined for the Gregorian system, and using this information the angle at which secondary spillover occurs can be readily deduced. Thus, when placing an equivalent lens at a distance f_{eff}, the size it must be to produce spillover in equivalent angular regions is easily computed. An outline of the mathematical procedure is given below.

The partially coherent aperture field of a horn operating at the highest end of Planck HFI (857 GHz) can be decomposed into TE/TM waveguide modes, or HE/EH hybrid modes, as described in section 2.3.3. To begin, each modal field undergoes Fresnel transformation to the plane of the lens, where the fresnel transform of a field $\psi(x_0, y_0, z_0)$

to a plane at any distance from the aperture is generally given as

$$\psi(x,y,z) = j\frac{e^{-jkL}}{\lambda(z-z_0)}\int_{-\infty}^{\infty}\int_{-\infty}^{\infty}\psi(x_0,y_0,z_0)\ \exp(-\frac{jk}{2(z-z_0)}((x-x_0)^2+(y-y_0)^2))dxdy \tag{4.1}$$

where L is the distance from the aperture to the plane of interest. Taking the aperture field in terms of waveguide modes, where ψ now represents one of the component modal fields, and expressing (4.1) in cylindrical coordinates we obtain the far field at any distance, $L = z$, (in this case the distance from aperture to lens), given by

$$\begin{aligned}(\mathbf{e}_{tel})_{nl}^{TE/TM}(r_T,\phi_T,z) &= \frac{j}{\lambda z}\int_{\phi_0=0}^{2\pi}\int_{r_0=0}^{a}\mathbf{e}(r_0,\phi_0)\\ &\times\exp(-jkz)\ \exp(-jk(r_0^2+r_T^2)/2z)\ \exp(jkr_0r_T\cos(\phi-\phi_0)/z)\ r_0dr_0d\phi_0\end{aligned} \tag{4.2}$$

where a is the horn aperture radius and $\mathbf{e}(r_0,\phi_0)$ the component modal field at the aperture of the horn.

The telescope field must then undergo a fourier transform to recover the beam on the sky, such that for each waveguide mode

$$\begin{aligned}(\mathbf{e}_{sky})_{nl}^{TE/TM}(r_S,\phi_S,z) &= \frac{j}{\lambda zz'}\int_{\phi_T=0}^{2\pi}\int_{r_T=0}^{r}\int_{\phi_0=0}^{2\pi}\int_{r_0=0}^{a}\mathbf{e}(r_0,\phi_0)\ \exp(-jkz)\\ &\times\exp(-jkr_T^2/2z)\ \exp(jkr_0r_T\cos(\phi_0-\phi_T)/z)\ \exp(-jkz')\ \exp(-jkr_T^2/2z')\\ &\times\exp(jkr_T\sin\theta_S\cos(\phi_T-\phi_S))\ \exp(jkr_T^2/2f)\ r_0dr_0d\phi_0\ r_Tdr_Td\phi_T\end{aligned} \tag{4.3}$$

where r is the radius of the telescope aperture, z' is the distance between telescope aperture and sky field location, and $kr_s^2/2z' \to 0$ in the limit $z' >> r_s^2/\lambda$. An additional phase transformation term is included on transformation from the telescope to the sky, accounting for the focussing effect of the telescope, given by $T(r_T) = \exp(jkr_T^2/2f)$. This leads to a cancellation of terms in (4.3) when $z = f$, however we can also define the distance, Δ, between the horn aperture and its phase centre (i.e. the focus of the telescope) by writing $\exp(-jkr_T^2/2z)\ \exp(jkr_T^2/2f) = \exp(-jkr_T^2(\Delta/2fz)$. As $\Delta \to 0$ the integrals become numerically unstable, so it is useful to define this value directly in simulations. The phase centre of the Planck multi-moded horns lie behind the aperture, meaning a positive value for Δ in all cases.

A useful relationship comes from Born and Wolf [71] who showed that, integrating analytically over ϕ, the following solution will be obtained for modes with $\cos(n\pm1)\phi$ or $\sin(n\pm1)\phi$ variation (naturally so for waveguide modes whose definition are given in

section 2.3

$$\int_0^{2\pi} \exp(ix\cos\alpha)\ \exp(in\alpha)d\alpha\ =\ 2\pi i^n J_n(x) \tag{4.4}$$

Thus, it is found that two of the integrands may be rewritten as:

$$\begin{aligned}\int_{\phi_0=0}^{2\pi} \exp(jkr_0r_T\cos(\phi_0-\phi_T)/z)\ \begin{bmatrix}\cos(n\pm1)\phi_0\\ \sin(n\pm1)\phi_0\end{bmatrix} d\phi_0 \\ = J_{n\pm1}(kr_0r_T/z)2\pi i^{n\pm1}\begin{bmatrix}\cos(n\pm1)\phi_T\\ \sin(n\pm1)\phi_T\end{bmatrix}\end{aligned} \tag{4.5}$$

and

$$\begin{aligned}\int_{\phi_T=0}^{2\pi} \exp(jkr_Tr_S\cos(\phi_T-\phi_S)/z)\ \begin{bmatrix}\cos(n\pm1)\phi_T\\ \sin(n\pm1)\phi_T\end{bmatrix} d\phi_T \\ =\ J_{n\pm1}(kr_Sr_T/z)2\pi i^{n\pm1}\begin{bmatrix}\cos(n\pm1)\phi_S\\ \sin(n\pm1)\phi_S\end{bmatrix}\end{aligned} \tag{4.6}$$

This leaves only a double integral over r_T and r_0, however we can define the integral over r_0 as:

$$\Im_{n\pm1}(\chi_{nl},kar_T/z)\ =\ \int_{r_0=0}^{a} J_{n\pm1}(\chi_{nl}r_0/a)\ J_{n\pm1}(kr_0r_T/z)\ r_0\ dr_0 \tag{4.7}$$

such that on integration we obtain

$$\Im_{n\pm1}(\chi_{nl},\alpha)\ =\ \frac{a^2(\ \chi_{nl}\ [J_{n\pm1}(\alpha)J'_{n\pm1}(\chi_{nl})]\ -\alpha\ [J_{n\pm1}(\chi_{nl})J'_{n\pm1}(\alpha)]\ )}{(\alpha)^2-\chi_{nl}^2}, \tag{4.8}$$

where we have simplified by writing $\alpha\ =\ kar_T/z$. Equation 4.3 (in angular coordinates) can thus be written as a combination of one dimensional integrals given by:

$$\begin{aligned}I_{n\pm1}(\theta_S,\phi_S)\ =\ \int_{r_{T=0}}^{r} \Im_{n\pm1}(\chi_{nl},\alpha)\ J_{n\pm1}(kr_T\sin\theta_S) \\ \times\exp(-jk(\Delta)r_T^2/2f^2)(2\pi i^{n\pm1})\begin{bmatrix}\cos(n\pm1)\phi_S\\ \sin(n\pm1)\phi_S\end{bmatrix} r_T\ dr_T\end{aligned} \tag{4.9}$$

Thus, the far field on the sky of a given mode can be written as a sum of one-dimensional integrals across both co-polar and cross-polar directions, and is written as:

$$\begin{aligned}(\mathbf{e}_{sky})_{nl}^{TE/TM}(\theta_S,\phi_S)\ =\aleph^{TE/TM}(I_{n-1,l}^{TE/TM}(\theta_S,\phi_S)\pm(I_{n+1,l}^{TE/TM}(\theta_S,\phi_S)))\hat{\mathbf{i}} \\ \pm\ (I_{n-1,l}^{TE/TM}(\theta_S,\phi_S)\pm(I_{n+1,l}^{TE/TM}(\theta_S,\phi_S)))\hat{\mathbf{j}},\end{aligned} \tag{4.10}$$

where the modal coefficient $\aleph$ is given by $\aleph^{TE} = D_{nl}$ and $\aleph^{TM} = C_{nl}$, as derived in section 2.3. Finally, the total partially coherent field on the sky is obtained by quadrature summation of all modal fields using the expression given in [59];

$$I^{FF}(\theta,\phi) \;=\; \sum_{n}\left(\sum_{j}|\sum_{i}(S_{21}^{(n)})_{ij}\mathbf{e}_{i}^{(n)FF}|^{2}\right). \tag{4.11}$$

Thus, simply substituting $(\mathbf{e}_{sky})_{nl}^{TE/TM}(\theta_S,\phi_S,z)$ for the field in the equation above gives the total field on the sky of all modes combined. Of course the focussing effect of the mirrors in the actual telescope will raise the sidelobes to some degree unaccounted for by this model, which assumes direct propagation to the sky beyond the lens rim. To account for this we must incorporate the gain of the system. Gain in a multi-moded system, however, is slightly different from the general concept of antenna gain, so at this point we will take a brief detour to outline the added subtlety inherent in calculating the gain of a multi-moded system.

4.1.2 Telescope Optimisation

The Planck telescope is designed to provide high gain over very small angular scales, thus maximising the resolution of the telescope. To obtain the optimal equivalent beam from the projected aperture telescope, the correct telescope-equivalent lens radius must be known, as the integration in equation 4.9 is performed over r_T. This is rather difficult to calculate geometrically, as the dual reflector system of the actual telescope is being replaced by a single paraxial lens in contrast to the off-axis design of the actual telescope. To find the correct radius its value was varied, and the beam on the sky modelled, as shown in figure 4.5. At r_T=500 mm the beam is significantly wider than at higher values, with the first sidelobes at 35 dB below peak. The beam-size is truncated most at r_T=750 mm, with sidelobes first at 45 dB below peak, and this value was chosen for modelling.

As mentioned previously, the difference between the focal length of the telescope and the distance from the horn phase centre to the telescope, given by $\Delta = f - z$, has a significant impact upon the accuracy of the projected aperture technique. As $\Delta \to 0$, the integrand of equation 4.3 becomes numerically unstable, and will take longer to calculate. At the same time the benefit of having the phase centre of the horn near the aperture is seen in figure 4.6, where the beam on the sky is plotted with variation in Δ and for r_T=750 mm. For a value of Δ=4 mm the beam width spans 0.2 °, while at Δ=1 mm it is truncated at angles above 0.13 °. Approaching Δ=0 mm the beam width

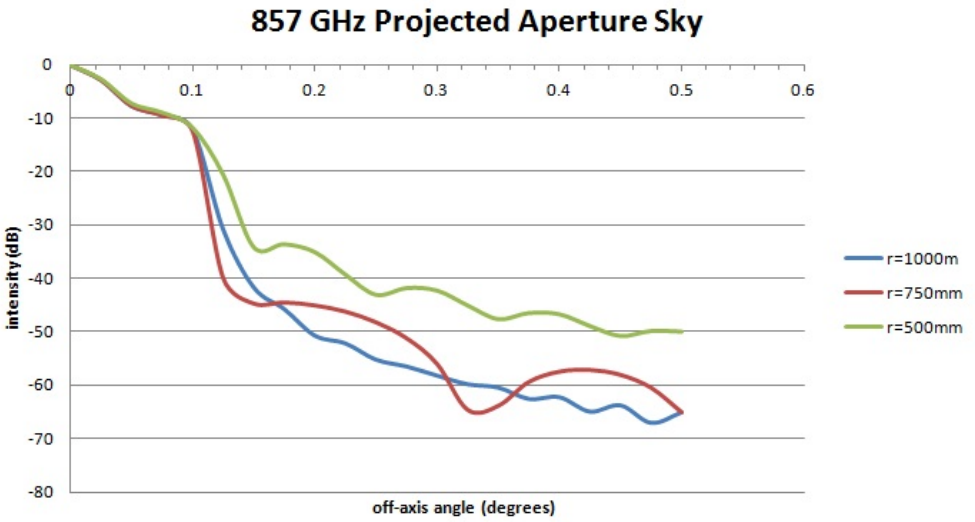

FIGURE 4.5: Variation in beam on the sky with r_T, where on-axis peaks are normalised to 0 dB in all cases.

reduces further, however the improvement is minimal compared with the trade-off in time required to calculate the integrals for very small values of Δ. Δ=4 mm is in fact a good approximation to the actual phase centre of the horn [59], and was used for all calculations.

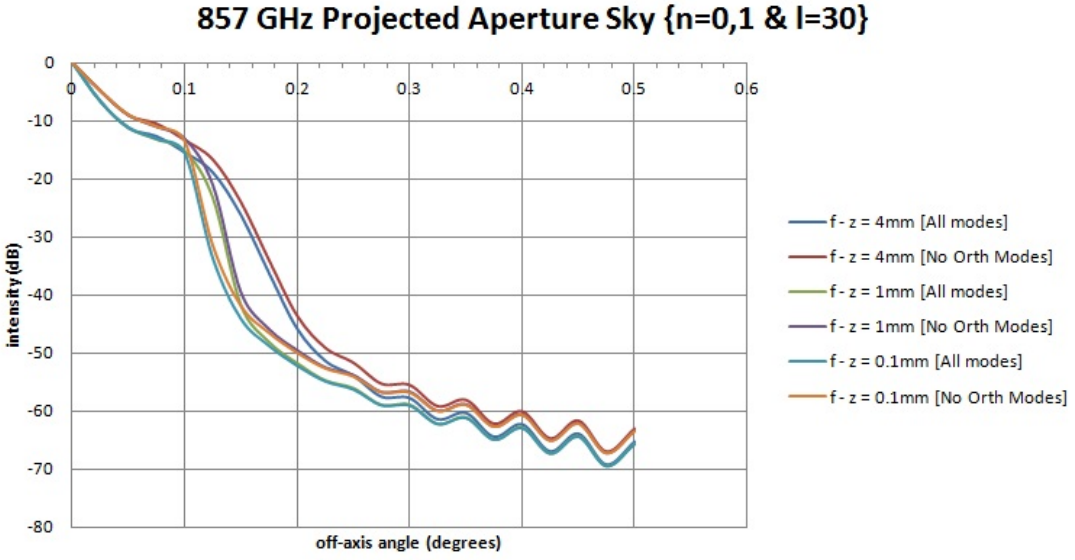

FIGURE 4.6: Beam on the sky for different Δ values, two azimuthal orders, and 30 modes per order, where beam peaks are normalised to 0 dB in all cases.

The mode content of the beam propagated through the telescope also impacts the beam on the sky to some extent. In figure 4.6 the main beam out to 0.5 ° is shown, where values of $n = 1, 2$ and $l = 30$ respectively define the azimuthal orders and number of modes per order propagated to the sky. This includes the fundamental $n = 1$ modes through

which the majority of power is coupled, however at 857 GHz there are five azimuthal orders of modes, and though higher order modes couple less power to the telescope their contribution should not be neglected. Figure 4.7 shows the main beam on the sky plotted for the same variation in Δ, but for different mode content as compared with figure 4.6. Crucially, by adding all higher order modes, the main beam becomes broader and flatter, before tapering away quickly. This is a result of modes with central nulls broadening the main beam, which increases gain. Halving the number of modes per order does not have a significant effect on the beam (which can be seen by comparing the plots in figure 4.7), however in all cases the importance of including all orthogonal modes is clear. They increase the on-axis gain of the beam by ~ 3 dB for all variations of Δ and mode content, while simultaneously truncating the beam width to an appreciable degree.

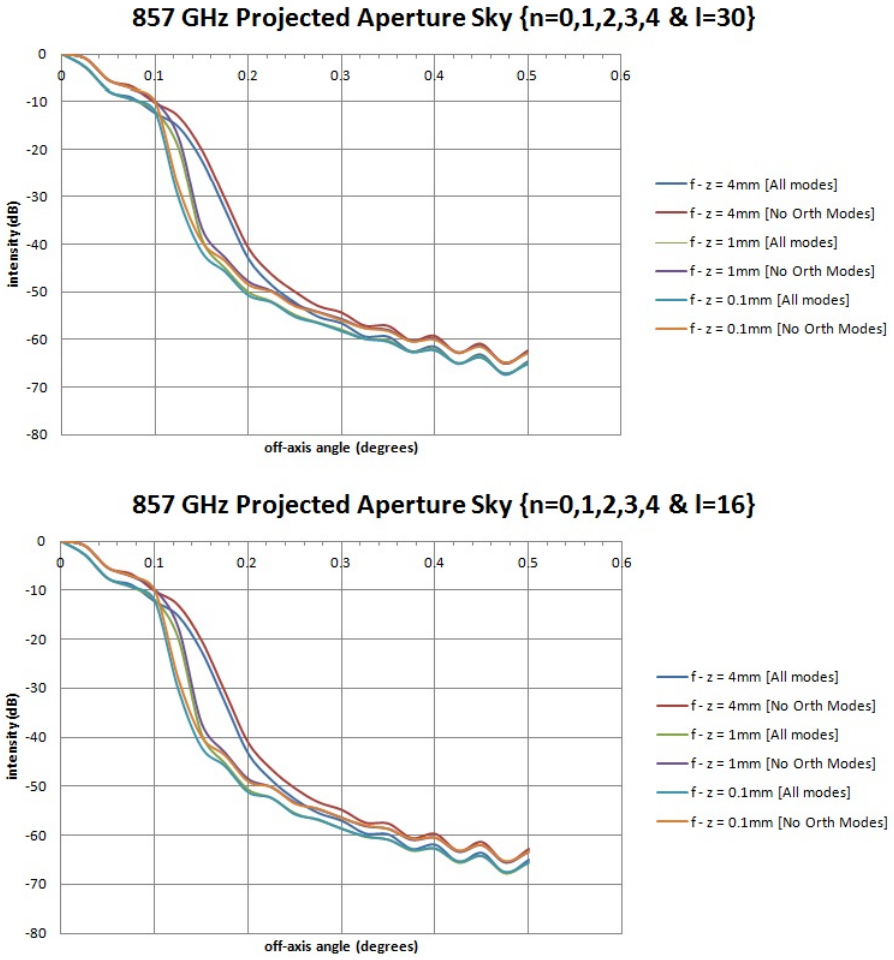

FIGURE 4.7: (Top) Beam on the sky for different Δ values, five azimuthal orders and 30 modes per order. (Bottom) Five azimuthal orders, and 15 modes per order. On-axis maxima are normalised to 0 dB in all cases.

As seen already, there are some limitations to the technique as $\Delta \to 0$, however another limiting factor is the angular scale to which the main beam can be effectively modelled.

As θ increases away from the main beam the integration takes longer to complete, and beyond θ 1° it will break down completely. For this reason only $\pm 1°$ extent of the main beam can be modelled accurately, however this does not affect the sidelobes due to spillover, which are modelled using the horn far-field beam pattern rather than using a Fresnel transformation. The sidelobe is simulated using the portion of the horn far-field beam pattern which passes the lens and goes directly to the sky, arising between 30° and 35° from the main beam in the paraxial system. In the real system this is equivalent to the angular extent of the secondary seen by the horn, which is illuminated by spillover from the primary, as illustrated in figure 4.8.

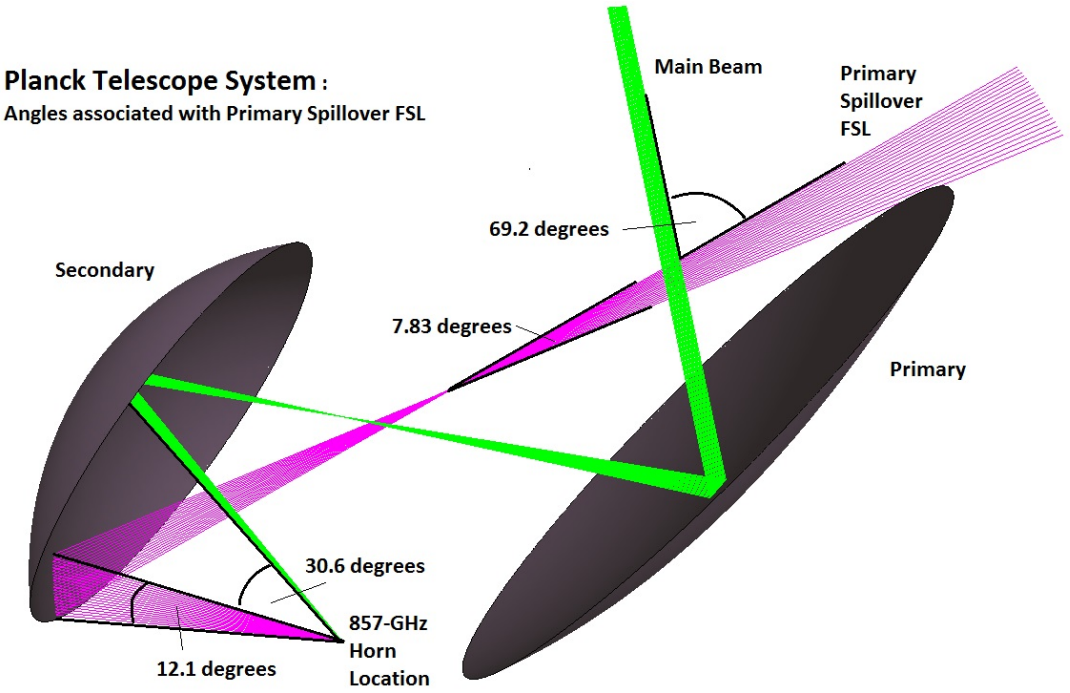

FIGURE 4.8: Ray diagram illustrating the angles associated with the primary FSL being simulated. In the actual telescope, the primary spillover sidelobe is expected roughly 69° from the main beam. The projected aperture system is paraxial, however, thus the primary spillover sidelobe arises a mere 30° from the main beam.

4.1.3 Projected-Aperture Sky Beams

To correctly simulate sidelobe levels by the projected aperture technique, the main beam focussed by the telescope must be added to that which misses the edge of the telescope-equivalent lens. This simulates the expected spillover from the parts of the beam that miss the primary, however due to the paraxial nature of the system it will be seen in a different angular region of the sky than would be the case in the actual telescope (see figure 4.8). It will also have a different shape to the spillover which would in reality be seen, as the beam curvature incurred on reflection from the secondary is ignored here.

The beam instead, is simply modelled as the far-field beam of the horn which travels directly to the sky, undergoing no reflection effects. Here, however, the different gains of the two beams must be considered. In a complete model of the Planck system, such as that done in GRASP9, the power in both main beam and sidelobe share reference to the total power output from the horn, and their correct levels with respect to each other are readily known. In the projected aperture technique, however, the main beam intensity is calculated with respect to the total power in the portion of the horn beam which strikes the lens. The sidelobe intensity, on the other hand, is deduced from the total power emitted by the horn. To find the correct levels of one with respect to the other, the total gain of each beam must be calculated. The results of this are shown in figure 4.9, where the overlap between telescope gain, horn gain, and horn gain in the region beyond the lens gives the expected levels of spillover with respect to the main beam. Figure 4.9 shows the results for three different horn beams (the good, bad and worst case horns described in section 3.4.1 and the GTD beams for which are illustrated in figures 3.53, 3.54 and 3.55).

As outlined in section 3.2, and illustrated by figure 4.8 only a 7.8 ° region of the sky couples primary spillover to the telescope, so the tapered sidelobe pattern of the horn far-field shown in figure 4.9 does not accurately reflect the sidelobe structure of the telescope. In figure 4.9 only 12.1 ° of the horn far-field spillover beam from 30.6 ° out to 42.7 ° (the angular extent of the secondary illuminated by the primary FSL) should be incorporated into a full sky beam. In reality, the sidelobe will also be seen much further from the main beam than assumed by the paraxial model, from 69.2 ° to 77 ° away from the main beam (illustrated in figure 4.8). The portion of the beam which forms the sidelobe is also inverted on the sphere due to reflection from the secondary, however this is not of critical importance due to the lack of features. The final beams with sidelobes chopped to 7.8 ° width are shown in figure 4.10, where the red and blue plots indicate the sidelobe beam with and without account of primary spillover. The low-level noise in the plots was generated by 'pasting' data for an equivalent sky beam from a standard HFI 100 GHz telescope beam into regions outside of the main beam and spillover. Here the noise level is so low that this was deemed a useful work-around to the inability to model regions off-axis in the 857 GHz band.

These can be compared with figures 3.53 3.54 and 3.55, where the sidelobes simulated using GTD are outlined. While the GTD simulations depict total intensity as a function of angle, the projected aperture beams simulate total gain of the telescope, however the difference between the levels of the main beam and sidelobe are the same in each case. The width of the sidelobe is somewhat smaller in the case of the projected aperture beam, however it does not take into account off-axis reflection from the secondary, which

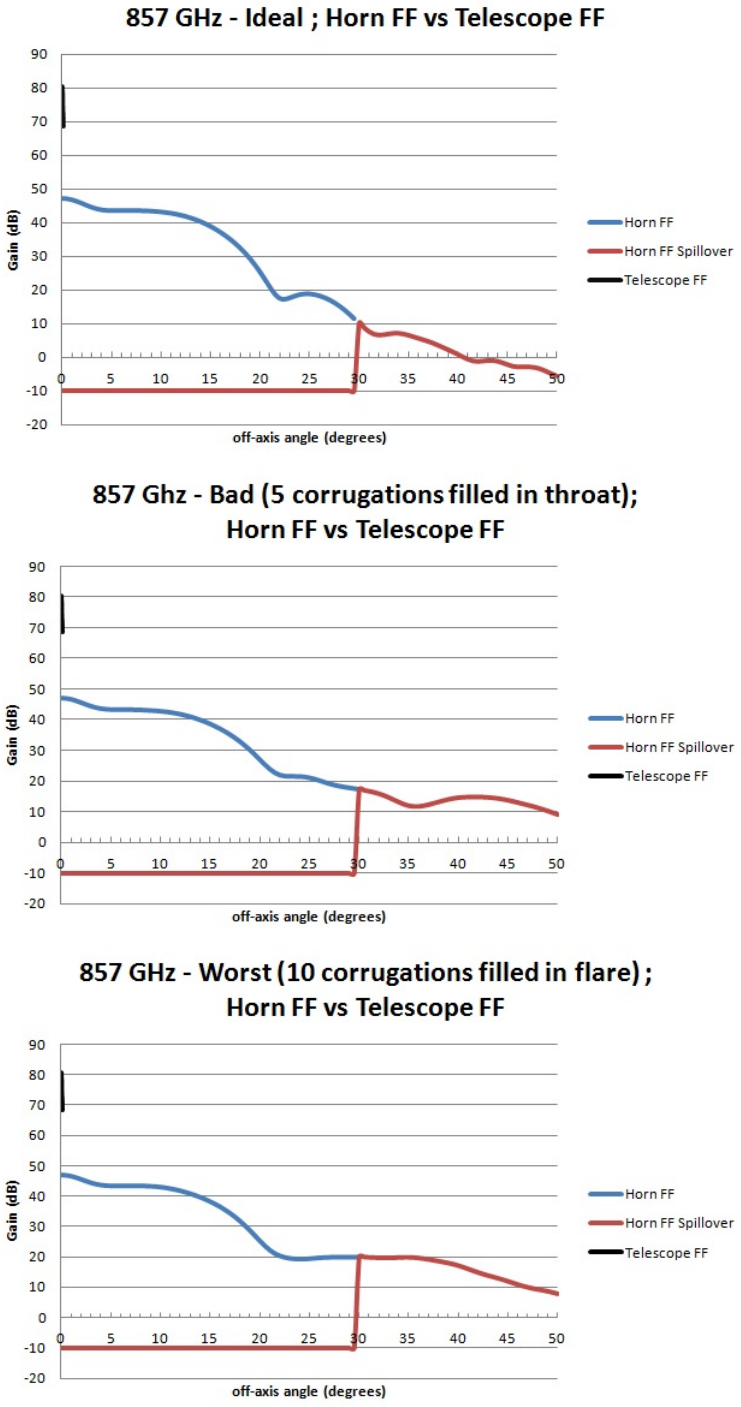

FIGURE 4.9: Overlap between telescope far-field gain and horn far-field gain, where the horn far-field beyond $\sim 30^\circ$ represents spillover from the telescope. The three beam patterns used correspond to the ideal, bad and worst case horns described in section 3.4.1.

results in a broader sidelobe beam on the sky. Although the projected aperture technique provides a good attempt at modelling sidelobe levels in the absence of more rigorous methods, the paraxial nature of the technique is a definite limitation. Furthermore, the real sidelobe projected on reflection from the secondary spans $\sim 60^\circ$ around the

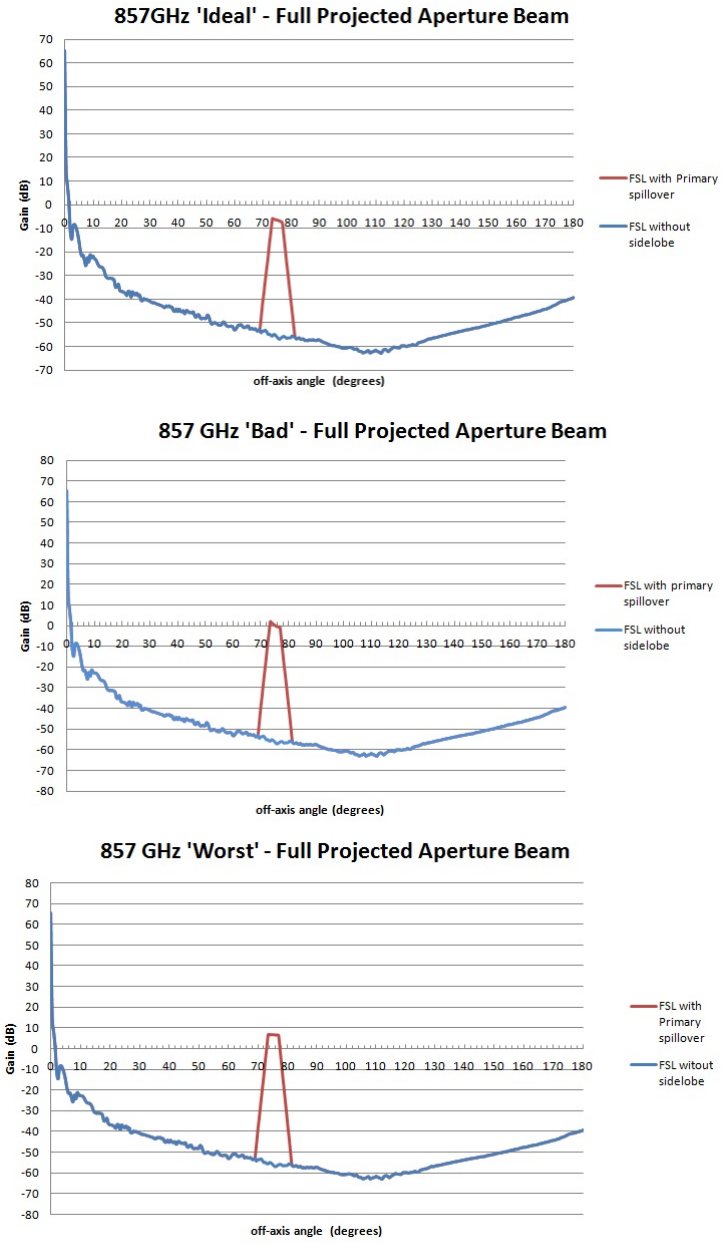

FIGURE 4.10: Final projected aperture beams for the good, bad and worst-case horns, where main beam is normalised to the on-axis intensity of a GRASP9 simulated multi-moded 857-GHz beam.

sphere in ϕ (see figure 3.46 for a depiction of the telescope sky coordinates), tapering in width away from the central peak as the reflectors and baffles block more and more of the secondary reflected beam. This cannot be accurately simulated using the projected aperture technique due, again, to the paraxial nature of the system, and the inability to incorporate the baffles present in the actual system. However, the projected aperture technique does give us a quick and intuitive way to model the high-frequency channels approximately, and is a useful check of the more detailed GTD calculations.

4.2 Gaussian Beam Mode Model of Planck 857-GHz Spillover

Another useful technique for the modelling of telescope systems is the use of Gaussian beam modes (GBM), which has been discussed in chapter 2. With this technique, the aperture field of a standard horn antenna can be decomposed into a sum of orthonormal Gauss-Laguerre modes (in spherical coordinates) so that the aperture field $f(u, z)$ is written

$$f(u, z = 0) = \sum_{m=0}^{\infty} a_m E_m(u) \tag{4.12}$$

where $E_m(u)$ is the Gauss-Laguerre mode of order m, and u is a point on the aperture plane. a_m are the expansion coefficients of each mode, which are determined by

$$a_m = \int E_m^*(u) f(u, z = 0) du. \tag{4.13}$$

Gaussian beam modes exhibit the useful properties that their relative amplitude distribution doesn't change on propagation, only its beam width and phase evolve in a manner which is easy to calculate. (The amplitude and phase of the sum of the modes evolves of course). Thus the field, $f(u, z)$, at any distance, z, from of the aperture can be retrieved by multiplying the known aperture coefficients by the Gauss-Laguerre modes at that plane.

As with the projected aperture technique discussed previously, the telescope system will be modelled as an equivalent paraxial lens system, where in this case a dual-lens configuration can be implemented. Unfortunately this does impose a limit on the replication of the actual Planck beam patterns, however GBM does not suffer from the restriction in angular extent of the integral calculation experienced with the projected aperture technique. The field can be accurately determined at any point, and extremely quickly, by decomposing the field into Bessel functions inherent to both waveguide modes and Gauss-Laguerre modes. Herein we shall outline the mathematical construction of the sky beam, and thus estimate the Planck 857-GHz band spillover, using as an example the three test cases of Section 3.4.1. The paraxial description of the system and various system parameters are shown in figure 4.11.

The cartesian description of the TM and TE modal fields in 2.28 and 2.34, which suffices to describe the field in any cylindrically symmetric waveguide, depends on Bessel functions of order J_{n+1} and J_{n-1}, where n is the azimuthal order of the modal field. A

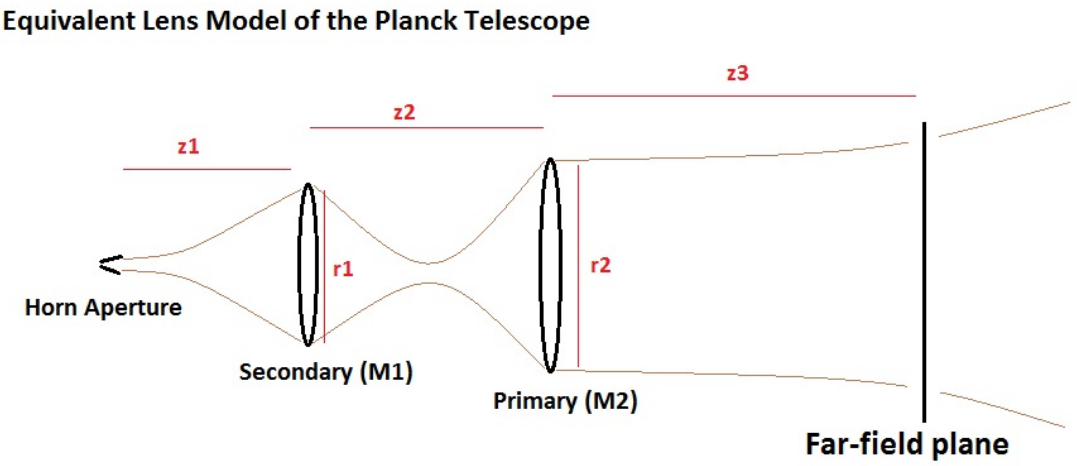

FIGURE 4.11: Paraxial description of the Planck telescope with lenses in place of reflectors. Distances (*z1*,*z2*,*z3*) and lens radii (*r1*,*r2*) are required to calculate the propagation of Gauss-Laguerre modes.

Gaussian beam mode description of the field uses Gauss-Laguerre modes:

$$E_p^n(r,\varphi,z) = \left(\frac{2p!}{\pi(p+n)!}\right)\frac{1}{w(z)}\left(\frac{\sqrt{2}r}{w^2}\right)^n L_p^n\left(\frac{2r^2}{w^2}\right) \\ exp\left(-\frac{r^2}{w^2(z)} - jkz - \frac{j\pi r^2}{\lambda R(z)} - j(2p+n+1)\phi_0(z)\right) exp\left(jn\varphi\right). \tag{4.14}$$

and here there is a dependence on Laguerre polynomials of order L_p^{n+1} and L_p^{n-1}. (In equation 2.97 the equation was governed by variables p and m, which have been replaced with p and n here to better illustrate the commonality with the modal field equations.) In each case the function provides a circularly symmetric description of one modal field of order n, and the symmetry between the two field description formalisms can be exploited for the purposes of telescope modelling using the GBM technique.

Separating and summing the J_{n+1} and J_{n-1} components of the waveguide mode aperture field, one can obtain a new description of the field in terms of Bessel functions rather

than the traditional x,y-component descriptions outlined previously:

$$\begin{aligned} e_{nl}(J_{n-1}) &= D_{nl}\left(J_{n-1}(q_{nl}r/a)\begin{pmatrix}\cos(n-1)\phi\\ -\sin(n-1)\phi\end{pmatrix}\right)+ \\ &\quad C_{nl}\left(J_{n-1}(p_{nl}r/a)\begin{pmatrix}\cos(n-1)\phi\\ -\sin(n-1)\phi\end{pmatrix}\right) \\ e_{nl}(J_{n+1}) &= D_{nl}\left(J_{n+1}(q_{nl}r/a)\begin{pmatrix}\cos(n+1)\phi\\ -\sin(n+1)\phi\end{pmatrix}\right)- \\ &\quad C_{nl}\left(J_{n+1}(p_{nl}r/a)\begin{pmatrix}\cos(n+1)\phi\\ -\sin(n+1)\phi\end{pmatrix}\right) \end{aligned} \tag{4.15}$$

Equivalently, after performing a singular value decomposition of the scattering matrices of a horn as described in Section 2.3.4, the vector field of any eigenmode at the aperture of a multi-moded horn can be written as:

$$\bar{\mathbf{E}}_{svd} = \sum Y_{nl}^{svd}\ [e_{nl}(J_{n-1})\hat{\mathbf{e}}_1 + e_{nl}(J_{n+1})\hat{\mathbf{e}}_2] \tag{4.16}$$

or, by separating the vector components, as:

$$\bar{\mathbf{E}}_{svd} = [\sum Y_{nl}^{svd} e_{nl}(J_{n-1})]\ \hat{\mathbf{e}}_1\ + [\sum Y_{nl}^{SVD} e_{nl}(J_{n+1})]\ \hat{\mathbf{e}}_2 \tag{4.17}$$

where Y_{nl}^{svd} is the SVD-generated modal coefficient of the particular eigenmode field. The Gauss-Laguerre representation of the same vector field at the aperture of a multi-moded horn can be written in terms of the same unit vectors as:

$$\bar{\mathbf{E}}_{Lag} = [\sum_{0}^{p} a_{np} L_p^{n-1}(w_{ap}, \phi_{ap}, z_{ap})]\ \hat{\mathbf{e}}_1 + [\sum_{0}^{p} b_{np} L_p^{n+1}(w_{ap}, \phi_{ap}, z_{ap})]\ \hat{\mathbf{e}}_2 \tag{4.18}$$

To transition between waveguide and free space, an overlap integral between the two waveguide modal fields and the corresponding Gauss-Laguerre field equation is performed at the aperture, returning a set of Laguerre modal coefficients up to order p, and these suffice to describe the field:

$$\begin{aligned} a_{np} &= \int_0^r \bar{\mathbf{E}}_{Svd} \cdot \bar{\mathbf{E}}_{Lag}^{n-1}\ \ rdrd\phi \\ b_{np} &= \int_0^r \bar{\mathbf{E}}_{Svd} \cdot \bar{\mathbf{E}}_{Lag}^{n+1}\ \ rdrd\phi \end{aligned} \tag{4.19}$$

Looking again at 4.15, the only variation between the component fields is the trigonometric cos/sin dependence of each modal component, which is a function of n and ϕ.

However on integration across ϕ it is found that

$$\int \hat{\mathbf{e}_1} \cdot \hat{\mathbf{e}_2} \, d\phi \;=\; 0 \tag{4.20}$$

due to cancellation of trigonometric terms, which simplifies both integrals to a dependence on r. Conveniently, in each integral only the appropriate J_{n-1} or J_{n+1} component of $\bar{\mathbf{E}}_{Svd}$ will couple to each of $\bar{\mathbf{E}}_{Lag}^{n-1}$ and $\bar{\mathbf{E}}_{Lag}^{n+1}$, after which the field at any distance, z, from the aperture can be recreated. By implementing the ray matrix formalism outlined in Section 2.3.6 this can be extended to reproduction of the beam on propagation through the lens-equivalent telescope described in figure 4.11. Under this formalism the beam width, w, radius of curvature, R, and phase slippage, ϕ_0, can be recovered at any point in the lens system, and ultimately on the sky. Spillover beyond each of the two lenses represents the equivalent expected spillover of the telescope, and is correctly accounted for by ray matrix propagation from the plane of the corresponding lens to the sky.

On reaching the lens-equivalent secondary the beam is calculated by summing the aperture coefficients (a_{np}, b_{np}) times the Gauss-Laguerre modes at that distance from the aperture. This is the equivalent distance of the secondary from the 857-1 horn location on the Planck FPU, $z_{sec} = 0.911\,\mathrm{m}$. On implementing the ray matrix procedure a new beamwidth (w_{sec}), radius of curvature (R_{sec}), and phase slippage (ϕ_{sec}) are also obtained, and these are entered into the Gauss-Laguerre equation before summing with the original aperture coefficients.

$$\begin{aligned} E_{sec}(n-1) &= \sum_{0}^{p} a_{np} L_p^{n-1}(w_{sec}, \phi_{sec}, z_{sec}) \\ E_{sec}(n+1) &= \sum_{0}^{p} b_{np} L_p^{n+1}(w_{sec}, \phi_{sec}, z_{sec}) \end{aligned} \tag{4.21}$$

The beam is split into two components at the rim of the lens; one component is truncated by the lens, while the other component represents spillover past the lens. The new coefficients c_{np} and d_{np}, representing the truncated beam, are found by performing an integral out to the radius of the lens, $r_{sec} = 0.525\,\mathrm{m}$, which accounts for the fact that in reality the secondary is rotated, and thus has a smaller cross-section of incidence along

the line of sight (LOS) of the horn beam:

$$\begin{aligned} c_{np} &= \int_0^{r_{sec}} 2\pi r E_{sec}(n-1) L_p^{n-1}(w_{sec}, \phi_{sec}, z_{sec}) dr \\ d_{np} &= \int_0^{r_{sec}} 2\pi r E_{sec}(n+1) L_p^{n+1}(w_{sec}, \phi_{sec}, z_{sec}) dr \end{aligned} \tag{4.22}$$

Propagation from secondary to primary is performed in a similar manner to before, where the distance between the two lenses is given by $z_{pri} = 1.645\,\mathrm{m}$, and the ray matrix beam parameters for the secondary truncated beam at the plane of the primary lens are given by w_{pri}, R_{pri}, and ϕ_{pri}. Thus, we calculate the beam at the plane of primary as:

$$\begin{aligned} E_{pri}(n-1) &= \sum_0^p c_{np} L_p^{n-1}(w_{pri}, \phi_{pri}, z_{pri}) \\ E_{pri}(n+1) &= \sum_0^p d_{np} L_p^{n+1}(w_{pri}, \phi_{pri}, z_{pri}) \end{aligned} \tag{4.23}$$

and the beam is split into two components. The truncated beam components required for calculation of the main beam on the sky are given by an integral over the radius of the primary, $r_{pri} = 0.782\,\mathrm{m}$, which accounts for the angular width of the primary as seen by the secondary in the physical telescope:

$$\begin{aligned} f_{np} &= \int_0^{r_{pri}} 2\pi r E_{pri}(n-1) L_p^{n-1}(w_{pri}, \phi_{pri}, z_{pri}) dr \\ g_{np} &= \int_0^{r_{pri}} 2\pi r E_{pri}(n+1) L_p^{n+1}(w_{pri}, \phi_{pri}, z_{pri}) dr. \end{aligned} \tag{4.24}$$

The primary spillover coefficients are a replica of the truncated secondary coefficients but with the coefficients representing the truncated portion of the beam on the primary subtracted, thus leaving only the component which misses the lens. These are given by:

$$\begin{aligned} h_{np} &= c_{np} - f_{np} \\ i_{np} &= d_{np} - g_{np}. \end{aligned} \tag{4.25}$$

The main beam on the sky is then calculated from the coefficients representing the main beam truncated by the primary, h_{np} and i_{np}, where the parameters w_{sky}, and ϕ_{sky} are found by ray matrix calculation from the primary to an arbitrary far-field distance here

set to $z_{sky} = 1000\,\mathrm{m}$:

$$\begin{aligned} E_{main\ beam}(n-1) &= \sum_{0}^{p} f_{np} L_p^{n-1}(w_{sky}, \phi_{sky}, z_{sky}) \\ E_{main\ beam}(n+1) &= \sum_{0}^{p} g_{np} L_p^{n+1}(w_{sky}, \phi_{sky}, z_{sky}). \end{aligned} \tag{4.26}$$

Finally, to calculate the field due to spillover from the primary, the beam parameters w_{waist} and ϕ_{waist} must first be found by ray matrix propagation from the secondary to the waist position between the two lenses. Further propagation to the sky from this point gives the beamwidth ($w_{pri\ sp}$) and phase slippage ($\phi_{pri\ sp}$) parameters correct for the primary spillover beam, which will travel a distance $z_{waist-sky} = R_{sec} + z_{pri} + z_{sky}$ to the sky. R_{sec} here represents the radius of curvature of the beam at the secondary, which is naturally the negative of the distance from the secondary to the next beam waist. When summed with z_{pri} the distance from the beam waist to the primary is found, which in turn is summed with z_{sky} to give the total distance travelled by the primary spillover beam from the waist. The two equations representing primary spillover are then given by:

$$\begin{aligned} E_{pri\ spillover}(n-1) &= \sum_{0}^{p} h_{np} L_p^{n-1}(w_{pri\ sp}, \phi_{pri\ sp}, z_{waist-sky}) \\ E_{pri\ spillover}(n+1) &= \sum_{0}^{p} i_{np} L_p^{n+1}(w_{pri\ sp}, \phi_{pri\ sp}, z_{waist-sky}). \end{aligned} \tag{4.27}$$

Having generated the fields of the main beam and spillover for a single mode using equations 4.26 to 4.27, the total field on the sky is found by quadrature summation of the $E(n-1)$ and $E(n+1)$ field components, and subsequent quadrature summation of these with all other hybrid mode field components. For completeness the beams on the sky at 730 GHz (for the three horn geometries seen previously in Section 3.4.1), are shown in figure 4.12. Similar to the projected aperture model, the paraxial system will give rise to spillover at an unrealistic angle from the main beam. To rectify this the spillover beam has once again been moved the appropriate distance from the main beam such that it can be compared with the GRASP model in Section 3.4.1. As with the projected aperture technique, the beam pattern is a function of telescope gain rather than intensity, however the difference between main beam and spillover level remains consistent across all models, and here can be seen to vary between 70 dB below peak for the worst-case horn, up to 73 dB below peak for the ideal horn. Unaccounted for in this model are the projection effects of the secondary reflector which will naturally invert the fraction of the aperture beam pattern which forms the sidelobe pattern on the sky (as outlined in Section 4.1.1), and also amplifies the sidelobe somewhat as a 12.1 ° cross-section of the secondary forms a 7.8 ° sidelobe on the sky. For this reason

the difference between the sidelobe levels of each beam are quite small in the case of the paraxial GBM system.

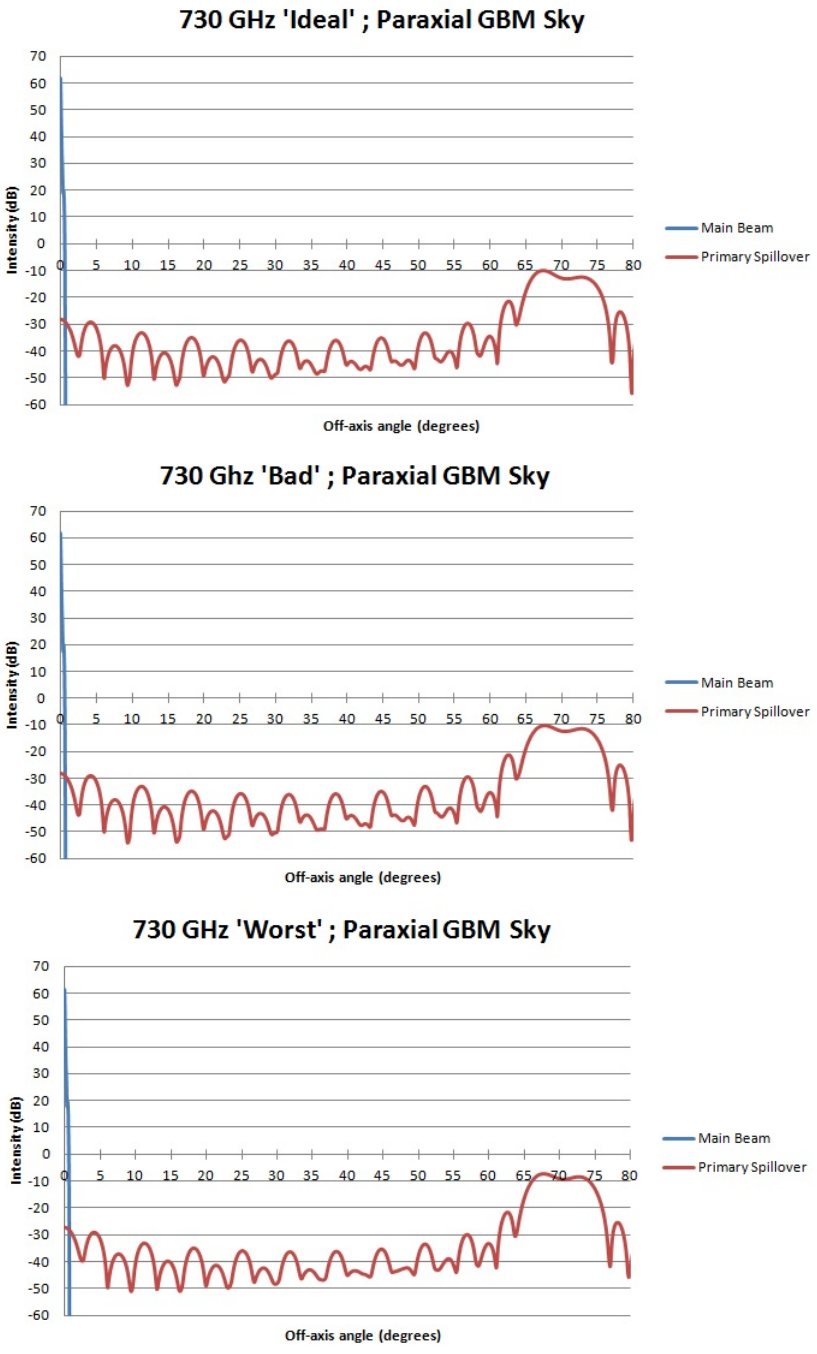

FIGURE 4.12: GBM simulated sky beam cuts of the three Planck 857-GHz horn test cases at 730 GHz, where the main beam and primary spillover beam have been calculated.

This elegant technique improves upon the computation time of the projected aperture technique, due to the reduction of the integrals to a radial dependence allowing for quicker calculation. Further development would see incorporation of the projection effects of the actual telescope, thus giving a truer representation of the spillover levels

by lifting the constrictions of the paraxial system. In any case, both techniques provide a quick, intuitive check of the complete GRASP9 GTD model of section 3.4.1.

4.3 Investigation of Surface Deformation on Planck Reflectors

An additional issue investigated in this thesis is the periodic surface deformations introduced onto the reflector surfaces from print-through of the reflector supporting structure. This causes an effect similar to that of a diffraction grating, whereby images of the main beam appear at regular intervals and small angular distances from the main beam itself. The closer the size of the reflector distortion approaches the wavelength of the incident radiation, the more prominent the diffraction effect appears on the sky. The main beam images formed as a result of the effect are referred to as 'grating' lobes, and were first highlighted by measurement of surface inaccuracies on the mirrors after manufacturing [72]. The contour plot of figure 4.13 highlights the various deformations measured across the surface of the primary reflector. Most noticeably on the left-most part of the surface, horizontal straight lines were seen at regular intervals, crossed intermittently by similarly straight lines at 45 ° and 90 ° with respect to them. The same features are less prominent on the right hand side, however their regularity could not be ignored. They arise form core print-through, and their implications on main beam properties will later be investigated by the author.

An analysis of the effects of this surface deformation at 857 GHz was performed by TICRA in 2000, where the print-through was modelled as a linearly varying surface function, paving the way for an upgraded GRASP9 implementation of quilting distortions as a second order function with which the user could better define their reflector surface. By generating 10 μm dimples linearly spaced across the surface of the primary they saw a noticeable effect on the beam far-fields, with distinct resonant peaks only 30 dB to 40 dB below peak, as shown in figure 4.14. This choice of dimple size illustrated a worst case scenario for complete surface degradation, however in many regions of the surface dimples of this size are seen to arise, most noticeably as the periodic straight lines of core print-through mentioned previously.

In the TICRA modelling at 857 GHz, however, a simple Gaussian fit to the aperture field of the horn was performed, and this was propagated through the system. Extensively discussed in this thesis is the incoherent multi-moded nature of the Planck 857-GHz beams, and the necessity to decompose the aperture field into multiple modal fields,

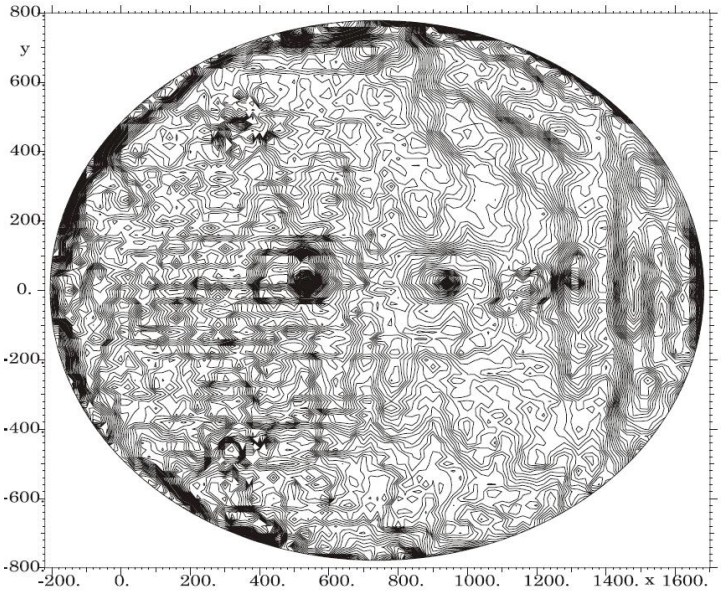

FIGURE 4.13: Contour plot of deformations (most noticeable as horizontal strips lining the left hand side), caused by imprint of the mirror support structures on the surface of the primary reflector, with intervals of 1 μm between contours. The surface deformations averaged -3 μm from the ideal plane, with a maximum of 51 μm and minimum of -42μm. [72]

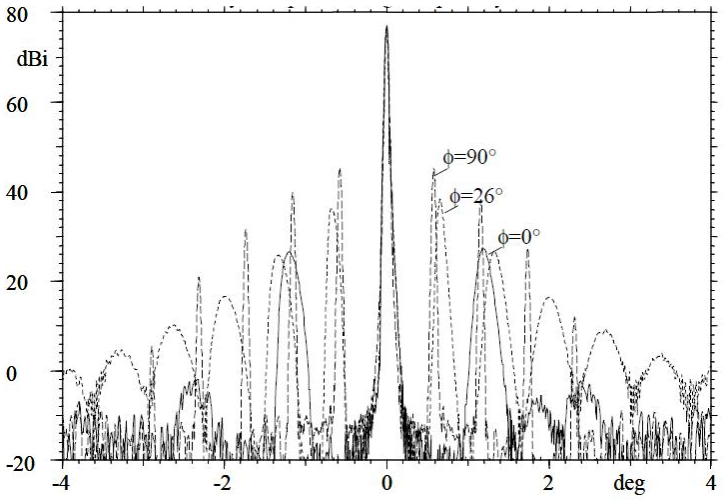

FIGURE 4.14: The simulated effect of primary reflector surface deformations on the 857-GHz beams for a Gaussian fit to the horn aperture field. [73]

each of which must then be propagated through the telescope separately. Modelling the 857-GHz aperture as a simple Gaussian discounts all of the complex phase information inherent in each incoherent field, and on which the nature of their propagation depends. For this reason the effects have been remodelled here, with a full account taken of the 857-GHz fields.

Measurements of the Planck beams [72] at 100 GHz also displayed grating lobes either side of the main beam. Here they were seen further from the main beam than at 857 GHz,

which was as expected due to the wavelength dependence of the grating effect. They peaked at $\sim 4.3\,^\circ$ off-axis, with smaller lobes symmetrically spaced at smaller off-axis angles, as highlighted in figure 4.15. Here again the grating lobes arise from surface deformation due to the dimpling of the support structure, which must be equivalent to a regular surface distortion at 30 mm intervals.

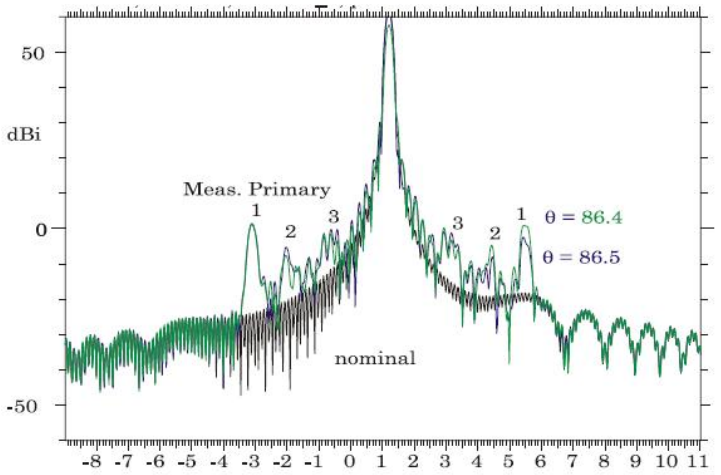

FIGURE 4.15: The measured effect of primary reflector surface deformations on the Planck 100-GHz beam [73]

Following the TICRA analysis, the core print through, also referred to as quilting, is modelled here as a second order function across a surface within the boundaries of an equilateral triangle of side length, S=30 mm. These triangles form hexagonal structures across the surface of the reflector, which on a larger scale are visible as the distinctive horizontal lines in figure 4.13. Each triangle is bordered by unit vectors $\hat{s}$ and $\hat{t}$ as shown in figure 4.16.

A graphical representation of the deformation in 3D is given in figure 4.17.

The variation of the surface height from nominal is described by a second order equation, which is implemented in each equilateral triangle of the complete hexagonal structure. It is written as :

$$f(s,t) = 27 \times peak \times (st - (st^2 + s^2 t)) \tag{4.28}$$

which fulfills the symmetry requirements and boundary conditions of the surface.

These periodic structures cause grating lobes in the far-field of the telescope, the position of which are described by a typical λ/D relationship, such that the longer the wavelength the further from the main beam these lobes appear. The angular distance of any lobe from the main beam is given by

$$\sin\theta_{gr} = \lambda/S \tag{4.29}$$

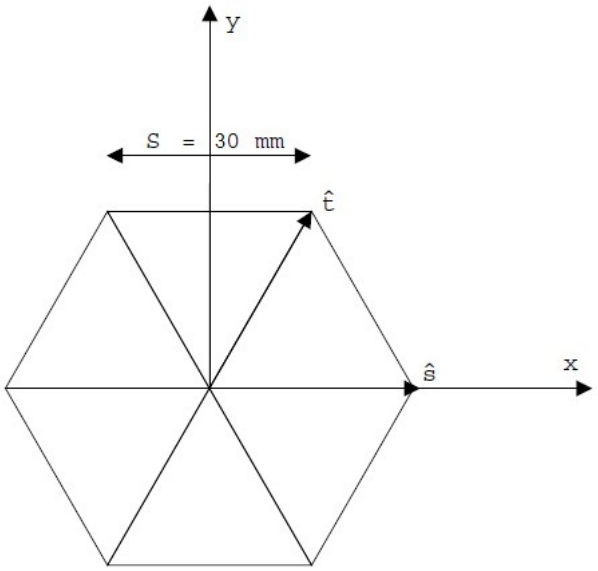

FIGURE 4.16: Coordinate system in which core print-through can be represented as a hexagonal surface deformation. [72]

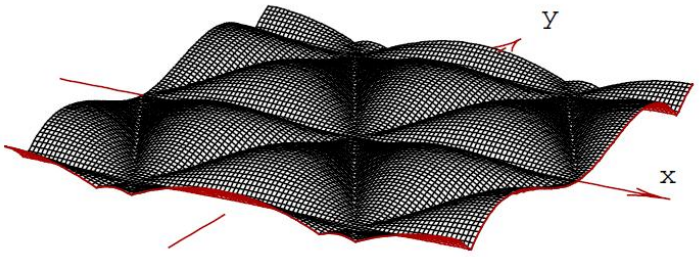

FIGURE 4.17: Core print-through visualised by 3D graphical representation. [72]

for $\phi = 30\,^\circ$, $90\,^\circ$, $150\,^\circ$, etc. or

$$\sin\theta_{gr} = \lambda/S\sqrt{3} \tag{4.30}$$

for $\phi = 0\,^\circ$, $60\,^\circ$, $120\,^\circ$, $180\,^\circ$, etc. Here ϕ is the radial direction along which a cut through the beam is taken, as described in section 3.4.1 and by figure 3.46, λ is the wavelength of the radiation, and S the side length of the honeycomb structure. While the equation above suffices to describe the innermost grating lobes, alternate lobes will arise at integer multiples of θ away from the main beam.

A 'Quilting Surface' is now available in GRASP9, which requires definition of either a hexagonal, square or triangular pattern, in which the side length and peak at the centre of each shape are defined. The peak describes the variation in surface height from the nominal case, while the side length of whichever shape is defined will remain the same on all sides. This is implemented throughout this work and the dimensions of the surface

will be described later.

The spacing of the hexagonal supports on the underside of the primary mirror is ~ 30 mm, which can be implemented by means of a hexagonal grid defined by the GRASP9 surface described above. The mapping of a hexagonal grid across a surface is illustrated in figure 4.18.

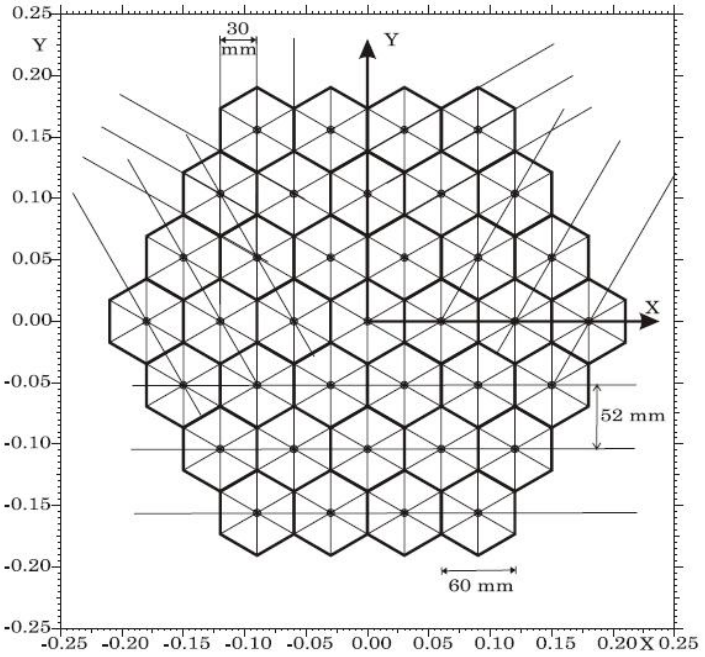

FIGURE 4.18: Hexagonal 'Quilting' surface as implemented in GRASP9 for Planck mirror support structures of 30 mm side length. The positive x-axis is aligned with $\phi = 0°$ on the sky, and ϕ increases anti-clockwise rom this axis. [72]

The 52 mm spacing between the centres of each hexagon is equivalent to the spacing between the mirror supports. This is replicated in the measurements of mirror deformations shown in figure 4.13, where noticeable contour periodicities appear with similar 52 mm spacing along the surface.

4.3.1 Effects of Deformations at 101 GHz

As previously with the full Planck sidelobe model, an initial simulation was performed at a lower frequency HFI band to verify that the appropriate model parameters had been specified. The aperture field of a nominal 101-GHz corrugated horn modelled at 101 GHz was taken as the source in the system. For the purposes of this work, the outer structures of the telescope such as the baffles and the grooves are not considered, as they add very little power into and around the main beam. Instead, the dual reflector model originally outlined in section 3.2 was used, where the application of surface deformations

to both secondary and primary reflectors was considered. The three cases considered were:

1. 2 μm distortions on the secondary reflector only
2. 2 μm distortions on the primary reflector only
3. 2 μm distortions on both primary and secondary reflectors

At the highest HFI band, the 2 μm dimple size amplifies the grating effect. At 101 GHz the effect will be at a much lower level, however the same dimple size is used here for convenience. TICRA used 10 μm dimples to form a worst case scenario, and this size will be simulated for the 857-band, however the 2 μm distortions are a more realistic average and still prove sufficiently large to see noticeable effects on the main beam.

In all three test cases the resulting beams were compared against a model of ideal surfaces on both reflectors, highlighting any deviation from the expected main beam pattern, out to 10 $^\circ$ off-axis. Figure 4.19 shows the four cases considered, and the resulting beam cut at $\phi = 8^\circ$ on the sky. This coordinate system is slightly misaligned with the plane of symmetry of the telescope, and thus with the dimpling structure on the mirrors, so no lobes are seen along this cut.

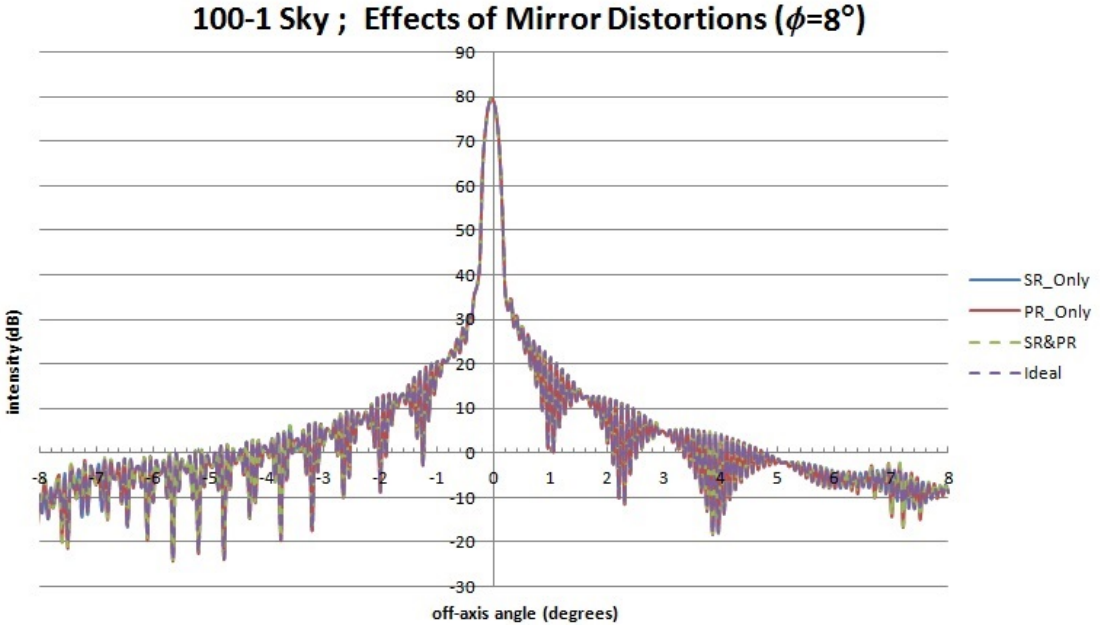

FIGURE 4.19: The modelled effect of primary and secondary deformations on the Planck 101-GHz beam. Lobes will only arise in specific angular regions, while for the most part the beam will resemble that of the nominal non-deformed reflector case.

There is very little noticeable difference between all four cases in this example, however the effects of core print through will not form a continuous lobe pattern around the main beam. Instead, the grating lobes arise in certain angular regions determined by the angle at which the beam illuminates honeycomb pattern on the reflector. At 101 GHz, the grating lobes due to distortions on the primary are expected to be found as $\Delta\theta = 6.565\,^\circ$ for $\phi = 0\,^\circ$, $60\,^\circ$, $120\,^\circ$, etc., and $\Delta\theta = 11.42\,^\circ$ for $\phi = 30\,^\circ$, $90\,^\circ$, $150\,^\circ$, etc., found using equations 4.29 and 4.30. Taking cuts around the sphere in ϕ in figures 4.20 and 4.21, the red data series represents the lobes at $\phi = 0\,^\circ$ and $\phi = 30\,^\circ$ respectively. The blue data series highlighting lobes due to distortions on the secondary reflector can be ignored here.

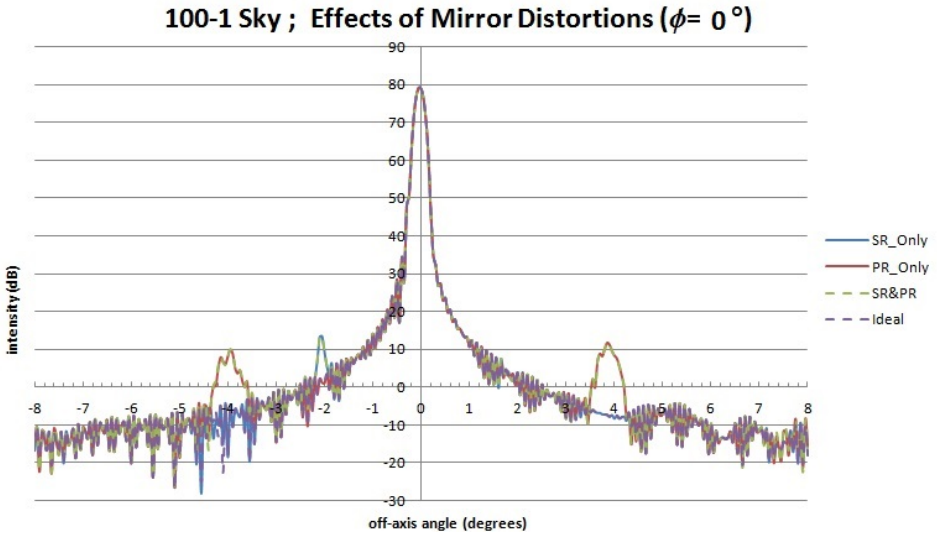

FIGURE 4.20: The modelled effect of primary and secondary deformations on the Planck 101 GHz beam at $\phi = 0\,^\circ$

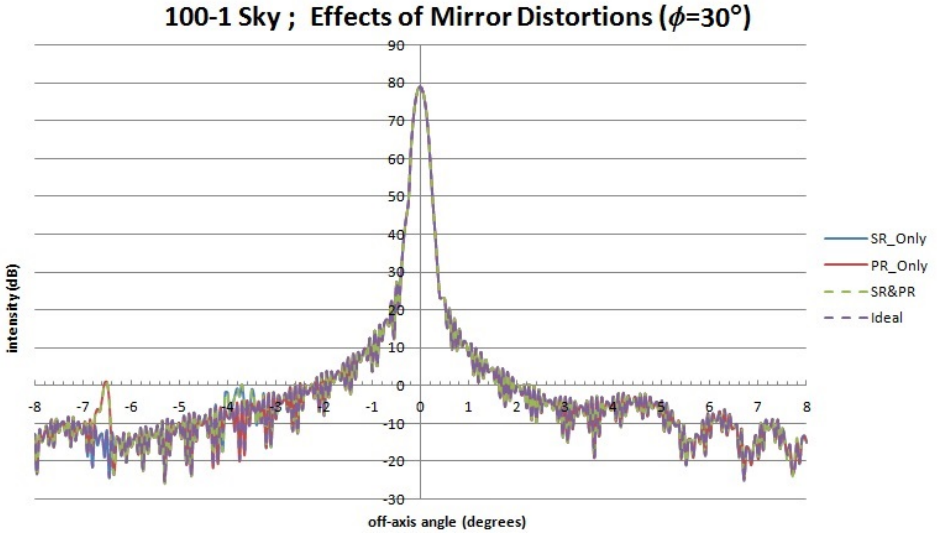

FIGURE 4.21: The modelled effect of primary and secondary deformations on the Planck 101 GHz beam at $\phi = 30\,^\circ$

Immediately obvious in figure 4.20 is the sharp near-in sidelobe structure suddenly visible centred approximately 3.8° off-axis either side of the main beam, giving a value of $\Delta\theta \sim 7.6\,^\circ$. The lobe structure was expected at $\Delta\theta = 6.565\,^\circ$ from calculations, however it is highly likely the field accuracy of the simulation isn't sufficient for a very accurate determination of the dimpling sidelobes, which rise to only 70 dB below peak, and thus are extremely sensitive to the accuracy of field determination. The difference between the two values can also to some extent be explained by the angle of incidence of the source beam with the reflector, which impacts the apparent size of the dimpling structures seen by the incident beam. There is a $32.5\,^\circ$ tilt of the honeycomb structure with respect to the line-of-sight of the secondary reflected beam, which results in an expected value of $\Delta\theta = \lambda/S\cos(32.5\,^\circ) = 6.81\,^\circ$ for the near-in structure.

Continuing around the sphere, further grating lobes are seen to occur. In figure 4.22 the second grating lobe of the first set described by equation 4.29 is seen a few degrees away from the expected $\phi = 60\,^\circ$.

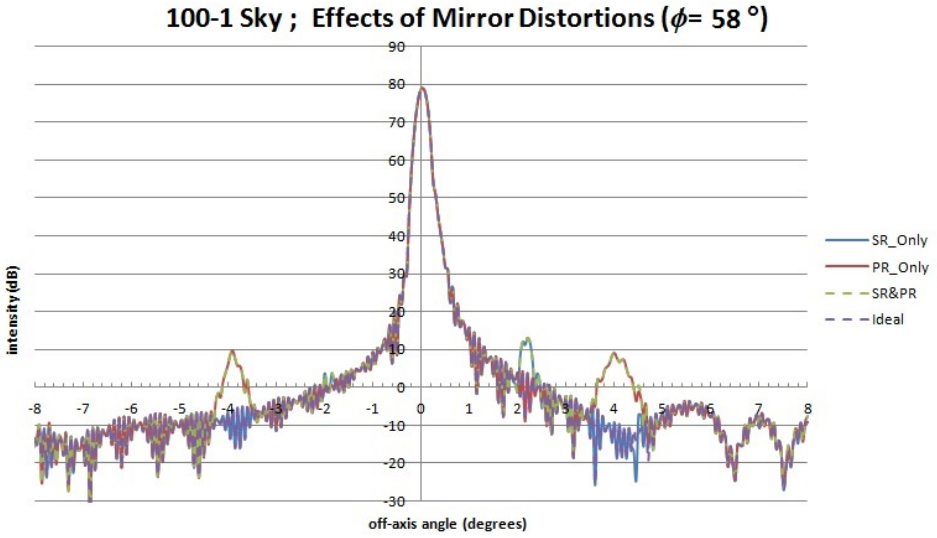

FIGURE 4.22: The modelled effect of primary and secondary deformations on the Planck 101 GHz beam at $\phi = 58\,^\circ$

The above figures were used solely to illustrate distortions to the primary, however further grating lobes arising from distortions on the secondary reflector. These can be seen at lower levels than the primary distortions, but also smaller angular distances from the main beam, as highlighted in figure 4.23. Again, the lobes arise roughly $60\,^\circ$ apart as expected, at $\phi = 7\,^\circ$ and $\phi = 64\,^\circ$ on the sky, corresponding to $\phi = 0\,^\circ$ and $\phi = 60\,^\circ$ from the plane of the secondary reflector.

The levels of the grating lobes modelled at the 101-GHz band are all generally quite low (roughly 60 to 70 dB below peak), since the height of the surface deformations is an

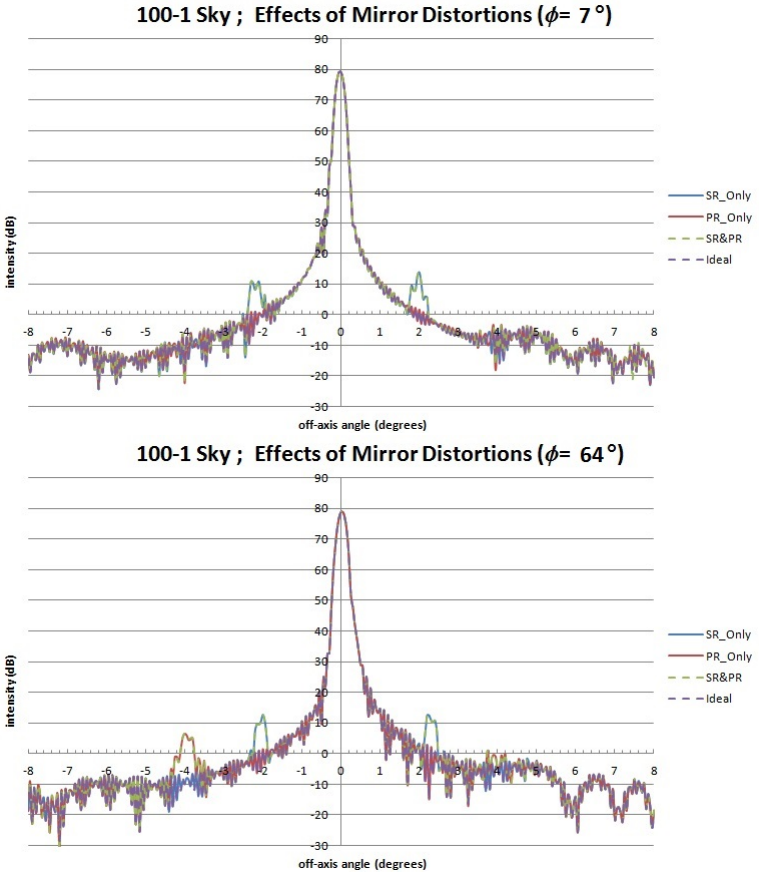

FIGURE 4.23: The modelled effect of secondary deformations on the Planck 101 GHz beam at (top) $\phi = 7\,^\circ$ and (bottom) $\phi = 64\,^\circ$ w.r.t. the $\phi = 0\,^\circ$ axis of symmetry of the telescope.

order of magnitude larger than the wavelength of the incident radiation. This is not the case at higher frequencies, where the same surface deformation size is of the order of the wavelength of the radiation incident upon it. It is with this in mind that we move to the more important modelling of the highest HFI band, 857-GHz, and the grating effect arising from the multi-moded sources in this band.

4.3.2 Effects of Deformations at 730 GHz & 800 GHz

2 μm Deformations at 730 GHz

As mentioned previously, simulations performed at the 857-GHz band used a (single-moded) Gaussian fit to the beam of an 857-GHz horn [73], rather than incorporating the multi-moded nature of the beam at this frequency. Herein we take the mutually incoherent modal fields making up the 857-GHz horn beam at 730 GHz, and propagate to the sky, summing in the same manner as for the FSL modelling. 730-GHz was chosen

because it was the lowest frequency in the band, and therefore the easiest to model for reasons mentioned previously. The component modal fields of the 730-GHz beam are illustrated in figure 3.41.

As before, modelling was undertaken for the two cases where either the secondary or primary mirror is distorted, and a third case where both were distorted. Using equations 4.29, grating lobes are expected at integer multiples of $\theta = 0.78\,^\circ$ for $\phi = 0\,^\circ$, $60\,^\circ$, $120\,^\circ$. This is verified in figure 4.24, where the $\phi = 0\,^\circ$ lobe structure peaks at $\approx 0.75\,^\circ$ away from the main beam, in good agreement with expected angular distance. Immediately noticeable is the increased level of the sidelobes when compared with those at 101 GHz. Here the sidelobes rise above 20 dB, and less than 50 dB below peak.

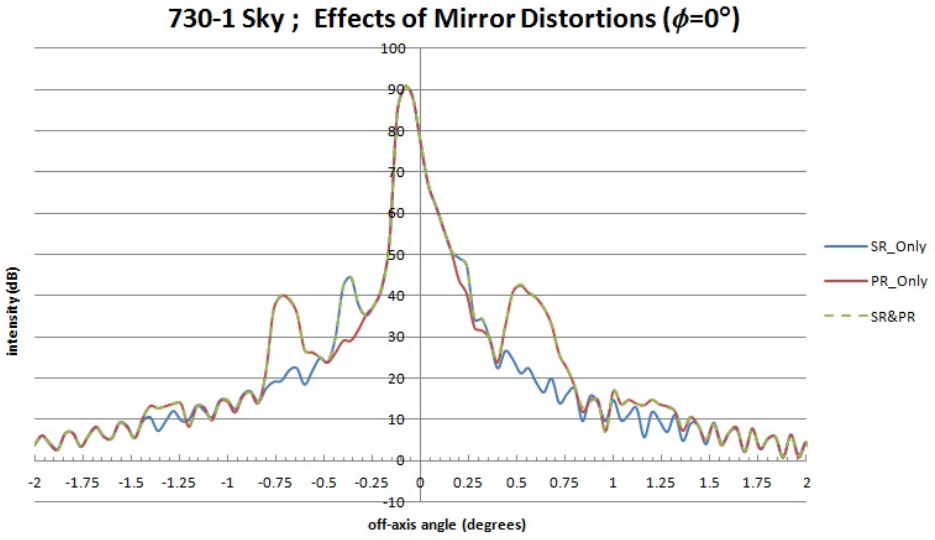

FIGURE 4.24: The modelled effect of primary and secondary deformations on the Planck 730 GHz beam at $\phi = 0\,^\circ$.

Similarly, taking equation 4.30, second order grating lobes are expected at integer multiples of $\theta = 0.45\,^\circ$ for $\phi = 30\,^\circ$, $90\,^\circ$, $150\,^\circ$. Figure 4.25 illustrates the first occurrence of these lobes, which are seen at $\approx \theta = 0.95\,^\circ$ for $\phi = 30\,^\circ$. The levels of these grating lobes is almost 20 dB down on the inner-most lobes, however the grating effect does deteriorate in intensity with increasing distance from the main beam.

To better illustrate the genrral symmetry of the lobe structure around the main beam, the most prominent 2 μm lobe locations distributed are shown in figure 4.26.

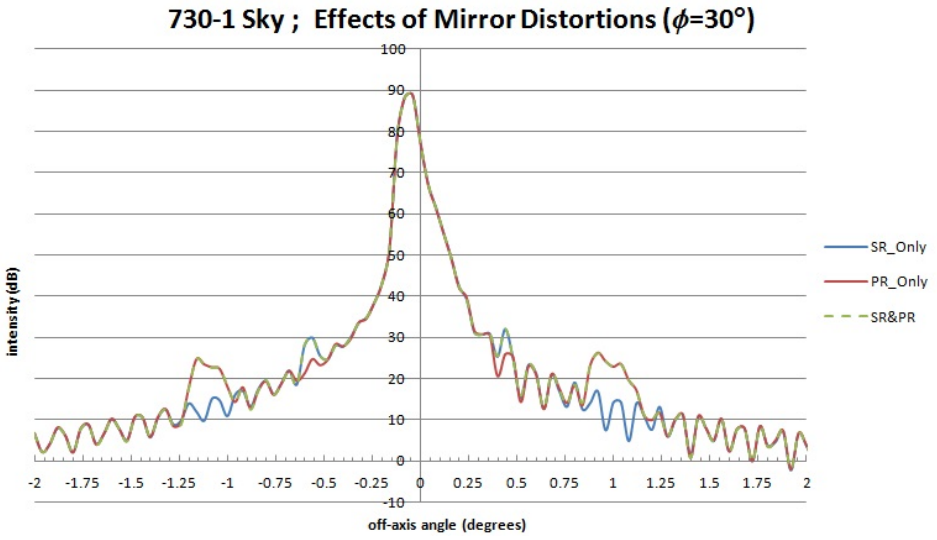

FIGURE 4.25: The modelled effect of primary and secondary deformations on the Planck 730 GHz beam at $\phi = 30\,^\circ$.

10 μm Deformations at 730 GHz

To compare against TICRA modelling of the dimpling surface which was shown in figure 4.14, the dimpling size was increased from 2 μm to 10 μm, and the same modelling routine adopted. On changing the dimple size, the equivalent increase in dB intensity of the grating lobes is expected to be roughly 10log(10 μm/2 μm)= 14 dB with respect to the 2 μm lobes.

Figure 4.27 displays the grating lobes along the $\phi = 0\,^\circ$ axis for 10 μm distortions at 730 GHz. By comparison with figure 4.24 the nearest-in lobes are seen to increase by approximately 14 dB, and peak at roughly 35 dB below the main beam. Weaker lobes due to primary dimpling are now also visible at integer multiples of the first grating lobe, however they reach only 60-70 dB below peak, and form a much broader profile than the sharper inner lobes.

Figure 4.28 displays the grating lobes along $\phi = 30\,^\circ$, which are of course of lower intensity than the nearer-in $\phi = 0\,^\circ$ lobes.

Taking further cuts around the sphere, figure 4.29 displays the grating lobes along with $\phi = 60\,^\circ$ and $\phi = 90\,^\circ$, which once again appear much lower in intensity. However one must note that the main beam level has also fallen appreciably by rotation around ϕ. This is due to minor misalignment between the field grid coordinate system and the boresight direction of the 857-1 horn beam on reflection from the primary. Although calculated such that the main beam peak is measured at $\phi = 0\,^\circ$, on rotation about ϕ

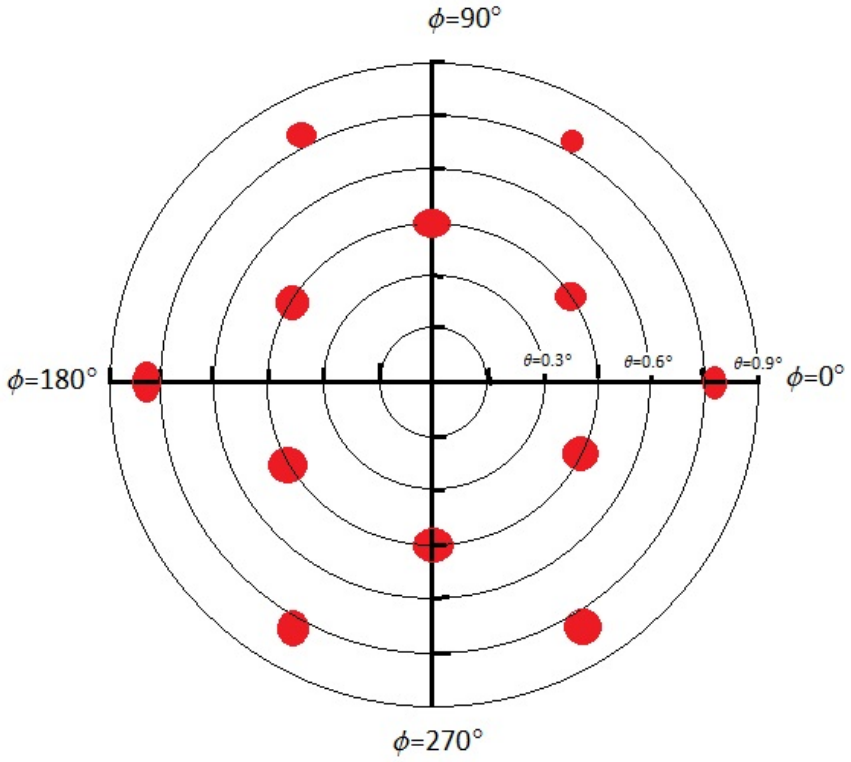

FIGURE 4.26: Illustrative map of the 2 μm lobe locations modelled at 730 GHz out to 1 ° around the main beam.

the cut no longer intercepts the peak of the main beam. This also means the grating lobes no longer appear symmetrically with ϕ either side of the beam, as illustrated by the second plot in figure 4.29. Having rotated by 90 ° only one of the lobe peaks is aligned with the main beam, while the other arises on rotation by another 5 ° about the sphere.

The impact of the size of core-print through on lobe strength is clearly quite large as you go from the 2 μm to the 10 μm distortions. This is largely expected due to the size of the dimple peaks approaching the wavelength of the incident radiation. For completeness the $\phi = 0\,^\circ$ beam patterns for the 2 μm and 10 μm distortions overlaid on the primary reflector only is shown in figure 4.30, where the expected 14 dB increase in grating lobe level is clearly illustrated. Notice also that the angular distance of the grating lobes from the main beam is independent of dimple size.

A second comparison is shown in figure 4.31 between $\phi = 0\,^\circ$ beam patterns for 2 μm and 10 μm distortions on the secondary reflector. The grating lobes are closer to the main beam, and are at slightly larger intensities than those of the primary. This is due to the beam from the secondary being focussed by the primary, increasing the relative

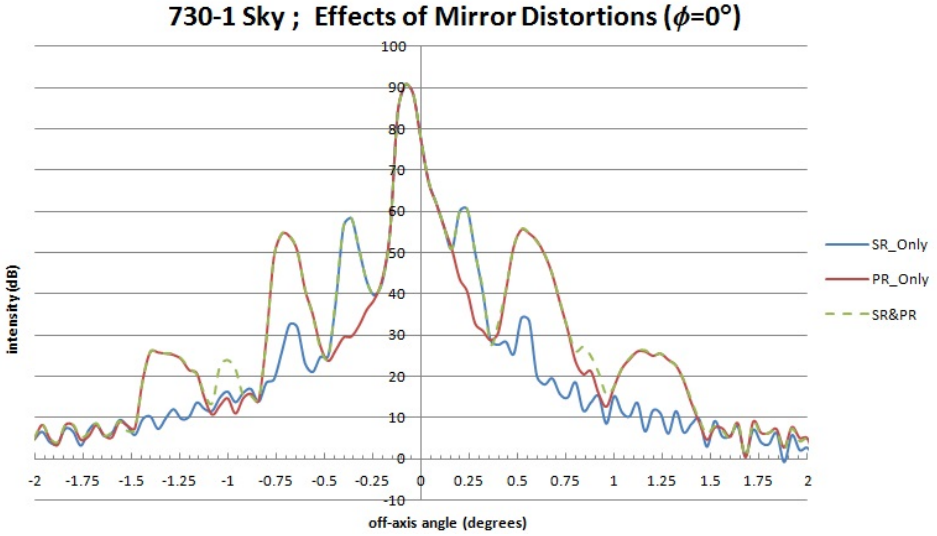

FIGURE 4.27: The modelled effect of primary and secondary deformations on the Planck 730 GHz beam at $\phi = 0\,^\circ$.

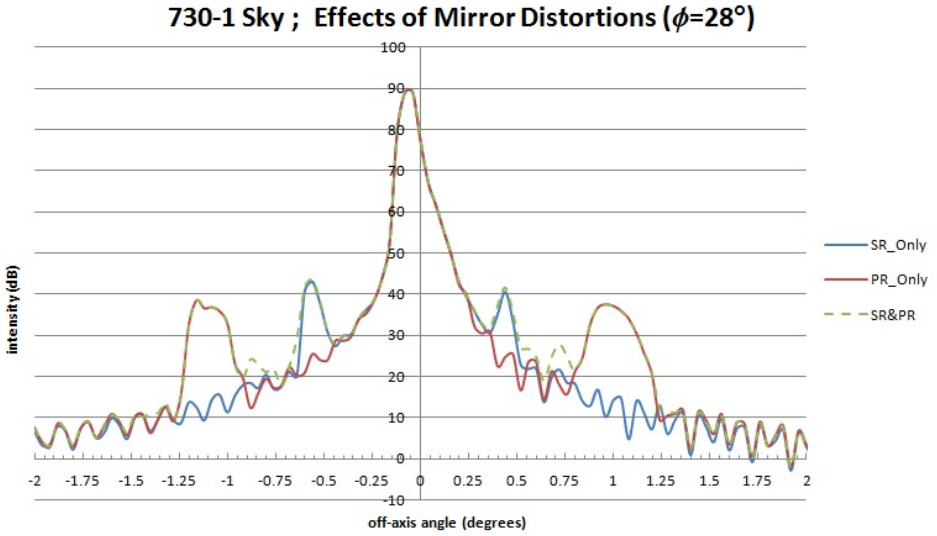

FIGURE 4.28: The modelled effect of primary and secondary deformations on the Planck 730 GHz beam at $\phi = 28\,^\circ$.

power in each lobe while also reducing their angular extent and angular distance form the main beam.

Gaussian Beam Comparison at 730 GHz

The TICRA model of surface deformations at 857 GHz, a sample of which was shown in figure 4.14, were performed by fitting a Gaussian to the aperture of the B2B 857-horn. Although a good approximation to the beam, the different phase evolutions of the various independent modes making up the aperture field may result in a different field

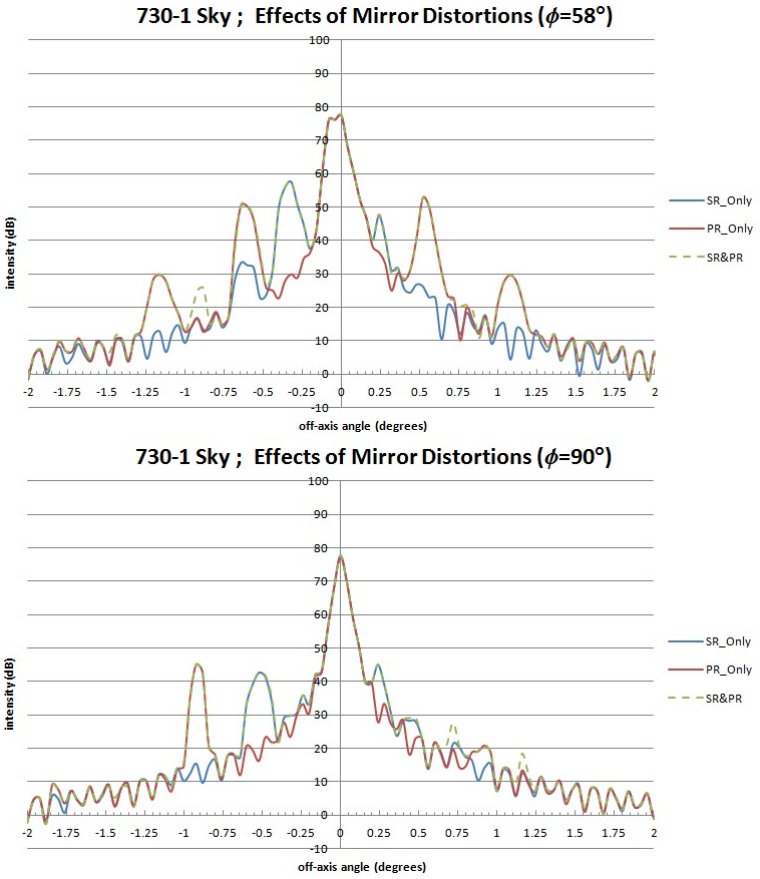

FIGURE 4.29: The modelled effect of secondary deformations on the Planck 730 GHz beam at (top) $\phi = 58\,^\circ$ and (bottom) $\phi = 90\,^\circ$

on the sky to that obtained by propagation of this equivalent Gaussian. To assess the possibility that a single-mode approximation would not be a good model to use when investigating the effect of distortions, a Gaussian was fit to the 730 GHz aperture beam, and propagated to the sky. This was then compared with the multi-moded 730 GHz beam patterns illustrated in the previous section, as shown below in figure 4.32 for 2 μm distortions on the primary reflector only.

The Gaussian beam pattern is normalised to the peak intensity of the multi-moded beam, in order to compare the relative grating lobe levels. The accuracy achieved when modelling a Gaussian is high in comparison with that of the multi-moded beam, over 100 dB below peak. In the case of the multi-moded beam, the low level structure inhibits accurate determination of lobe strength outside of the innermost lobe, as highlighted by the Gaussian comparison. While there is clearly significant grating lobe structure between $1\,^\circ$ and $1.5\,^\circ$, this is almost invisible in the multi-moded beam. In fact, beyond the 2nd order grating lobes any further orders are indistinguishable from the low level structure. This is illustrated by the third grating lobe, clearly visible between $1.5\,^\circ$ and $2\,^\circ$ off-axis in the Gaussian beam pattern, but hidden below the low level structure of the

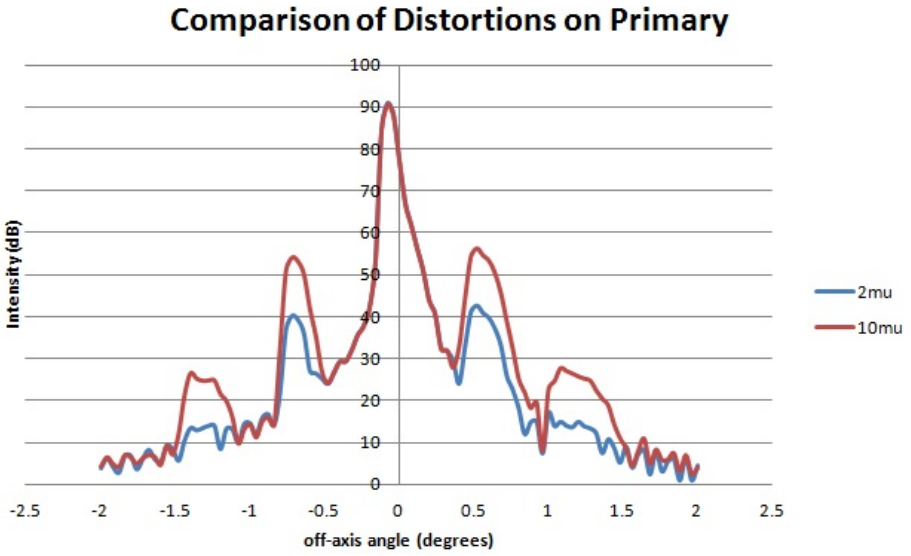

FIGURE 4.30: Comparison between $\phi = 0\,^\circ$ beam patterns for $2\,\mu$m and $10\,\mu$m distortions on the primary mirror.

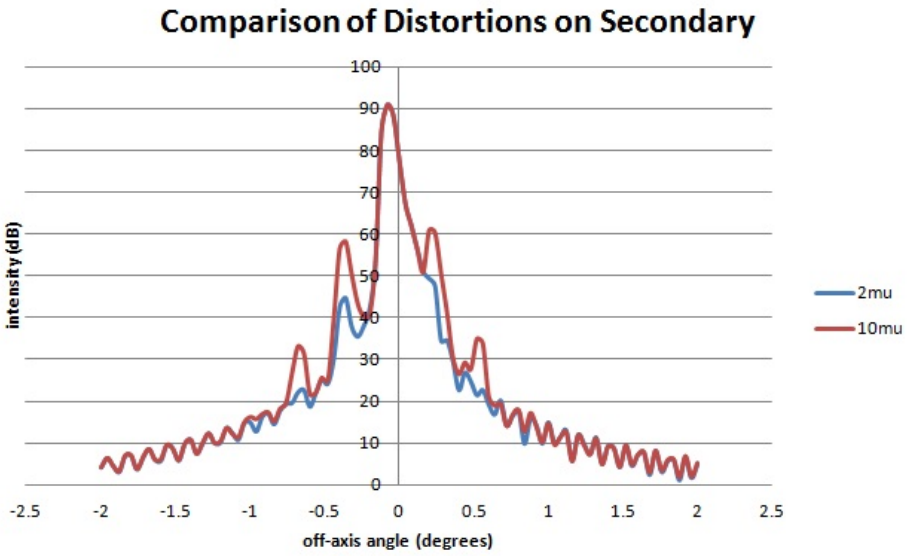

FIGURE 4.31: Comparison between $\phi = 0\,^\circ$ beam patterns for $2\,\mu$m and $10\,\mu$m distortions on the secondary mirror.

multi-moded beam simulation. The peak intensities of the grating lobes is almost identical in both cases, however the angular extent of the lobes are slightly underestimated by the Gaussian model. This is due to the fact that multi-moded beams are naturally wider than single-moded beams due to broadening of the main beam from higher order mode contribution. As the grating lobes are simply images of the main beam, they will also appear wider in the multi-moded case than for an equivalent Gaussian.

A similar comparison between Gaussian and multi-moded beam patterns due to $10\,\mu$m

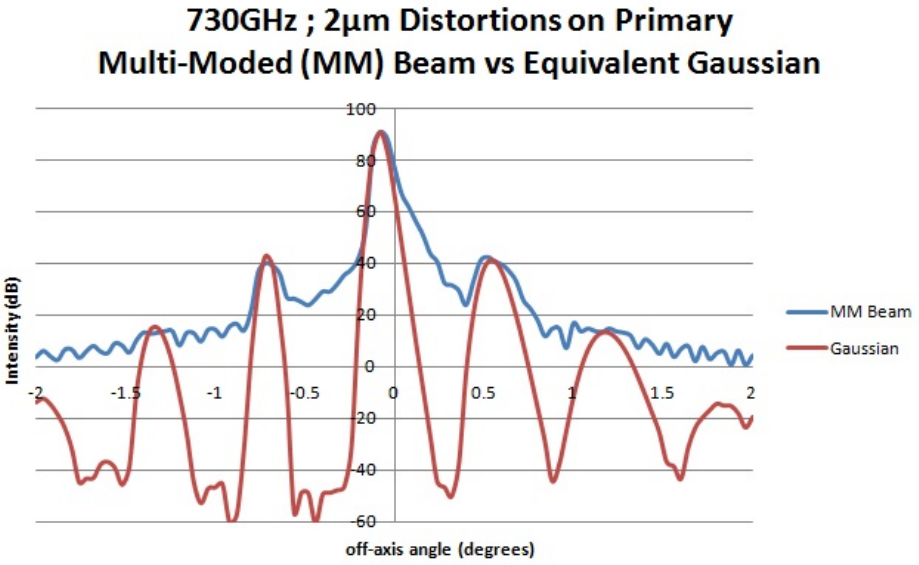

FIGURE 4.32: 730 GHz comparison between $\phi = 0\,^\circ$ cuts of the multi-moded beam pattern, and that of an equivalent Gaussian, for 2 μm distortions on the primary.

deformations on the primary reflector is shown in figure 4.33. Once again the multi-moded beam is broader than the Gaussian, however the 2nd order peaks are clearly visible in this case. The third order lobes remain invisible in the multi-moded case, however once again the grating lobe levels are well matched in both cases. Importantly, there is agreement between the levels of the TICRA modelled grating lobes which lie roughly 30 dB to 35 dB below peak in figure 4.14.

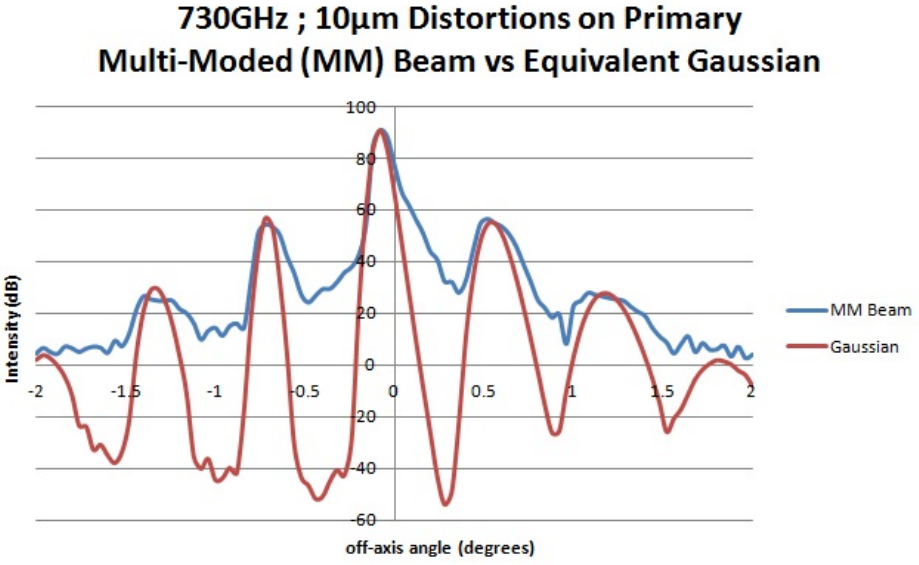

FIGURE 4.33: 730 GHz comparison between $\phi = 0\,^\circ$ cuts of the multi-moded beam pattern, and that of an equivalent Gaussian, for 10 μm distortions on the primary.

Modelling the same surface deformations on the secondary only, a comparison between Gaussian and multi-moded beam patterns are shown in figure 4.34. In the case of 2 μm

distortions only the 1st order grating lobes are visible in the multi-moded model, whereas for 10 μm distortions up to 2nd order lobes are seen. Again the grating lobe levels are in good agreement between both models, however the multi-moded beam lobes are of course somewhat broader than is predicted by the Gaussian model.

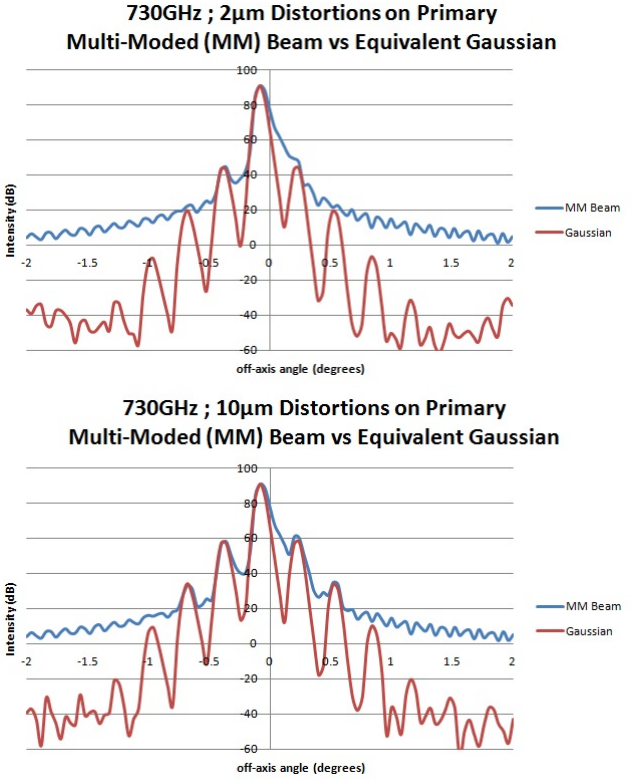

FIGURE 4.34: 730 GHz comparison between $\phi = 0\,^\circ$ cuts of the multi-moded beam pattern, and that of an equivalent Gaussian, for 2 μm (top) and 10 μm (bottom) distortions on the secondary.

2 μm and 10 μm Distortion Comparison at 800 GHz

The wavelength dependence of the angular scales at which the grating lobes appear was verified by comparison with the beams at 800 GHz. This is close to the frequency limit for PO, beyond which the maximum RAM capacity of the computer cluster used to perform these simulations is reached. This was performed for 2 μm and 10 μm distortions on the primary reflector only, and the equivalent 730 GHz beam overlaid for comparison, as shown in figure 4.35.

The distance between the first order grating lobes is given by $\Delta\theta_{gr} = \arcsin(\frac{\lambda_1 - \lambda_2}{S\sqrt{3}}) = 0.0397^\circ$, where λ_1 and λ_2 are the wavelengths corresponding to 800 GHz and 730 GHz respectively. This is validated by comparison of the first order lobe peaks at each frequency in figure 4.35. Notably, the grating lobe levels increase by 2 dB in moving

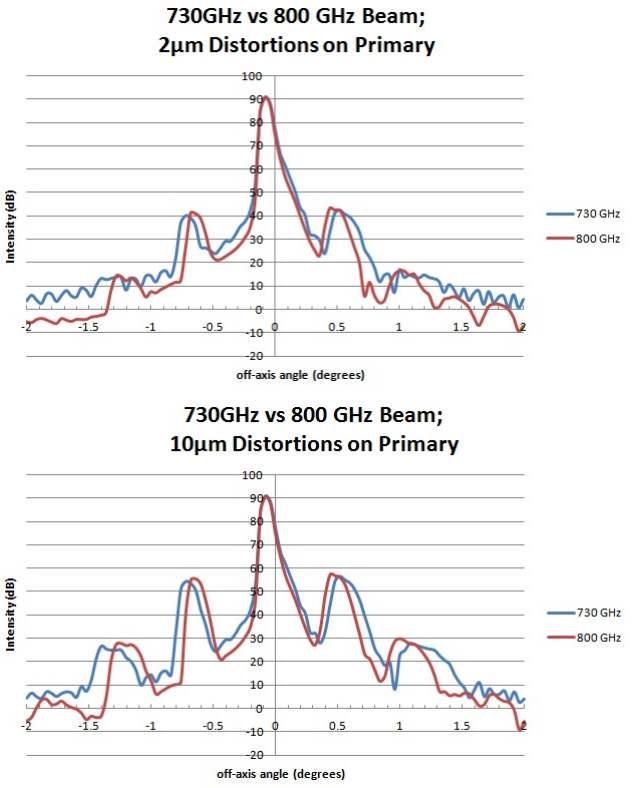

FIGURE 4.35: Comparison between $\phi = 0\,^\circ$ cuts of the 730-GHz and 800-GHz multi-moded beam pattern, for $2\,\mu$m (top) and $10\,\mu$m (bottom) distortions on the primary.

to 800 GHz, naturally continuing to rise as wavelength approaches the order of the size of the dimples. A comparison between the 800-GHz beams for both $2\,\mu$m and $10\,\mu$m distortions on the primary is shown in figure 4.36, where the expected 14 dB increase in lobe level is again observed for the same $8\,\mu$m increase in dimple size as seen at 730 GHz.

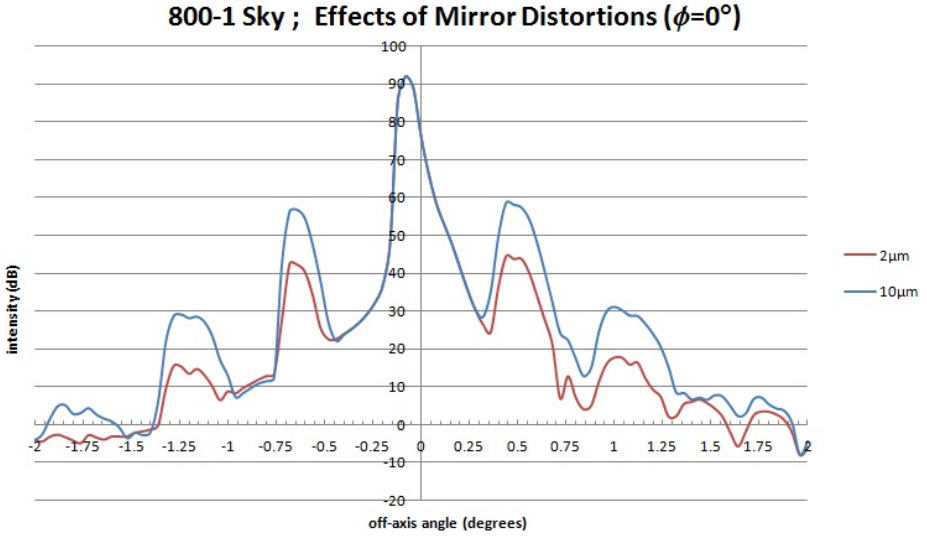

FIGURE 4.36: 800 GHz comparison between $\phi = 0\,^\circ$ beam patterns for $2\,\mu$m and $10\,\mu$m distortions on the primary.

4.4 Conclusion

In this Chapter we investigated various alternatives to the PO and GTD techniques seen in chapter 3, which could be used to quickly estimate the FSL levels of the Planck telescope using equivalent paraxial lens system. The projected aperture technique was first described, where under Fresnel transformation of the aperture field from source to sky via a single lens equivalent to the dual-reflector system, it was shown that rough estimates of FSL level could be easily drawn. There were some limitations to the technique, in so far as the Fresnel integral used to perform the Fresnel transformation from lens to sky becomes unstable as $\Delta \to 0$, meaning the integrand will take longer to calculate.

The GBM technique is quite similar in many respects, using a paraxial lens system (in this case two lenses) and performing overlap integrals at each lens to recover the coefficients of the field at that point. It is much more powerful than the projected aperture technique, as it uses an elegant equivalence between waveguide mode theory and GBM theory, whereby the waveguide mode fields at the aperture of a horn can be summed according to a common Bessel function dependency, which is shared by a similar set of Gauss-Laguerre modes. To compare against the GRASP9 model, the 'ideal', 'bad' and 'worst'-case horns, but were seen to rise no more than 70 dB from peak for even the worst-case scenario. The disagreement between GTD and GBM techniques may be a result of the paraxial approximation, which does not take into account the projection effects of the telescope. There is, however, scope for development of this technique, and the potential to include projection effects unaccounted for here. This may resolve the inaccuracies of the current model, and could provide a useful tool for quick modelling of telescope systems, particularly useful for FSL work, but also any other cases for which PO and GTD take considerable time. A table of the various techniques implemented in modelling of the Planck system is given in figure 4.37, highlighting the benefits and challenges encountered using each.

The final section dealt with the modelling of regular distortion son the Planck mirrors, caused by print through of the mirror supports onto the surface of the reflector. This causes the reflector to act somewhat like a diffraction grating, more-so when the size of the deformations approach the order of the wavelength of the radiation propagating through the system. Although modelling at precisely 857 GHz was not possible due to RAM limitations of the computer cluster used in NUIM, the modelling of the distortions at 730-GHz showed that multi-moded grating lobe levels were in agreement with those of a Gaussian fit to the 730-GHz aperture beam, in case of both 2 μm and 10 μm distortions. This was replicated at 800 GHz, indicating that there would likely be little difference

Method	Frequency	Notes
1) Projected Aperture Tecnique (PA)	857	*Paraxial* Single-Lens System
		Fresnel Transform Source to Sky
		Integrals fail beyond 1°
		Quick *estimation of PR-FSL*
		180° cuts expanded to fill 4π
2) PO & PTD (in GRASP9)	101 & 730	Full RFFM Planck model
		Difficulties incorporating blockages
		Lengthy computations
		Accurate Main Beam (used for Toy Beam from PA)
3) GO & GTD (in GRASP9)	101 & 730	Full RFFM Planck model
		Much better account of blockages/reflections
		Vastly superior to PO
		Accurate Full-sky Model of FSL structure
4) GBM Technique	730	*Paraxial* Dual-Lens System
		GBM & Ray Matrix Source to Sky
		Quick estimation of PR FSLs
		Symmetric cuts only
		Can be extended to off-axis equivalent & SR spillover

FIGURE 4.37: Table comparing the various techniques implemented throughout this thesis for the modelling of the Planck system.

between the Gaussian beam model previously implemented by TICRA, and a more correct multi-moded model such as that implemented here. The multi-moded grating lobes were a few degrees wider than the Gaussian lobes in all cases, which is naturally so as the lobes are merely images of the main beam regularly spaced around it. The multi-moded beam is significantly wider than a fundamental Gaussian due to the additional higher order mode content, and thus the grating lobes are also wider.

In the next chapter we undertake modelling of further telescope systems in GRASP9, highlighting the manner in which one should approach some of the challenges that come along with the modelling of unique systems. Both are test-beds set-up in Cardiff University, the first of which is a telescope simulator used to perform pre-flight measurements of the Planck HFI flight horns. This is modelled with a view to checking whether potential horn imperfections could have been seen in measurement. The second system which we will encounter is the test-bed for an interferometer known as FIRI, and for which various issues relating to power-throughput will be investigated.

Chapter 5

Modelling of Other Telescope Systems

In earlier chapters I described the modelling of a single reflector system, as well as the dual reflector system of the Planck telescope. This led on to a full structural model of the Planck telescope, including all potential reflective surfaces on the service module, particularly the baffles. This chapter is concerned with the quasi-optical modelling of various other unique telescope systems in GRASP9. The first system investigated will be the telescope simulator used for pre-flight measurement of the Planck HFI horns. This dual reflector system comprises two rather unusual surfaces not accounted for in the GRASP9 repository, which had to be modelling in a non-trivial way, which will be outlined in section 5.1. The second system to be outlined is that of FIRI (Far Infrared Instrument), a multi-beam interferometer which also poses novel challenges, the modelling of which will be described in section 5.2.

5.1 Modelling of the Cardiff Test Bed for the Planck Telescope

One suspected cause of the features seen in the Planck HFI 857GHz channel maps (and shown in figure 1.26) was manufacturing imperfections in the horns. The etching of corrugated horns naturally becomes more difficult as one moves towards higher frequencies, due to the reduced size of all features with shorter wavelength, and at the highest frequency band of the Planck telescope the process was extremely difficult to perform.

This being the case, it is not difficult to imagine that some corrugations of these delicate horns may not have been etched out correctly. As has been shown in Chapter 3, minor imperfections can have a large effects on the beams from multi-moded horns, however very little physical evidence of imperfection may appear on visual inspection, and thus very little evidence supporting the possibility has been recorded. With the flight horns naturally irretrievable, analysis was instead undertaken of the few measurements performed with these horns pre-flight. Specifically, this section outlines work done in modelling of a telescope simulator, used for pre-launch verification of the Planck HFI flight horns. The simulator was set-up at Cardiff University in 2008, with a view to performing a detailed analysis of the 545-GHz and 857-GHz channel multi-moded horns to be used on the instrument.

The aim of this work is to model the beam patterns of the altered geometry (simulating manufacturing defects) 857 GHz Planck horns through the telescope simulator, and investigate whether, due to the relatively low noise floor of the equivalent measurements, any features arising from imperfections in the horns would go unnoticed. To this end, the three altered horn geometries created for the previous modelling campaign (Section 3.4.1) will again be used, and their performance modelled in an equivalent system to the Cardiff test bed shown below in figure 5.1. The original system set-up comprised a mercury arc-lamp source of aperture diameter 3.5 mm, which on propagation through the reflector system was focussed onto the aperture of the horn antenna under test. The arc lamp simulated a source on the sky which, based on the Planck detector plate scale of 2.113 arcmin/mm, and telescope simulator source/image scale of 0.239 equates to a an extended source on the sky of width $3.5\,\text{mm} \times 0.239 \times 2.113\,'/\,\text{mm} = 1.77'$.

The horn antenna was coupled to a bolometric detector in a He3 cryostat via a series of additional horns and filters. Various properties of this complex arrangement are not accurately known, so for the purpose of this work only the modal fields from a single 857 GHz back-to-back (B2B) horn fed by a standard waveguide will be assumed.

The reflector system comprises two paraboloids, the secondary with a focus at the Planck detector aperture, and the primary with a focus at the arc-lamp source. The primary mirror is one petal of a multi-facetted reflector first used as in the Pronaos balloon-borne telescope [74]. It formed the primary mirror of an on-axis Cassegrain system, with a focal length of roughly 1.8 m and radius of 1.0225 m. The centre hole natural to a Cassegrain design has a radius of 127.5 mm, and the single petal covers an arc of 60 °. The shape of the reflector is clearly shown in figure 5.2 which outlines the GRASP9 description of the system.

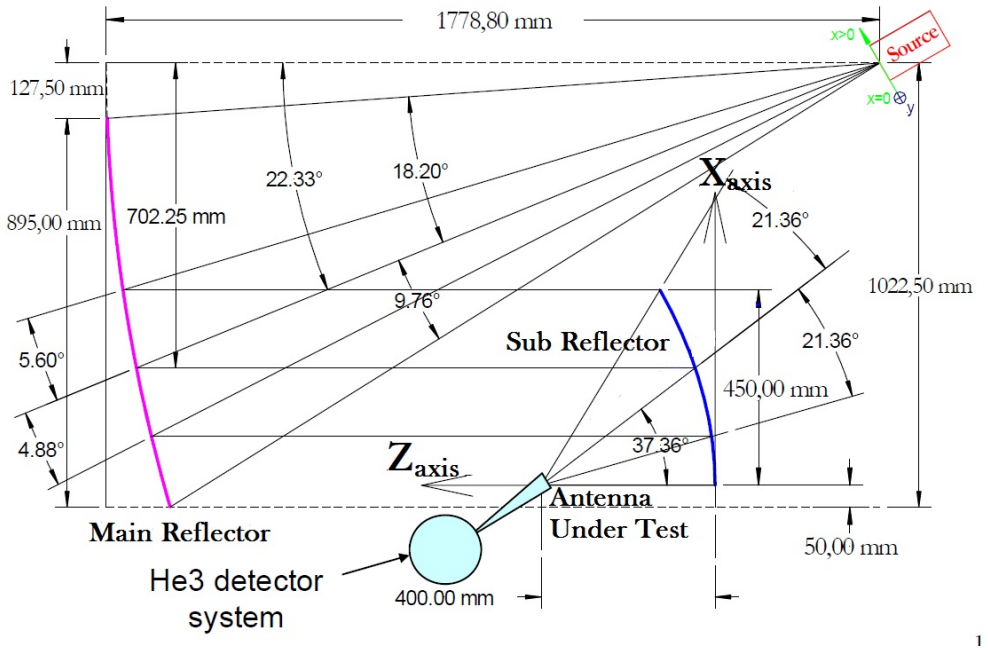

FIGURE 5.1: Geometrical description of the telescope simulator used to validate the Planck HFI flight horns.

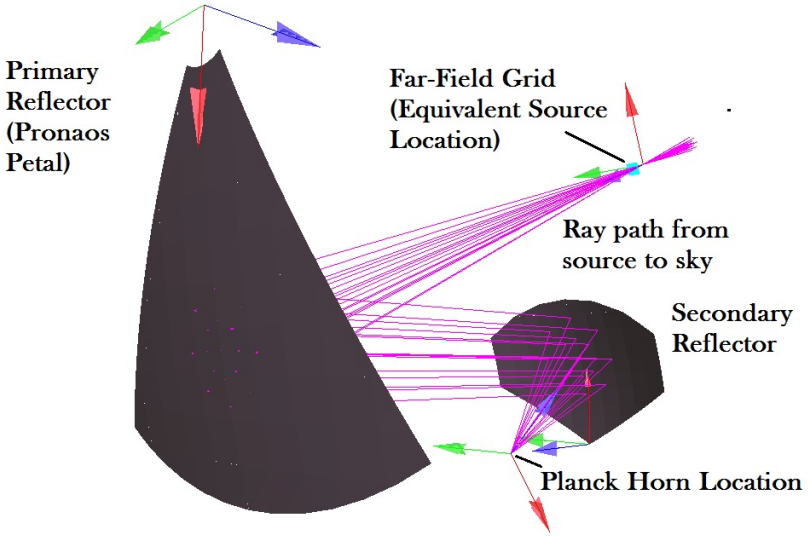

FIGURE 5.2: GRASP9 'open-GL' plot of the telescope simulator used to validate the Planck HFI flight horns.

The similarly shaped parabolic secondary reflector, also shown in figure 5.2, has a focal length of 400 mm, and projects an arc of 120 °. The Planck B2B horn sits at the focus of this reflector, while the arc lamp source was positioned at the focus of the primary mirror. The dimensions of each reflector are given in figure 5.3.

Creating these relatively unusual reflector shapes in GRASP9 requires the use of a 'tabulated rim, xy-input'. The file containing the tabulated data must be of *.rim extension, with the rim description formatted as shown in figure 5.4. The 'x' and 'y'

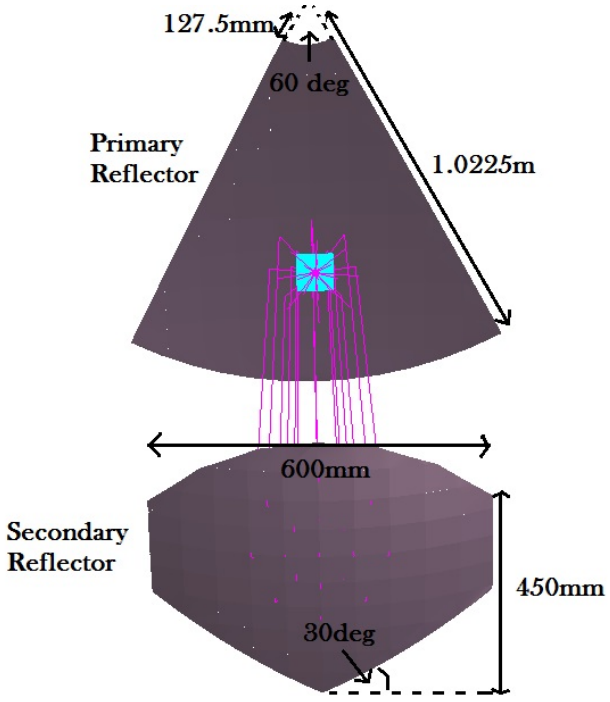

FIGURE 5.3: GRASP9 'open-GL' plot of the telescope simulator with dimensions of the two reflectors outlined.

values in the file are distances in two dimensions from the coordinate origin of the reflector, such that by defining the relevant number of reflector apexes, and numerous points in between, GRASP9 will interpolate the shape required. LINE1 to LINE13 in figure 5.4 describe the arc rim of the reflector across its 60 ° span, with the numerous intermediary points allowing GRASP9 interpolate the curvature of the rim. Notice, however, that to generate the radial straight edges of the rim, only the two corner points either end of the section need be specified. GRASP9 then automatically assumes a straight edge and generates the rim appropriately.

5.1.1 Planck 857-GHz Modal Fields

The geometry of the back-to-back multi-moded horn antenna used at 857 GHz was shown in figure 4.1. Horns with multi-moded field output are used in all Planck HFI bands tasked with measuring and removing foregrounds (353-GHz, 545-GHz and 857-GHz), and their corrugated structures couple the bolometric detector feed systems to the telescope. The bolometers are incoherent detectors, meaning they absorb the total power from all modes propagating in the feed system. Thus, the larger the number of modes afforded by the design of waveguide and horns, the greater the level of power coupled to

```
PRFM tabulated rim
          x-values    y-values
LINE1    -511.250    ,885.510    corner_point
LINE2    -432.130    ,926.700
LINE3    -349.720    ,960.840
LINE4    -264.640    ,987.660
LINE5    -177.560    ,1006.970
LINE6    -89.120     ,1018.610
LINE7    0.000       ,1022.500
LINE8    89.120      ,1018.610
LINE9    177.560     ,1006.970
LINE10   264.640     ,987.660
LINE11   349.720     ,960.840
LINE12   432.130     ,926.700
LINE13   511.250     ,885.510    corner_point
LINE14   63.750      ,110.418    corner_point
LINE15   43.608      ,119.811
LINE16   22.140      ,125.563
LINE17   0.000       ,127.500
LINE18   -22.140     ,125.563
LINE19   -43.608     ,119.811
LINE20   -63.750     ,110.418    corner_point
```

FIGURE 5.4: Standard formatted input for a tabulated rim, where this example describes the rim of the telescope simulator primary reflector.

the detectors, meaning greater sensitivity. The waveguides feeding the system are overmoded, meaning they transmit more than just the fundamental mode, and the shape of the horns further adjusts the modal content of the field coupling to the telescope. This ideally allows good control of sidelobe power which when combined with more power due to the increased number of modes means greater sensitivity to the sources that these bands are expected to characterise. As the frequency of the band increases the number of modes excited in the horn also increases, meaning greater sensitivity towards the higher end of the channel. At 730 GHz, only 10 modes (5 hybrid modes and their orthogonal mode set) are present, however at the highest end of the band there are double the number of modes, as was shown in figure 3.33. This naturally results in lengthier simulations due to the greater number of modes to be propagated, as well as the higher frequency affecting PO calculation.

Far-field plots of the fundamental and higher-order modes which make up the partially coherent field of the 857-GHz channel, and which will be used in to model the beam patterns through the telescope simulator, are shown in figure 5.5, where the power in each mode is plotted logarithmically against a scan angle around the sphere. These are the modes which are excited in the horn structure at 860 GHz, however the same modes suffice to describe the field at 857 GHz also as the mode content does not vary considerably over this small range.

The greatest contributor to total power is, of course, the fundamental HE11 mode, and in general, modes of azimuthal order $n = 1$ contribute the greatest amount of power to

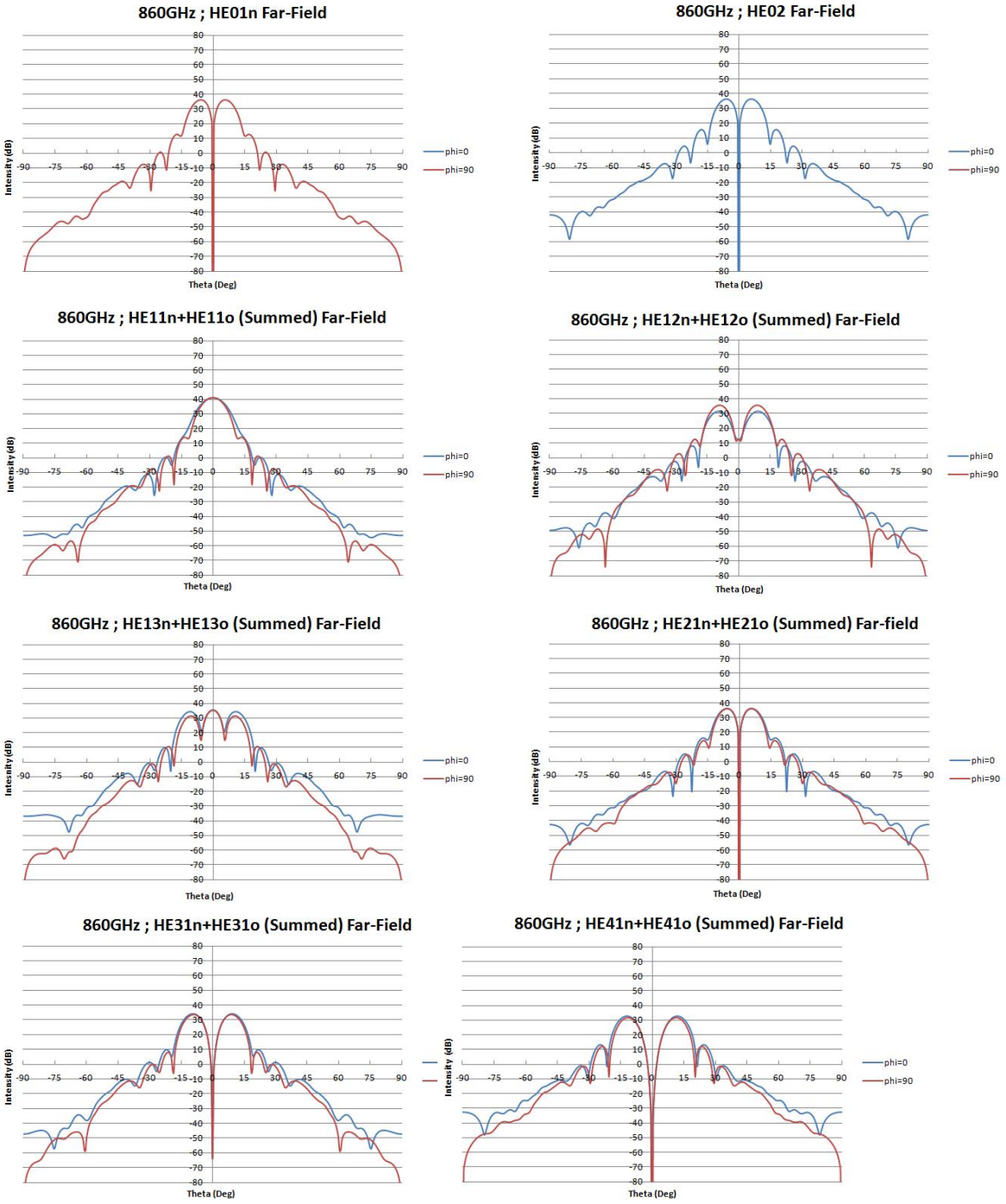

FIGURE 5.5: Beam patterns of all ten hybrid modes present at the aperture of the Planck 857 back-to-back horn modelled at 860 GHz. Here each mode and its orthogonal have been summed in quadrature for convenience of illustration.

the main beam. Higher order modes broaden the beam, increasing sensitivity due to the greater amount of power coupled to the telescope. The absolute contribution of each mode is more obvious in figure 5.6, which shows the contribution of each mode to total intensity plotted on a linear scale rather than in dB.

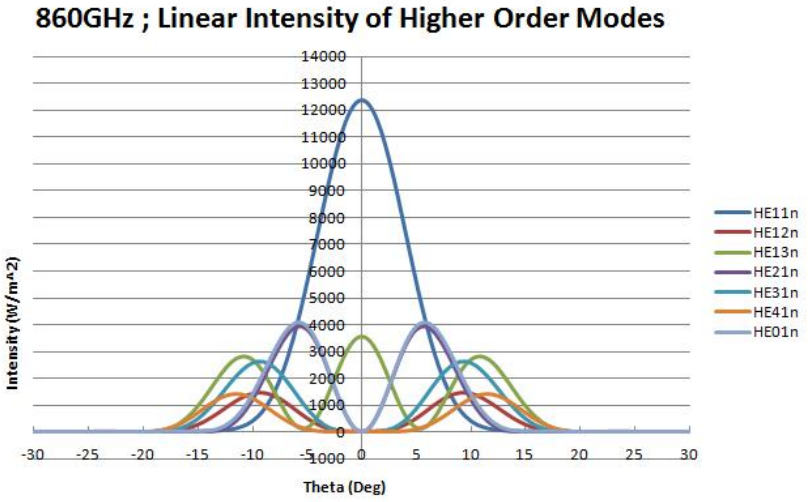

FIGURE 5.6: Linear intensity of each mode at the aperture of the Planck 857 horn (calculated at 860 GHz), highlighting the overwhelming contribution of the fundamental hybrid mode to main beam power. 'n' in the legend refers to the 'normal' rather than the 'orthogonal' mode being displayed. The orthogonal modes have identical intensity patterns but at varying angles of rotation away from the plane in which the above modes are measured.

To reproduce the entire beam pattern of the horn at any point, all modes and their orthogonal set must be summed in quadrature. Thus on complete summation the far-field beam pattern of the 857 horn at 860 GHz is shown in figure 5.7. The entire beam spans roughly 30 ° with high on-axis gain due to the increased power from a greater number of modes, which in turn means greater sensitivity.

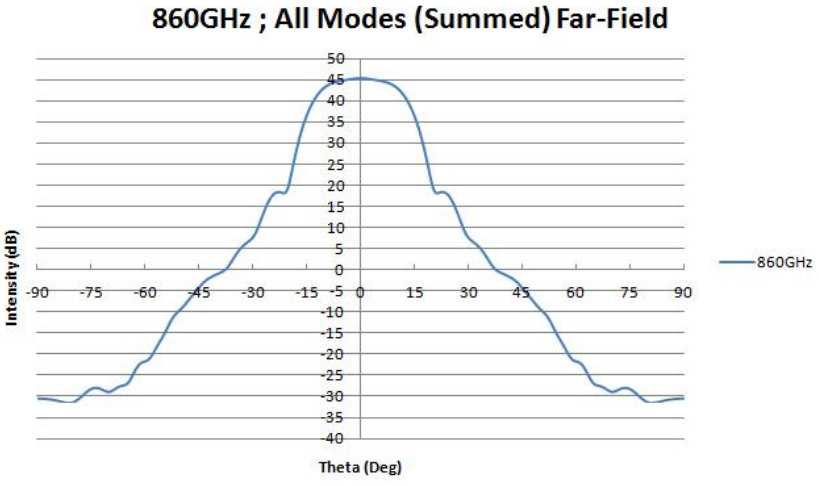

FIGURE 5.7: Summed far-field beam pattern of the Planck 857 horn at 860 GHz. Notice the broad angular extent of the peak, resulting from the large number of higher order modes excited in the horn structure. Sidelobes are also considerably lower and less prominent than one would expect for a single moded beam, such as that generated by the Planck 101 horn, and shown in figure 3.14.

.

5.1.2 Modelled Beam Patterns

To provide insight into whether the effects of horn manufacturing error could be seen in telescope simulator trial, the far-field beam patterns of three altered geometry horns were modelled at the location of the arc-lamp source, and compared against measurements. The two sources of data pertaining to the measurement campaign arose from a presentation of results to the Planck Core Team in July of 2008 [75], in which antenna response and telescope simulator far-field beam patterns were produced, for both 545 and 857 GHz multi-moded horns. Some of these beam patterns will be highlighted below for comparison with modelled results.

The antenna response far-field beam patterns were of significant interest to a modelling campaign undertaken in parallel to this work, in which various altered horn geometries were simulated using SCATTER, and their resultant far-field patterns analysed [69], some of which were illustrated in Section 3.4.1. By analysing these measurements, the levels which sidelobes would need to reach before imperfections in horn etching become noticeable above the measurement noise floor were deduced. Six back-to-back flight horns (labelled 857-1A to 857-1F) were tested, and the beam patterns for Planck 857-1B at 511 GHz are shown below in figure 5.8. Overlaid are the patterns for horns with various number of corrugations filled (simulating incomplete etching) in the throat section of the front-end. Observing the comparison for increasing number of corrugations filled, the general trend towards higher sidelobes and broader main beam is quite clear. It is not entirely linear however, as the case of four corrugations filled seems to show less deviation from the ideal beam pattern than one would see for the case of filling only two or three corrugations. In any case, there are some features at roughly the same level as the noise so it is possible the some imperfections would have been imperceptible to measurement. This is in keeping with the hypothesis that horn imperfections, overlooked in pre-flight measurement, could now be the cause of the strange features seen in difference maps at these highest HFI bands. At this frequency the Planck-857 horns are single-moded (denoted 'sm' in the plot), meaning that comparative modelling will not describe all potential effects arising from changes to individual modal fields due to imperfections. "PF857F-1B+PF857B-1B" refers to the fact that both front, 'F', and back, 'B', of the 857 back-to-back horn were in combined use for the measurement.

Unfortunately, the antenna response measurements and subsequent comparative simulations were performed at 511 GHz, well below the operating band of the horn. The telescope simulator measurements on the other hand, were performed at 857 GHz, and for this reason a comparative analysis with simulator results has been performed by the

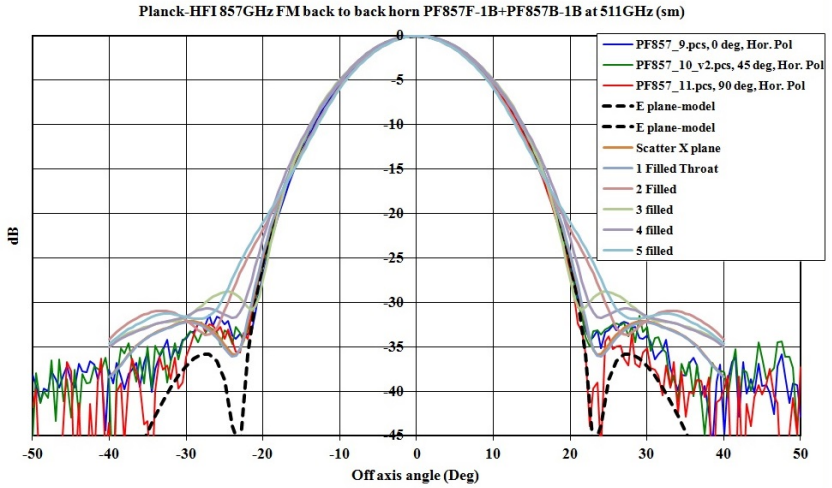

FIGURE 5.8: Comparison between antenna response beam pattern measurement of the Planck 857-1B flight horns performed at 511 GHz, and simulated beam patterns based on various levels of horn alteration [69].

author. The original beam measurement of the 857 GHz horn taken using the arc-lamp source is shown below in figure 5.9. The first aim was to use the GRASP9 model of the experimental set-up to try and explain the size and asymmetry of the measured beams.

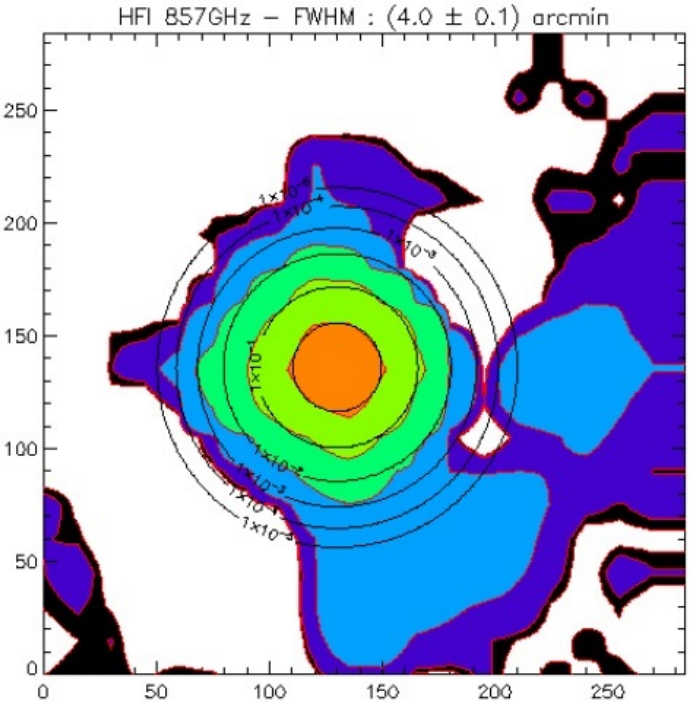

FIGURE 5.9: Telescope simulator far-field beam pattern of the Planck-857 B2B horn at 857 GHz (coloured contours), with overlaid Gaussian contours highlighting the asymmetry of the beam pattern.

Unfortunately due to the lack of valid information regarding the measurement process, the scale along both axes in figure 5.9 not known. The beam FWHM is given, however,

as $\sim 4'$, thus taking the Planck plate scale of $\sim 2'/\,\mathrm{mm}$ mentioned previously, one would expect an equivalent beam FWHM of approximately 2 mm. This was tested by modelling of the 'ideal', 'bad', and 'worst' case horns, the individual modal fields for each of which was propagated through the telescope simulator. The resulting beams are shown in figure 5.10, modelled on square grids in mm across both planes. The contours in the diagram representing 3 dB changes in intensity, and describe features down to 30 dB from the main beam. The first contour is seen roughly 2 mm from the beam peak (in red).

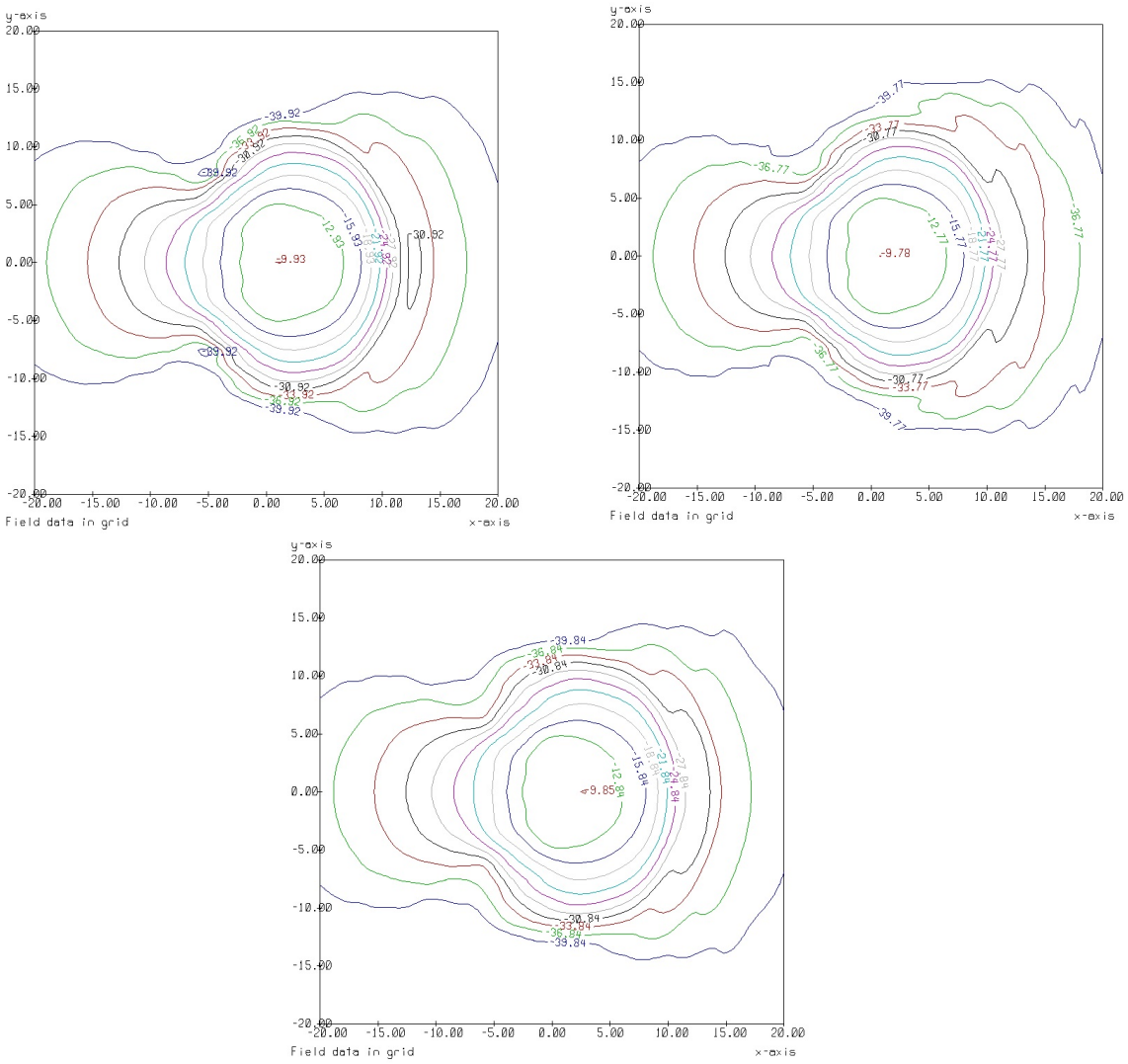

FIGURE 5.10: GRASP9 telescope simulator far-field beam pattern of an 'ideal'(top), 'bad'(middle),and 'worst-case'(bottom) Planck-857 B2B horn, modelled at 857 GHz. All partially coherent modal fields summed in quadrature at equivalent distance to the arc-lamp source on the test-bed.

Though identical scales cannot be verified, the general shape of the beam at the output plane resembles that of the simulator measurements. Beam divergence in the negative-x direction, instantly obvious in the model, can be discerned in measurement also by

comparison of the Gaussian contours overlapping the actual beam in figure 5.9. The fit is seen to be much worse in the negative-x direction, however along positive-x it is much more Gaussian in nature. The modelled beams are asymmetric about the vertical (y-) axis, which is also in good accordance with measurement. Crucially, however, any differences in beam pattern from horn to horn based on imperfections would be in no way obvious on analysis of the telescope simulator beam patterns.

5.2 FIRI

The FIRI (Far Infrared Interferometer) space telescope is envisaged as a multi beam interferometer that will break current constraints on angular resolution obtainable at infrared wavelengths. If launched it would perform measurements for approximately five years. It was conceived of by the European Space Agency (ESA) in 2004 to combat the limitations imposed on infrared astronomy by current technology. Because of the long wavelengths in the infrared, any single reflector system would require an extremely large dish to obtain better angular resolution than is currently available. Herschel, for instance, is a single reflector system launched by ESA in 2008 which suffers under this constraint, achieving barely 7 arcseconds resolution in observations. Also, almost half of all the light emitted by stars is at far infra-red wavelengths, which have yet to be deeply explored.

Ground-based infrared astronomy commonly uses long baseline interferometers to maximise their capability, however the Earth's atmosphere absorbs radiation in a large part of the infrared range, from 30-300 μm, meaning only low resolution images can be obtained. FIRI has been proposed to remedy this, initially designed as a multi-craft long baseline telescope it has since been revised to one large spacecraft from which two telescope platforms will be unfolded and extended over a smaller variable baseline. These two cryogenically cooled telescopes will constitute a typical Michelson interferometer, enabling up to 1 arcsecond resolution across a wide bandwidth ranging from 25 to 300 μm. Though the more obvious choice was a multi-craft interferometer achieving much larger baselines, and thus greater resolution, the novel technologies likely to arise from development of a multi-boom telescope will be of great use in future missions. This coupled with the reduced monetary input and operational complexity required for a single satellite system provided enough incentive to further its development.

The three primary scientific objectives of the mission are investigation of the formation and life cycles of planetary systems, stars and galaxies, each of which will be expanded

on below. The fundamental processes underlying their evolution have key signatures in the infrared, and thus FIRI is a prime candidate to further our knowledge of them.

The primary objective is generation of spectral maps of proto-stars under various conditions, by penetrating the surrounding gas at infrared. This will allow for greater understanding of star formation processes by evaluating the internal chemical structure, with special attention paid to the H2 emission line around 28 μm. Further insight may be gained by observation of the collapse of the interstellar cores, as well as observation of binary systems, and cluster forming regions with star formation condensations.

Secondary to this is the study of planetary formation, enabled by observation of the star forming regions mentioned previously. The temperature of the dust in proto-planetary disks grows when a proto-planet is moving through it, however the tiny fractional changes due to the frictional heating has been difficult to measure accurately using Earth-based systems. A space-based observation platform provides the perfect opportunity to resolve the warmer dust inaccessible from Earth, which will take on resonant structures proportional to the size and speed of objects moving through it. Observation of this will also further our understanding of the relationship between planets and the extra-solar mass which will later form the Kuiper Belt.

Another scientific goal of FIRI is to measure star formation by observation of supernova remnants and HII emission lines in regions of dense star formation between redshifts of $1 \leq z \leq 5$ [76]. The star formation rate can be deduced by observation of emission lines between 30 μm and 100 μm, particularly the CII line at 158 μm, which will also allow the redshift of the various sources to be measured.

Looking further afield, FIRI will also provide insight into the early Universe. One of the key tasks here is the observation of star forming clouds at high redshifts of $10 \leq z \leq 20$. The HII lines at 17 μm and 28 μm are doppler shifted to 170-560 μm at these distances, and appear at extremely weak levels (as low as $10^{-24}\,\mathrm{W/m^2}$). These are also difficult to detect from Earth, but should be seen by FIRI.

FIRI will also investigate the Cosmic Infrared Background (CIB), which peaks at 160 μm and should resolve upwards of 90% of background sources. This will involve measurement outside of the solar system ecliptic to minimise zodiacal light.

There are other proposals for future far-infrared telescopes and the best design is still being debated. FISICA is an EU-funded project to investigate issues associated with FIRI-like missions. As part of this, the author has developed a physical optics model of

a test-bed, built in Cardiff University, to investigate the proposed double-Fourier beam-combiner. It is being modelled to assess the effects of system diffraction, misalignment, and other potential issues related to the test-bed set-up.

5.2.1 The FIRI Test Bed

The FIRI test-bed is modelled here in GRASP9 to test its viability as a suitable configuration for the eventual telescope design. The experimental configuration comprises a source simulator and a spectral/spatial interferometer [77]. The source simulator comprises a large spherical mirror of focal length f=2.1 m illuminated by an axially aligned source at a distance of f/2. This mimics a distant source by illuminating two smaller off-axis paraboloid mirrors situated 7 m from the reflector. These primary mirrors, of identical dimensions and 300 mm focal length, couple radiation to smaller secondary paraboloid mirrors. Each of these then feed one of the spatial arms of the interferometer. By placing various sources at the focus of the main reflector, various types of sky source can be simulated. In the work of this thesis both single and double slits are used to represent single and multiple sources on the sky (coherent at this stage), information about which can be accurately resolved by interferometric techniques. A geometrical representation of the focussing mirror system is shown in figure 5.11.

The distance between these two telescopes dictates the baseline separation of the interferometer, which can vary between 100 mm and 500 mm, limited only by the configuration of the internal mirror system of the interferometer. A schematic of the interferometric set-up is shown in figure 5.12, where the two telescopes are represented by the curved mirrors on the far left of the diagram.

The design is a direct detection interferometer, which allows simultaneous measurement of high resolution images and source spectra over a wide field of view. To vary the baseline of the telescope, or to vary the path length difference between beams, requires adjustment of the spatial and spectral sections of the telescope. The spectral section is the region labelled 'B' in figure 5.12, which includes one of the two focussing telescopes as well as the flat mirror, M5. The spatial section consists of two flat mirrors M2 and M3, which are seen along 'C' and 'D'. When the baseline distance between the telescopes is increased by any amount, say 100 mm, the spectral section is moved such that the distance between M1 and M2 decreases by half that distance, in this case 50 mm. M2 moves in tandem, such that a total path length change of 100 mm along 'C' and 'D' compensates for the reduced path length along the lower telescope.

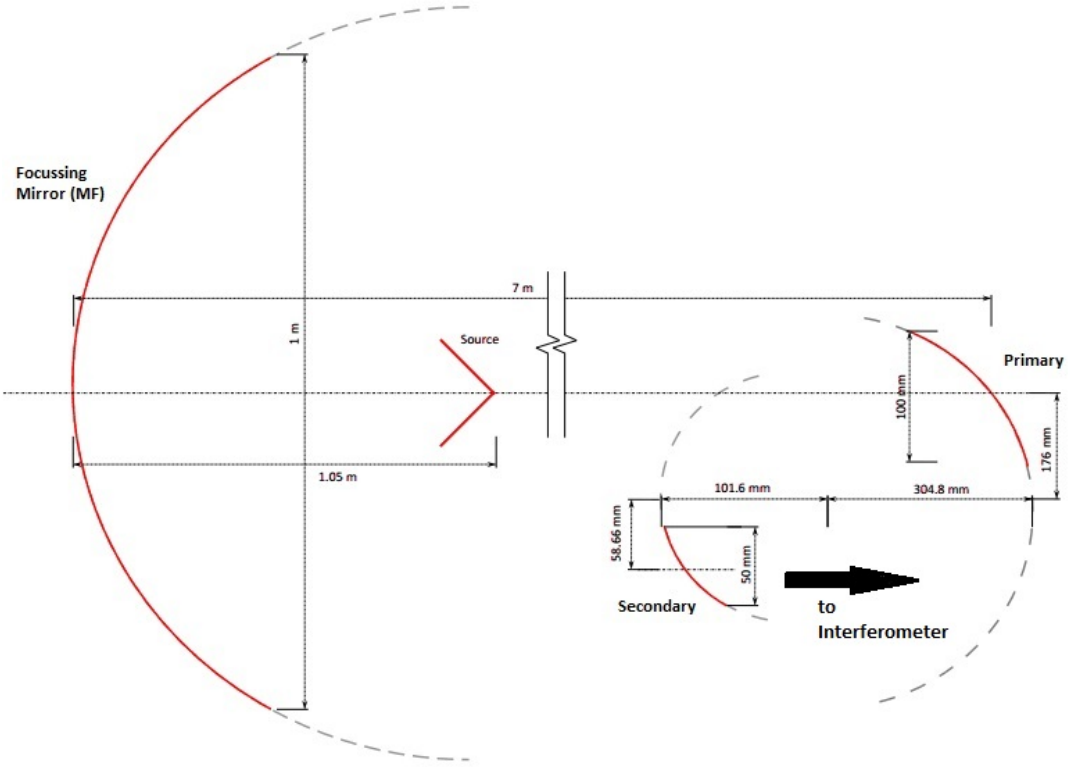

FIGURE 5.11: Geometrical description of the FIRI test-bed focussing telescope, comprising a large main mirror, which illuminates identical primary mirrors on two interferometer arms, A and B. These then feed their respective secondary mirrors, which prorogate power through the interferometric mirror system.

The path length along 'ACDE' is the same as along 'BGHI', such that having travelled along either the lower spatial or upper spectral arms the beams are combined at the polarised beam-splitter labelled 'BS' in figure 5.12 after travelling the same distance. Half of the signal from each path is retained and propagated along 'I', 'J' and 'K' to the detector array labelled 'DET', where the interference pattern is formed. The other 50% is dumped into a load aligned along 'I' beyond 'BS'. Varying the baseline allows spatial information about the source to be recovered. To recover spectral information, the length of the spectral arm is varied so that there is a variable path length difference between the beams arriving at the beam splitter.

The GRASP9 model of the system is shown in figure 5.13, where, for illustration, rays have been traced from a planar source in the near-field of the primary mirrors to simulate a distant source. All flat mirrors in the system are square with 50 mm side length, with the exception of M8 which measures 100 mm along each side. All small flat mirrors, except M8, are rotated by 45 ° about the direction of propagation. This diamond orientation maximises the cross-section of incident beam captured by each reflector, crucial

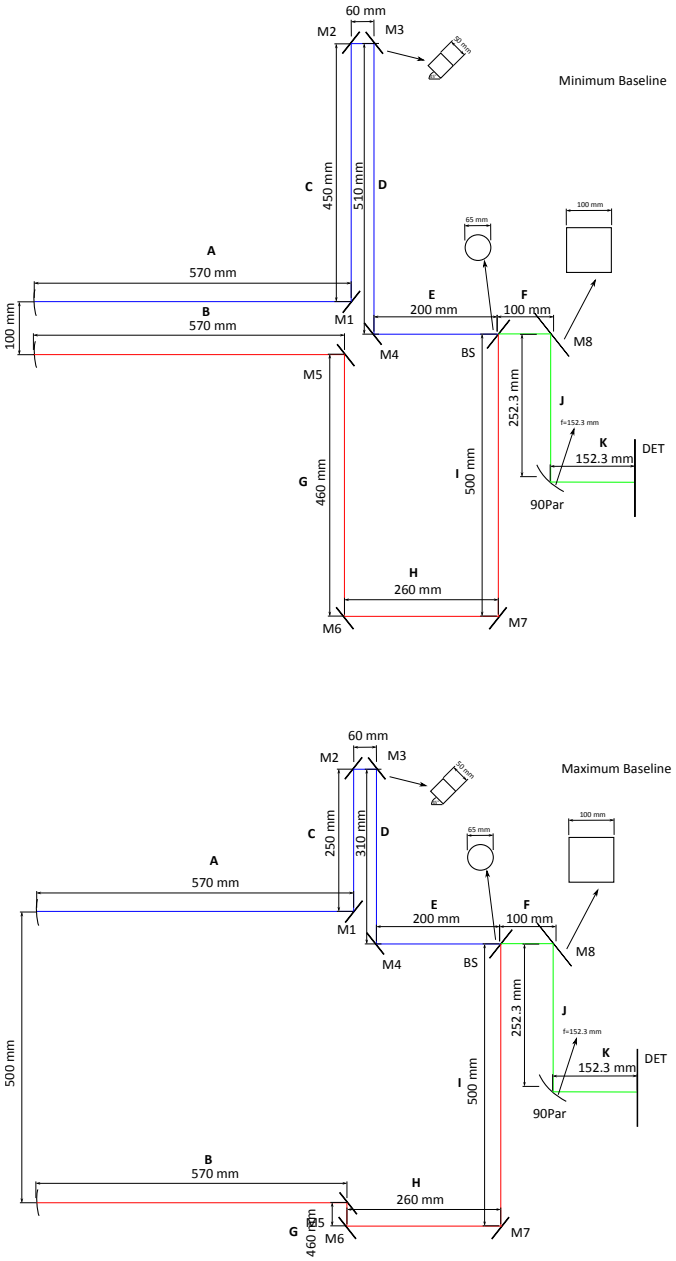

FIGURE 5.12: Geometrical description of the FIRI interferometer, displaying sections A and B, and the constituent ray paths traced along each for minimum and maximum baseline separation. [78]

due to the long travel distance over which the beam must remain collimated in a system of small reflectors.

The beam-splitter is implemented by using the 'Power Splitting' option in GRASP9, which when chosen allows the power transmission and reflection percentages to be chosen as long as a combined 100 % power is observed. In this implementation, only 50 % of the total power through both paths will be directed to M8 and onward to the detector. The other 50 % is dumped onto a load as illustrated in figure 5.14.

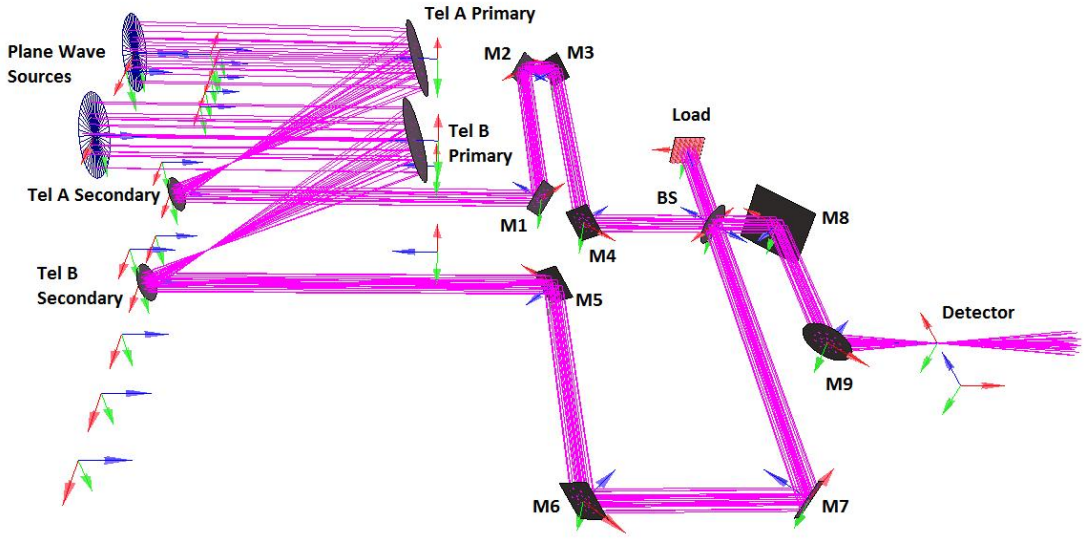

FIGURE 5.13: 3D view of the GRASP9 modelled FIRI interferometer test-bed, displaying telescopes A and B at 100 mm baseline separation. Plane wave inputs mimic the radiation from a distant source illuminating both mirrors. The combined beam from both paths is brought to a focus at $2f$ distance from the parabolic mirror M9, which has focal length of 76.15 mm.

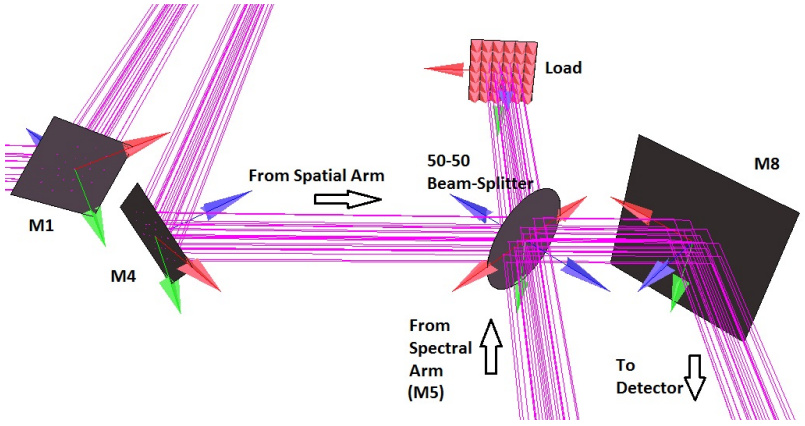

FIGURE 5.14: Beam-splitter implementation in the GRASP9 model of the FIRI system, with relevant input and output paths.

Initial test-bed measurements highlighted power loss in the system beyond that expected on implementation of the 50-50 beam-splitter, but crucially at longer baseline separations the power loss increased. This was investigated by illuminating both telescope primary mirrors with a plane wave source, and monitoring the power incident on each of the reflectors relative to the power at the primary. The path length along both A and B is reduced with increasing distance between the arms, thus greater power throughput would be expected with increasing baseline length. To verify this, the baseline of the interferometer was varied in 100 mm steps between the minimum arm separation of 100 mm and maximum separation of 500 mm, and simulations performed at the lowest end of the test-bed band (λ =2 mm), at which the largest levels of spillover would be

expected. This is shown in figure 5.15.

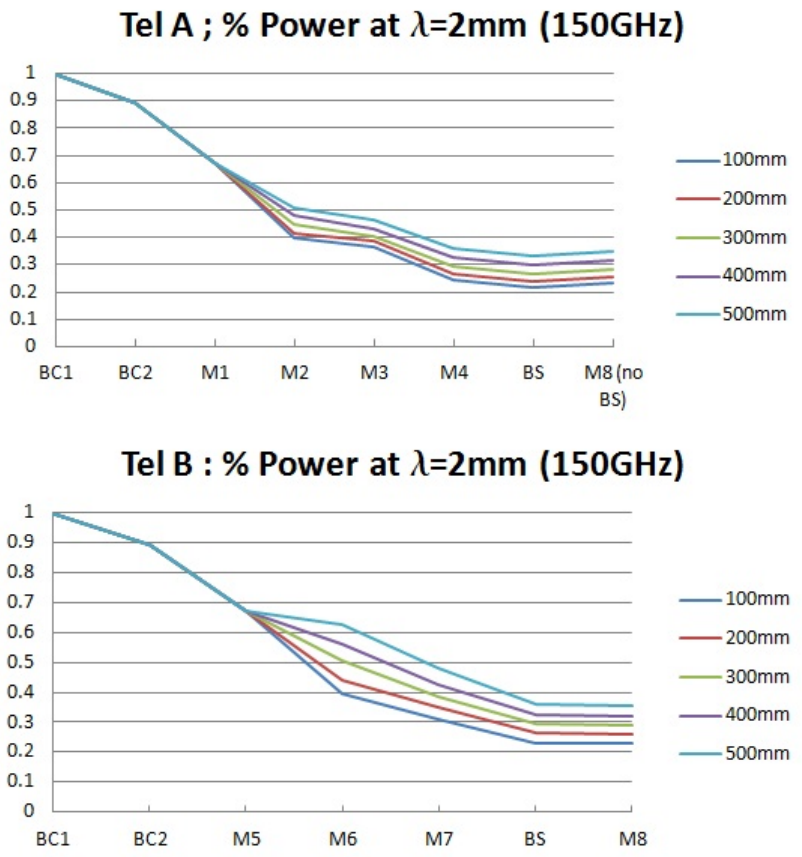

FIGURE 5.15: Power throughput along telescope arm A (top) and arm B (bottom) at λ =2 mm, where each arm is fed by a plane wave source coupling 100 % power to each primary. Results for 5 baselines of between 100 mm and 500 mm in length are shown.

The inclusion of the larger M8 reflector highlights minimal power loss beyond M4 and M5. Along arm A the beam-splitter and M8 are fed directly by M4, as inclusion of the beam-splitter in calculation of M8 power would eliminate half of the incident power. Along arm B the splitter is modelled as an ideal reflector, thus maintaining a true representation of power loss from spillover alone. The majority of power loss in the system is seen to arise from spillover beyond the first two mirrors of each arm, with a consistent 25 % loss at M1 (this path length does not vary with baseline) and another 25 % at M2 for a 100 mm baseline separation. This combined 50 % loss reduces to 40 % for the maximum baseline separation, in which case M1 and M2 are actually closest together. There is a 10 % difference in the power loss along M1-M2 across the same range of baselines, varying from 25 % power loss at 100 mm to 15 % power at 500 mm. However this loss is not replicated along M3-M4, which will always have a slightly longer path length than M1-M2 (see figure 5.11). Here a 2 % difference is observed, varying between 12.5 % at the 100 mm baseline and 10.5 % at the 500 mm baseline, while the overall power loss of 11.5 % is significantly less than along the shorter path M1-M2, due

in part to the collimating effect of the quasi-roof mirror M2-M3. A maximum 78.5 % power loss across the entire arm is observed for the 100 mm baseline, reducing to 66 % for the widest separation.

The difference in power loss is much greater along arm B, due to the M5-M6 distance varying by 100 mm for each increment in baseline separation, whereas M1-M2 varied by only 50 mm. Here power loss is as high as 25 % along M5-M6 for a 100 mm baseline, and as low as 5 % for the 500 mm baseline. Again, figure 5.11 illustrates the distance between M5 and M6 for maximum and minimum baseline separation, which explains the dramatic change in power loss seen in figure 5.15. Similarly to path A, total power loss at the beam-splitter is as high as 77 % for a 100 mm separation and lower at 64 % for the maximum separation.

As the level of spillover is naturally wavelength dependent, wavelength was also varied across the operating band from λ =2 mm to λ =0.29 mm, and the equivalent power loss calculated. This is shown for arm A in figure 5.16, and for arm B in figure 5.17.

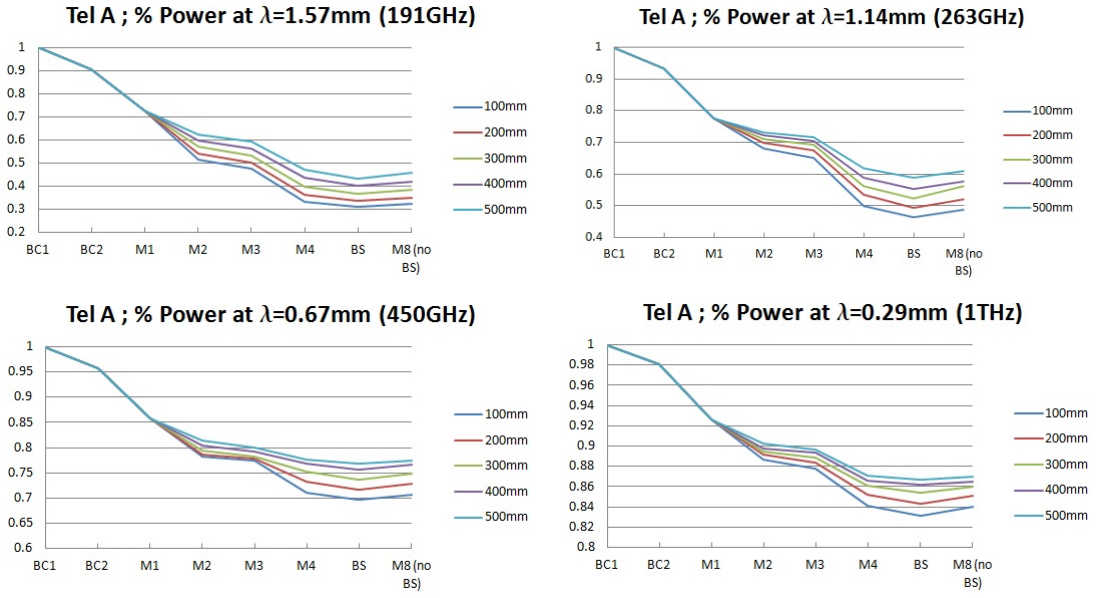

FIGURE 5.16: Power throughput percentage (y-axis) along telescope arm A at λ =1.57 mm, λ =1.14 mm, λ =0.67 mm and λ =0.29 mm. Results are shown for 5 baselines between 100 mm and 500 mm in length.

Immediately obvious is the steady reduction of power loss with shorter wavelength, with well over 80 % of power retained at retained at the highest end of the band for the worst case of 100 mm separation. This increases to upward of 86 % for a 500 mm separation, while at band centre (λ =1.14 mm) over 60 % of power is retained for the same separation.

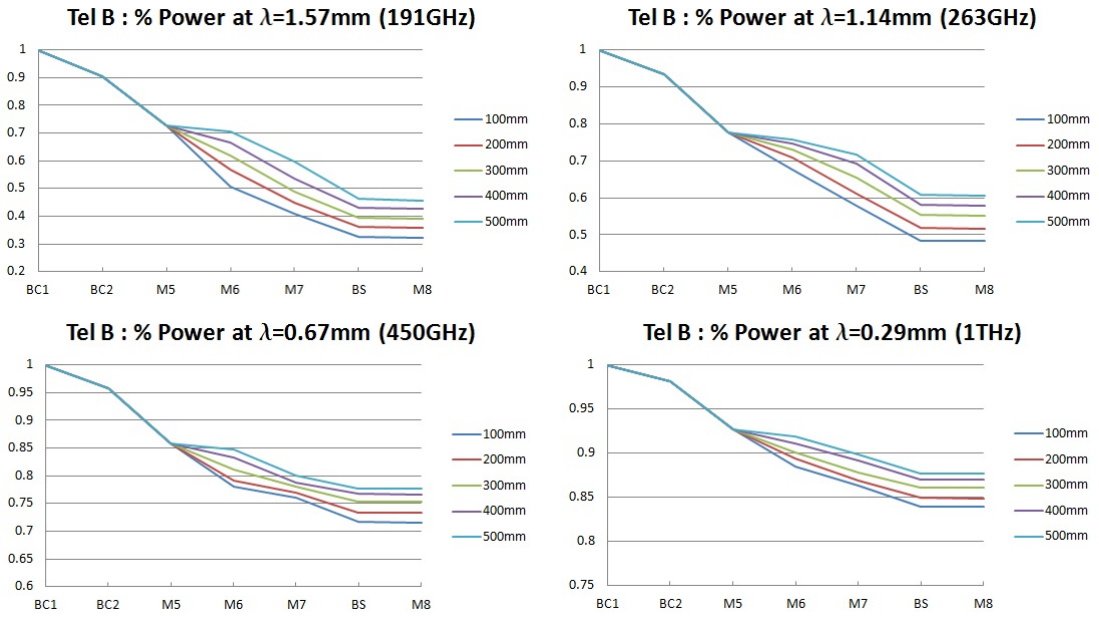

FIGURE 5.17: Power throughput percentage (y-axis) along telescope arm B at λ =1.57 mm, λ =1.14 mm, λ =0.67 mm and λ =0.29 mm. Results are shown for 5 baselines between 100 mm and 500 mm in length.

5.2.2 Investigation of Beam Interference

A basic analysis can be performed by interfering two or more beams in the combiner to recover information about the original state of the beams.

One key property of an interferometer is its ability to resolve the angular scale of an object on the sky by observing the visibility of the fringe pattern returned at different baseline separations, where the visibility of an interference pattern is given by $V = I_{max} - I_{min}/I_{max} + I_{min}$, and varies between $V = 0$ for a perfectly resolved source and $V = 1$ for a perfectly unresolved source. A star of a small angular size on the sky resembles a point source, such that radiation originating from any point on the object will have travelled the same distance to the telescope as light from any other point on it, meaning all radiation received from the source is in phase. Thus, on combination of beams through both arms, regardless of baseline separation, nearly perfect constructive and destructive interference will be observed with variation in path length difference (Δ) between the arms. This is clearly illustrated in figure 5.18 where a 1 mm by 7 mm single slit source simulates a point source on the sky, creating almost perfect constructive and destructive interference on the output plane across all baselines. One complete sinusoidal oscillation of the fringe pattern is observed over a path length difference of λ, as the beams begin in phase at $\Delta = 0$, slowly move out of phase for $\Delta > 0$, and return in phase again at $\Delta = 2$ mm. The variation in peak power across the five baselines is

due entirely due diffraction in the system, which is greater at lower frequencies. As the baseline increases the path length along both arms decreases as illustrated in figure 5.12, resulting in less diffraction through the sequence of flat mirrors. This means greater power reaching the detector, and subsequently higher peaks in the interference pattern observed.

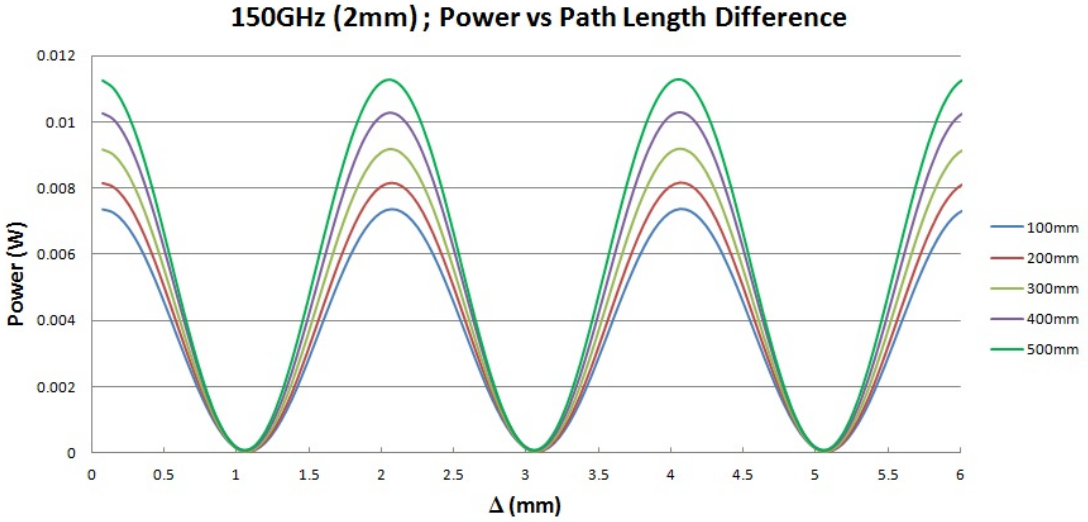

FIGURE 5.18: Interference pattern at the output plane for a 1 mm wide single-slit source supplied with 4π W and modelled at λ =2 mm (150 GHz). The path length difference between the two arms increases from 0 mm to 6 mm (3λ), and the resulting beam combined power is shown for five baseline separations, from minimum (100 mm) to maximum (500 mm).

Similar fringe patterns modelled for a further four, equally spaced, wavelengths across the band are shown in figures 5.19 and 5.20. The inability of the telescope to resolve the 1 mm slit is made readily apparent by the near perfect destructive interference observed at $\phi = 180\,^\circ$ phase offset between the beams. As frequency goes up diffraction becomes less problematic, and at $\lambda = 0.29$ mm the power at the detector also decreases slightly with increasing baseline. This effect would not be seen when observing a real point source, it is merely a result of the point source simulation technique used in the test-bed arrangement. At higher frequencies, with less diffraction, the finite width of the fixed focussing mirror means it fails to illuminate the lower arm in figure 5.12 with the same amount of power as it did at shorter baselines.

To model the resolving capacity of the telescope, the fringes from the 1 mm slit were compared against those from a 100 mm slit, supplied with the same power at the input. The 100 mm $\times$ 700 mm slit simulates a much broader source on the sky (although still coherent), and should generate quite different fringe patterns at the output plane. As mentioned previously, all light from a point-like source is in phase at the aperture of the telescope, regardless of baseline separation, however for a broader source this is not the

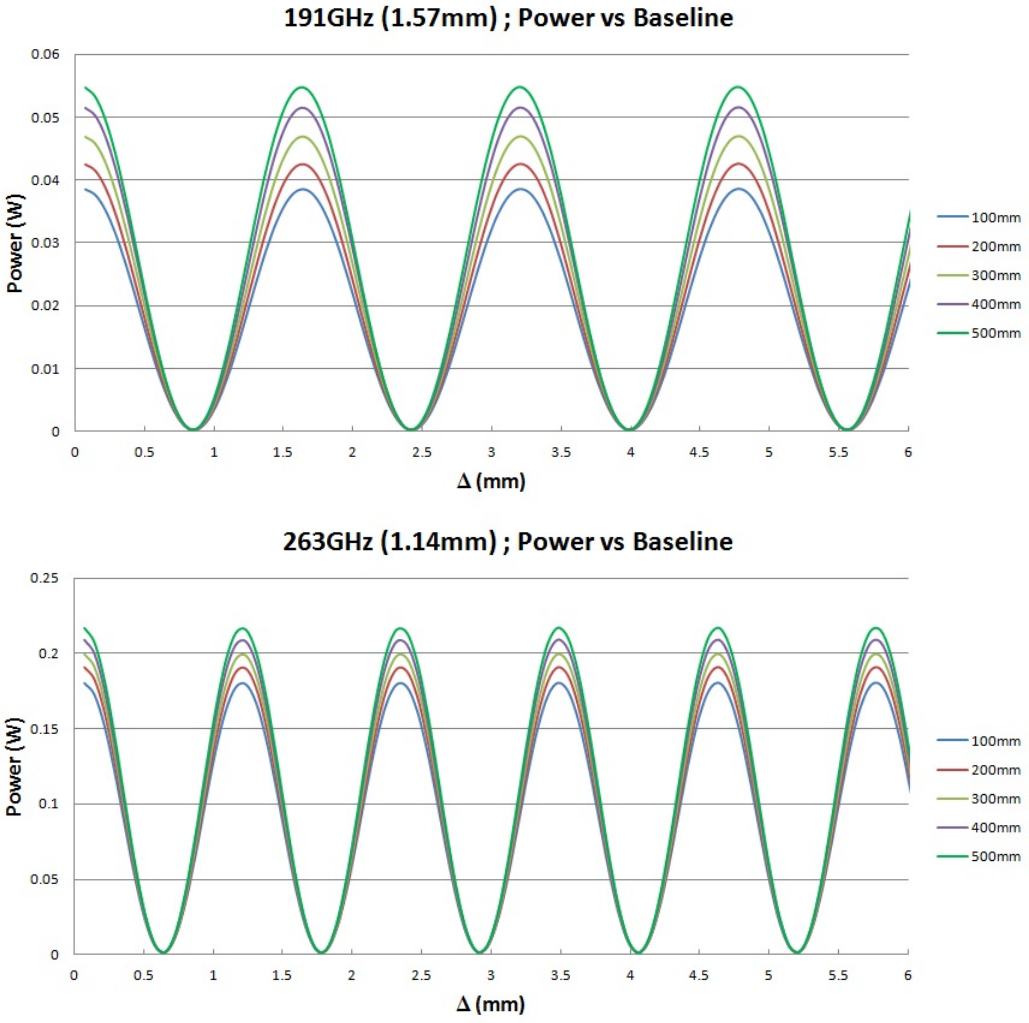

FIGURE 5.19: Interference pattern at the output plane for a 1 mm wide single-slit source modelled at λ =1.57 mm (top) and λ =1.14 mm (bottom). The path length difference between the two arms increases from 0 mm to 6 mm, and the beam combined power is shown at five baseline separations from minimum (100 mm) to maximum (500 mm).

case. At shorter baselines the broader source may well remain unresolved, however as the baseline of the telescope increases, the path length distance of light travelling from two separate sides of the source will manifest itself as a phase difference in the signal received. As the radiation received from different parts of the source are never fully in phase, varying the path length difference between the arms will generate an interference pattern of much lower peak to trough amplitude than that of the smaller source. This amplitude is known as the interferometric visibility, which describes an interferometer's ability to resolve sources on the sky. A comparison between the fringe patterns recovered for a 1 mm and 100 mm slit source at 100-mm baseline separation is shown in figure 5.21, where the limited ability of the telescope to resolve the broader source is highlighted by the high visibility of the fringes ($V \sim 1$).

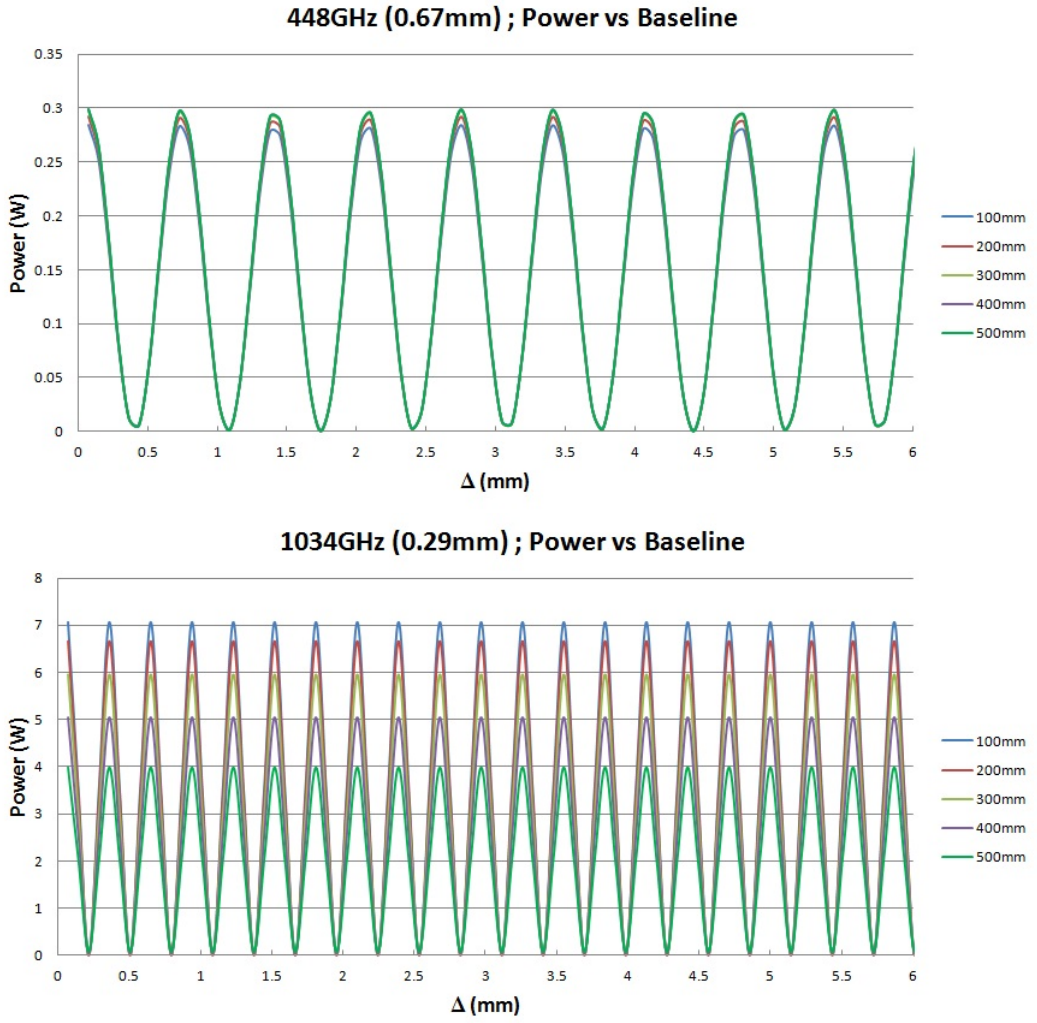

FIGURE 5.20: Interference pattern at the output plane for a 1 mm wide single-slit source modelled at λ =0.67 mm (top) and λ =0.29 mm (bottom). The path length difference between the two arms increases from 0 mm to 6 mm, and the beam combined power is shown at five baseline separations from minimum (100 mm) to maximum (500 mm).

Increasing to the largest baseline separation of 500 mm, the interferometer's ability to resolve the broader source is dramatically improved, as illustrated by the much lower visibility of the fringes ($V \sim 0.2$). This illustrates the power of interferometry, which dispenses of the need for large single dish telescopes to increase resolution. Instead, one can take two smaller telescopes, separate them by as much distance as is feasible for the integrity of the system and, assuming the beams from both telescopes are combined correctly, it is equally as powerful as a large dish whose diameter is equivalent to the distance between these two smaller ones. In this case a $D = 500$ mm telescope has been simulated by two smaller 100 mm reflectors which are separated by the D.

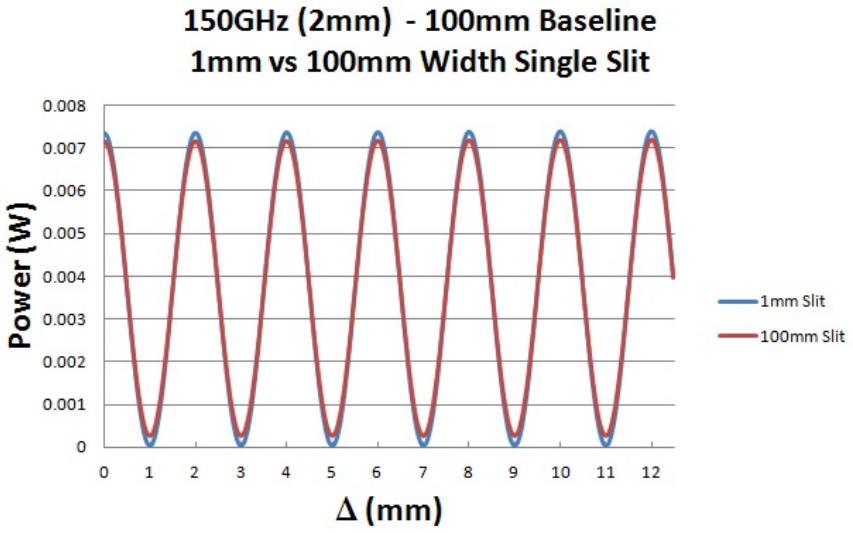

FIGURE 5.21: 100 mm baseline interference pattern for a 1 mm slit vs a 100 mm slit modelled at $\lambda = 2$ mm (150 GHz).

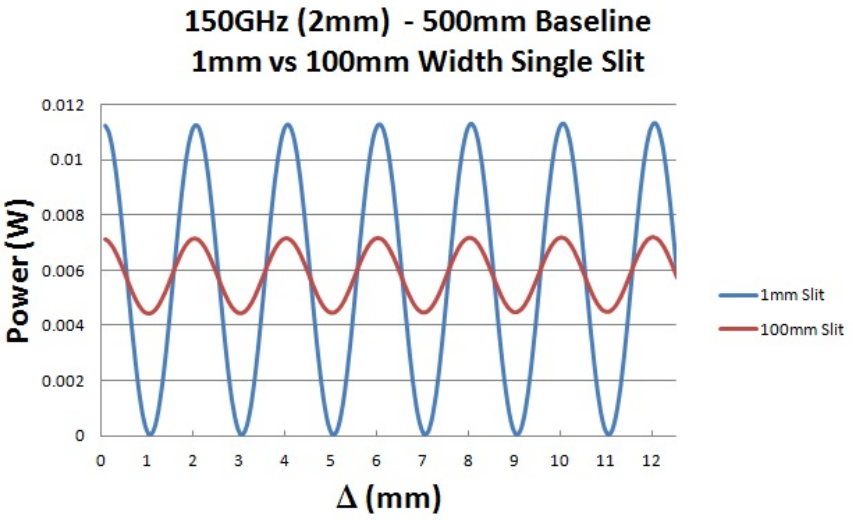

FIGURE 5.22: 500 mm baseline interference pattern for a 1 mm slit vs a 100 mm slit modelled at $\lambda = 2$ mm (150 GHz).

5.2.3 Recovery of Source Frequencies from Fringe Pattern

In reality an observed source will rarely be monochromatic, instead emitting at multiple frequencies. This creates a much more complex interference pattern at the output, as radiation from different frequencies will move in and out of phase at different rates. This is illustrated in figure 5.23, where the component beams originating from a 1 mm slit emitting at 150 GHz (2 mm) and 167 GHz (1.8 mm), were summed coherently for a baseline separation of 100 mm, thus simulating the interference pattern of a multi-frequency source. The slowly oscillating sinusoidal envelope of the fringe pattern is

indicative of a more complex frequency spectrum than that seen for a monochromatic source.

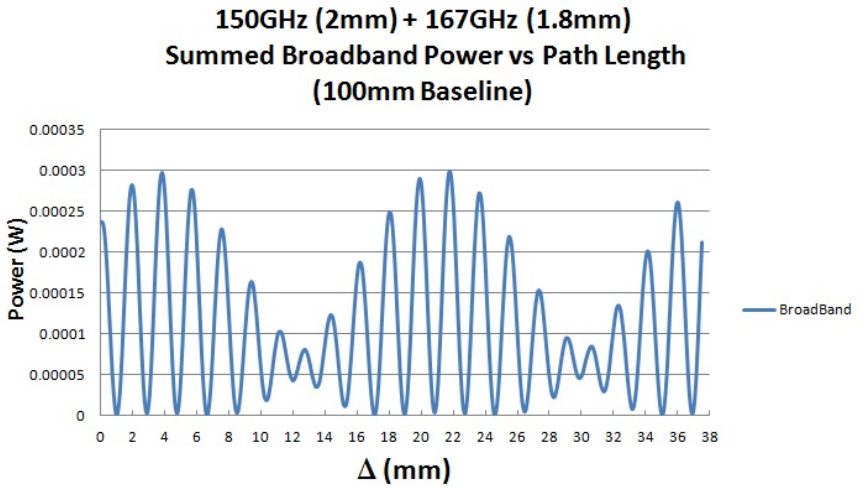

FIGURE 5.23: Interference pattern generated by a multi-frequency (150 GHz and 167 GHz) single slit source modelled at 100 mm baseline.

To recover the spectrum of the source a Discrete Fourier Transform of the fringe pattern is performed, converting the data from the spatial domain to the wavelength domain. The wavelengths of emission can then be observed by plotting the power in the beam pattern as a function of the resulting wavelength spectrum, as shown in figure 5.24, where the spikes in the spectrum indicate the two wavelengths of source emission.

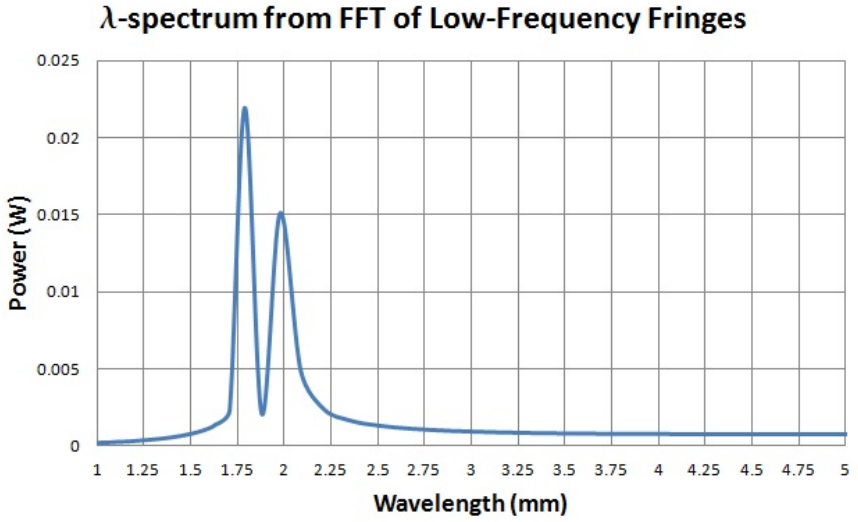

FIGURE 5.24: Wavelength spectrum recovered by FFT of the interference pattern shown in figure 5.23. The spikes at 1.8 mm and 2 mm respectively correspond to the 167 GHz and 150 GHz frequencies at which the source emitted.

Performing a similar analysis at the highest end of the band, the same single-slit source emitted at 1034 GHz (0.29 mm) and 940 GHz (0.32 mm), and again the beam patterns

were coherently summed across a 100 mm baseline. To maintain continuity a 10 % bandwidth spans the distance between the two frequencies, which was the case for the low frequency model also. The interference pattern is shown in figure 5.25, and is quite similar in form to that of figure 5.23, however notice that the envelope of the high frequency model oscillates much more rapidly with Δ than the low frequency model does.

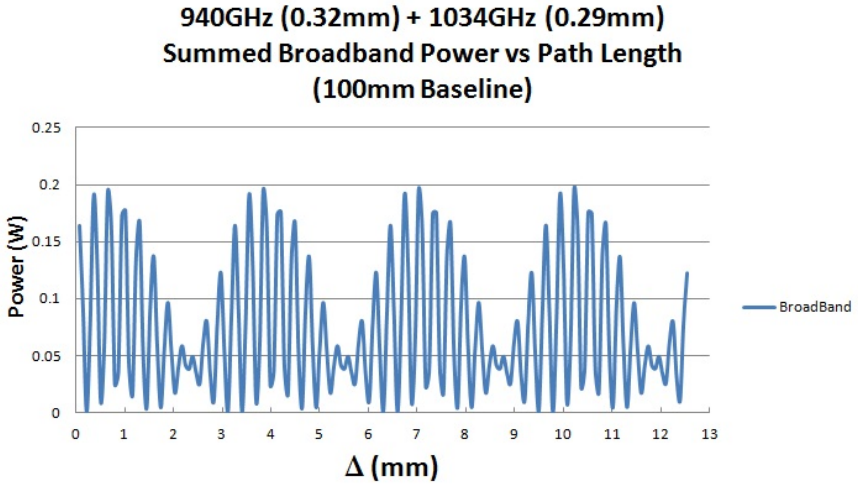

FIGURE 5.25: Interference pattern generated by a multi-frequency (940 GHz and 1034 GHz) single slit source modelled at 100 mm baseline.

Performing an FFT of the pattern the wavelength spectrum of the source is once again obtained, as shown in figure 5.26. In comparison with figure 5.24 it is clear that there is much more power in the high frequency beam than in the low frequency beam, as expected due to diffraction in the system.

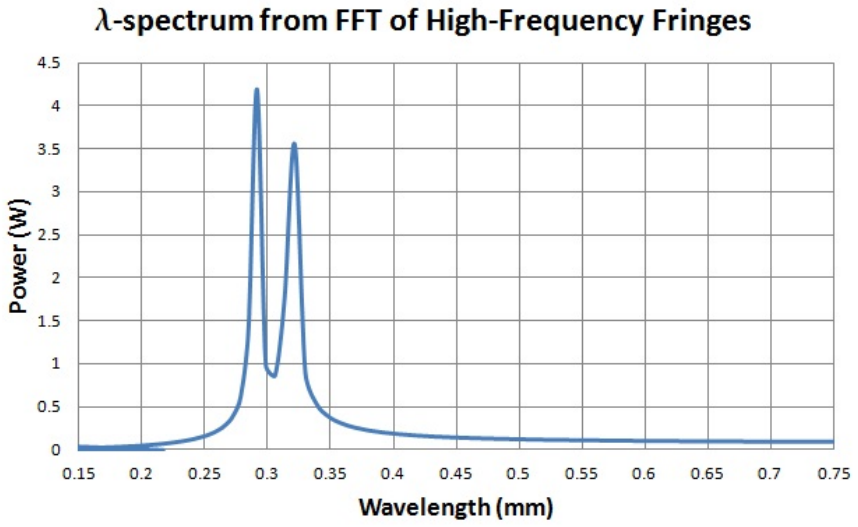

FIGURE 5.26: Wavelength spectrum recovered by FFT of the interference pattern shown in figure 5.25. The spikes at 0.29 mm and 0.32 mm respectively correspond to the 1034 GHz and 940 GHz frequencies at which the source emitted.

Now that the optical model has been set up, it can be used to analyse the effect of the optical system on the image and frequency spectrum of observed sources.

5.3 Conclusion

In this Chapter we implemented various complex systems in GRASP9, illustrating the broad range of telescope systems one can design and the flexibility with which unusual features can be defined. We first modelled the Cardiff telescope simulator used for pre-flight validation of the HFI flight horns, outlining the implementation of two unusual reflector designs, and then testing whether effects due to horn imperfections would be noticeable in measurements. Although the asymmetric measured beam patterns were replicated by the model, it was concluded that any difference in the beam pattern arising from imperfections in the horn would very likely go un-noticed in measurement. It follows that the features seen in the difference maps of all but one of the HFI flight horns may be a result of minor imperfections in the horns, which could not be seen in pre-flight measurement.

The second telescope system investigated was that of the FIRI test-bed, an interferometer whose set-up we replicated in GRASP9. Power throughput along both arms of the telescope was modelled for a range of baselines spanning the full extent of the telescope, and a range of frequencies spanning the telescope bandwidth. Although significant power loss was measured on the test-bed this could not be seen in modelling of a perfectly aligned system, thus it was concluded that the test-bed may be misaligned. Further interferometric analysis was performed to illustrate the power of the interferometric technique, and the resolution capabilities of the telescope. This model will be developed in the future to analyse the effect of various system parameters on the images and spectra obtained by a FIRI-like beam combiner.

In the next and final Chapter we will investigate the properties of 'ultra-Gaussian' horns, with a view to optimising their implementation in the STEAMR atmospheric physics experiment.

Chapter 6

Modelling of Multi-Moded Horns for STEAMR

This chapter outlines the experimental work undertaken in modeling, measuring and optimising a special type of corrugated feed horn, it is hoped will be used in the 'Stratosphere-Troposphere Exchange And climate Monitor Radiometer' (STEAMR), an ESA mission in development, which is set to measure atmospheric properties with implications for global warming, pollution and even particle physics.

6.1 Introduction

STEAMR [79] is one of a new generation in telescopic design, comprising a complex optical system of 8 mirrors through which 14 incident beams are transmitted to corresponding detector horns on the focal plane unit (FPU). These detectors provide very low sidelobe levels and high gain over a 40 GHz bandwidth ranging from 320 GHz to 360 GHz.

This work is predominantly concerned with the characterisation of an 'ultra-Gaussian' feed horn, built to provide the required beam truncation and low sidelobe levels throughout the STEAMR optics. A number of software packages are used to perform modeling, one of which is SCATTER, software developed by the experimental physics department in NUI Maynooth [59] to calculate the aperture field of corrugated horn antennae using the mode-matching technique described in section 2.3.3. The aperture field is then

propagated to the near and far-field of the telescope by a Gaussian Beam Mode (GBM) approach, allowing the evolution of the horn beam to be completely characterised.

Microwave Wizard(μWW), a specialised software package developed by MICIAN [80], is also used for the purposes of horn analysis. It also implements the mode-matching technique to model horns, however it differs from SCATTER in that it also implements the finite-element method (FEM) to characterise the fields produced by a horn or by other components which are difficult to otherwise model. In common with GRASP9, it uses a Spherical Wave Expansion (SWE) method when calculating the near and far-field beam patterns of the horn. It is computationally slower than SCATTER but provides a good secondary method of verifying results.

GRASP9, developed by TICRA[49], was also used for the modeling of an ideal ultra-Gaussian feed, as outlined in Chapter 2. The manufactured ultra-Gaussian horn which was delivered to the Institute of Applied Physics, Bern (IAP) for testing in October 2011.

6.1.1 The Instrument

Concern over global warming and related issues such as atmospheric pollution have risen considerably in recent years. The rapid evolution of climate is causing more regular occurrences of extreme conditions in many worldwide locations, while also leading to intolerable change in the habitats of many niche species.

Gathering detailed data from the planet's upper atmosphere with which to provide a scientific basis for dealing with the problem is one of many critical goals for the near future. Achieving this is quite difficult as the platforms required to take a scientific instrument to the required altitudes are rare and relatively expensive. With this in mind, the European Space Agency (ESA) is conducting the Earth Explorer missions, developed in direct response to challenges identified by the scientific community. Earth Explorer missions are split into two categories; 'Core' and 'Opportunity'. Through a process of selection both are implemented in separate cycles to ensure a steady flow of missions addressing key Earth-science questions. Core missions are the largest and address complex issues of scientific interest, while Opportunity missions are smaller and supported scientifically by the proposing team alone.

The 'Process Exploration through Measurement of Infrared and millimeter-wave' (PREMIER) mission is one of three candidate Earth Explorer Core missions set for launch in

2016. Recent testing has proven it to be highly-feasible. Initially using a high-altitude aircraft capable of carrying scientific instruments to suitable heights for conducting accurate observations, the ultimate goal of the project is to provide thorough insight into how Earth's climate and the chemistry of the atmosphere are intertwined.

STEAMR is a Swedish contribution to the PREMIER mission being provided to ESA. The instrument is specifically designed to provide accurate measurements of the global distributions of key target species such as ozone, water vapour and carbon monoxide in the Upper To Lower Troposphere (UTLS). To achieve good vertical and horizontal resolution, it will utilize a small linear array of receivers, which will image different altitudes simultaneously backward along the satellite track, thereby providing unique information about the 2-dimensional structure of the atmosphere in the orbital plane. The mission has its provenance from the earlier IR emission sounders MIPAS Envisat, launched in 2002, HiRDLS and TES Aura[81] launched in 2004, and millimetre wave limb emission sounders MLS Aura[81] and SMR Odin[82], launched in 2001.

The instrument is designed as a multi-beam limb-sounding radiometer, which will monitor the atmosphere by means of 14 beams between mid-latitude altitudes of 6-28 km. These 14 beams comprise two sets of seven beams polarised orthogonally at $\pm 45\,^{\circ}$. The antenna far-field beams have elliptical amplitude profiles with major axes in the azimuthal plane to maximise vertical sampling. To ensure minimal overlap in the beams they are also azimuthally displaced by 10 km with respect to their nearest counterpart, as shown in figure 6.1.

The receiver system, shown in figure 6.2 consists of a heterodyne array of 14 receivers on planar broad-band (8 GHz) Schottky diode mixers, sub-harmonically pumped to operate over a 40 GHz spectral bandwidth from 320 GHz to 360 GHz[84]. The frequency emitted from both sidebands is down-converted to an intermediate frequency (IF) in the 9-21 GHz range, which is then filtered, amplified and spectrally resolved using auto-correlation spectrometers that provide a maximum instantaneous bandwidth of 8 GHz, with a baseline spectral resolution of 10 MHz. A general overview of the receiver chain is given by Sobis et al.[85].

Figure 6.3 shows a schematic diagram of the STEAMR optics. The M1 and M2 reflectors are concave hyperboloids, and make up the Ritchey-Chretien telescope. Mirror M3 is an astigmatic convex hyperboloid, and is followed by two astigmatic concave hyperboloids, M4 and M5, all of which are shown in the schematic in figure 6.3. All three serve to fold and shape the incident beam amplitude and phase in both azimuth and elevation. These 'fully astigmatic' mirrors are bi-conics designed especially for off-axis imaging, with the

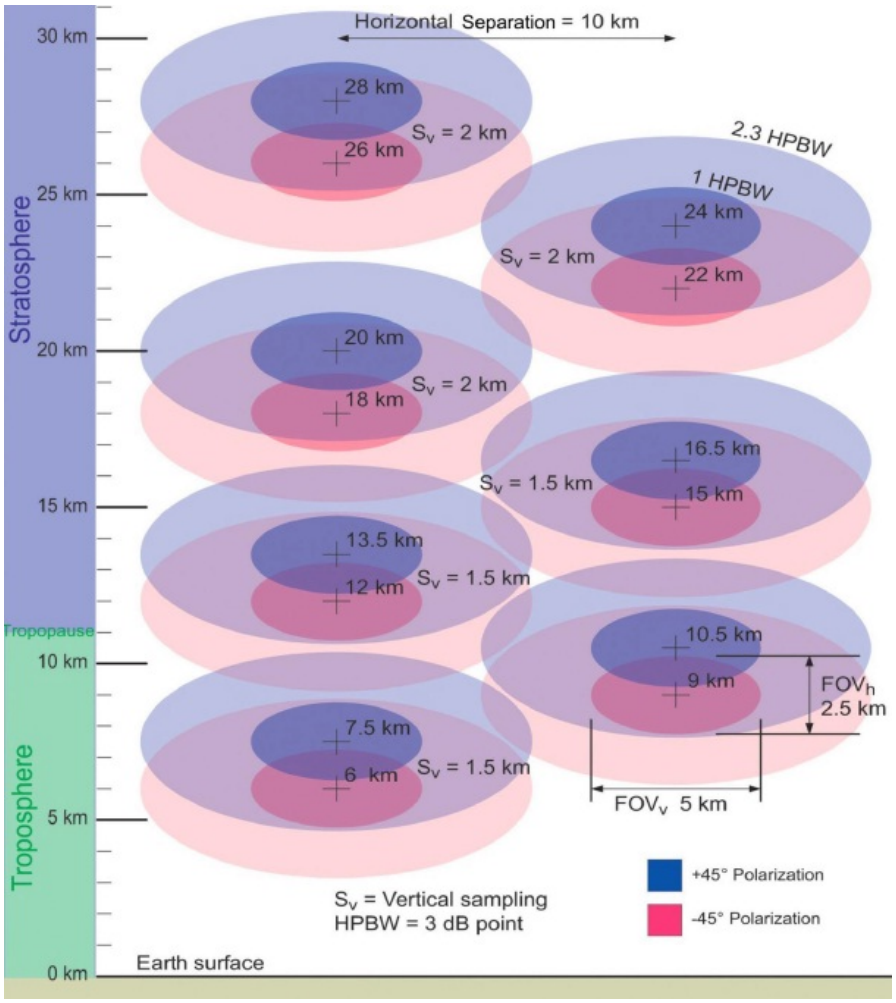

FIGURE 6.1: Illustration of the beam separation attained at the FPU, and relative spatial distance between beams on the sky. [83]

surface curvature in the azimuth and elevation planes being described by two different conic geometries[86]. The two focal points of each mirror occupy different locations, meaning that incident elliptical beams create elliptical beams with different properties on reflection. However, by careful design and tweaking of the focal lengths of both mirror axes, a plane can be found at which both azimuth and elevation Gaussian beam $\frac{1}{e}$ amplitudes and guoy phase shift are simultaneously matched.

The final astigmatic mirror M6 refolds the beam to the focal plane, which is essentially an image of the far-field with a 1.5π phase shift from M1. After careful design it was ensured that the beams return to maximum separation of 18.2 dB on the focal plane, in keeping with the antenna far-field overlap levels shown in figure 6.1.

This is then the location at which a focal-plane unit has been designed to re-separate the incoming beams into their two sets of seven, with orthogonal polarisations, by means of a wire-grid polariser. Each beam is then imaged to its appropriate feed via one of two

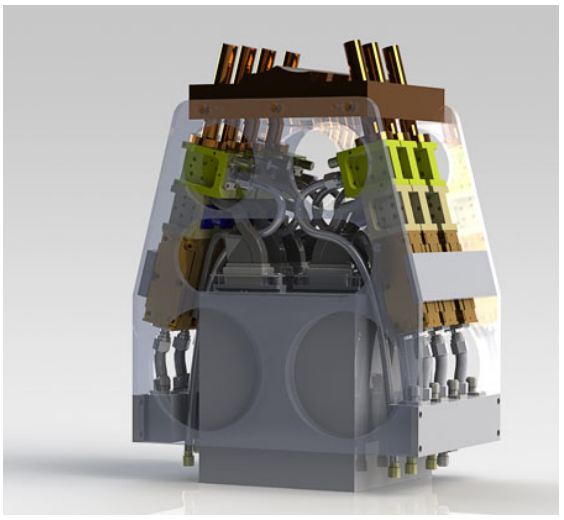

FIGURE 6.2: Cutaway model of the heterodyne detection system to be used on board STEAMR. [83]

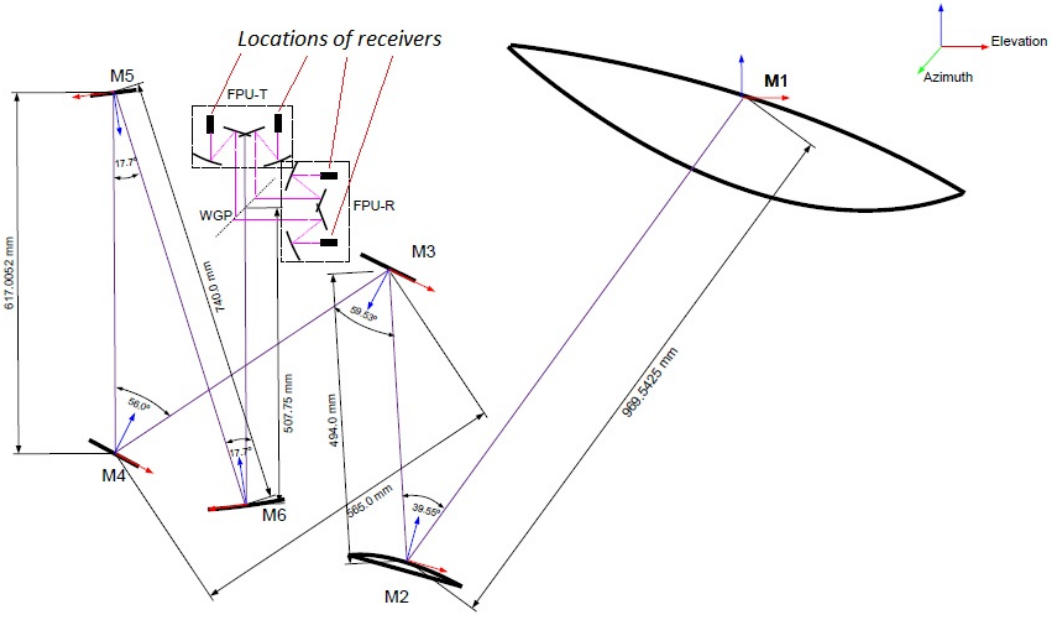

FIGURE 6.3: Optical layout of the current model for the STEAMR receiver optics. [83]

facet reflector arrays, on which mirrors M7 and M8 are located[87]. M7 is an off-axis concave paraboloid while M8 is an off-axis concave hyperboloid, serving to image each beam to its individual feed horn.

The horns in question are of the conical corrugated variety, and are 'ultra-Gaussian' in design [88], with the aim of providing low sidelobe levels and high directivity of the main beam in keeping with optical system requirements. They were manufactured by Thomas Keating Ltd and delivered to IAP Bern in September, 2011.

The entire reflector system is shown in figure 6.3, including the complete Focal Plane Array optics, with wire grid polariser splitting the polarisations between 'FPA-Transmission' and 'FPA-Reflection'.

6.2 Corrugated Feed Horns

Corrugated horns were first developed in the 1960s, in response to increasing demand for feeds with better directivity and gain, high co-polar pattern symmetry, and low cross-polarisation. The main driver behind their development was the communications industry, however further applications were found in radar technology and reflector antenna design. Although they were originally quite mechanically inefficient and difficult to manufacture, their electrical superiority outweighed these disadvantages, making them the generally accepted superior horn design by the 1980s. The development then of the modal-matching technique (see section 2.3.3) around this time consolidated their superiority, as it provided a good method of performance prediction based on computational analysis.

A typical corrugated horn consists of a smooth-walled rectangular waveguide supporting the single fundamental TE_{10} mode, which feeds the corrugated waveguide section, flaring to create a conical structure to the aperture (see figure 6.4). The transition from waveguide feed to the corrugated flare is known as the throat region and this controls the input impedance of the horn. The angle of divergence used in the flare section will have a large bearing on the co-polar beam pattern, while the corrugation geometry throughout the flare defines the cross-polar pattern. Finally, the aperture radius r, will define the co-polar beamwidth based on combinations of the previous factors, and in the case of reflector antenna systems relevant to this work, the beamwidth is generally required to be narrow.

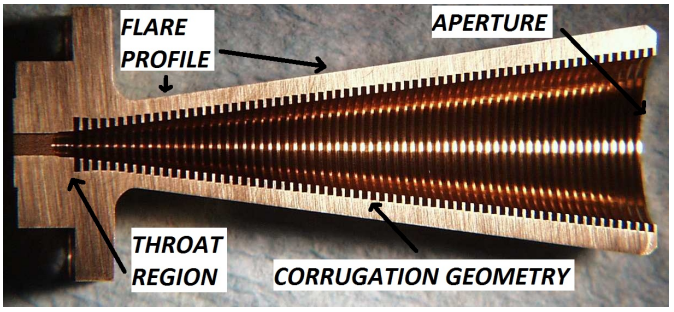

FIGURE 6.4: Cross-section of a standard conical corrugated horn [ZAX mm-wave corporation website].

6.2.1 Hybrid-Mode Feeds

The operation of hybrid-mode feeds is best explained by considering how corrugations affect the field propagating through the horn, creating desirable properties of low sidelobe level and a high degree of axial symmetry, while also minimising cross-polarisation levels [53]. This requires the electric and magnetic field boundary conditions to appear the same, which cannot be achieved using a waveguide supporting pure TE and TM modes. Instead, a 'hybrid-mode' waveguide is required, in which the electric and magnetic fields are exactly balanced to give pattern symmetry and low cross-polarisation. The two types of hybrid-mode are HE_{nm} and EH_{nm}, where a HE mode is the sum of $TE+TM$ modes, and an EH mode is the difference between them, $TE-TM$. The dominant HE_{11} mode created in a conical horn is thus a linear combination of both TE_{11} and TM_{11} modes, and produces the aperture electric fields:

$$\begin{aligned} E_x &= A_1 J_0(Kr) - \frac{(X-Y)}{kr} A_2 J_2(Kr) cos2\phi \\ E_y &= \frac{(X-Y)}{kr} A_2 J_2(Kr) sin2\phi \end{aligned} \tag{6.1}$$

where K and k are the transverse and free-space wavenumbers, $J_0(kr)$ and $J_2(kr)$ are Bessel functions of the first kind, A_1 and A_2 are amplitude coefficients and X and Y are the impedance and admittance at the aperture boundary ($r = r_1$), where:

$$\begin{aligned} X &= -j \frac{E_\phi}{H_z} (\frac{\varepsilon_0}{\mu})^{1/2} \\ Y &= +j \frac{H_\phi}{E_z} (\frac{\varepsilon_0}{\mu})^{1/2}. \end{aligned} \tag{6.2}$$

The values ε_0 and μ are the permittivity and permeability of free-space, respectively. We see that if the $(X-Y)$ term vanishes our aperture field $E_y = 0$ and no cross-polar component of the aperture field exists. Since the radiated field is a Fourier transform of the aperture field this property is carried forward. This however, can only occur when both X and Y are finite and equal, or both are zero. The latter is generated by the corrugated walls setting up the 'balanced hybrid mode' condition [64], which is satisfied once the two requirements are met.

Firstly, enough corrugations per wavelength must be created such that the azimuthal electric field will be zero at the corrugation edges, $E_\phi = 0$, thus $X = 0$. Secondly, by setting the corrugation peak to trough depth at $\approx \frac{1}{4}\lambda$ we ensure no currents are set up along the walls of the horn, since currents on the immediate inner wall would be 180 ° out of phase with those of the opposite side. Thus $H_\phi = 0$, and $Y = 0$. This however,

is idealised for a specific wavelength, outside of which the admittance, $Y \neq 0$, leads to a non-negligible cross-polarisation component away from a specific frequency.

6.2.2 Cylindrical-Wave Analysis

Cylindrical waves can be used to model the field characteristics of all types of shaped horns either metal or dielectric, be they homogeneous or inhomogeneous. Although we assume an inhomogeneous corrugated horn, the same principles apply to all cases, such that the field in a generic waveguide can be written as:

$$\begin{aligned} E &= E_t(u_1, u_2)e^{-\gamma z} + E_z(u_1, u_2)e^{-\gamma z} \\ H &= H_t(u_1, u_2)e^{-\gamma z} + H_z(u_1, u_2)e^{-\gamma z}, \end{aligned} \tag{6.3}$$

, E_t and H_t are the transverse components of the field, while E_z and H_z are the axial components satisfying the 2D EM-wave equations:

$$\begin{aligned} \nabla_t^2 E_z + K^2 E_z &= 0 \\ \nabla_t^2 H_z + K^2 H_z &= 0. \end{aligned} \tag{6.4}$$

. In a homogenous waveguide one of the axial components will equal zero, however for an inhomogeneous waveguide both components exist, so that both of the equations in (6.4) apply. The wavenumber is given by $K^2 = \omega^2 \varepsilon_0 \mu + \gamma^2$ and the transverse Laplacian operator in circular coordinates:

$$\nabla_t^2 = \frac{1}{r}\frac{\partial}{\partial r}\left(r\frac{\partial}{\partial r}\right) + \frac{1}{r^2}\frac{\partial^2}{\partial \phi^2} \tag{6.5}$$

, has solutions which are products of Bessel functions and trigonometric functions. This results in two separate equations defining TE and TM modes. For TM_{nm} modes the axial electric field is fully described by:

$$\begin{aligned} E_z(r, \phi) &= A_n J_n(Kr)\, e^{jn\phi} \\ J_n(Ka) &= 0 \end{aligned} \tag{6.6}$$

such that in a waveguide of radius a, the wavenumber is given by the roots of the Bessel function of order n. Similarly TE_{nm} modes are described by the axial magnetic field as:

$$\begin{aligned} H_z(r, \phi) &= B_n J_n(Kr)\, e^{jn\phi} \\ J_n'(Ka) &= 0. \end{aligned} \tag{6.7}$$

In this case the roots of the derivative of the order n Bessel function define the wavenumber. Neglecting any asymmetry in the horn itself, all modes will have an azimuthal value of 1, and junctions will excite only TE_{1m} and TM_{1m} modes.

6.2.3 Ultra-Gaussian Corrugated Feed Horns

Conical corrugated feed horns of a regular design couple 98 % of total radiated power to a fundamental Gaussian at the aperture, however in modern complex Quasi-optical systems it is common for multiple feeds to be coupled together. This can lead to higher order modes having unwanted effects on the beam pattern, which as a result makes the GBM approach to horn analysis less appealing. However, a relatively recent innovation, the so-called 'ultra-Gaussian' [89] feed, increases coupling to a fundamental Gaussian at the aperture of the horn from 98 % to 99.88 % [90], allowing a return to the straightforward (single mode) GBM analysis methods for field computation (see figure 6.5).

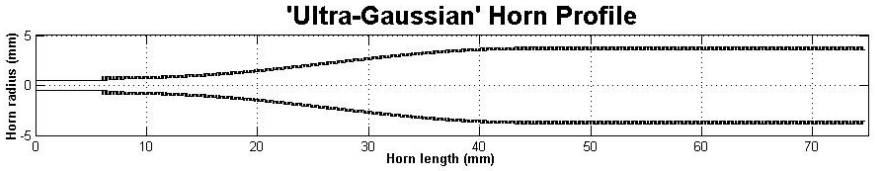

FIGURE 6.5: Geometry of an 'ultra-Gaussian' conical corrugated horn. The throat and flare section feeds a long phasing section in which the hybrid mode content is optimised

An ultra-Gaussian horn varies from the standard conical corrugated horn in that rather than transmitting all of its power in the fundamental HE_{11} mode, a HE_{12} component is deliberately added to the total field by careful design of the throat section of the horn, where the field is initially formed. As both modes are initially out of phase and evolve at different speeds, the introduction of a so-called 'phasing section' after the initial flare allows both modes to be brought into phase at the aperture. This results in a significant increase in efficiency and coupling to a Gaussian beam. The typical trade-off comes in beam width which is closer to $w = 0.5a$ than the traditional $w = 0.6435a$ associated with a scalar horn at the aperture, resulting in a larger main beam. With the extended phasing section they are also larger than traditional conical horns, which may cause minor difficulties in packing in the modern detector arrays generally required for reflector systems. The field produced by the ultra-Gaussian is ideally symmetric in orthogonal E & H planes, with low sidelobes and high on-axis gain.

Theoretical modeling of the ultra-Gaussian horn designed for STEAMR by Thomas Keating Limiting [89] was performed using 40 modes (20 TE and 20 TM) in SCATTER,

which makes use of the mode-matching technique (as described in section 2.3.3) to calculate the modal composition of the field at every section along the length of the horn. Modelled far-field patterns at three frequencies (323 GHz, 340 GHz and 357 GHz) covering the band are shown in figure 6.6, where cuts are taken through the E-plane and H-plane (0 ° and 90 °, respectively) as well as through the cross-polar plane (45 °), where peak intensity is normalised to 0 dB.

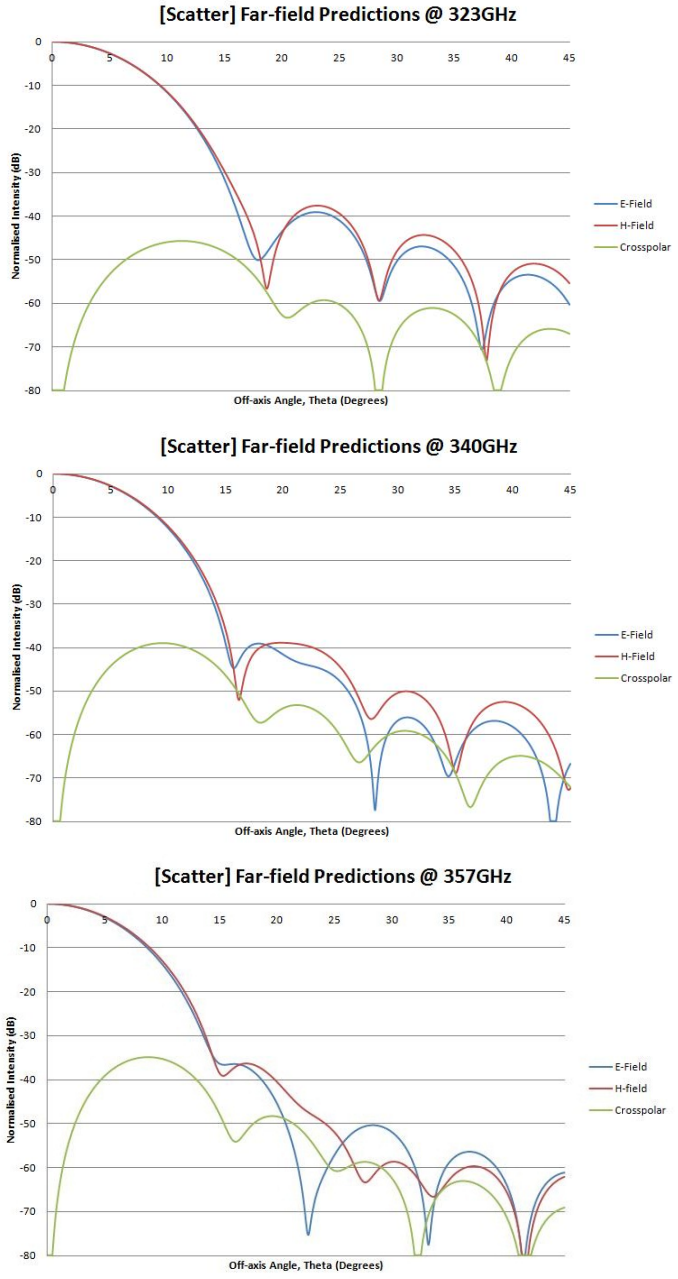

FIGURE 6.6: Far-field predictions of the ultra-Gaussian E and H-plane beam pattern, as well as cross-polar power, at each of three frequencies (323 GHz, 340 GHz and 357 GHz) across the band. These were performed using SCATTER mode-matching software with 20 TE and 20 TM modes at the input.

The main beam symmetry in figure 6.6 is readily apparent and extends down to small levels, in the region of the first sidelobe levels at -40 dB. Towards the higher end of the band a shoulder replaces the first null at slightly higher intensities of -37 dB. The performance of the horn, however, is quite acceptable, with good symmetry between orthogonal planes.

The horn in question was also modelled in the software package Microwave Wizard [80] (developed by, and hereafter referred to as Mician) for comparison against the SCATTER generated fields using the same number of modes (40). As with SCATTER, Mician uses the mode-matching technique for horn modelling. For propagation of the aperture field into free space Mician uses a spherical wave expansion (SWE) method of analysis, where SCATTER uses the GBM approach. Comparisons between calculated fields, therefore, proves a valuable test of modelling accuracies.

To simulate the response of a complex passive waveguide structure such as a corrugated horn in Mician, it first has to be broken down into its basic building blocks (waveguides and discontinuities), which form part of the Mician waveguide component libraries. The program then uses the method described in Section 2.3.3 to calculate the scattering parameters for each block. The impact of higher-order mode interactions is thereby strictly taken into account, and the basic building block concept eliminates the need for creating a full 3D model of the structure. While complex features such as the rectangular-to-circular junction at the waveguide input end of the horn can also be accurately modelled by the 3D finite element method (FEM) solver. Mician gains an advantage over many other commercial software packages through its freedom from reliance upon this time-consuming method, instead providing a more efficient implementation of mode-matching theory where possible.

Figure 6.7 shows the fundamental building blocks required to model the ultra-Gaussian horn in Mician, with 'Port 1' providing mode content at a specific frequency, or across a band. This is then connected to a rectangular-to-circular waveguide transition by means of an 'Empty' waveguide section of zero length and appropriate width, after which propagation into the corrugated section of the horn is undertaken. A 'sub-circuit' of steps and discontinuities describes both the tapered section and phasing section of the horn (which can be viewed in separate panes), and again each is connected by means of an empty waveguide section. The 'Radiation' element after the final step allows a near or far-field pattern to be calculated by means of SWE. This in turn enables optimisation of the horn to be undertaken by specifying required field conditions, and allowing Mician to alter the geometry of the horn to meet these requirements.

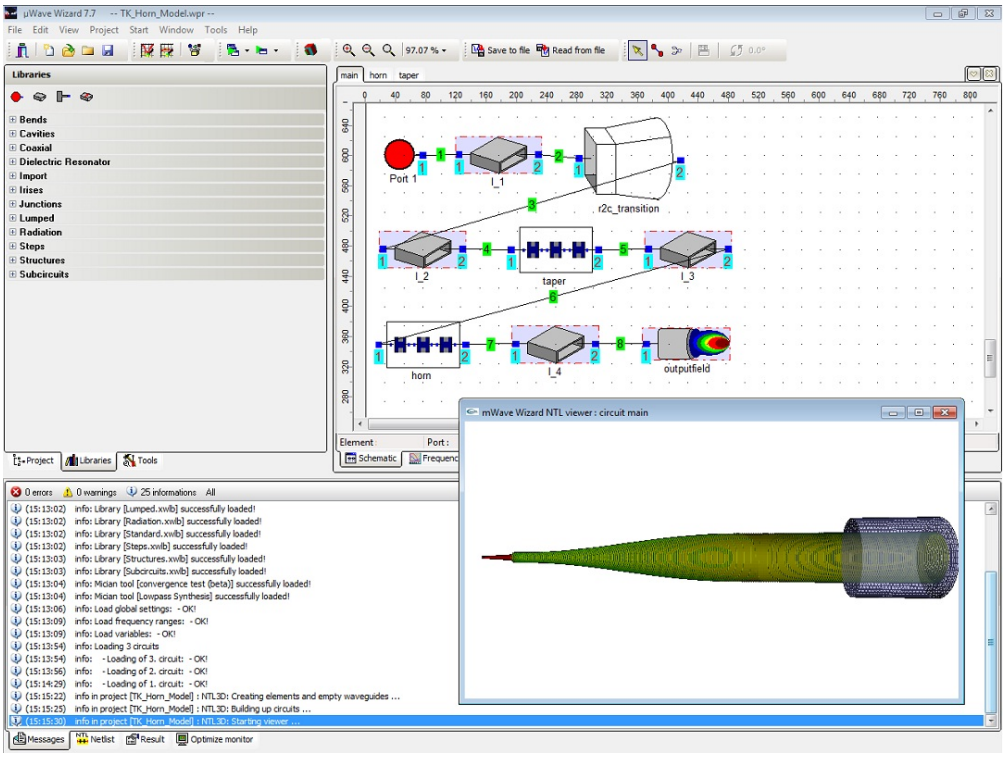

FIGURE 6.7: Illustration of the Mician program interface with libraries listed on the left, and project elements displayed with connections in the display-pane to the right. An image of the complete object being modelled can be generated from the GUI, and is shown bottom-right.

Figure 6.8, and figures A.1 and A.2 in the appendix, display comparisons between the SCATTER and Mician modelled E, H and cross-polar far-field patterns of the ultra-Gaussian horn, and at three frequencies spanning the band of the system. Cuts were taken out to 45 ° off-axis and the intensity normalised to 0 dB at peak.

It is immediately clear that agreement between the SCATTER and Mician models is very high at the lower end of the band. Although some divergence in the main beam size is visible in E-plane cuts, the sidelobe levels are very well matched in both models down to extremely low levels of power in off-axis regions. Cross-polar levels vary by approximately 10 dB between the models, but at low-level power this is quite acceptable, especially given the good overall comparison in main beam and sidelobe pattern between the models.

Toward the upper end of the band, agreement between the models dropped quite significantly, especially regarding sidelobe shape. This arises from inaccuracies in the Mician model rather than that of SCATTER. In Mician one must choose a cut-off frequency for modal calculations of optimally ten times the operating frequency. This leads to exceedingly large computation times so instead was set to three times the operating frequency

(1 THz), which causes miscalculation of beam properties towards higher frequencies.

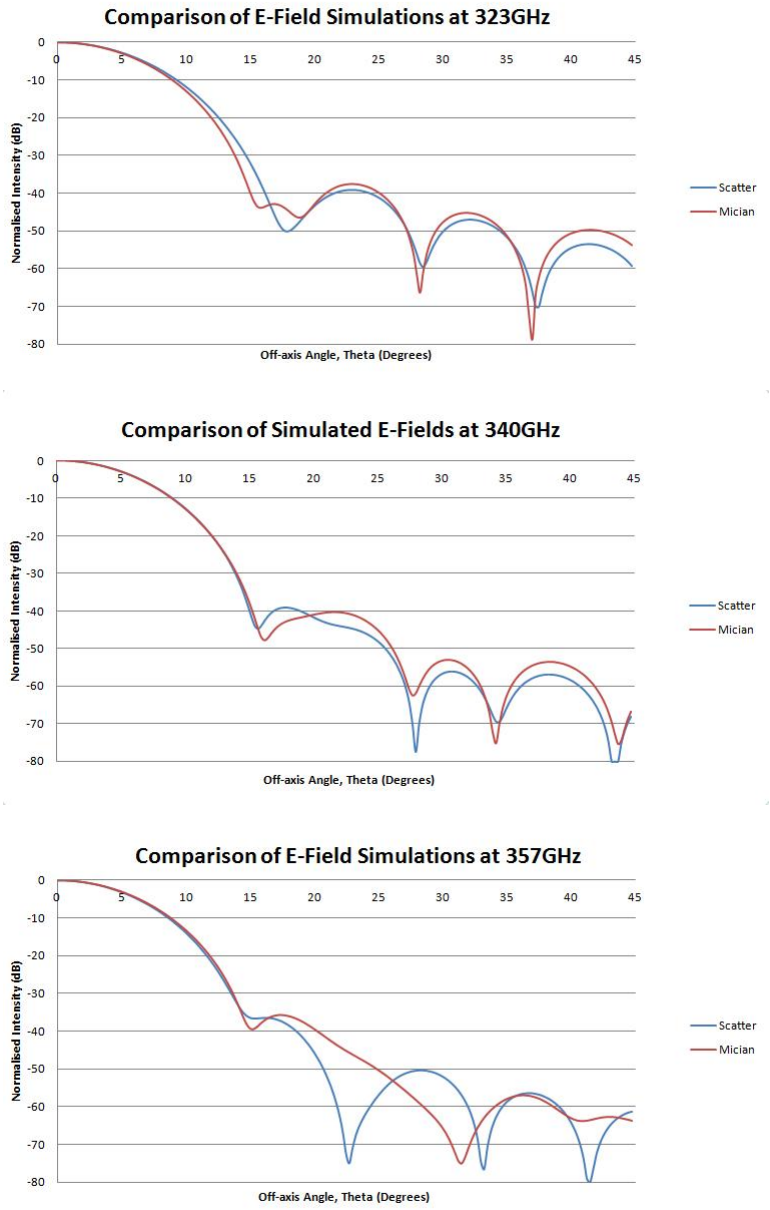

FIGURE 6.8: Comparisons between SCATTER (blue) and Mician (red) modelled E-plane far-field beam patterns across the band at 323 GHz, 340 GHz and 357 GHz.

Overall agreement between the models is quite high, especially considering SCATTER doesn't facilitate the inclusion of a rectangular-to-circular waveguide transition, or the final step into free-space. The agreement thus shows that it is ok to use SCATTER for these purposes, and provides a solid basis on which to further investigate the properties of the ultra-Gaussian horn.

6.3 Investigation of the Performance of a Modified Ultra-Gaussian Horn

As mentioned previously, the ultra-Gaussian horn modelled in this chapter was developed for STEAMR in response to demands for high gain feeds with very low sidelobe levels and cross-polarisation. These restraints were imposed by the proximity of the 14 incoming beams on the antenna FPA, however creating beams which will not overlap above levels of -25 dB in the confined space available on the FPA is quite a challenge.

Theoretically the greatest performance is obtained from the ultra-Gaussian feed when both HE_{11} and HE_{12} modes are brought into phase at the aperture, providing the greatest coupling to a fundamental Gaussian. This necessity for phase matching will naturally determine the length of the horn, as an elongated phasing section is required to bring them into phase (see figure 6.5). This can make the horns quite large, and create difficulty when compactness is required on an already restrictive FPA. With this in mind, we investigate here the effects on the horn beam pattern and system spillover with removal of corrugations from the phasing section of the horn. This has the aim of reducing the horns length for more comfortable inclusion on the FPA, without too much degradation of the beam pattern.

6.3.1 Variation of Hybrid Mode Content in GRASP9

An investigation of the beam pattern evolution by mode content variation was first undertaken in GRASP9, where a Hybrid Mode Conical Horn object with appropriate frequency of operation, aperture radius, and hybrid mode content was defined based on data provided by the manufacturers. The hybrid mode content modelled by *Corrug* (in-house software developed and used privately by TK Ltd. for horn optimisation), and is highlighted in figure 6.9 which shows the contribution of each hybrid mode to the overall field (squaring and summing the amplitude coefficients of all modes present would give a value of unity).

When creating a hybrid mode horn there are design factors which contribute above all else to the mode content at the aperture. Namely, the throat section in which the amplitude of each mode is adjusted, and the elongated phasing section through which both modes are brought into phase. Thus by varying the amplitude coefficients of the most prominent modes and alternately varying the phase offset between them,

Mode	Amplitude Coefficient	Phase (degrees)
HE11	0.9822	36.29
HE12	0.1854	36.64
EH12	0.0174	-48.08
HE13	0.0215	-64.73
EH13	0.0017	-65.89
HE14	0.0054	53.94
EH14	0.001	86.41
HE15	0.0019	88.02
EH15	0.0009	101.86
HE16	0.0016	-176.02
EH16	0.0006	87.46

FIGURE 6.9: Table of hybrid modes and their relative amplitudes and phases at the aperture of the ideal ultra-Gaussian, modeled in GRASP9. Clearly the vast majority of the power propagates in the HE_{11} and HE_{12} modes.

investigation was performed into whether horn length could be reduced with very little trade-off in beam Gaussianity.

As designed, the HE_{11} and HE_{12} modes contain almost 100 % of the total power in this particular horn, and come into phase at the aperture. Thus, to test the effects on the horn beam pattern due to alteration in mode content, the phase between these two modes was varied linearly between 0 ° and 90 ° in 15 ° increments. Increasing the phase offset resulted in a decrease in coupling to a fundamental Gaussian at the aperture. This is shown clearly in figure 6.10, where although narrowing of the main beam becomes apparent towards higher offset, the sidelobe pattern degrades considerably over the interval, rising by almost 20 dB.

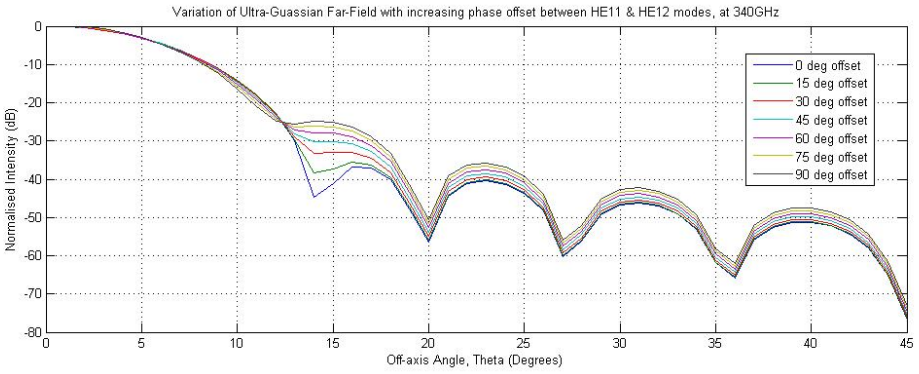

FIGURE 6.10: Variation of the beam far-field at band centre for 15 ° incremental phase offset between HE_{11} and HE_{12} modes from 0 ° to 90 °.

There is no distinct advantage to offsetting hybrid mode phase alone, as sidelobe power contributes significantly to the gain of the feed. If one were to alter the throat corrugations of the horn the amplitude coefficients of these modes could also theoretically be varied. To investigate the effect of coupling variation with HE_{12} amplitude, a number of far-field beam cuts were taken, varying the amplitude coefficient of the HE_{12} mode

between 0 and 0.25, and appropriately scaling the HE_{11} coefficient so that the sum remained equal to unity. This was performed at phase offsets of 0 °, 45 ° and 90 °, as shown in figure 6.11.

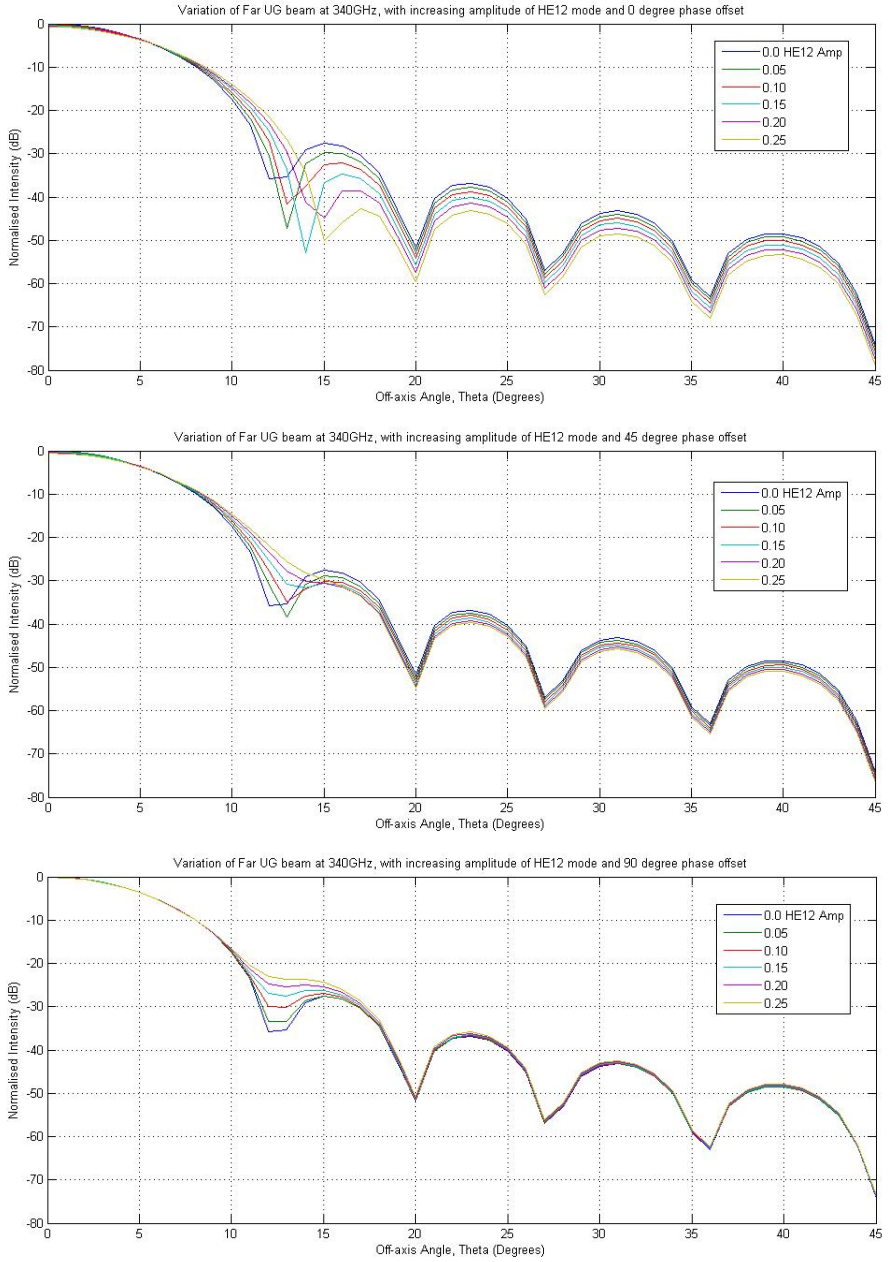

FIGURE 6.11: Variation of beam pattern at band centre with increasing amplitude contribution from the HE_{12} mode, at 0 ° (top), 45 ° (middle) and 90 ° (bottom) phase offset between HE_{11} and HE_{12} modes.

Looking solely at the model for 0 ° phase offset, the main beam narrows quite significantly by reduction in the HE_{12} contribution. The advantage of having the HE_{12} mode is in sidelobe reduction, which for a HE_{12} amplitude coefficient of 0.2 (the current horn, as designed, has a value of 0.1854) provides a 10 dB improvement over a beam which has no HE_{12} component.

When compared with increasing the phase offset, HE_{12} amplitude enhancement has much less effect. Any improvement to the beam arises from the slightly lower sidelobes produced by increasing contribution from the HE_{12}, however the main beam does become wider as a result, observable in the flattening of first null to form a shoulder. In general the first sidelobe remains 10 dB higher at 45 ° offset than without phase offset, and at 90 ° (the worst possible alignment of phase for beam quality) this increase in sidelobe power approaches 15 dB. In any case, widening of the main beam impacts upon the optimised 25 dB beam overlap on the FPA, thus cannot be accepted in return for lower sidelobes and greater Gaussianity.

6.3.2 Investigation of the Effect of Corrugation Removal

Removal of corrugations from the aperture of the horn should have a similar impact on the beam as offsetting the phase between the HE_{11} and HE_{12} modes. With this in mind a number of 'chopped' geometries were modelled (i.e. an optimised horn which has had corrugations removed from it's aperture), however it should be noted that in all cases the optimised horn is not re-optimised after corrugation removal. In each iteration four corrugations were removed from the total length of the horn, creating a large number of altered lengths varying between the present 573 corrugations and a much shorter horn length of 400 corrugations. Corrugations are only ever removed from the elongated phasing section of the horn, as tampering with the flare section would result in undesirable variation of modal contributions to the total field. The overall effect of corrugation removal on the far-field beam pattern of SCATTER generated aperture fields is illustrated in figure 6.12, where a number of altered horns with between 4 and 128 corrugations removed is shown. Models were run at either end of the band and band centre, however only the band centre profiles are shown here for illustration of the overall effect.

For removal of only a small number of corrugations the effect on the main beam is minimal. The only noticeable change occurs at the first null, which increases to form a shoulder before the first sidelobe disappears completely with upwards of 32 corrugations removed. Even though the main beam does become narrower for the largest number of corrugations removed, the potential improvement to beam overlap on the FPA is negated by the formation of a first sidelobe at -20 dB. This is not ideal for the low sidelobe levels required by STEAMR, as it also significantly decreases the Gaussianity of the beam. Based on similar results found at either end of the band it was found that shortening the horn will cause appreciable depredation of the beam, beyond that deemed acceptable. The simulations performed at band ends can be found in appendix

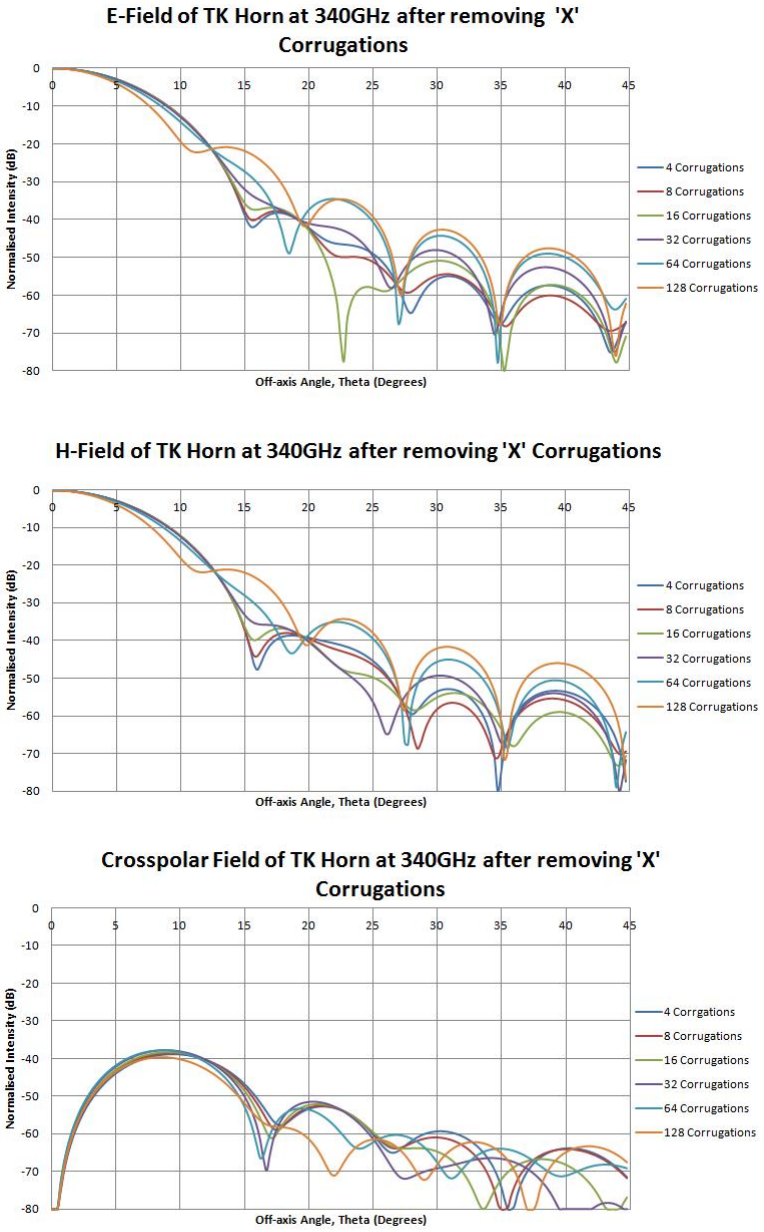

FIGURE 6.12: Overlapping far-field beam patterns for varying length of the aforementioned corrugated ultra-Gaussian horn ('TK Horn').

A; figures A.5 and A.6. (In general, graphs illustrating the main points are given in this main text, however if the reader is interested in further details regarding the simulations done across the band, those can be found in the appendix.)

One of the crucial aspects to which the optical design has been tailored is spillover on the system reflectors. As there are 14 beams travelling through the optics of the telescope striking different areas of each reflector, minimising the spillover loss is key. The FPA mirrors M7 and M8 are rather restricted in terms of area, however spillover levels of the order 10^{-2} dB have been achieved on M7, and even lower 10^{-3} dB levels on M8, using

the ultra-Gaussian horn in its unaltered state. To test whether this could be improved upon, the 'chopped' geometry fields modelled previously were propagated through the full FPA system also.

Regarding the model setup, a truncated version of the STEAMR optics, including only the two FPA mirrors M7 and M8 and a tabulated planar source at an appropriate distance from and orientation to the M8 reflector was modelled in GRASP9. The GRASP9 object 'tabulated source' requires a two-dimensional grid of field values in appropriate file format. In this case it would describe the aperture field of our ultra-Gaussian horn. Using the STEAMR optics as a test-bed for alterations to horn length, the field created at the aperture for each new length of horn could be propagated through the optical system, and the spillover on reflectors and beam patterns in the far-field could be investigated.

The horn being modelled consisted of 573 corrugations in its manufactured form, and each corrugated section will henceforth be referred to as either a 'tooth' or a 'trough' depending on whether the horns radius for that particular corrugated section is smaller (tooth) or larger (trough) than that of the preceding section. As manufactured the final corrugation of any corrugated horn will be a tooth. This allows the transition from corrugation to free-space to be modelled as a transition from tooth to infinite trough, meaning the scattering matrix formalism allows a forward transmitted 'S21' component of the field from the final corrugated section to be defined as the aperture field of the horn.

Bearing this in mind, only an even number of corrugations could be removed when altering the horn length, to ensure the aperture would always occur at a tooth rather than a trough. Multiple aperture fields could then be created using altered geometries of the horn in question, by feeding them into the mode-matching software SCATTER. As explained in section 6.2.1 corrugated horns will only excite modes of azimuthal order of unity ($n = 1$) under the assumption that no asymmetry is present in the horn. Propagating 30 modes ($m = 1$ to $m = 30$) at $n = 1$ for each of the TE and TM components of the field provides sufficient accuracy with which to model the aperture field of the horn. This works in a similar manner to PO convergence, whereby one keeps increasing the sampling (in this case the number of modes representing the field) until identical results are obtained over a wide range.

Expected spillover values, calculated using PO in GRASP9, are shown for an ideal ultra-Gaussian in figure 6.13, displaying a clear decrease in spillover towards the higher end of the band. This is the result of both hybrid modes coming closer in phase toward

	M8 Spillover(dB)	M7 Spillover (dB)
323GHz	0.0063dB	0.0279dB
340GHz	0.0034dB	0.0165dB
357GHz	0.0017dB	0.0113dB

FIGURE 6.13: Spillover values at three frequencies across the band, on both M8 and M7 facet sub-reflectors for the unaltered ultra-Gaussian horn.

the higher end of the band, which in turn provides better coupling to a well-behaved Gaussian at the aperture, and less spillover. At band centre the unaltered ultra-Gaussian yields a 0.0034 dB spillover on M8, which naturally increases to 0.0165 dB when the beam strikes M7. When corrugations are removed from the aperture of the horn an improvement to these levels was observed, as shown in figure 6.14. Spillover on M8 falls as low as 0.0016 dB with removal of between 25 and 30 corrugations. On M7 spillover drops much less, to a minimum of 0.016 dB, but for a much smaller number of corrugations removed. One immediate difficulty in potential optimisation of horn length, would be in choosing the number of corrugations to remove when no one number is optimal for both mirrors.

It should be noted from the diagram that as the number of corrugations removed increases further, the hybrid modes move further out of phase, until the modes are 90 ° out of phase with each other. At this point the main beam becomes less well-behaved with larger sidelobes and, therefore, much larger levels of spillover.

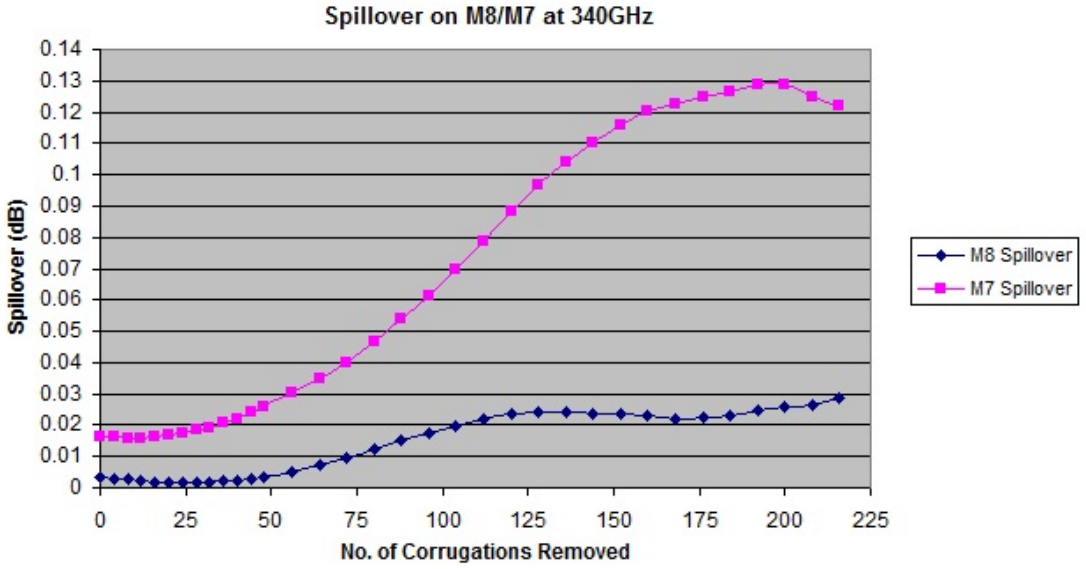

FIGURE 6.14: Spillover on both M8 and M7 sub-reflectors, with removal of corrugations from the aperture of the ultra-Gaussian horn

Widening the scope of the model to include both ends of the band causes a more complex

relationship to emerge. Modelling the spillover on M8 alone, and for removal of a maximum of 80 corrugations, the dependance of spillover on frequency is clearly visible (see figure 6.15). With removal of over 56 corrugations spillover increases across the band. With fewer corrugations removed spillover does indeed reduce to a minimum, but for a different number of corrugations removed at each frequency. Ideally we require a band-wide reduction of spillover to minima for a similar number of corrugations removed, which is unfortunately not the case. The hybrid mode phases evolve at different speeds depending on the frequency of operation, thus they come into phase with each other at different locations inside the horn. To improve the spillover by optimising for one frequency, would in turn degrade our beam in other regions of the band.

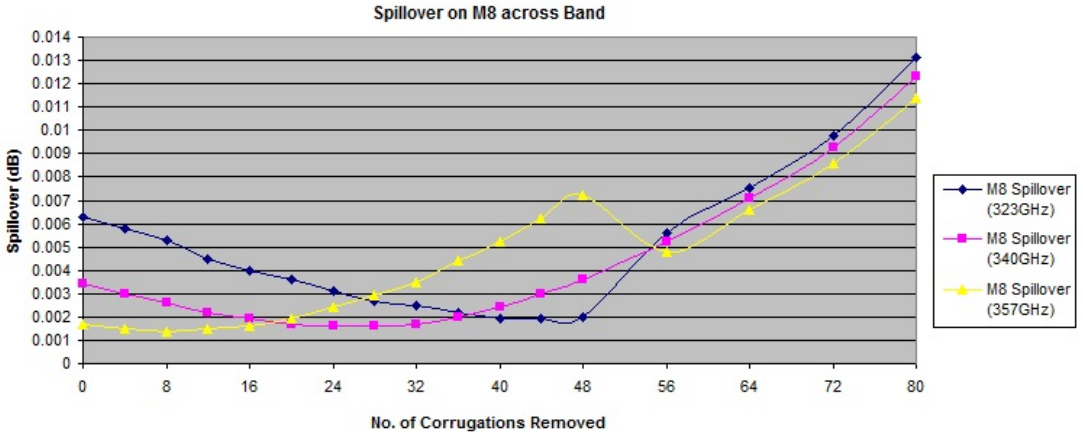

FIGURE 6.15: Spillover on the facet-reflector M8, for up to 80 corrugations removed at three frequencies across the band.

There is, however, a general improvement to be had regarding spillover on M8, as figure 6.16 clearly demonstrates.

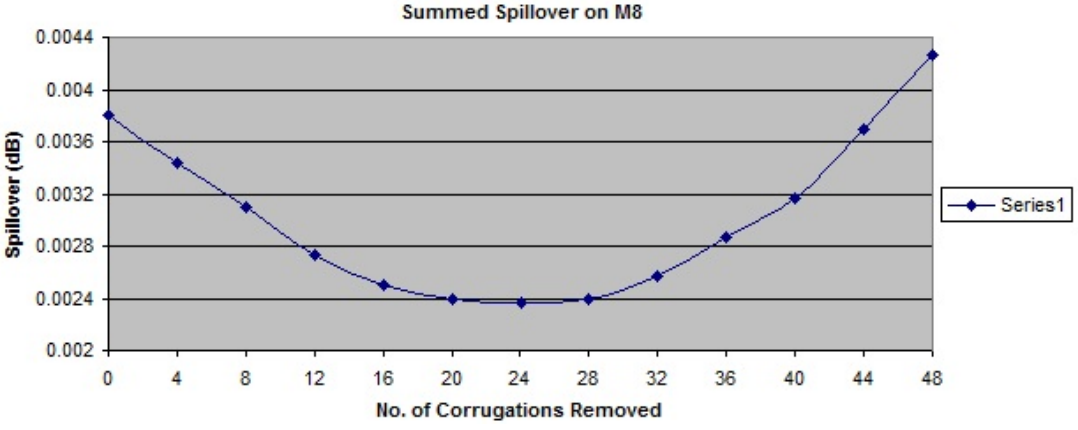

FIGURE 6.16: Summed spillover on M8 at three modelled frequencies, for up to 48 corrugations removed.

There appears to be much less improvement in spillover on M7 by removal of corrugations, as shown in figure 6.17. At this point spillover has increased by an order of

magnitude due to beam-spread, making slight improvements of the order 10^{-1} less obvious.

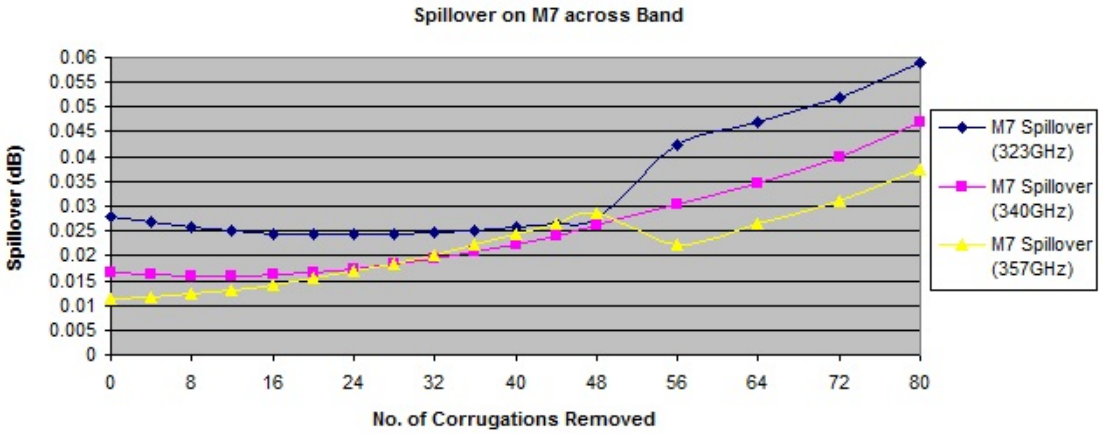

FIGURE 6.17: Spillover on the facet-reflector M7, for up to 80 corrugations removed at three frequencies across the band.

Summing total spillover across the modelled frequencies verifies this. Although very slight improvement is to be had by removing 4 to 8 corrugations (see figure 6.18), this is eclipsed by the improvement on M8 gained by removing a larger number of corrugations.

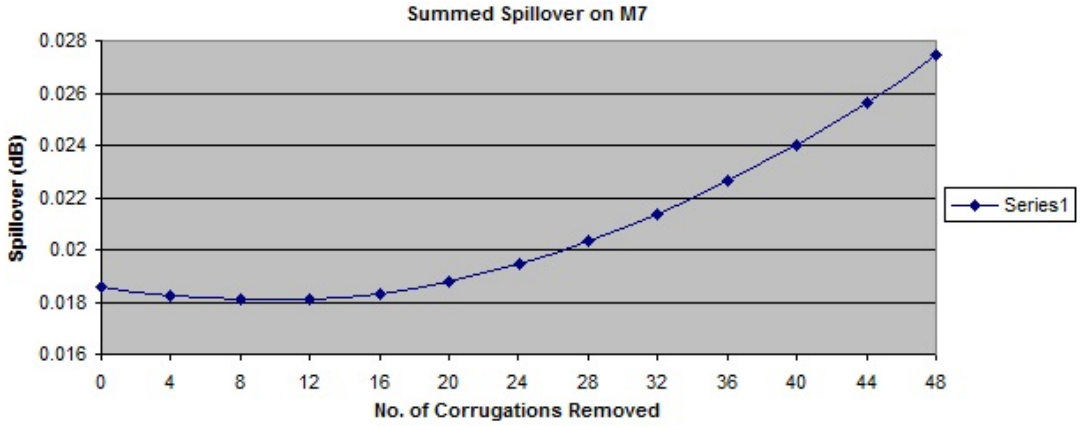

FIGURE 6.18: Summed spillover on M7 at all modelled frequencies, for up to 48 corrugations removed.

6.4 Conclusions

The corrugated horn investigated in this chapter was developed for STEAMR in response to a need for extremely low sidelobes and large gain, these attributes were met by the ultra-Gaussian design described herein. By the excitation of more than simply the fundamental mode in the throat section of the horn, increased coupling to a Gaussian is

obtained through the careful phase-matching all modes contributing a significant amount of total power to the beam.

When designing an ultra-Gaussian horn one must very thoroughly investigate the phase evolution of the hybrid modes being excited. Once this is understood the number of corrugations required to bring them into phase at the aperture can be determined. Since the mode phases will evolve at different speeds depending on the frequency, maximum coupling to a fundamental Gaussian can only be obtained over a small bandwidth. This is not ideal for a wide-band horn. Thus great care must be taken to ensure that phase-matching which provides ideal coupling at one frequency does not significantly degrade the beam at other frequencies in the operational band.

In this study it has been discovered that, although close to optimal, the performance of the horn can potentially be improved by removal of a number of corrugations from the aperture of the horn. In terms of beam spillover from the facet reflector M8, at least, there is the possibility of decreasing band-wide spillover by over 35 %. This does not translate to similar reduction on M7, however, which means that although noteworthy, the potential improvement does not merit a lengthy process of alteration to the horn design.

Chapter 7

Conclusions

This thesis is concerned with the modelling of quasi-optical telescope systems, where the methods used bridge the gap between the geometrical optics techniques of shorter wavelengths and the radio regimes at longer wavelengths. Particular emphasis was placed on the modelling of the HFI instrument onboard the CMB-measuring Planck telescope, with a view to simulating the far sidelobes (FSL) seen across multiple channels of the 857-GHz band. This, and all other telescope modelling was achieved using a variety of techniques, such as Gaussian beam modes (GBM) and physical Optics (PO), some of which required specialist software packages such as the General Reflector and Antenna Software Package (GRASP9) for rigorous implementation. Understanding the operation of multi-mode systems was one of the main goals of this thesis.

Chapter 1 began with a brief history of the Universe, outlining the origin of the Cosmic Microwave Background radiation, as well as its various properties, measurement of which is central to the Planck mission, and a cornerstone of this thesis. This was followed by a time-line of our knowledge of the CMB, from the first discovery of the 3 K signal by Penzias and Wilson in 1965, to the most recent developments of our understanding using state-of-the-art detection techniques, on projects such as WMAP, and most recently Planck. An overview of the Planck telescope followed, with a detailed description of the HFI instrument and the quasi-optical detection system implemented across all channels, as well the various goals of the mission and the early results. This led to a discussion of the HFI beams, and the unusual 'banana'-like features seen in some, but not all, of the difference maps made for each of the four 857-GHz channels. One possibility put forward, was that these features were caused by imperfections in the horn antennas used to couple radiation from sky to detector. At this short wavelength end of the spectrum the manufacturing tolerances for such horns are extremely low, and even small alterations

to the internal structure of the horns could severely impact their efficiency. It is this possibility which we set out to analyse in this thesis.

To model the potential effects of these manufacturing imperfections on the sky beam, a variety of analysis methods used in quasi-optical modelling were required, and in Chapter 2 the theory behind a number of these methods was outlined. We first described the GRASP9 software, which is widely used for the modelling of telescopes in the far-infrared, and provides a platform for all telescope modelling in this thesis. Various useful features of this package were outlined, followed by a detailed description of the analysis methods available in this package. PO and geometrical optics (GO) with the geometrical theory of diffraction (GTD) are predominantly used, and the mathematical theory behind each of these techniques was duly outlined. It was noted that due to the sampling requirements of PO, GO were GTD are preferred at the highest frequencies when modelling Planck far-sidelobe structure. Once the field at the aperture of a detector is known, or can be approximated using a Gaussian fit or otherwise, this package will accurately determine the field on the sky by propagation through free-space and off reflectors using the techniques outlined. Calculating the aperture field of a horn antenna, however, cannot be done using the same methodology, as the fields inside any waveguide structure require a different mathematical description to those in free-space. The modelling of fields inside a horn antenna is done using waveguide mode theory, which requires the field be broken down into a sum of modes, each of which will contain some portion of the total power fed to the horn from the detector cavity. By propagating each mode through the waveguide structure, accounting for all internal reflections and scattering of power from mode to mode, the field at the aperture of the horn can be calculated. A by-product of this determination of fields using either cylindrical or rectangular waveguide mode analysis, is the ability to accurately assess the impact of internal imperfections on the field at the aperture of the horn, which naturally proved useful for modelling the aforementioned imperfections suspected of the Planck 857-GHz horns. The final analysis method described in this chapter was the Gaussian beam mode (GBM) technique, which is used to propagate fields through free-space in a similar fashion to waveguide modes which prorogate fields through hollow structures. This is an extremely powerful technique, which can provide a useful alternative to often time-consuming PO and GTD techniques in description of telescope systems. We concluded the chapter by modelling and measuring of the beam pattern from a rectangular horn, and performed a useful comparison between the PO technique implemented in GRASP9 and the GBM technique constructed in Mathematica, with good agreement illustrated between both techniques, and with measurement also.

In Chapter 3 we moved on to the modelling of telescope systems using the techniques

outlined previously. This Chapter was dedicated specifically to the modelling of the Planck telescope in particular, with a view to characterising the FSL structure seen in the difference maps at 857-GHz. This involved taking account of the numerous reflections in the system from baffles and other payload structure which might intercept the light from the sky, and thus proved a complex task. We instead began by modelling a simple single reflector system using PO, outlining the precise field summations which must be performed to retrieve FSL information from behind a reflector. The field on the sky was then compared against a GTD model of the same system, highlighting the regions in which both differ, namely where caustics occur in GTD field calculation. Good agreement was however observed between both techniques in modelling of FSL structure. We then moved to the modelling of slightly more complex dual-reflector system, namely the Planck telescope but without inclusion of blockages such as baffles or other payload components. A more complicated field summation process was required here, which was thoroughly outlined, highlighting the difficulty in using PO for FSL modelling in even relatively simple systems. With this in mind we turned to modelling of the full Planck system, including all blockages, and highlighted the advantage of GO and GTD over PO in this case, due to the ease with which many possible reflections and diffractions can be taken into account using the former technique. Due to the complexity of the model, it was decided to rigorously test the method at lower frequency where the calculation time is much reduced. Thus, FSL simulations were first performed for the single-moded 101-GHz band, comparing PO with GTD, and following this at 353 GHz. Here we first highlighted a key issue with high-frequency optical modelling, namely the multi-moded nature of systems at these frequencies. Whereas at 101 GHz, one coherent field sufficed to describe the total field radiated from the horn, at 353 GHz, and especially at 857 GHz, the total field is composed of multiple partially-coherent fields, each of which must be propagated to the sky independently, and recombined there by quadrature summation to retrieve the correct field distribution. This significantly increases the computation time of the model, more-so at higher frequencies where not only does the system become more multi-moded (thus requiring more fields to model it), but the sampling required by PO and the number of rays traced by GTD increases dramatically also. The limitations of both techniques in this regard were duly outlined, illustrating the difficulty of modelling FSL structure for the 857-GHz band. Full-sky models of the 857-GHz band at 730 GHz (the lowest frequency of the band, containing the least modes, and thus proving the quickest to model) were completed using a rigorous GTD analysis, and predictions of the FSL levels made for three sample horns; one ideal, one with five corrugations filled in the front of the throat section of the horn ('bad'), and one with five corrugations filled in the back of the throat section of the horn ('worst'). These were chosen as the most appropriate cases to model based on altered horn geometry far-field beam patterns highlighting the effects on beam-width and sidelobes in each case. It was shown that

the FSL structure is expected to peak approximately 50 dB below the main beam, with slight variation from horn to horn.

Chapter 4 continued the Planck modelling, but developed two further techniques to provide quick estimates of the FSL levels. The first of these was the projected aperture technique, in which the Planck system was modelled as an equivalent paraxial lens system, and the aperture field of the horn Fresnel transformed from aperture to lens, from aperture to sky, and from lens to sky, thus providing information about both the main beam, and spillover beyond the lens. Once the correct gain of the telescope has been calculated, this is used to accurately determine the relative levels of main beam and sidelobe, which again were found to peak at roughly 50 dB below the main beam for the worst-case scenario of horn imperfection. A paraxial GBM model of the Planck system was also created, which proved quicker again than the projected aperture technique, using an elegant equivalence between waveguide mode theory and GBM theory, whereby the waveguide mode fields at the aperture of a horn can be summed according to a common Bessel function dependency, shared by a similar set of Gauss-Laguerre modes. As an example of it's implementation the 730-GHz FSL was modelled for the usual three cases, but were seen to rise no more than 70 dB from peak for even the worst case scenario. The disagreement between GTD and GBM techniques is not fully understood, however may be a result of the paraxial approximation, in which the projection effects of the secondary are not considered. There is undoubtedly scope for further development of this elegant technique, with potential for incorporation of projection effects, thus removing the paraxial limitation. This may resolve the inaccuracies of the current model, and provide a platform for quick and powerful modelling of telescope systems when PO and GTD prove too computationally intensive. The final section of this chapter was dedicated to modelling of surface deformations on the Planck reflectors at 857-GHz, which previously had been performed using a single-moded Gaussian fit to the 857-GHz beam. The regularly spaced surface deformations caused the reflector to act as a diffraction grating, leading to grating lobes appearing at regular intervals around the main beam. These were seen to occur at roughly 35 dB below peak for 10 μm deformations and 50 dB below peak for 2 μm deformations when modelling at 730 GHz. This increased to 30 dB below peak at 800 GHz, and it is assumed they would increase further as dimple size approaches the order of the incident wavelength. It was not feasible to model at precisely the 857 GHz, however a Gaussian fit to the aperture beam was performed at 800 GHz and compared with the multi-moded beam model, showing very little noticeable difference in grating lobe height, except that the multi-moded grating lobes were broader than those of the Gaussian.

In Chapter 5 the modelling of two further telescope systems was performed, the first

a telescope simulator used in Cardiff to measure the beam patterns of the Planck HFI flight horns pre-launch. Having made the assumption that the FSL 'bananas' were a result of horn imperfections, it was thought that these may have been seen in pre-launch testing. The aim of this work was to verify whether any beam features arising from horn imperfections could go unnoticed in test-bed measurements using the telescope simulator. The simulator was composed of two mirrors, which were petals of larger telescopes, and thus formed irregular shapes, the definition of which in GRASP9 was outlined. Although the asymmetric measured beam patterns were replicated by the model, it was concluded that any difference in the beam pattern arising from imperfections in the horn would very likely go un-noticed in measurement. It follows that the features seen in the difference maps of all but one of the HFI flight horns may be a result of minor imperfections in the horns, which could not be seen in pre-flight measurement. The second telescope system to be investigated was the FIRI test-bed, a spectral/spatial interferometer vastly different in design to the Gregorian Planck systems previously analysed. The test-bed comprised a system of flat mirrors representing the two arms of the interferometer. These arms were fed by two telescopes separated by a variable baseline of between 100 mm and 500 mm, and fed by a simulated point source at the focus of a large mirror in the far-field of both telescopes. To attempt to simulate reported power loss in the system, the power throughput along both arms of the telescope was modelled for a range of baselines and a range of frequencies, however no significant power loss could be seen in modelling of the system, and it was concluded that the test-bed may be misaligned. The power of the interferometric technique and the resolution of the telescope was highlighted by further analysis, simulating a point source by a 1 mm slit, and a broad source by a 100 mm slit at the focus of the large mirror, then measuring the fringe patterns observed for each. This model will be developed in the future to analyse the effect of various system parameters on the images and spectra obtained by a FIRI-like beam combiner.

The work in Chapter 6 related to the STEAMR mission, and particularly investigation of the properties of corrugated 'ultra-Gaussian' horns. This was performed with a view to reducing the length of the horns, potentially allowing for more convenient placement of the horn array on the already compact focal plane unit of the telescope. A brief overview of the mission was first reported, with the scientific goals and system design detailed. We then moved onto the scattering matrix theory used in software such as SCATTER for modelling of the fields in corrugated horns, and specifically multi-moded horns such as those seen in the Planck HFI. This formed the basis for investigation of the effects of corrugation removal from the aperture of the 'ultra-Gaussian' horns proposed for STEAMR. In designing an ultra-Gaussian horn the phase evolution of the hybrid modes through the structure must be accurately known, such that the number of corrugations

required to bring them into phase at the aperture could be determined. Bandwidth limits the efficiency of the horn, as the mode phases will evolve at different speeds depending on the frequency, meaning maximum coupling to a fundamental Gaussian can only be obtained over a small bandwidth. It is thus prudent to ensure that phase-matching which provides ideal coupling at one frequency does not significantly degrade the beam at other frequencies. Here we discovered that the performance of the horn can be slightly improved by removal of a number of corrugations from the aperture of the horn, however removal of a large number of corrugations will severely degrade the horn. In terms of beam spillover from the facet reflector M8, at least, there was the possibility of decreasing band-wide spillover by over 35%. This did not translate to similar reduction on M7, however, which means that although noteworthy, the potential improvement did not merit a lengthy process of alteration to the horn design. Although not directly related to the Planck project, my work on FIRI and STEAMR illustrates how the techniques studied in order to model the Planck telescope can be applied to other far-infrared telescope missions.

This thesis makes a significant contribution to the understanding of the behaviour and modelling of multi-moded far-infrared telescope systems and will be of use not only for the Planck data analysis, but also future missions designed to meet ever-more demanding sensitivity requirements.

Appendix A

Appendix A : STEAMR Supplementary Data

This section contains further results which were not contained in the main body of the text due to space restrictions. They are ordered as follows:

1. Figure A.1 : Comparisons between modelled SCATTER and Mician H-field across the band
2. Figure A.2 : Comparisons between modelled SCATTER and Mician cross-polar field across the band
3. Figure A.3 : Variation of ultra-Gaussian far-field beam at 323 GHz with increasing amplitude contribution from the HE_{12} mode, at 0°, 45° and 90° phase offset between HE_{11} and HE_{12} modes
4. Figure A.4 : Variation of ultra-Gaussian far-field beam at 323 GHz with increasing amplitude contribution from the HE_{12} mode, at 0°, 45° and 90° phase offset between HE_{11} and HE_{12} modes
5. Figure A.5 : Overlapping SCATTER far-field beam patterns at 323 GHz, for varying length of the corrugated ultra-Gaussian horn ('TK Horn') after corrugations were removed
6. Figure A.6 : Overlapping SCATTER far-field beam patterns at 357 GHz, for varying length of the corrugated ultra-Gaussian horn ('TK Horn') after corrugations were removed

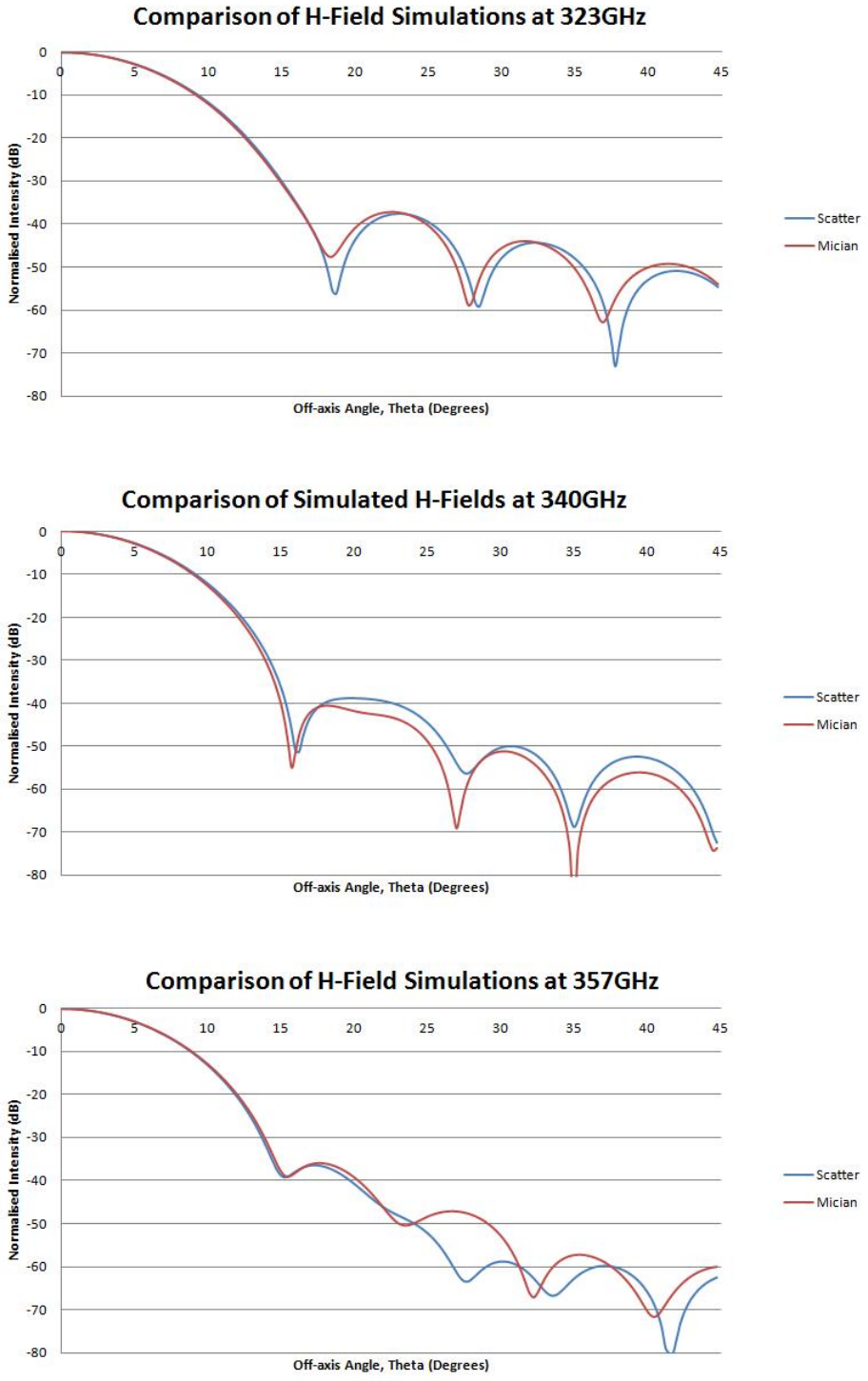

FIGURE A.1: Comparisons between SCATTER (blue) and Mician (red) modelled far-field beam patterns of the ultra-Gaussian horn at the lower end of the band (323GHz)

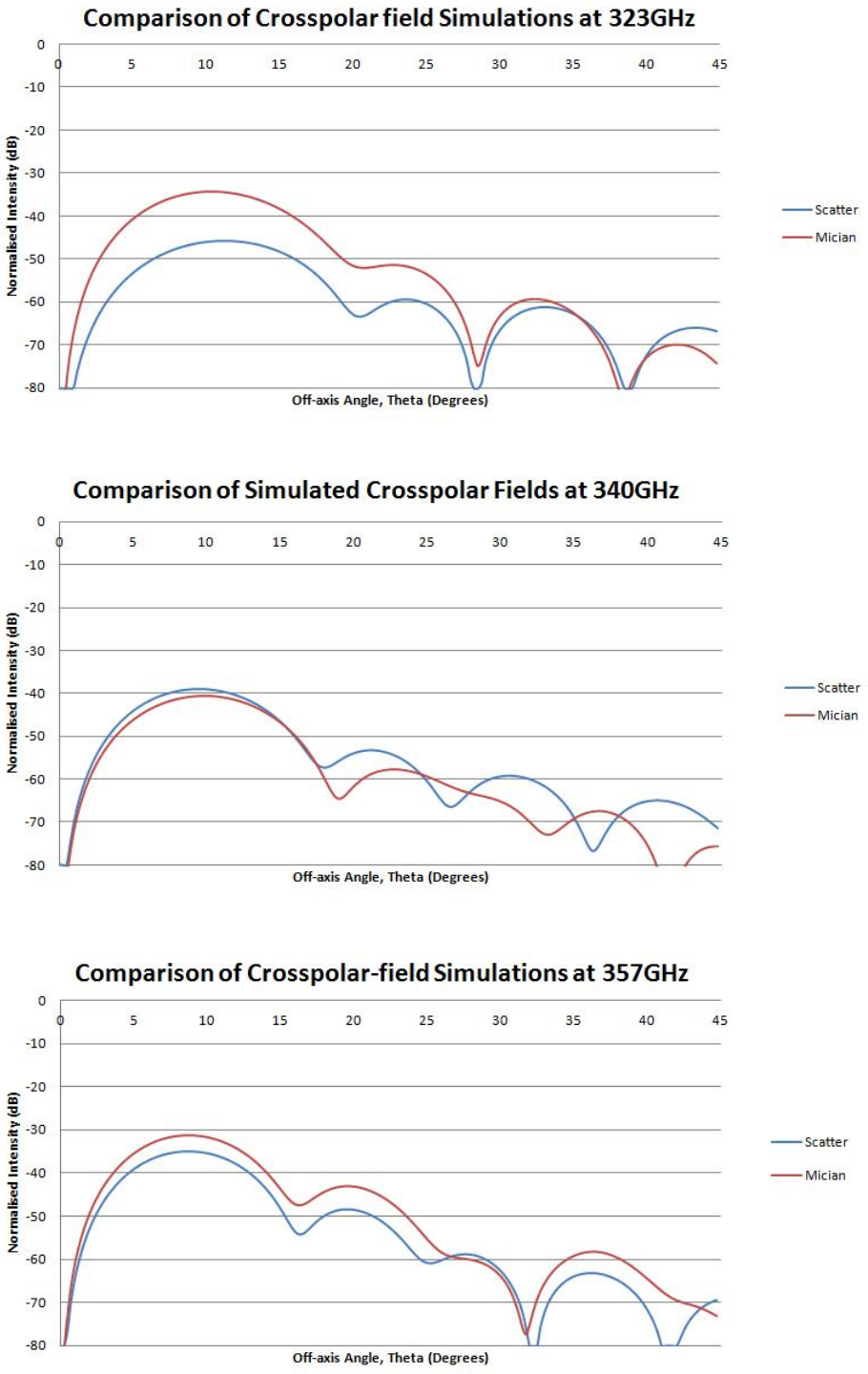

FIGURE A.2: Comparisons between SCATTER (blue) and Mician (red) modelled far-field beam patterns of the ultra-Gaussian horn at the upper end of the band (357GHz)

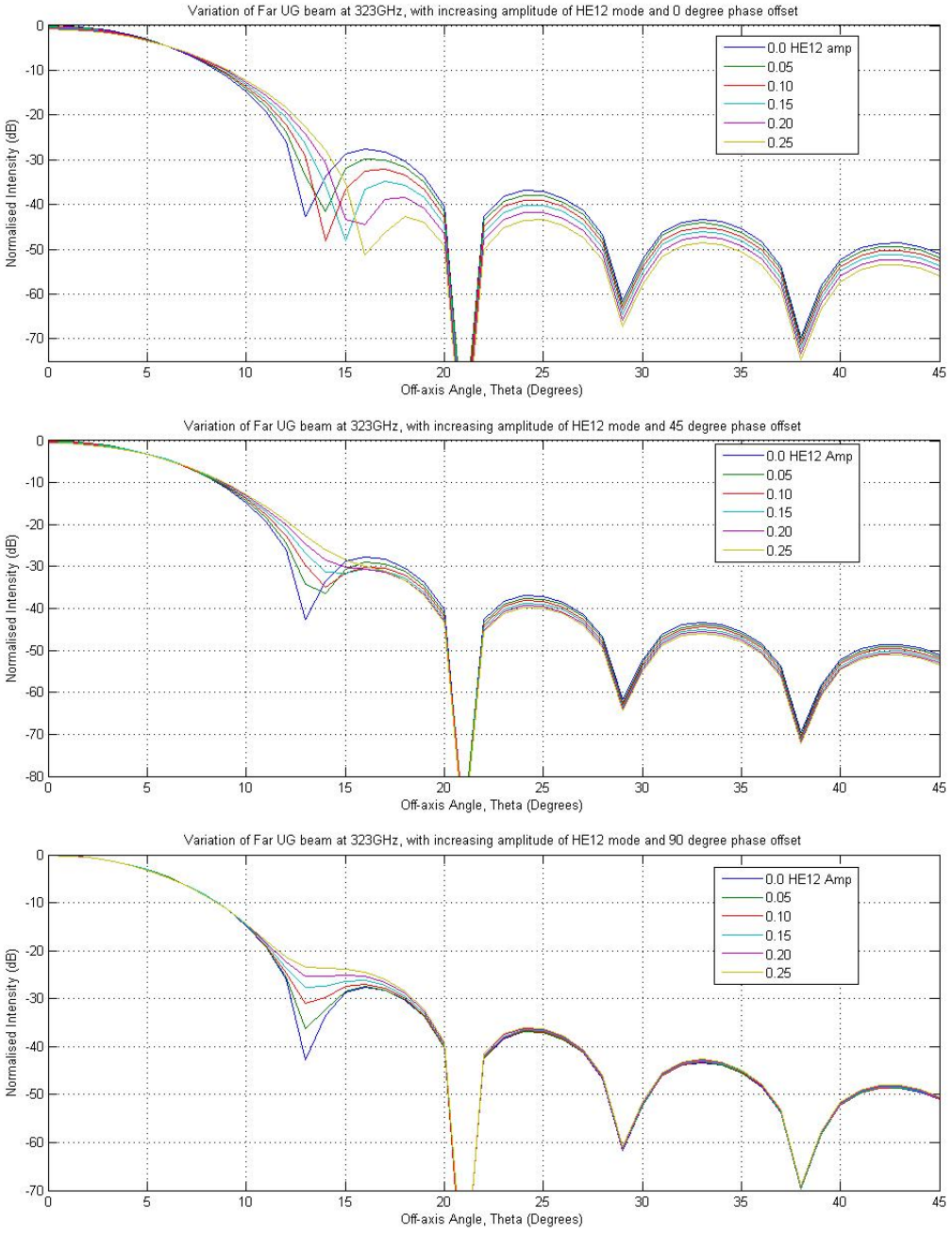

FIGURE A.3: Variation of beam pattern at 323GHz with increasing amplitude contribution from the HE_{12} mode, at 0°, 45° and 90° phase offset between HE_{11} and HE_{12} modes

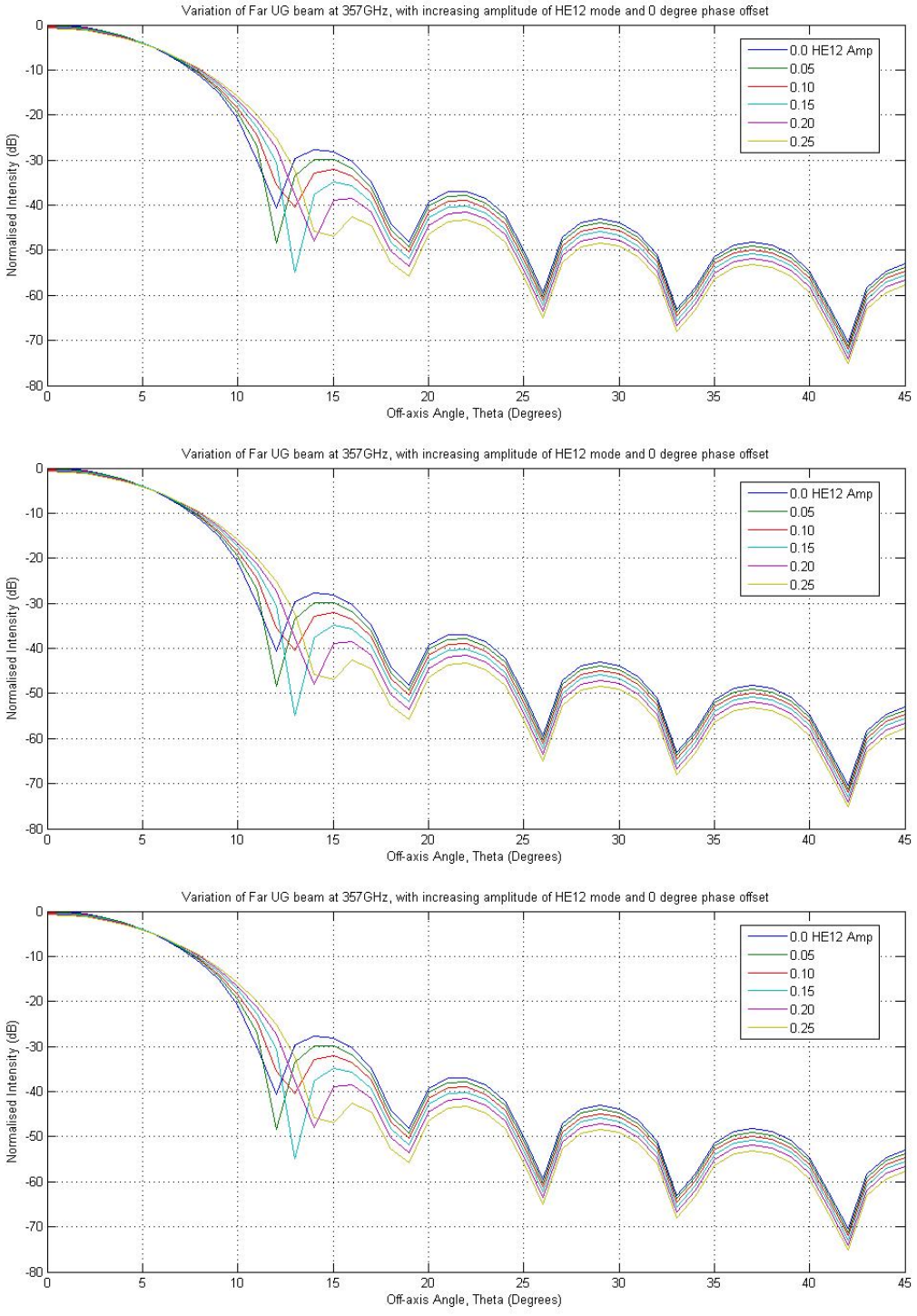

FIGURE A.4: Variation of beam pattern at 357GHz with increasing amplitude contribution from the HE_{12} mode, at 0°, 45° and 90° phase offset between HE_{11} and HE_{12} modes

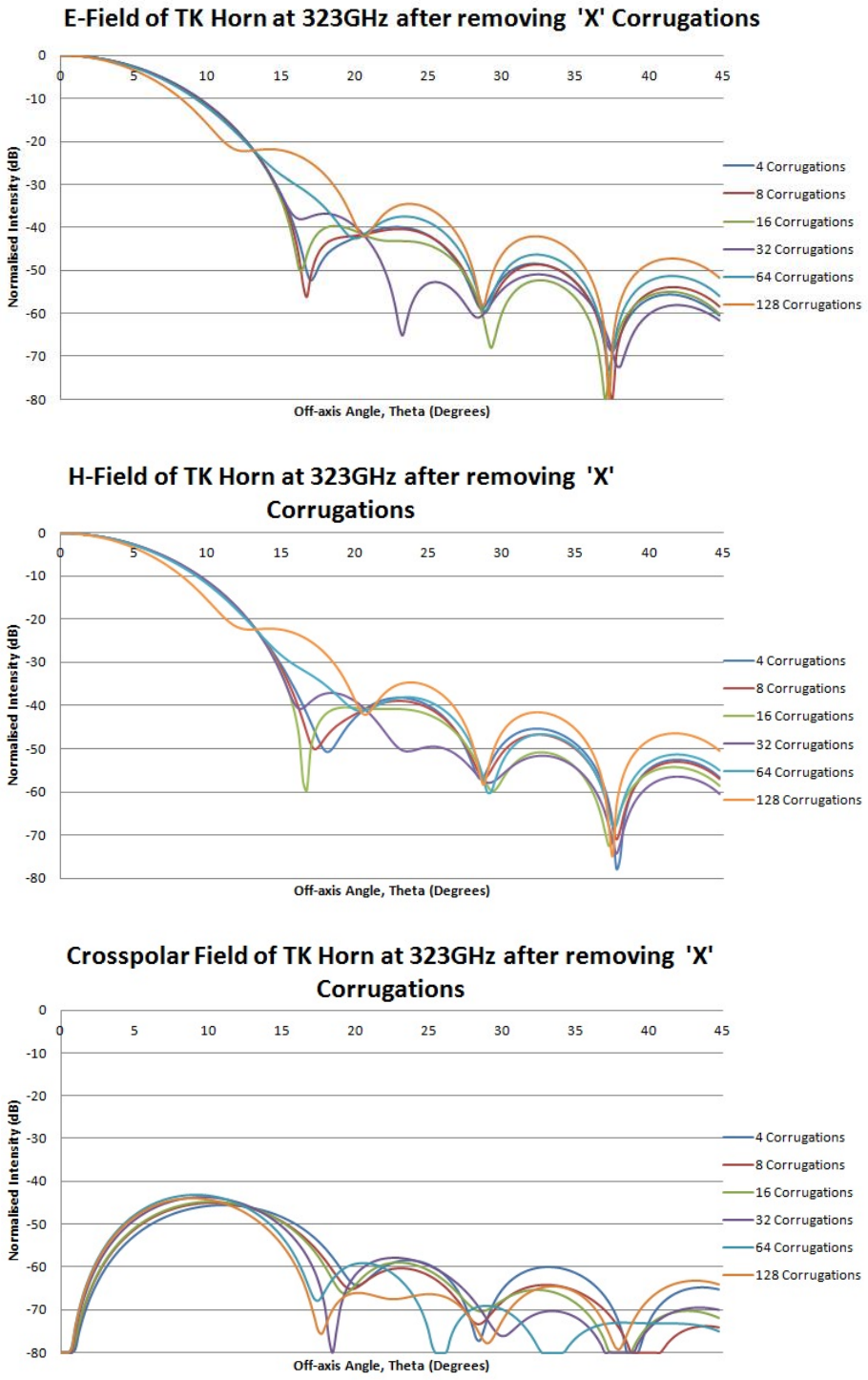

FIGURE A.5: Overlapping SCATTER far-field beam patterns at 323GHz, for varying length of the corrugated ultra-Gaussian horn ('TK Horn') after corrugations were removed

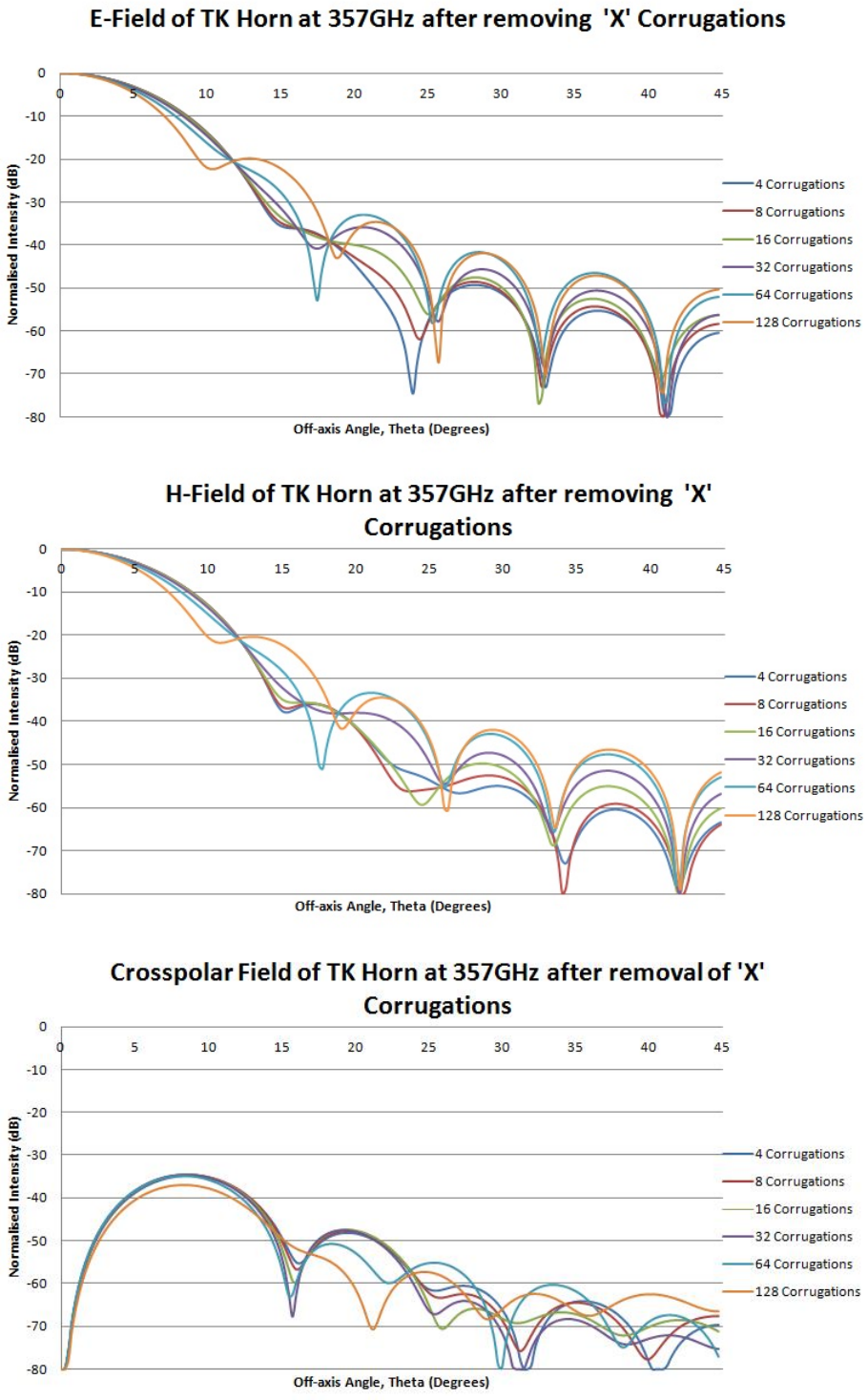

FIGURE A.6: Overlapping SCATTER far-field beam patterns at 357GHz, for varying length of the corrugated ultra-Gaussian horn ('TK Horn') after corrugations were removed

Bibliography

[1] A. Penzias and R. Wilson, "A Measurement of Excess Antenna Temperature at 4080 Mc/s.," *The Astrophysical Journal*, vol. 142, pp. 419–421, 1965.

[2] A. McKellar, "Evidence for the molecular origin of some hitherto unidentified interstellar lines," *Publications of the Astronomical Society of the Pacific*, pp. 187–192, 1940.

[3] G. Herzberg and J. Spinks, *Molecular Spectra and Molecular Structure: Diatomic Molecules*, vol. 1. Van Nostrand, 1950.

[4] A. Friedman, "On the Curvature of Space," *General Relativity and Gravitation*, vol. 31, no. 12, pp. 1991–2000, 1999.

[5] G. Lemaître, "Expansion of the Universe, The Expanding Universe," *Monthly Notices of the Royal Astronomical Society, Vol. 91, p. 490-501*, vol. 91, pp. 490–501, 1931.

[6] G. Gamow, "Expanding Universe and the Origin of Elements," *Physical Review*, vol. 70, no. 7-8, pp. 572–573, 1946.

[7] F. Hoyle, "The Synthesis of the Elements from Hydrogen," *Monthly Notices of the Royal Astronomical Society*, vol. 106, p. 343, 1946.

[8] R. Alpher and R. Herman, "Evolution of the Universe," *Nature*, vol. 162, pp. 774–775, 1948.

[9] R. Alpher and R. Herman, "Remarks on the Evolution of the Expanding Universe," *Physical Review*, vol. 75, no. 7, p. 1089, 1949.

[10] R. Dicke, P. Peebles, P. Roll, and D. Wilkinson, "Cosmic Black-Body Radiation.," *The Astrophysical Journal*, vol. 142, pp. 414–419, 1965.

[11] A. Guth, "Inflationary universe: A possible solution to the horizon and flatness problems," *Physical Review D*, vol. 23, no. 2, p. 347, 1981.

[12] G. Smoot, M. Gorenstein, and R. Muller, "Detection of Anisotropy in the Cosmic Blackbody Radiation," *Physical Review Letters*, vol. 39, no. 14, pp. 898–901, 1977.

[13] G. Smoot, C. Bennett, A. Kogut, E. Wright, J. Aymon, N. Boggess, E. Cheng, G. De Amici, S. Gulkis, M. Hauser, *et al.*, "Structure in the COBE Differential Microwave Radiometer First-Year Maps," *The Astrophysical Journal*, vol. 396, pp. L1–L5, 1992.

[14] "Harmonic Multipoles and the CMB Sky." http://find.spa.umn.edu/~pryke/logbook/20000922/. Accessed: 2014-2-25.

[15] A. Challinor, "Polarization and Weak Gravitational Lensing of the CMB," in *Polarization and Weak Gravitational Lensing of the CMB*, Xth School of Cosmology, 2010.

[16] P. Mauskopf, K. Isaak, M. Griffin, P. Hargrave, D. Morozov, A. Orlando, M. Bruijn, H. Hoevers, P. de Korte, and J. van der Kuur, "Development of TES detectors for low-background far infrared space astronomy," in *Infrared Millimeter Waves and 14th International Conference on Teraherz Electronics, 2006. IRMMW-THz 2006. Joint 31st International Conference on*, pp. 205–205, IEEE, 2006.

[17] Y. Zeldovich, "A Hypothesis, Unifying the Structure and the Entropy of the Universe," *Monthly Notices of the Royal Astronomical Society*, vol. 160, p. 1P, 1972.

[18] J. Mather, E. Cheng, R. Eplee Jr, R. Isaacman, S. Meyer, R. Shafer, R. Weiss, E. Wright, C. Bennett, N. Boggess, *et al.*, "A Preliminary Measurement of the Cosmic Microwave Background Spectrum by the Cosmic Background Explorer (COBE) Satellite," *The Astrophysical Journal*, vol. 354, pp. L37–L40, 1990.

[19] C. Netterfield, P. Ade, J. Bock, J. Bond, J. Borrill, A. Boscaleri, K. Coble, C. Contaldi, B. Crill, P. De Bernardis, *et al.*, "A Measurement by BOOMERANG of Multiple Peaks in the Angular Power Spectrum of the Cosmic Microwave Background," *The Astrophysical Journal*, vol. 571, no. 2, p. 604, 2008.

[20] J. Kovac, E. Leitch, C. Pryke, J. Carlstrom, N. Halverson, and W. Holzapfel, "Detection of Polarization in the Cosmic Microwave Background using DASI," *arXiv preprint astro-ph/0209478*, 2002.

[21] C. Bennett, M. Bay, M. Halpern, G. Hinshaw, C. Jackson, N. Jarosik, A. Kogut, M. Limon, S. Meyer, L. Page, *et al.*, "The Microwave Anisotropy Probe Mission," *The Astrophysical Journal*, vol. 583, no. 1, p. 1, 2008.

[22] C. Dickinson, R. Battye, P. Carreira, K. Cleary, R. Davies, R. Davis, R. Genova-Santos, K. Grainge, C. Gutiérrez, Y. Hafez, *et al.*, "High-sensitivity measurements

of the cosmic microwave background power spectrum with the extended Very Small Array," *Monthly Notices of the Royal Astronomical Society*, vol. 353, no. 3, pp. 732–746, 2004.

[23] T. Pearson, B. Mason, A. Readhead, M. Shepherd, J. Sievers, P. Udomprasert, J. Cartwright, A. Farmer, S. Padin, S. Myers, *et al.*, "The Anisotropy of the Microwave Background to l= 3500: Mosaic Observations with the Cosmic Background Imager," *The Astrophysical Journal*, vol. 591, no. 2, p. 556, 2008.

[24] C. Reichardt, P. Ade, J. Bock, J. Bond, J. Brevik, C. Contaldi, M. Daub, J. Dempsey, J. Goldstein, W. Holzapfel, *et al.*, "High-resolution CMB Power Spectrum from the Complete ACBAR Data Set," *The Astrophysical Journal*, vol. 694, no. 2, p. 1200, 2009.

[25] F. Bouchet, M. Piat, and J. Lamarre, "The Planck Milestone," *Comptes Rendus Physique*, vol. 4, no. 8, pp. 861–870, 2003.

[26] L. Valenziano *et al.*, "The Low Frequency Instrument on-board the Planck satellite: Characteristics and performance," *New Astronomy Reviews*, vol. 51, no. 3-4, pp. 287 – 297, 2007.

[27] J. M. Lamarre *et al.*, "The Planck High Frequency Instrument, a third generation CMB experiment, and a full sky submillimeter survey," *New Astronomy Reviews*, vol. 47, no. 11-12, pp. 1017 – 1024, 2003.

[28] J. Puget, "Planck Intro - Ecole Doctoral," 2013.

[29] G. Smoot, "Cmb synchrotron foreground," in *Microwave Foregrounds*, vol. 181, p. 61, 1999.

[30] "ESA Planck Webpage." http://sci.esa.int/planck. Accessed: 2013-08-20.

[31] P. Collaboration, P. Ade, N. Aghanim, C. Armitage-Caplan, M. Arnaud, M. Ashdown, F. Atrio-Barandela, J. Aumont, C. Baccigalupi, A. Banday, *et al.*, "Planck 2013 results. XVIII. Gravitational lensing-infrared background correlation," *arXiv preprint arXiv:1303.5078*, 2013.

[32] A. Lazarian and B. Draine, "Resonance paramagnetic relaxation and alignment of small grains," *The Astrophysical Journal Letters*, vol. 536, no. 1, p. L15, 2000.

[33] P. Collaboration, P. Ade, N. Aghanim, M. Arnaud, M. Ashdown, J. Aumont, C. Baccigalupi, A. Balbi, A. Banday, R. Barreiro, *et al.*, "Planck early results. XX. New light on anomalous microwave emission from spinning dust grains," *arXiv preprint arXiv:1101.2031*, 2011.

[34] P. Collaboration, P. Ade, N. Aghanim, C. Armitage-Caplan, M. Arnaud, M. Ashdown, F. Atrio-Barandela, J. Aumont, C. Baccigalupi, A. Banday, *et al.*, "Planck 2013 results. I. Overview of products and scientific results," *arXiv preprint arXiv:1303.5062*, 2013.

[35] "NASA Planck Webpage." http://photojournal.jpl.nasa.gov/catalog. Accessed: 2013-08-20.

[36] P. Collaboration, P. Ade, N. Aghanim, C. Armitage-Caplan, M. Arnaud, M. Ashdown, F. Atrio-Barandela, J. Aumont, C. Baccigalupi, A. Banday, *et al.*, "Planck 2013 results. XVI. Cosmological parameters," *arXiv preprint arXiv:1303.5076*, 2013.

[37] G. Hinshaw, D. Larson, E. Komatsu, D. Spergel, C. Bennett, J. Dunkley, M. Nolta, M. Halpern, R. Hill, N. Odegard, *et al.*, "Nine-year Wilkinson Microwave Anisotropy Probe (WMAP) observations: cosmological parameter results," *arXiv preprint arXiv:1212.5226*, 2012.

[38] F. Villa, M. Bersanelli, C. Burigana, R. Butler, N. Mandolesi, A. Mennella, G. Morgante, M. Sandri, L. Terenzi, and L. Valenziano, "The Planck telescope," *arXiv preprint astro-ph/0112173*, 2001.

[39] J. Tauber, N. Mandolesi, J. Puget, T. Banos, M. Bersanelli, F. Bouchet, R. Butler, J. Charra, G. Crone, J. Dodsworth, *et al.*, "Planck pre-launch status: The Planck mission," *Astronomy and Astrophysics*, vol. 520, 2010.

[40] M. Bersanelli, N. Mandolesi, R. C. Butler, A. Mennella, F. Villa, B. Aja, E. Artal, E. Artina, C. Baccigalupi, M. Balasini, *et al.*, "Planck pre-launch status: Design and description of the Low Frequency Instrument," *Astronomy and Astrophysics*, vol. 520, 2010.

[41] F. Bouchet, "The Planck High Frequency Instrument Sky," 2011.

[42] B. Maffei, F. Noviello, J. Murphy, P. Ade, J.-M. Lamarre, F. Bouchet, J. Brossard, A. Catalano, R. Colgan, R. Gispert, *et al.*, "Planck pre-launch status: Hfi beam expectations from the optical optimisation of the focal plane," *Astronomy and Astrophysics*, vol. 520, p. A12, 2010.

[43] "Jet Propulsion Laboratory, Caltech, Planck Webpage." http://planck.caltech.edu. Accessed: 2013-08-20.

[44] P. Collaboration, P. Ade, N. Aghanim, C. Armitage-Caplan, M. Arnaud, M. Ashdown, F. Atrio-Barandela, J. Aumont, C. Baccigalupi, A. Banday, *et al.*, "Planck

2013 results. VI. High Frequency Instrument data processing," *arXiv preprint arXiv:1303.5067*, 2013.

[45] J. Tauber, H. Norgaard-Nielsen, P. Ade, J. Amiri Parian, T. Banos, M. Bersanelli, C. Burigana, A. Chamballu, D. de Chambure, P. Christensen, *et al.*, "Planck pre-launch status: The optical system," *Astronomy and Astrophysics*, vol. 520, 2010.

[46] P. Collaboration, P. Ade, N. Aghanim, C. Armitage-Caplan, M. Arnaud, M. Ashdown, F. Atrio-Barandela, J. Aumont, C. Baccigalupi, A. Banday, *et al.*, "Planck 2013 results. VII. HFI time response and beams," *arXiv preprint arXiv:1303.5068*, 2013.

[47] P. Collaboration, P. Ade, N. Aghanim, C. Armitage-Caplan, M. Arnaud, M. Ashdown, F. Atrio-Barandela, J. Aumont, C. Baccigalupi, A. Banday, *et al.*, "Planck 2013 results. XIV. Zodiacal emission," *arXiv preprint arXiv:1303.5074*, 2013.

[48] G.-G. Reflector, "Antenna Farm Analysis Software," *TICRA, Læderstræde, Copenhagen, Sweden*, 2007.

[49] TICRA. http://www.ticra.com/. Accessed: 2013-12-16.

[50] G. Pilbratt, "Herschel space observatory mission overview," in *Astronomical Telescopes and Instrumentation*, pp. 586–597, International Society for Optics and Photonics, 2003.

[51] A. Wootten, "Atacama large millimeter array (ALMA)," in *Astronomical Telescopes and Instrumentation*, pp. 110–118, International Society for Optics and Photonics, 2003.

[52] K. Pontoppidan, "Grasp Technical Description," 2002.

[53] P. Clarricoats and A. Olver, *Corrugated Horns for Microwave Antennas*. IET, 1984.

[54] R. E. Collin and F. J. Zucker, *Antenna theory*. McGraw-Hill New York, 1969.

[55] P. M. Johansen, "Uniform physical theory of diffraction equivalent edge currents for implementation in general computer codes," in *Antennas and Propagation Society International Symposium, 1996. AP-S. Digest*, vol. 2, pp. 784–787, IEEE, 1996.

[56] R. G. Kouyoumjian and P. H. Pathak, "A uniform geometrical theory of diffraction for an edge in a perfectly conducting surface," *Proceedings of the IEEE*, vol. 62, no. 11, pp. 1448–1461, 1974.

[57] "All About Circuit (Volume II), Transmission Lines : Waveguides." http://www.allaboutcircuits.com/vol_2/chpt_14/8.html. Accessed: 2013-12-16.

[58] S. Ramo, J. R. Whinnery, and T. Van Duzer, *Fields and waves in communication electronics*. Wiley. com, 2007.

[59] E. Gleeson, *Single and Multi-moded Corrugated Horn Design for Cosmic Microwave Background Experiments*. PhD thesis, Ph. D. Thesis, NUI Maynooth, 2004.

[60] D. M. Pozar, "Microwave engineering, 2nd," *New York*, 1998.

[61] A. Wexler, "Solution of waveguide discontinuities by modal analysis," *Microwave Theory and Techniques, IEEE Transactions on*, vol. 15, no. 9, pp. 508–517, 1967.

[62] P. Masterman and P. Clarricoats, "Computer field-matching solution of waveguide transverse discontinuities," in *Proceedings of the Institution of Electrical Engineers*, vol. 118, pp. 51–63, IET, 1971.

[63] R. Colgan, *Electromagnetic and quasi-optical modelling of horn antennas for far-IR space applications*. PhD thesis, Ph. D. Thesis, NUI Maynooth, 2001.

[64] A. Olver, P. Clarricoats, A. Kishk, and L. Shafai, "Microwave horns and feeds, 1994."

[65] P. F. Goldsmith *et al.*, *Quasioptical systems*. Ediciones Díaz de Santos, 1998.

[66] C. Dragone, "Offset multireflector antennas with perfect pattern symmetry and polarization discrimination," *AT T Technical Journal*, vol. 57, pp. 2663–2684, 1978.

[67] "Planck RFFM Model." Received via private communications with Tully Peacocke.

[68] TICRA, "Grasp9 Multi-GTD Manual."

[69] I. MacAuley, *In preparation*. PhD thesis, Ph. D. Thesis, NUI Maynooth, 2014.

[70] P. T. Peacocke, "Optical analysis of the heterodyne instrument for the far infra-red: Methods and results," Master's thesis, Masters Thesis, NUI Maynooth, 2007.

[71] M. Wolf and E. Born, *Principles of optics: electromagnetic theory of propagation, interference and diffraction of light*. Cambridge: University Press, 1980.

[72] P. Nielsen, "Planck Telescope RF Performance Independent Verification Phase1 RF performance from measured mirrors," 2005.

[73] P. Nielsen, "Rf effect of core print-through distortion on the PLANCK telescope," tech. rep., S-801-05, dated Marts, 2000.

[74] G. Serra, M. Giard, F. Bouchou, X. Dupac, F. Gabarrot, C. Meny, I. Ristorcelli, J. Lamarre, J. Bernard, F. Pajot, B. Stepnick, and J. Torre, "{PRONAOS} : a two meter submillimeter balloon borne telescope," *Advances in Space Research*, vol. 30, no. 5, pp. 1297 – 1305, 2002.

[75] P. Ade, L. Moncelsi, G. Savini, and J. Zhang, "Cardiff Multimoded Beam Measurements," in *Planck HFI Core Team Meeting - July 2008*, 2008.

[76] F. P. Helmich and R. Ivison, "Firia far-infrared interferometer," *Experimental Astronomy*, vol. 23, no. 1, pp. 245–276, 2009.

[77] W. F. Grainger, R. Juanola-Parramon, P. A. Ade, M. Griffin, F. Liggins, E. Pascale, G. Savini, and B. Swinyard, "Demonstration of spectral and spatial interferometry at thz frequencies," *Applied Optics*, vol. 51, no. 12, pp. 2202–2211, 2012.

[78] A. O'Donoghue, *In preparation.* PhD thesis, Ph. D. Thesis, NUI Maynooth, 2014.

[79] F. v. Schéele, U. Frisk, and S. Veldman, "The steam project," in *Small Satellites for Earth Observation: Selected Proceedings of the 5th International Symposium of the International Academy of Astronautics, Berlin, April 4-8 2005*, p. 263, Walter de Gruyter, 2005.

[80] Mician. http://www.mician.com/cms/. Accessed: 2013-12-9.

[81] M. R. Schoeberl, A. R. Douglass, E. Hilsenrath, P. K. Bhartia, R. Beer, J. W. Waters, M. R. Gunson, L. Froidevaux, J. C. Gille, J. J. Barnett, *et al.*, "Overview of the EOS Aura mission," *Geoscience and Remote Sensing, IEEE Transactions on*, vol. 44, no. 5, pp. 1066–1074, 2006.

[82] D. Murtagh *et al.*, "An overview of the Odin atmospheric mission," *Canadian Journal of Physics*, vol. 80, no. 4, pp. 309–319, 2002.

[83] M. Whale, M. Renker, A. Murk, O. Janson, and U. Frisk, "Optical design of the stratosphere-troposphere exchange and climate monitor radiometer (steamr) instrument," in *Antennas and Propagation (EUCAP), Proceedings of the 5th European Conference on*, pp. 275–279, IEEE, 2011.

[84] P. Sobis, A. Emrich, and J. Stake, "A 340 GHz 2SB Schottky receiver for the STEAMR limb sounder," in *Infrared Millimeter and Terahertz Waves (IRMMW-THz), 2010 35th International Conference on*, pp. 1 –2, 2010.

[85] P. Sobis, A. Emrich, and M. Hjort, "Steamr Receiver Chain," in *20th International Symposium on Space Terahertz Technology*, pp. 320–325, 2009.

[86] A. Wagner-Gentner, U. Graf, M. Philipp, and D. Rabanus, "A simple method to design astigmatic off-axis mirrors," *Infrared Physics and Technology*, vol. 50, no. 1, pp. 42 – 46, 2007.

[87] M. Whale, M. Renker, A. Murk, O. Janson, and U. Frisk, "Optical design of the stratosphere-troposphere exchange and climate monitor radiometer (STEAMR) instrument," in *Antennas and Propagation (EUCAP), Proceedings of the 5th European Conference on*, pp. 275 –279, 2011.

[88] P. Ade, R. Wylde, and J. Zhang, "Ultra-gaussian horns for clover–a b-mode cmb experiment," in *Twentieth International Symposium on Space Terahertz Technology, edited by: Bryerton, E., Kerr, A., and Lichtenberger, A., Charlottesville*, pp. 20–22, 2009.

[89] "TK Limited Ultra-Gaussian Corrugated Horns." http://www.terahertz.co.uk/index.php?option=com_content&view=article&id=189&Itemid=567. Accessed: 2013-12-9.

[90] P. A. Ade, R. J. Wylde, and J. Zhang, "Ultra-Gaussian Horns for ClOVER a B-Mode CMB Experiment," in *20th International Symposium on Space Terahertz Technology*, pp. 128–137, 2009.